Aperture Synthesis Observations of Low-mass Protostars in the Taurus Molecular Cloud:

Formation Processes of Protoplanetary Disks in Protostellar Envelopes

A dissertation presented
by

YOKOGAWA Sozo

Department of Astronomical Science,
School of Mathematical and Physical Science,
The Graduate University for Advanced Studies

2003

Acknowledgement

First of all, I would like to express my gratitude to Prof. Ryohei Kawabe, my supervisor, for his continuous encouragement and invaluable comments. I also thank Drs. Yoshimi Kitamura, Munetake Momose for their invaluable suggestions and comments on this work.

I thank Prof. Masato Ishiguro, Drs. Koh-Ichiro Morita, Sachiko K. Okumura, Kotaro Kohno, Koichiro Nakanishi, Takeshi Kamazaki for their effort to opperate the Nobeyama Millimeter Array. I am greatful to Hiroyuki Iwashita, Kazuyuki Handa, Toshikazu Takahashi, Naohisa Sato, Kiyoshi Nakajima for their excellent technical works for the Nobeyama Millimeter Array.

I also thank Dr. Yutaro Sekimoto for his teaching of radio astronomy, especially receiver developements. I have learned so much from discussion with Drs. Masato Saito, Hajime Ezawa, Nobuyuki Yamaguchi, Kazuyoshi Sunada, Nobuharu Ukita, Seiichi Sakamoto, Ken'nichi Tatematsu, Satoru Iguchi, Motohide Tamura, Shigeru Ida, and Tesuo Hasegawa. I also thank all of the ALMA-J office and the NRO members for their friendly help and encouragement.

I thank Toshihito Shibatsuka, Tomoki Saito, Masato Bando, Jin Koda, Tsuyoshi Sawada, Masahiro Sugimoto, Tomohiko Sekiguchi, Takeshi Okuda, Ryo Kandori, Sachiko Onodera for their fruitful discussions and encouragement.

Finally, I would like to thank my friends and family for their continuous support and encouragement.

Abstract

Formation process of a protoplanetary disk around a low-mass YSO is one of the most interesting issues in modern astronomy, which is deeply related to the origin of the solar system. Although previous survey observations of low-mass YSOs have revealed evolution from protostar phase to T Tauri star phase, such as dissipations of envelope gases, dust concentrations from envelopes to circumstellar disks, and expansion of accretion disks. However, the formation process of a protoplanetary disk, how and when the protoplanetary disk has formed, is not still understood.

In this thesis, I examine the structure and evolution of circumstellar envelopes and disks around protostars to reveal the formation process of a protoplanetary disk in a protostellar envelope through aperture synthesis observations of low-mass YSOs in the Taurus Molecular Cloud (TMC).

In the chapter I, since protoplanetary disks have large diversity of disk masses, radii and angular momenta, we tried to reveal one of the causes of the diversity: the outflow-triggered star formation in low-mass star-forming regions. We performed CS $J = 2 - 1$ and $J = 3 - 2$ observations of the class 0 protostar L1551 NE to investigate the interaction feature between L1551 NE and the outflow of the nearby protostar L1551 IRS 5, since L1551 NE is deeply embedded in the outflow of L1551 IRS 5. Significant CS emission around L1551 NE was detected at the eastern tip of the swept-up shell of the outflow of L1551 IRS 5, and the following new structures were successfully revealed: a compact disklike component with a size of ≈ 1000 AU just at L1551 NE, an arc-shaped structure around L1551 NE, open toward L1551 NE, with a size of ~ 5000 AU, i.e., a bow shock, and a distinct velocity gradient of the dense gas, i.e., deceleration along the outflow axis of L1551 IRS 5. Since the age of L1551 NE is comparable to the timescale of the interaction, it is plausible that the formation of L1551 NE was induced by the outflow impact. This is a first case of the outflow-triggered star formation in low-mass star forming regions.

In the following chapters II and III, we presented the results of aperture synthesis observa-

tions of ^{13}CO ($J = 1-0$) and ($J = 2-1$) line emissions toward the binary protostar L1551 IRS 5 and the single protostar HL Tau. ^{13}CO ($J = 1-0$) observations of L1551 IRS 5 have revealed the centrally condensed envelope. The envelope shows infall and rotation motion toward the central sources. The infall velocity of the envelope is consistent to the free-fall velocity around a central mass of $\approx 0.5\ M_{\odot}$, whereas the rotational velocity has a radial dependence of r^{-1}, suggesting the specific angular momentum of the gases has conversed during the contraction of the envelope. Furthermore, the ^{13}CO ($J = 2 - 1$) observations of L1551 IRS 5 show a disklike structure in the central part of the envelope. A distinct velocity gradient is detected along the major axis of the structure, whereas no prominent gradient is detected along the minor axis, suggesting a purely rotating disk. The disk radius estimated to be ≈ 500 AU. This radius is significantly larger than the centrifugal radius derived from the local specific angular momentum of the envelope of L1551 IRS 5, although a Keplerian disk is theoretically thought to form with the centrifugal radius in the envelope. The turbulent viscosity with a large coefficient of $\alpha \sim 1$ is likely to make a small disk with the centrifugal radius efficiently expand, whereas the gravitational interaction between the disk and the binary sources would not be efficient. It is also possible that the natal core of IRS 5 was not rigidly rotating but more rapidly rotating with large specific angular momentum in the inner part of the core.

^{13}CO ($J = 1 - 0$) observations of HL Tau have revealed the extended infalling envelope. A velocity gradient of the emission clearly aligns the minor axis of the envelope, whereas no prominent gradient is detected along the major axis of the envelope, suggesting that the envelope around HL Tau is almost infalling. Even in ^{13}CO ($J = 2 - 1$) imaging, a rotational disklike component could not be found, suggesting that a Keplerian rotating disk around HL Tau seems to be as small as 100 AU and is likely to be comparable to the typical centrifugal radius of the low mass YSOs in the TMC. In the chapter IV, we presented the ^{13}CO ($J = 1-0$) observations of the protostar Haro 6-5B. Although Haro 6-5B is considered as a protostar, only a compact disklike structure which exhibits rotation motion is detected with a tiny extended envelope, suggesting that most of the envelope has already dissipated. Since the rotation radius of Haro 6-5B is ≈ 400 AU which is comparable to that of L1551 IRS 5, Haro 6-5B might be a binary protostars.

In the chapter V, we examine the physical properties of low-mass YSOs, both our samples and the data of previous studies, to reveal a formation mechanism of a protoplanetary disk. In the case studies of a binary protostar L1551 IRS 5 and a single protostar HL Tau as describe in the chapter II and III, the rotation disk around L1551 IRS 5 is clearly revealed, whereas that around HL Tau is not detected. Furthermore, the envelope around L1551 IRS 5 shows

rotation motion with infall motion, whereas that around HL Tau shows almost only rotating, suggesting that the large amount of local specific angular momenta of envelopes might form a binary system and a large rotating disk. A comparison of the local specific angular momenta between single stars and binary systems, however, shows no obvious difference. These results suggest that differences between binary system and single star formations are quite subtle distinctions of physical properties of protostellar cores and envelopes.

Contents

Chapter 1

General Introduction

1.1 Historical Overview

Low-mass star formation is one of the most interesting issues in modern astronomy, which is deeply related to the origin of the solar system. The history of this issue, however, is not long-standing, and the scenario of low-mass star formation based on theoretical studies was proposed in the latter half of 1960s. Understanding of early evolution of low-mass stars has blossomed in the last few decade owing to improved observational techniques, particularly in infrared and millimeter/ submillimeter wavelengths. A breakthrough was brought by the IRAS (Infrared Astronomical Satellite), the all-sky survey telescope launched in 1983, which was operated at λ = 12, 25, 60 and 100 μm. One of the most important results of the IRAS concerning low-mass star formations is the discovery of excess emission from YSOs in these wavelengths. The excess emission was detected from more than a half of YSOs in nearby star-forming regions and their spectral energy distributions (SEDs) indicated that their emission was originated from circumstellar disks whose radii within a several $\times$ 100 AU. These disks seem to be nurseries of the planetary systems, and so called as "protoplanetary disks" which will form planetary systems in the future. After the IRAS era, the observations in millimeter and submillimeter wavelengths have progressed understanding of low-mass star formations further. The survey observations of low-mass YSOs at 1.3 mm wavelength with the IRAM 30 m telescope toward the Taurus-Auriga Molecular Cloud have revealed that the circumstellar disk mass ranges from 0.001 $M_{\odot}$ to 0.1 $M_{\odot}$ (Beckwith et al. 1990; Beckwith & Sargent 1996). As a result, the presence of circumstellar disks around low-mass YSOs has been widely accepted, and their physical parameters are consistent with those of the standard model of low-mass star formation (e.g., Hayashi et al. 1985). In 1990s, high spatial resolution imagings of YSOs have been performed using millimeter wave interferometers. Observations with molecular line emission such as CO(J=1-0) and its isotopes have directly revealed the presence of the Keplerian rotating disks around T Tauri stars whose radii of a several $\times$ 100 AU (e.g., Kawabe et al. 1993; Guilloteau et al. 1998; Dutrey et al. 1998). Observations of protostars have revealed extended envelopes with radii of a several $\times$ 1000 AU which exhibit infall motions toward the central stars (e.g., Hayashi et al. 1993; Saito et al. 1996). Typical mass accretion rate onto the central star/ disk system is estimated to be $\sim 5 \times 10^{-6}\ M_{\odot}\ \mathrm{yr}^{-1}$, and local specific angular momenta of the envelopes are of the order of $\sim 10^{-3}$ km s^{-1} pc. These specific angular momenta of infalling envelopes and rotationally supported disks are relatively constant, and are typically an order of magnitude smaller than those of molecular cloud cores. These results suggest if the dynamical collapse of molecular cloud cores take place inside radii of $\sim$ 0.03

pc while the region outside the radius remains dynamically stable (Ohashi et al. 1997). In addition, the detailed studies of the infalling envelope toward the protostar L1551 IRS 5 were performed by Momose et al. (1998). They revealed: 1) the velocity structure of the envelope are well explained with the combination of infall and rotational motion around the central stars. 2) the infall motions are well fitted with a radial dependence of r^{-1} rather than that of $r^{-1/2}$, suggesting the envelope contracts with conservation of the specific angular momentum of the envelope. Furthermore, survey observations toward YSOs have been performed, and millimeter continuum survey showed that the dust emission around protostar candidates is more extended than that around T Tauri stars (Ohashi et al. 1991, 1996; Looney, Mundy & Welch 2000), suggesting that disks as well as central stars grow by accretion of matter. More recently, high angular resolution imaging survey toward T Tauri stars have revealed the radial expansion of the accretion disk around T Tauri stars with decreasing their accretion luminosities (Kitamura et al. 2002).

1.2 Scenario of low-mass star formations

In this section, I briefly introduce the scenario of early evolution of low-mass stars. Overview of low-mass star formations is summarized in Figure 1.1. A start point of low-mass star formation is molecular cloud cores whose masses of order of $\sim$ several $\times M_{\odot}$, radii of $\sim$ several $\times 10^4$ AU (~ 0.1 pc) and temperatures of $10-30$ K. These cores are initially balanced between the self-gravities, inner pressures and outer pressures. However, they become gravitationally unstable and collapses will ensue when the balance has lost owing to such as magnetic field diffusion, some compression from outer environment. After the collapse of a core, a stage which the central stellar core contracts quasi-statically or dynamically succeeds (e.g., Hayashi et al. 1966: Shu et al. 1977: Larson et al. 1969). A YSO in the former stage is called as "protostellar core" and in the latter stage are called as "protostar", respectively. Protostars are usually surrounded by massive "envelopes" whose radius of $\sim$ several $\times$ 1000 AU, exhibiting infall motions toward the central stars and are also accompanied by active molecular outflows. Although young protostars have collimated outflows, as they evolve, the opening angle of their outflows has become widely spread and finally envelopes are dissipated by the outflow activities. After the protostellar phase, visible T Tauri stars which surrounded by circumstellar disks have appeared.

YSOs are frequently classified based on the shape of the spectral energy distributions (SEDs) from near- to far-infrared wavelengths, which emphasizes the properties of circumstellar

dust (Lada 1987; Wilking et al. 1989). The classification of classes I, II, III are defined as the shape of SEDs at the range of $1 - 10\mu$m as follows by Adams et al. (1987) (see also Figure 1.2):

$$n = \frac{d\log(\nu F_\nu)}{d\log(\nu)} = \frac{d\log(\lambda F_\lambda)}{d\log(\lambda)} \tag{1.1}$$

Class I YSOs have the indices "n" from 0 to 3, class II YSOs have those from -2 to 0 and class III YSOs have those from -3 to -2. After the introduction of these classes, much younger objects which are undetected at wavelengths shorter than 10 μm were discovered, and now those YSOs are classified as class 0 objects. The SEDs of the class 0 objects are well fitted by thermal radiation from cold blackbodies ($\sim$ several $\times$ 10 K). The central star and disk have grown through mass accretion from the envelope, and the accreted matter and its angular momentum have released through the powerful bipolar outflows. Typical age of the class 0 objects is $\sim 10^4$ yr. As they evolve, the outflow activities have been dispersing surrounding envelope. Although these evolved protostars accompanies by active outflow, the SEDs become much hotter, and are categorized as class I objects. Class 0 and I objects are corresponding to protostellar phase. Typical age of the class I object is $\sim 10^5$ yr. After the protostellar phase, the outflow activities have calmed down and the envelopes surrounding the central sources have dispersed, and visible T Tauri stars (classical T Tauri stars: CTTSs) are appeared, which is categorized as class II object. Most of CTTSs accompany by the circumstellar disks which exhibit Keplerian rotations and these disks are so called as protoplanetary disks. Typical age of the class II object is $\sim 10^6$ yr. Typical radii and masses of circumstellar disks around T Tauri stars are $\sim$ several $\times$ 100 AU and $0.001M_\odot - 0.1M_\odot$. When turbulences in these disks were settled, dust laryers formed at the mid-plane of the disks and coagulation of the dust particles has progressed and planetesimals have formed, and the IR excess emission has disappeared. These stars are called a weak-line T Tauri stars (WTTSs) and are categorized as the class III objects. Typical age of the class III object is $\sim 10^7$ yr. The distinction between CTTS and WTTS is made on the basis of H_α equivalent width (FWHM); CTTS has the line width wider than 10 $\mathring{A}$, whereas WTTS has one narrower than 10 $\mathring{A}$.

Evolution of the circumstellar disk masses around low-mass YSOs is shown in Figure 1.3. Although disk masses of protostars are poorly determined owing to the difficulty to separate disk components and envelope components, the data illustrate rough trend of the mass evolution around YSOs. CTTSs or class II objects whose ages are roughly order of $\sim 10^6$ yrs show their masses ranging from $0.001M_\odot - 0.1M_\odot$, but no apparent trends of evolution can be seen. Succeeding phase of WTTSs or class III ($\sim 10^7$ yrs), the distinct decrease of the disk mass can

be seen, suggesting that disappearance of the dust emission has occurred in this phase. This might be indicate that coagulation of the dust particles or planetesimal formation occurs in protoplanetary disks in this phase.

1.3 Motive of this thesis

Although previous survey observations of thermal emission from dust grains or line emission from molecules have revealed evolution from protostar phase to T Tauri star phase, such as dissipations of envelope gases, dust concentrations from extended envelopes to concentrated circumstellar disks, there still remain a lot of puzzle to be solved. In this thesis, I focus on the following issues.

1. How and when a Keplerian rotating disk (i.e., protoplanetary disk) has formed in a protostellar envelope ? Although infalling envelopes with rotational motions have been found toward several protostars recently, a protoplanetary disk which embedded in an envelope has not still discovered. To reveal a formation process of a Keplerian rotating disk in a infalling envelope, we tried to detect a rotating disk in an envelope using high-J transition molecular emission of ^{13}CO ($J = 2 - 1$).

2. What physical properties results in the formations of a single star and binary/ multiple stars. More than a half of YSOs in the Taurus Molecular Cloud accompany with binary or multiple systems. Is there any difference of disk radii, masses, and angular momenta between single protostars and binary protostars ?

3. Do low-mass star formations really occur spontaneously and progress in isolated environments ? Recent observations have revealed that dozens of parsec-scale Herbig-Haro flows driven by low-mass young stars, and they are thought to disrupt surrounding molecular cloud cores, suggesting that outflows can play important roles in neighboring star formation even in low-mass star forming regions. This star formation scenario will provide diversity of masses, sizes and angular momenta of protoplanetary disks or envelopes.

This thesis consists of 5 chapters. Each chapter presents observational studies of YSOs corresponding to successive stages of evolution from a class 0 object to a transient objects from class I to II phase. The outline of the thesis is as follows:

In the chapter I, aperture synthesis CS $J = 2 - 1$ and $J = 3 - 2$ observations of the class 0 protostar L1551 NE are presented. It is widely accepted that star formations in low-mass star

forming regions occur spontaneously under quasi static environment, the formation of L1551 NE, however, seems to be strongly affected by the outflow driven by L1551 IRS 5. This might be the first case of the outflow-induced star formation in low-mass star forming regions.

In the chapter II and III, aperture synthesis ^{13}CO $J = 2 - 1$ and $J = 1 - 0$ observations of the protostar L1551 IRS 5 and HL Tau are presented to reveal a Keplerian rotating disk in the infalling envelope. L1551 IRS 5 is a binary system and HL Tau is a single star.

In the chapter IV, aperture synthesis ^{13}CO($J = 1 - 0$) and millimeter continuum observations of the protostar Haro 6-5B are presented. ^{13}CO observations revealed the presence of a Keplerian rotating disk around Haro 6-5B without an infalling envelope, suggesting that Haro 6-5B is a transient source from protostar phase to classical T Tauri phase.

After I described each star in these chapters, I summarized this thesis in the chapter V.

1.4 Previous studies of the individual sources

1.4.1 Overview of the L1551 dark cloud

Individual sources of L1551 IRS 5, L1551 NE, and HL Tau except Haro 6-5B belong to the L1551 dark cloud complex. The 2MASS near-infrared image of the L1551 dark cloud region is shown in Figure 1.4. IRS 5, the brightest class I protostar of $\approx 30\ L_\odot$ in the Taurus Molecular Cloud (hereinafter TMC), can be seen as the bright yellow shrouded source at the center of the image. NE is the bright class 0 or I protstar and can be seen as the reddish object to the $150''$ northeast of IRS 5. Because IRS 5 and NE are deeply embedded in the dense dust and molecular gas, their emission is reprocessed into long-wavelength such as far-infrared and millimeter wavelengths. Even at near-IR wavelengths, the young stars themselves are not detectable, but associated reflected nebular can be detected. The blue-greenish emission fanning out to southwest of IRS 5 traces a outflow from that source. IRS 5 is evolved enough that its jet-like outflow has possibly excavated a cavity with large opening angle in the ambient medium. NE also has fan-shaped nebulosity extending to the southwest, but much of nebulosity is likely reflected light, possibly tracing an outflow blown cavity. The two bright stars to the north are the binary T Tauri star XZ Tau and the protostar candidate HL Tau.

Figure 1.5 is the total integrated intensity map of ^{13}CO (J=1-0) of L1551 dark cloud whose size of $20' \times 30'$ ($\sim$ 1pc) containing several YSOs. The positions of the individual sources are $(\alpha_{\rm B1950}, \delta_{\rm B1950}) = (04^h28^m40^s.2, +18°01'42'')$ for IRS 5. $(\alpha_{\rm B1950}, \delta_{\rm B1950}) = (04^h28^m50^s.6, +18°02'09'')$ for NE $(\alpha_{\rm B1950}, \delta_{\rm B1950}) = (04^h28^m44^s.4, +18°07'35'')$ for HL Tau.

It can be found that cavity structures which located to the southwest of IRS 5 and northeast of NE, suggesting that the outflows from the protostar has excavated the ambient gases. A cavity structure is also seen at the northeast of HL Tau.

1.4.2 L1551 NE

L1551 NE, which was discovered by Emerson et al. (1984), is the second brightest protostar ($L_{\rm bol} \approx 6L_{\odot}$) in the TMC, and is categorized as a class 0 or class I object (e.g., Barsony & Chandler 1993). The near-infrared image of NE shows a fan-shaped nebulosity extending to the southwest as in Figure 1.6. NE is located at $\sim 2'$ nouth-east to IRS 5 and is deeply embedded in the red-shifted outflow of IRS 5. Previous observations have revealed the interaction feature between NE and the outflow lobe of IRS 5: high-velocity CS emission was detected around NE, and the distribution of the emission has a clumpy and shell-like structure open toward IRS 5, suggesting that the swept-up shell of IRS 5's outflow has impacted on NE (Plambeck & Snell 1995). High angular resolution observations at $\lambda = 3.6$ cm have revealed that NE is a close binary of sources A and B with a separation of $0\farcs5$ at P.A. of 297° as shown in Figure 1.7 (Reipurth et al. 2002). The sources are likely to drive Harbig-Haro objects HH 28, HH 29, and HH 454 as well as the well collimated infrared [Fe II] jet (Devine et al. 1999; Reipurth et al. 2000). Recently, a X-ray emission associated to NE has found as shown in Figure 1.8, whose properties are as follows: 40 events with a distinctly hard spectrum extending to 7 keV, with soft energy cutoff around $2.0 - 2.5$ keV. This implies $\log N_H \sim 22.0 - 23.0$ cm^{-2}, or $A_V \sim$ tens, consistent with an origin from the protostar itself (Bally, Feigelson, & Reipurth 2003).

1.4.3 L1551 IRS 5

L1551 IRS 5 is the most luminous protostar in the TMC, whose bolometric luminosity is $\sim 30\ L_{\odot}$, with a massive molecular outflow and a large scale envelope (Snell, Loren & Plambeck et al. 1980; Kaifu et al. 1984). The spectral energy distribution (SED) of IRS 5 is classified as class I object. High resolution observations at 7 mm radio continuum with the VLA have revealed that IRS 5 is a protobinary system as shown in Figure 1.9 (Rodriguez et al. 1998). The projected separation of the binary is about $0\farcs3$ (~ 40 AU at the TMC), and each emission shows slightly elongated structure with diameters ~ 20 AU, which presumably are the circumstellar disk of a binary system. The proper motion of these binary has been monitored since 1983, and the binary mass is estimated to be $1.2M_{\odot}$ though it contains large ambiguity (Rodriguez et al. 2002). Near-infrared observations with subarcsecond resolutions

have also revealed the detailed structure of the reflection nebula around IRS 5 and the twin jets originated from those binary as shown in Figure 1.10 (Itoh et al. 2000). Recently, X-ray emission associated with a protostellar jet emanating from L1551 IRS 5 has been detected as shown in Figure 1.11 (Bally et al. 2003). The X-ray emission is unlikely associated with IRS 5 for the following reasons: First, the X-ray source is displaced from IRS 5 by $0\farcs5 - 1\farcs0$ to the southwest along the jet axis. Second, IRS 5 is deeply embedded in circumstellar matter and the X-ray spectrum is inconsistent with the column density of foreground material required to obscure IRS 5. Additionally, the X-ray source appears to be marginally resolved with an extension along the jet axis. The spectroscopic study of HH 154 jet of IRS 5 consists of predominantly low velocity [Fe II] emission with $V_{\rm lsr} \approx 100$ km s^{-1}, whereas a fast component of [Fe II] emisson $V_{\rm lsr} \approx 350$ km s^{-1} first appears at $0\farcs5 - 1\farcs0$ southwest to the source and gets brighter downstream as shown in Figure 1.12 (Pyo et al. 2002). The millimeter interferometric observations have also revealed detail structure around IRS 5. Thermal dust emission have revealed the presence of a compact disk with $100 \sim 400$ AU radius (Keene & Musson, 1990). Observations of molecular line emission have revealed the detail kinematics of the envelope as shown in Figure 1.13, suggesting that the envelope has rotating and infalling motion. The conservation of the specific angular momentum of the envelope gas during the infall has also revealed (Momose et al. 1998).

1.4.4 HL Tauri

HL Tau used to be an archetype of the flat spectrum T Tauri star, and now is regarded as a class I transient source from protostar to classical T Tauri star, whose $L_{\rm bol} \approx 7.6 L_{\odot}$. HL Tau is entirely reflection nebulosity at optical wavelengths, with no visible star as shown in Figure 1.14. Since the VLA observations of HL Tau could not found any companions, suggesting that HL Tau is a single star as shown in Figure 1.15. Previous ^{13}CO ($J = 1 - 0$) observations of HL Tau have revealed an extended gas envelope elongated perpendicular to the optical jet emerging from the star as shown in Figure 1.16. The size of the envelope is ~ 2000 AU, and it revealed the infall motion with rotational motion as shown in Figure 1.17. Furthermore, a wide field mozicing imaging of ^{13}CO ($J = 1 - 0$) emission around HL Tau as large as $3' \times 3'$ with the BIMA array have revealed the shell structure around XZ Tau and HL Tau. The distribution of the emission around HL Tau shifted to south-west, might suggesting the gas compressed from XZ Tau activities 1.18.

1.4.5 Haro 6-5B

Haro 6-5B is a member of the FS Tau system in the TMC, and was discovered by Mundt et al. (1984) as a Harbig-Haro object (HH157) located at the apex of the cone-like reflection nebulosity extending to the northeast, and the bipolar optical jet extends at P.A.= 54° (Mundt, Brugel, & Bührke 1987). In addition, Haro 6-5B has a strong optical polarization ($\sim$ 9%) oriented at P.A. = 147 $\pm$ 7°, which is perpendicular to the jet (Gledhill, Warren-Smith, & Scarrot 1986). Recently, high angular resolution images at visible and near-infrared (NIR) wavelengths taken by the Hubble Space Telescope (HST) revealed a dark lane, which probably corresponds to a dust disk around Haro 6-5B as shown in Figure 1.19, 1.20 (Krist et al. 1998; Padgett et al. 1999). The disk radius and inclination angle derived from the HST images are 250-300 AU and 70-80° (0° for face-on), respectively. Millimeter observations made by Osterloh and Beckwith (1995) and Reipurth et al. (1993) with single dish telescopes detected strong continuum emission toward Haro 6-5B, also suggesting that the circumstellar matter exists around this young star. The ^{13}CO imaging were also made by Dutrey et al.(1996), and the compact emission is detected around both Haro 6-5B and FS Tau A. However, insufficient sensitivity and velocity resolution pretend to reveal the detail spatial and velocity structure around the system.

CHAPTER 1. FIGURES

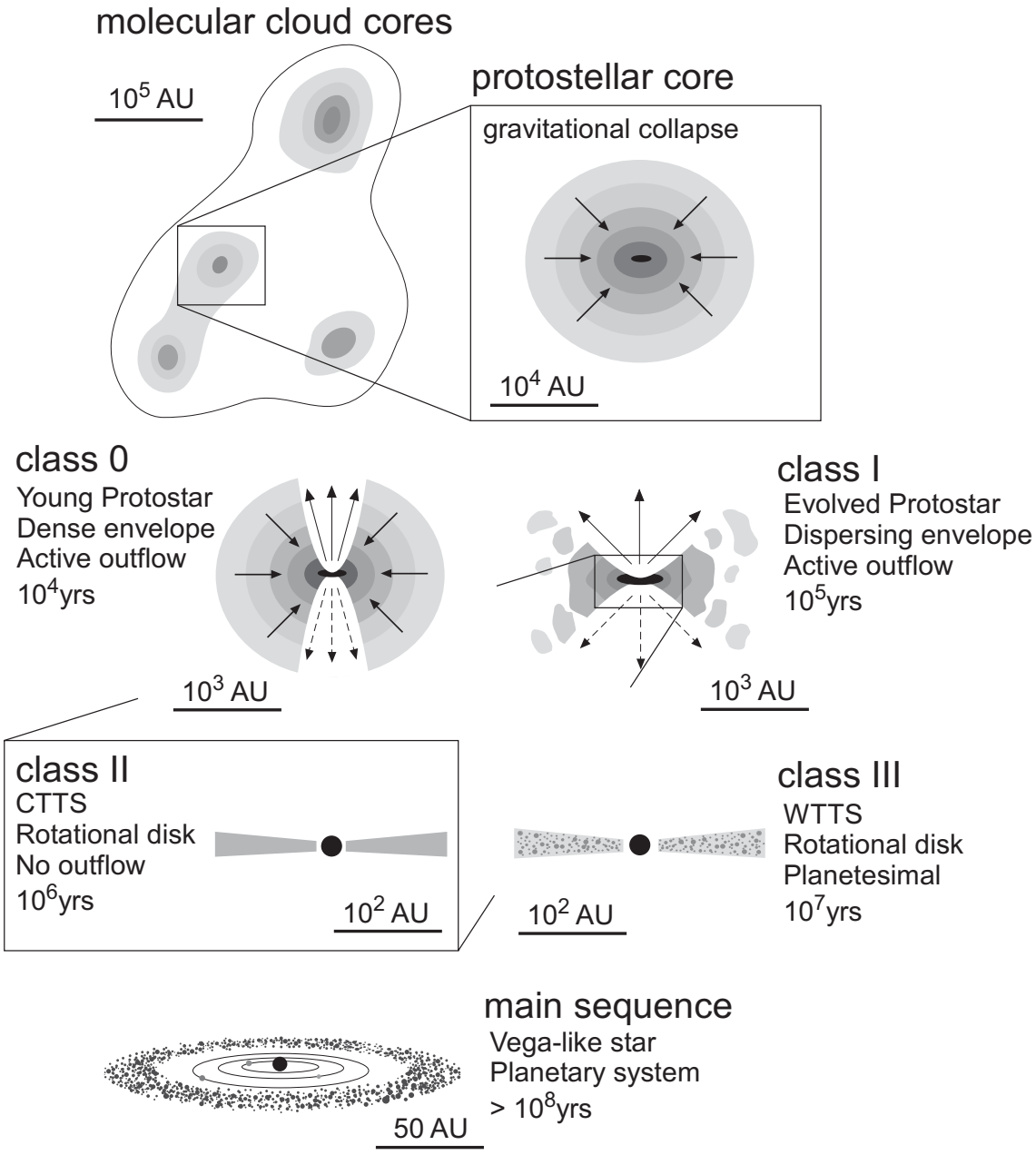

Figure 1.1: A schematic illustration of the evolution of a low-mass star from the molecular cloud core phase to the main-sequence phase.

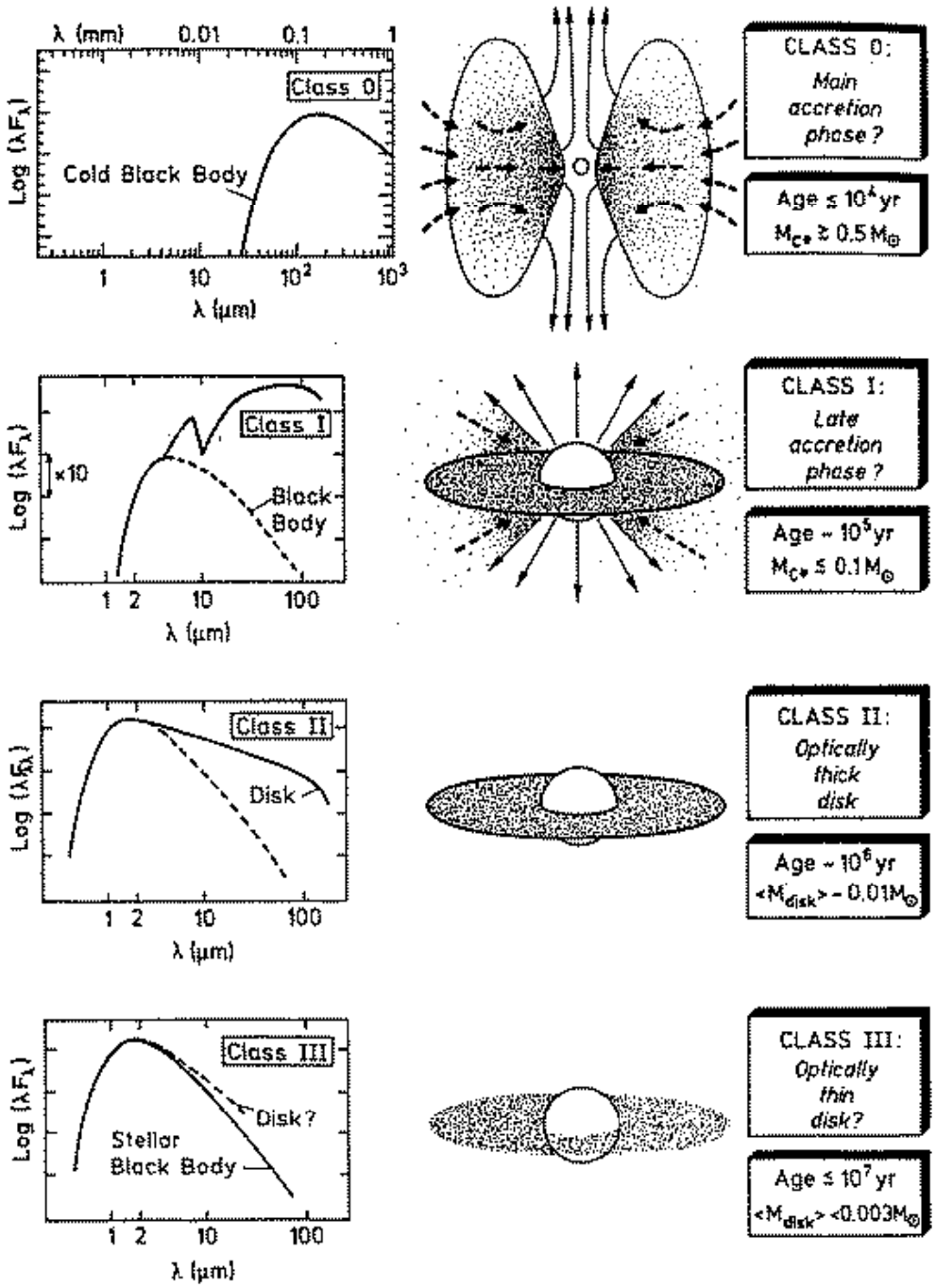

Figure 11 Evolutionary sequence of the spectral energy distributions for low-mass YSOs as proposed by André (1994). The four classes 0, I, II, and III correspond to successive stages of evolution.

Figure 1.2: Evolutionary sequence of the spectral energy distributions of low-mass YSOs. The four classes 0, I, II and III correspond to successive stages of evolution. (Lada 1987; Andre, Ward-Thompson, & Barsony 1993)

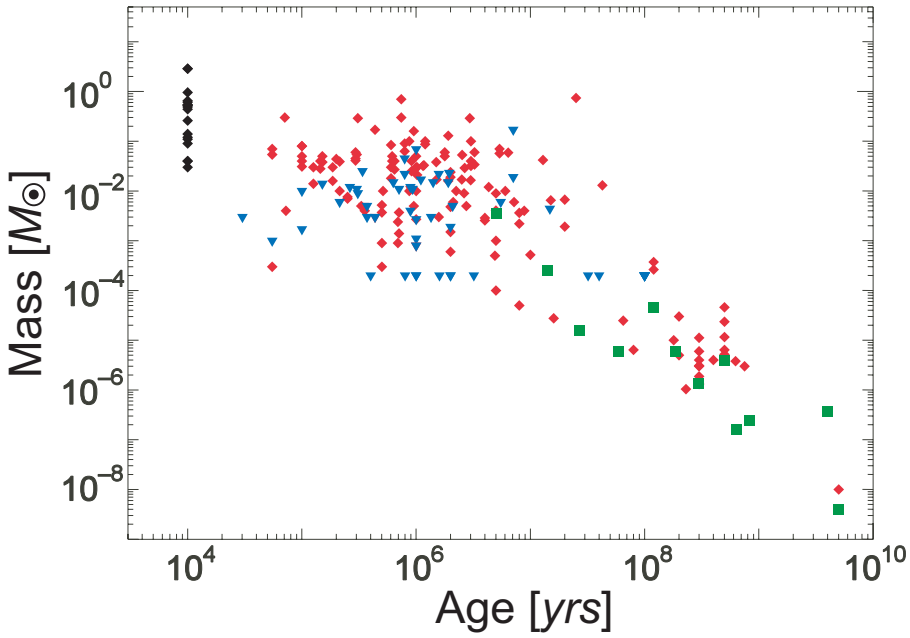

Figure 1.3: A time evolution of circumstellar disk masses around low-mass stars from pre-main sequence phase to main-sequence phase. We assume that the gas/ dust ratio is fixed to 100 for simplicity over the ranges. Red diamonds show detected objects, and blue triangles show undetected ones (3σ upper limits). Green squares indicate that the average masses of the nearby clusters. The masses of protostars are plotted as black diamonds for comparison, and their ages are assumed to be 10^4 yrs. The data are compiled from Beckwith et al. (1990), Reipurth et al. (1993), Osterloh & Beckwith (1995), Duvert et al. (2000), Spangler et al. (2001), and Kitamura et al. (2002).

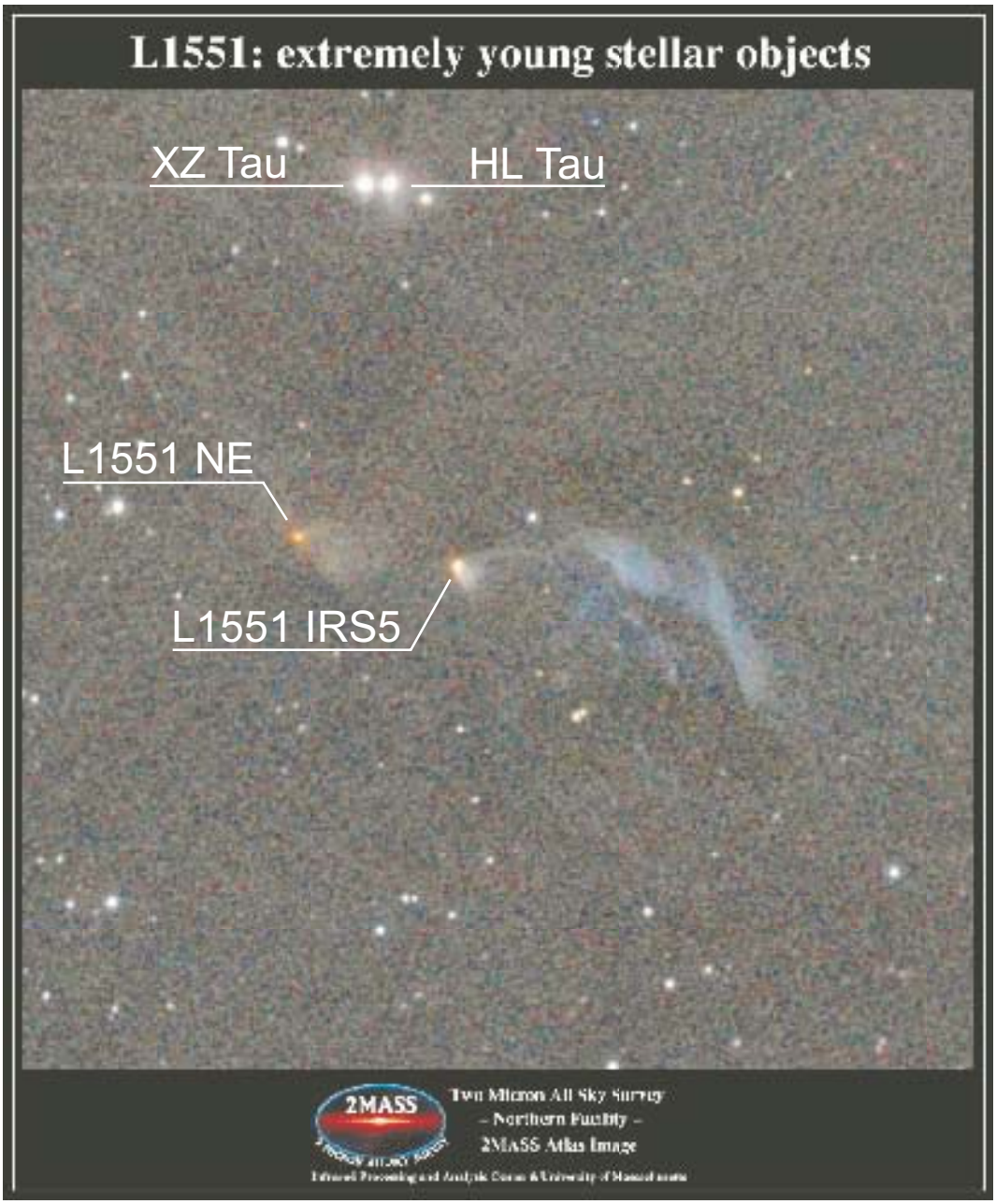

Figure 1.4: A 2MASS image of the L1551 dark cloud region in J, H, and K with limiting magnitude of 16, 15 and 15 respectively.

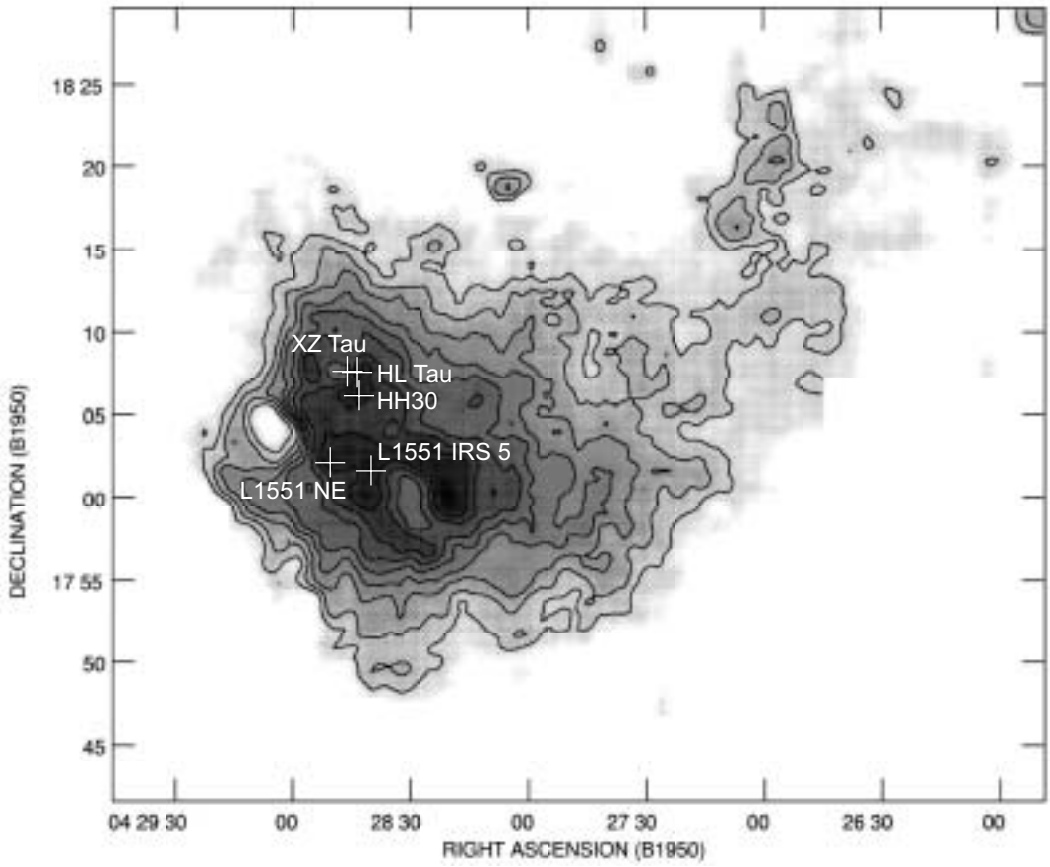

Figure 1.5: Total integrated intensity map of ^{13}CO(J=1-0) toward L1551 region integrated over 5.9 - 7.6 km s^{-1} in $V_{\rm lsr}$. The map is convolved with a 50″ gaussian to increase the signal to noise ratio. Cross marks are stellar positions of known young stars (Saito et al. 1999).

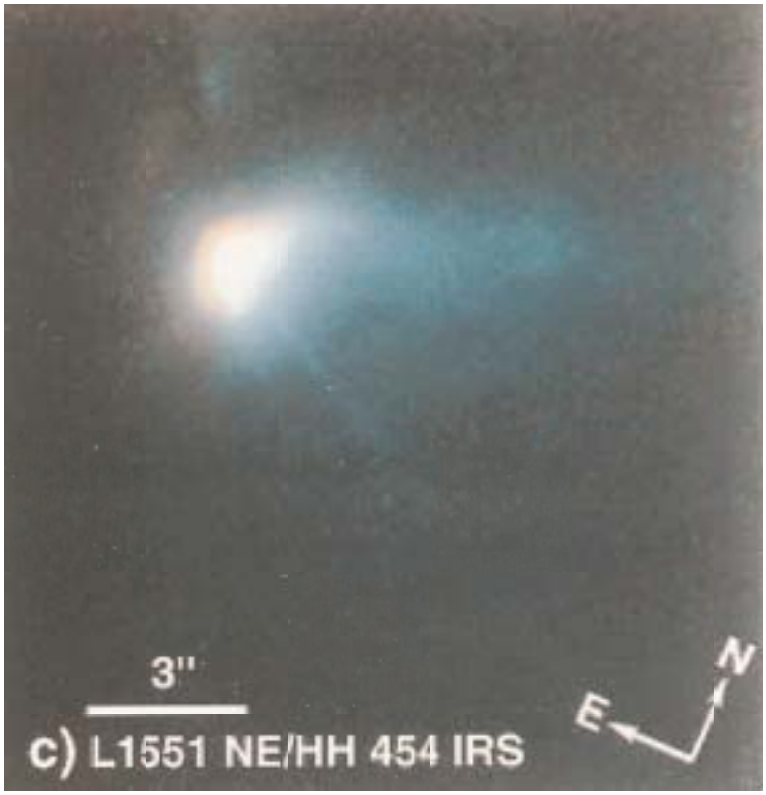

Figure 1.6: Color image of L1551 NE observed with the NIC2 camera on board HST. The F160W filter data is shown as blue-green, while the F205W filter data is shown as red. (Reipurth et al. 2000)

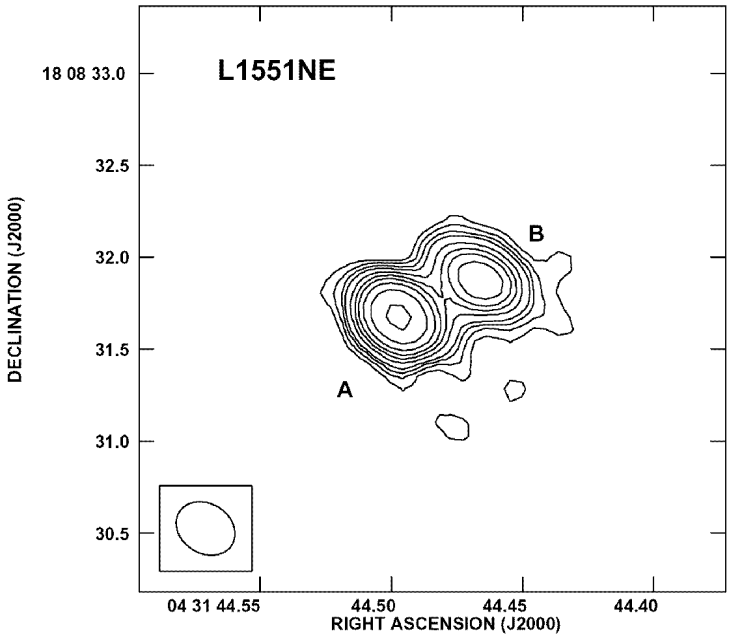

Figure 1.7: L1551 NE binary sources seen in a VLA map at 3.6 cm wavelength. Contour levels are -3, 3, 4, 5, 6, 8, 10, 12, 15, 30, 40, 60 times 8 μJy beam^{-1}, the rms noise of the iamge. The ellipse at bottom-left corner is the synthesized beam of $0\farcs34 \times 0\farcs27$ at P.A. of 57° (Reipurth et al. 2002).

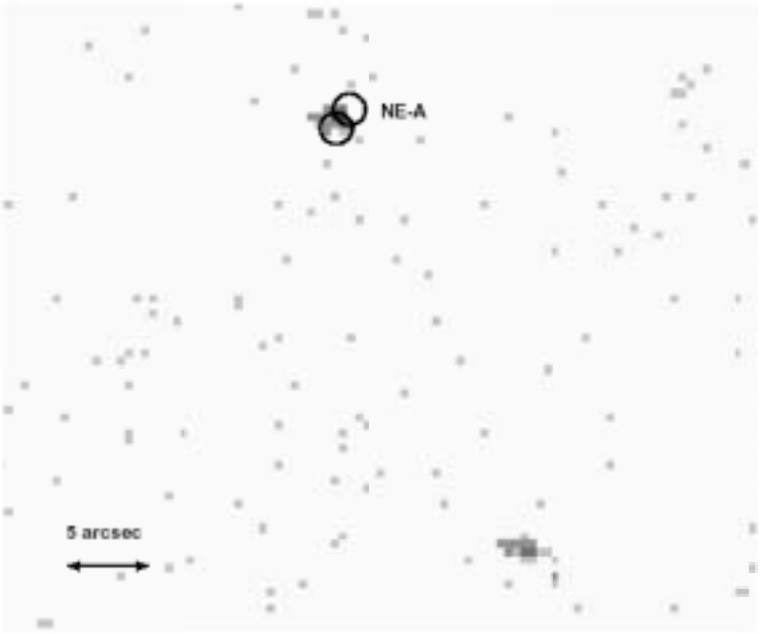

Figure 1.8: Closeup view of the X-ray source near L1551 NE (peak = 6 counts pixel^{-1}). The panel includes a nearby source to compare point spread function shapes. The image is displayed with a scale of 0.″5 per pixel. The protostellar positions from Reipurth et al. (2002) are shown. (Bally et al. 2002)

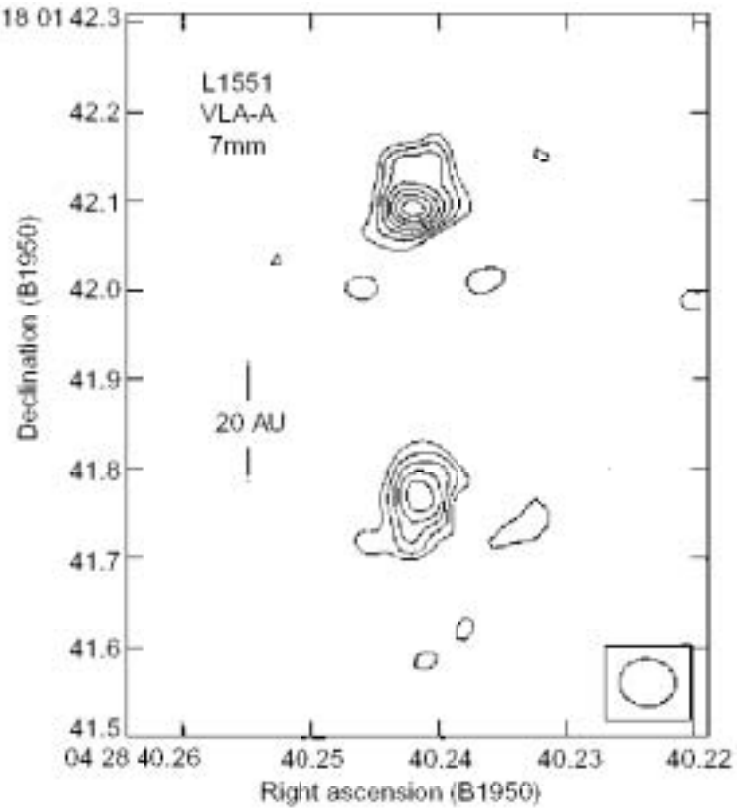

Figure 1.9: L1551 IRS 5 binary sources seen in a VLA map at 7 mm wavelength. Contour levels are -4, -3, 3, 4, 5, 6, 7, 8 and 9 times 0.24 mJy beam^{-1}, the rms noise of the image. The ellipse at bottom-right corner is the synthesized beam of $0.062'' \times 0.052''$ at P.A. of 85° (Rodriguez et al. 1998).

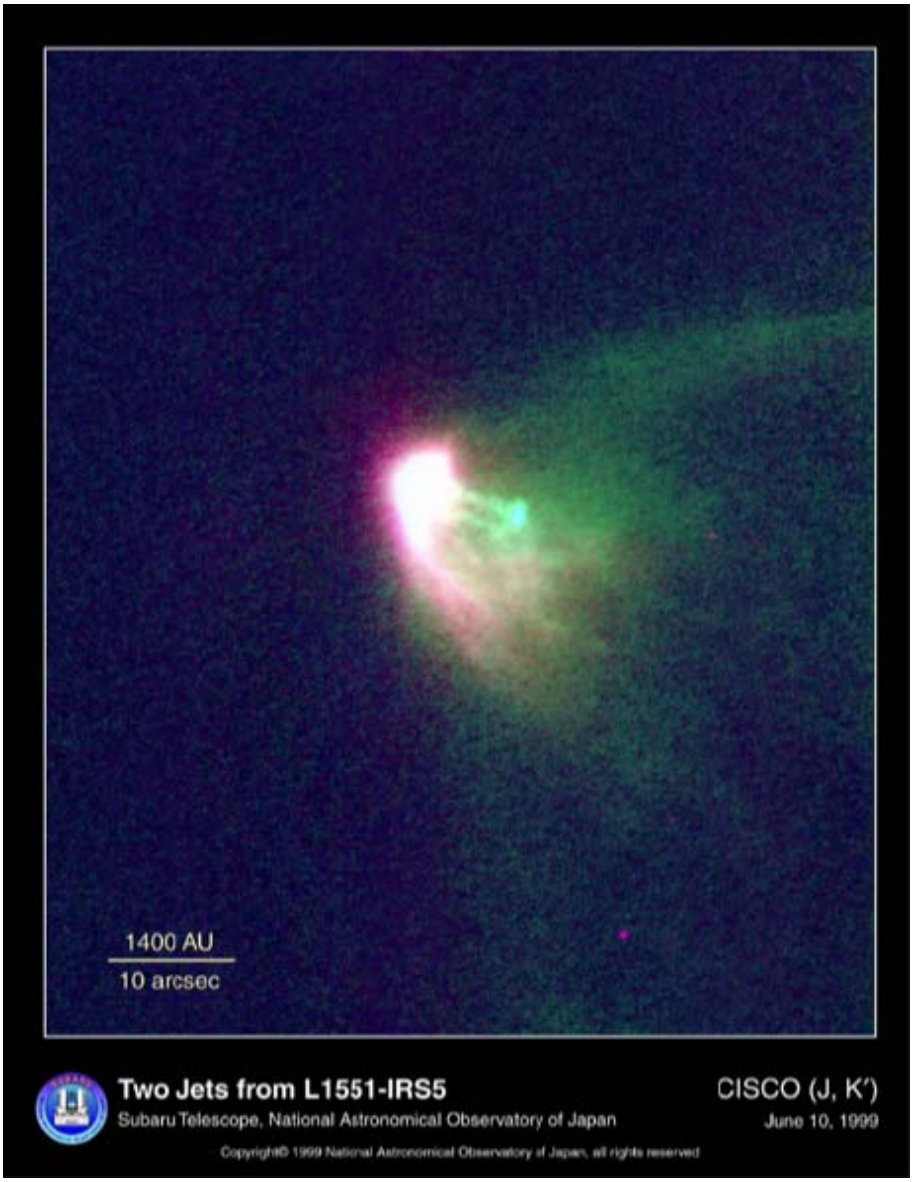

Figure 1.10: J-band and K'-band image of L1551 IRS 5 taken by the SUBARU 8.2 m telescope. The cavity wall of the blue-shifted outflow of IRS 5 are illuminated, and the twin jets from the central sources can be seen. The field of view is $23'' \times 23''$. North is up, and east is toward the left. (Itoh et al. 2000)

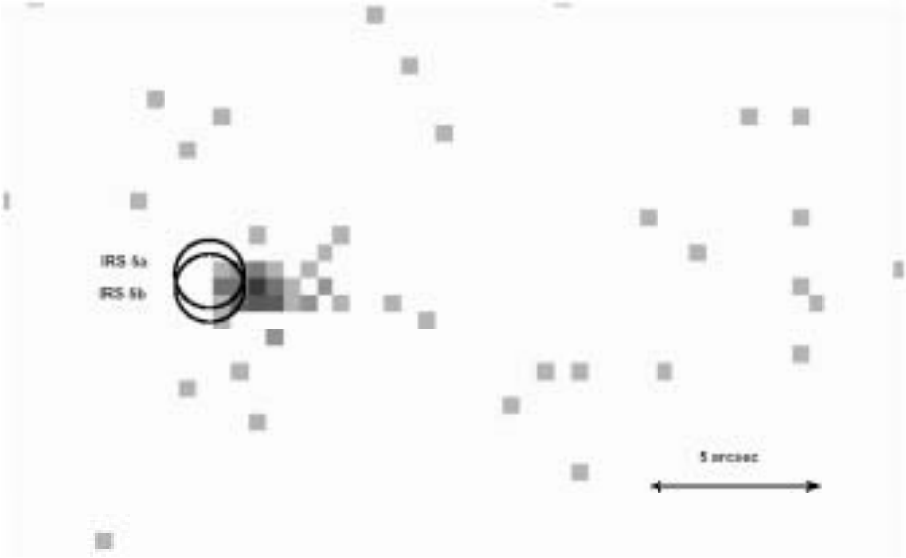

Figure 1.11: Closeup view of the X-ray source near L1551 IRS 5 (peak = 13 count pixel^{-1}). The image is displayed with a scale of 0.″5 per pixel. The protostellar positions from Rodriguez et al. (1998) are shown. (Bally et al. 2002)

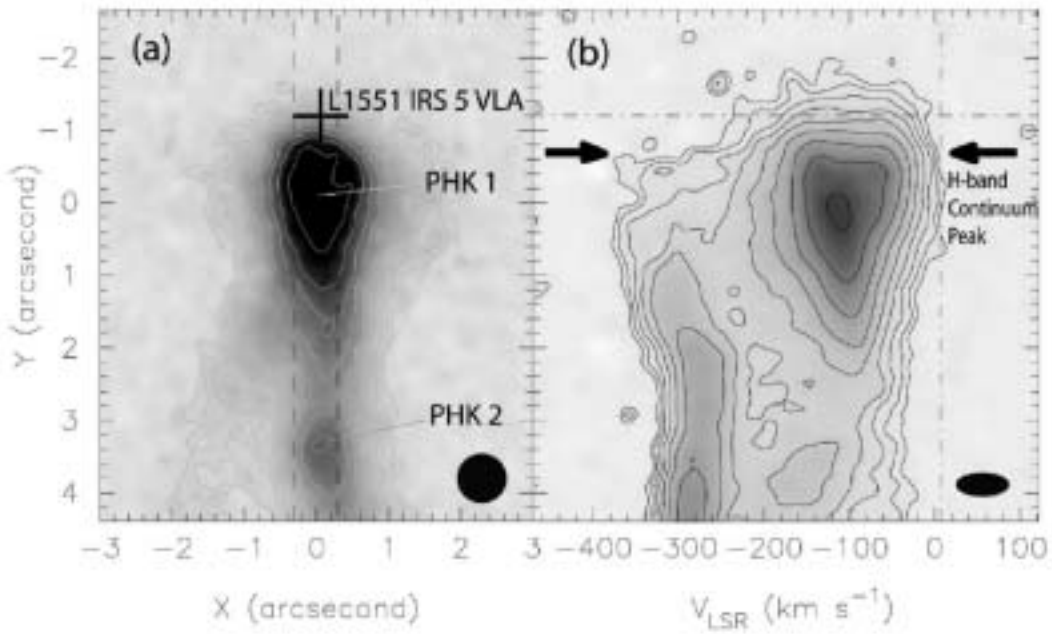

Figure 1.12: (a): Continuum-subtracted [Fe II] $\lambda = 1.644$ μm image of L1551 IRS 5. The parallel dashed lines indicate the slit position with 0.″6 width. The plus sign marks the midpoint of the two radio sources of L1551 IRS 5. The filled circle at the lower right corner show the seeing size of 0.″6. (b): Continuum-subtracted position-velocity diagram along the northern jet of L1551 IRS 5 at its base. The dash-dotted horizontal line indicates the position of the L1551 IRS 5 VLA sources. The dash-dotted vertical line shows the systemic velocity of the L1551 IRS 5 system of $V_{\rm lsr} = 6.2$ km s^{-1}. The two thick horizontal arrows indicate the position of the H-band continuum emission peak at Y = -0.″7. The ellipse located at the lower right shows the velocity resolution and the seeing size of 59 km s^{-1} and 0.″3, respectively. (Pyo et al. 2002)

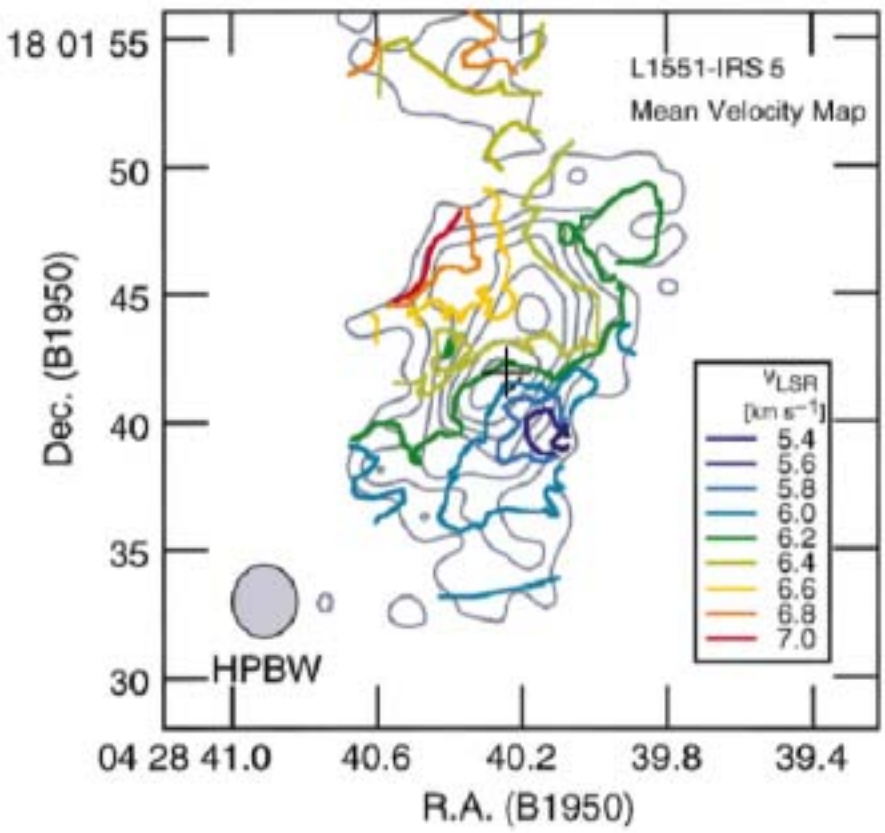

Figure 1.13: Intensity-weighted mean velocity map of L1551 IRS 5 obtained from the $C^{18}O$ (J=1-0) emission. The integrated intensity distribution is also shown by gray lines, whose contour spacing is 1.5 σ, starting at 3 σ (Momose et al. 1998). The lower-left ellipse indicates the synthesize beam.

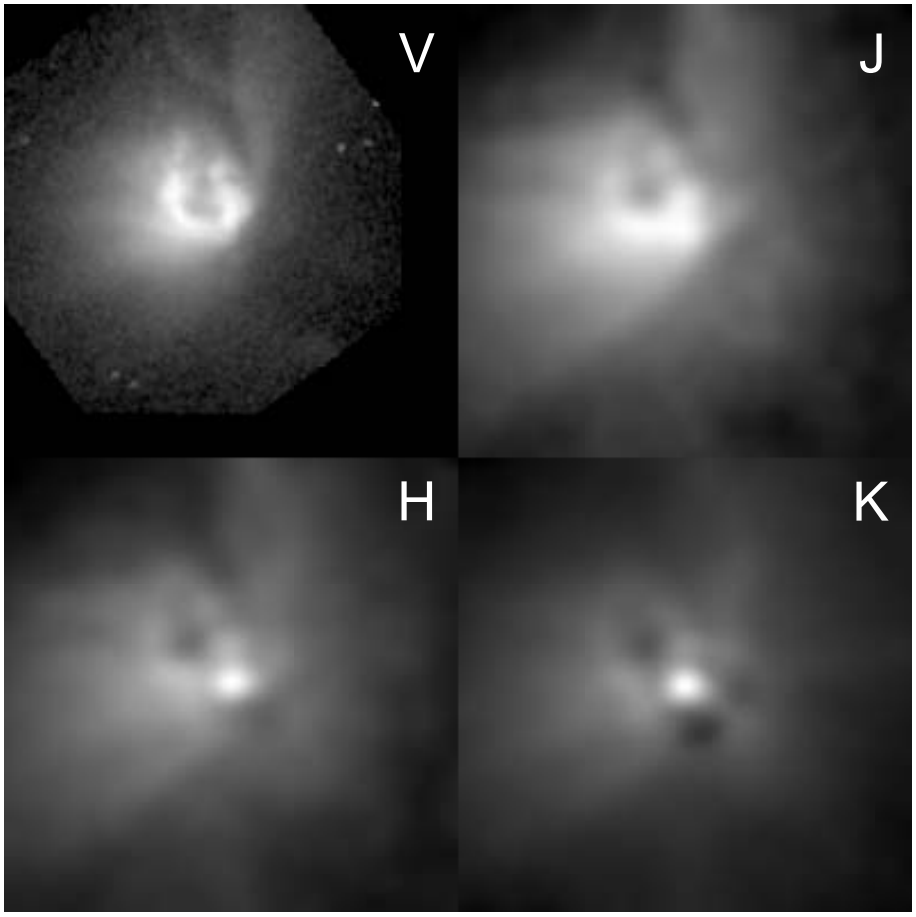

Figure 1.14: Top left panel is an HST WFPC2 image at V-band (Stapelfeldt et al. 1995). The others are adaptive optics near-IR images from Close et al. (1997). Top right image is at J-band (1.25 μm), the bottom left is at H-band (1.65 μm), the bottom right is at K-band (2.2 μm). Each panel corresponds to the area of $7\farcs5 \times 7\farcs5$ around HL Tau. North is up and east is toward the left.

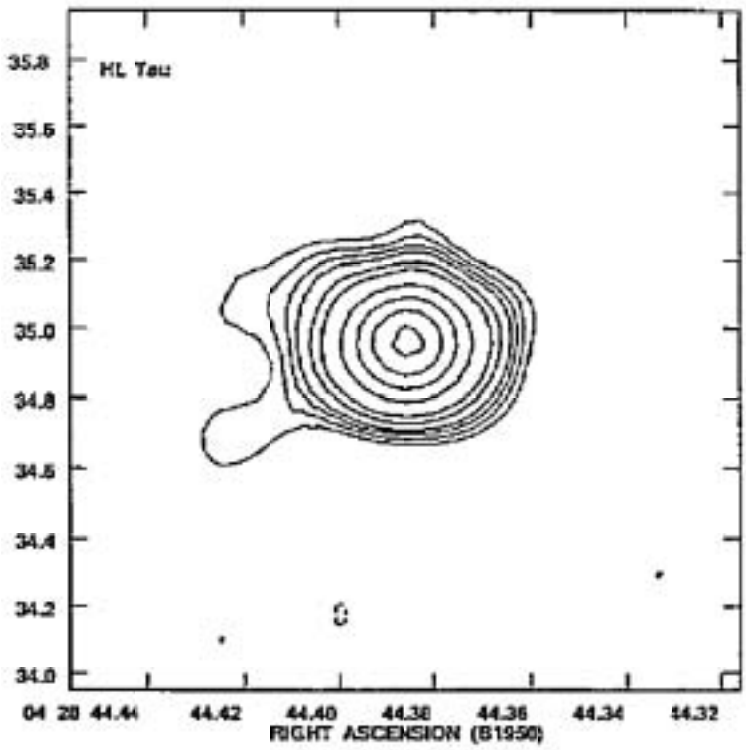

Figure 1.15: 3.6 cm continuum image of HL Tauri taken with the VLA. Contour levels are -4, -3, 3, 4, 5, 6, 8, 10, 15, 20, and 30 times 9 μJy beam^{-1}, the rms noise of the iamge. The synthesized beam is $0\farcs31 \times 0\farcs28$ at P.A. of -65° (Rodriguez et al. 1994).

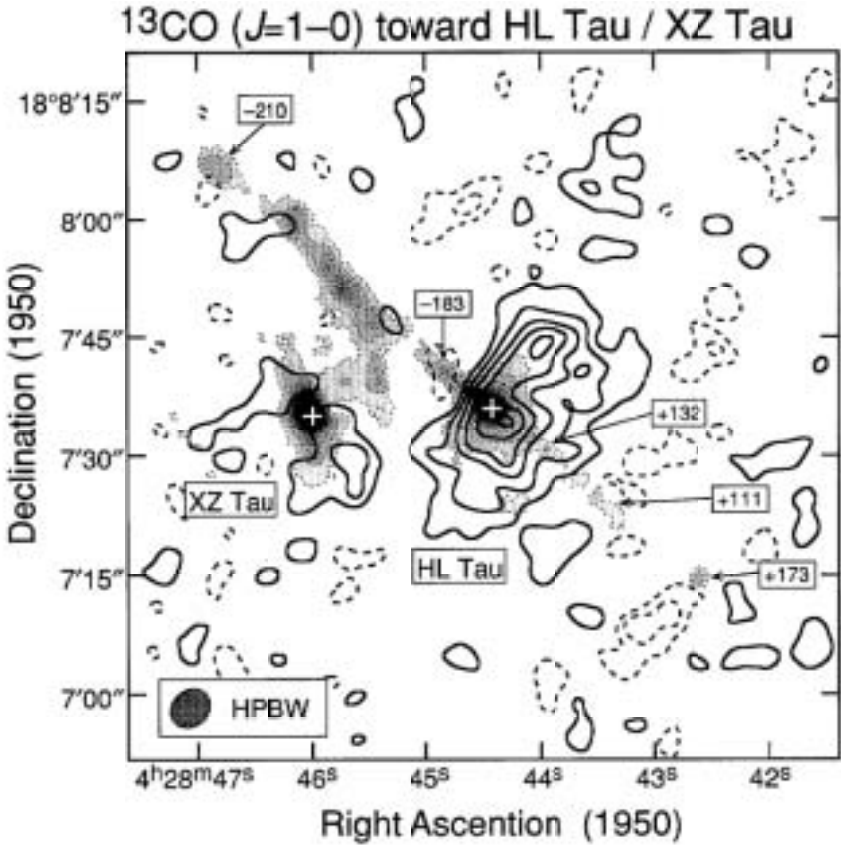

Figure 1.16: Integrated intensity map of the ^{13}CO (J=1-0) emission. Contours are drawn every 1.5 σ with the positive contours (thick lines) starting from the 1.5 σ level, and with the negative contours (dashed lines) decreasing from the -1.5 σ level. The corresponding 1 σ intensity is 0.34 Jy beam^{-1}. For comparison, optical jets observed in [S II] emissions (Mundt et al. 1988) were superposed in gray scale. Note that part of the jet located at $\sim 20''$ north and northwest of XZ Tau possibly comes from a different driving source called VLA 1, although it would appear to have its origin at HL Tau at a first glance (see Mundt et al. 1988). The heliocentric radial velocities in unit of km s^{-1} are indicated in the boxes at various locations along the jet from HL Tau. Two white crosses mark the positions of HL Tau and XZ Tau, respectively (Hayashi et al. 1993).

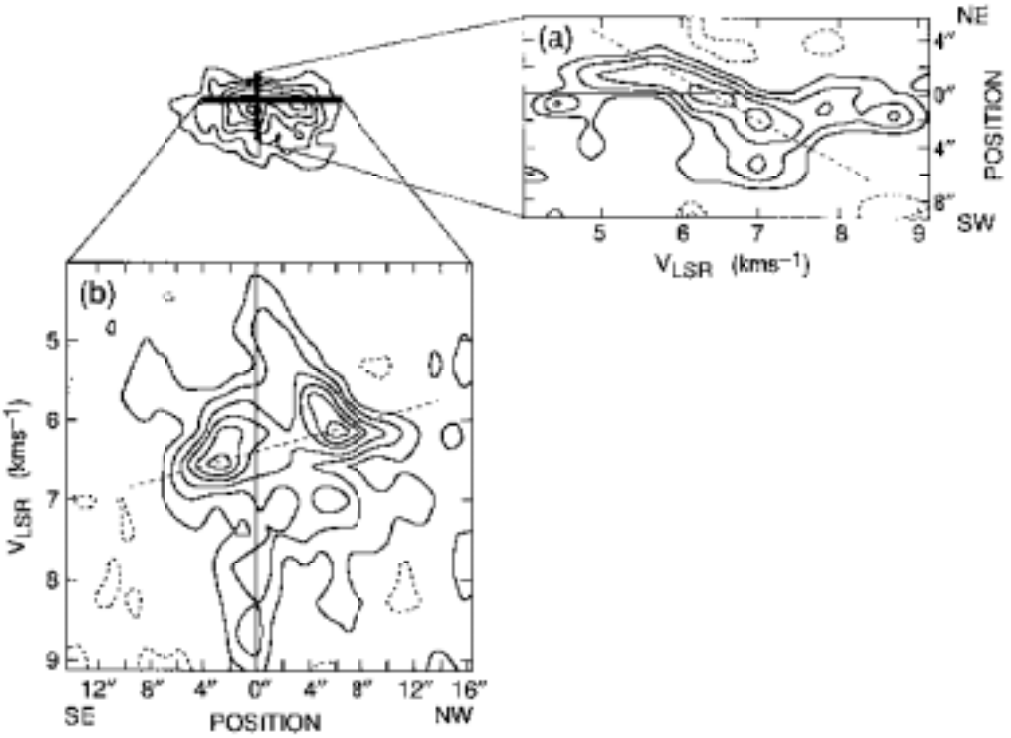

Figure 1.17: Position-velocity diagram across the minor (a) and major (b) axes are shown. Positive contours (thick lines) are drawn every 1.5 σ starting from the 1.5 σ level, while negative contours (dashed lines) decrease from -1.5 σ, with corresponding 1 σ specific intensity of 191 mJy beam^{-1} averaged over the velocity resolution of 0.425 km s^{-1}. Thin dotted lines show the major velocity gradient across each axis (Hayashi et al. 1993).

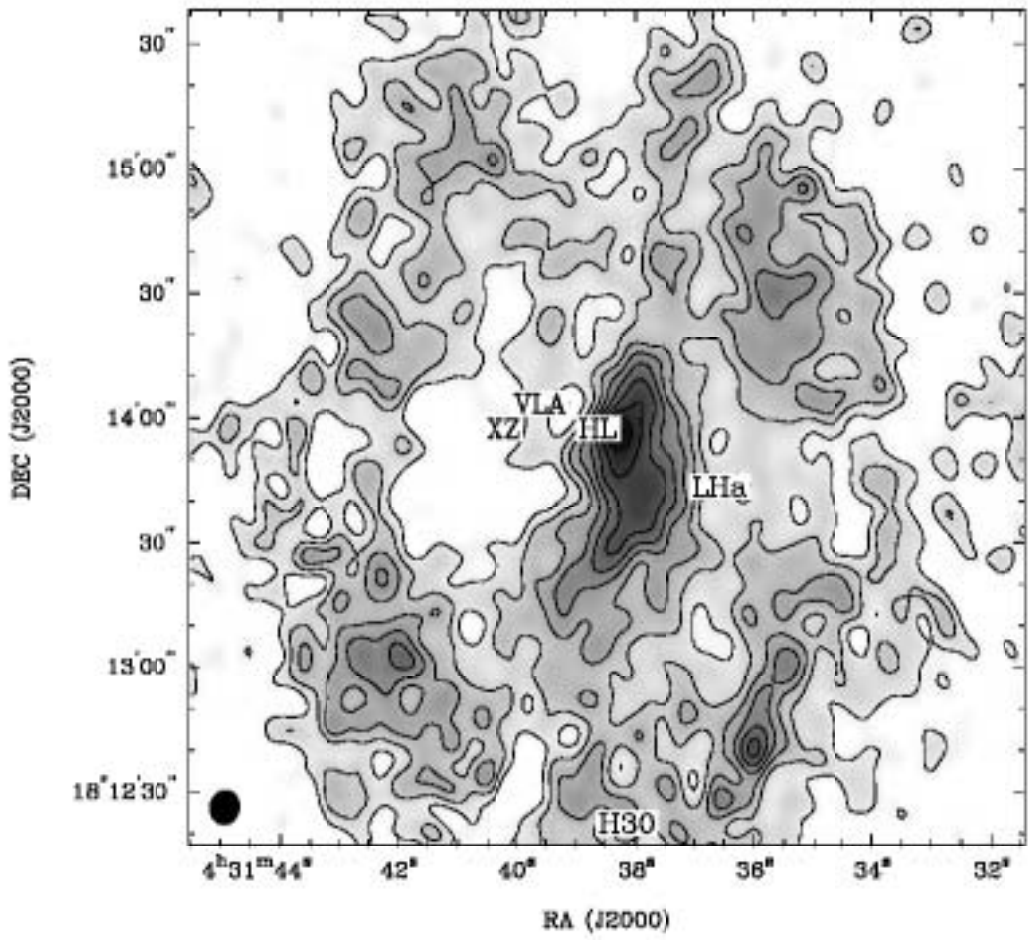

Figure 1.18: Integrated intensity map of ^{13}CO(J=1-0) emission from 4.5 km s^{-1} to 8.5 km s^{-1}. The positions of the young stellar objects XZ Tau, HL Tau, LkHα 358, and HH 30 are noted. VLA 1, observed only at radio wavelength (Mundt et al. 1990) is also shown. (The position of HL Tau is given as the optical centroid, which is dominated by scattered light and thus shifted from the true stellar position to the northeast by about 2″.) Peak brightness is 17.9 K. Contours are at -0.2, 0.2, 0.3, 0.4, 0.5, 0.6, 0.7, 0.8, 0.9 and 1.0 times the peak. In addition to the concentration of material near HL Tau, a cavity to the east is evident, and the entire structure suggests a ring or bubble centered near XZ Tau (Welch et al. 2000).

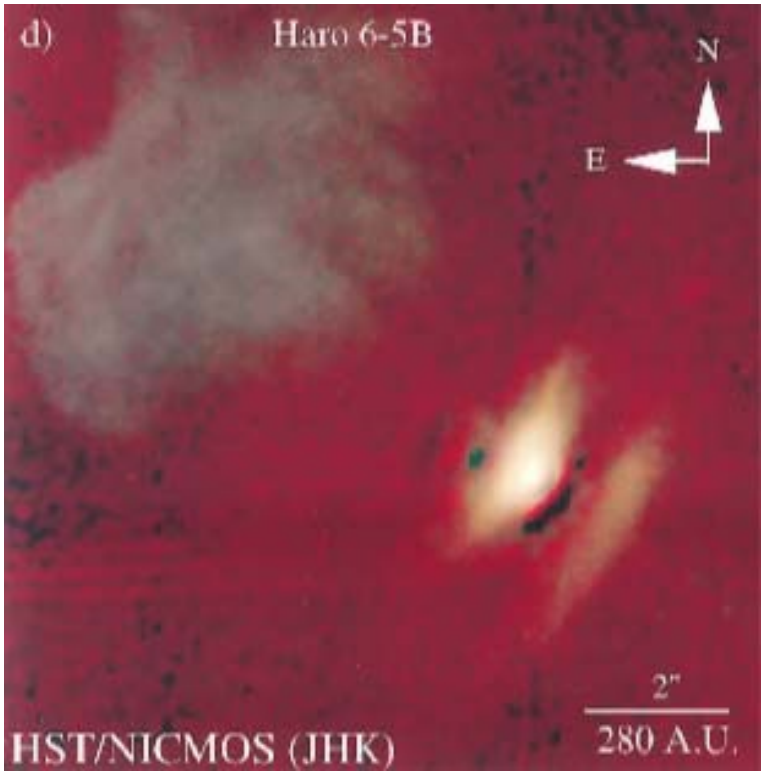

Figure 1.19: HST/NICMOS image of Haro 6-5B. The pseudo-true color composites of F110W (1.1 μm), F160W (1.6 μm) and F205W (2.05 μm) broadband observations. (Padgett et al. 1999)

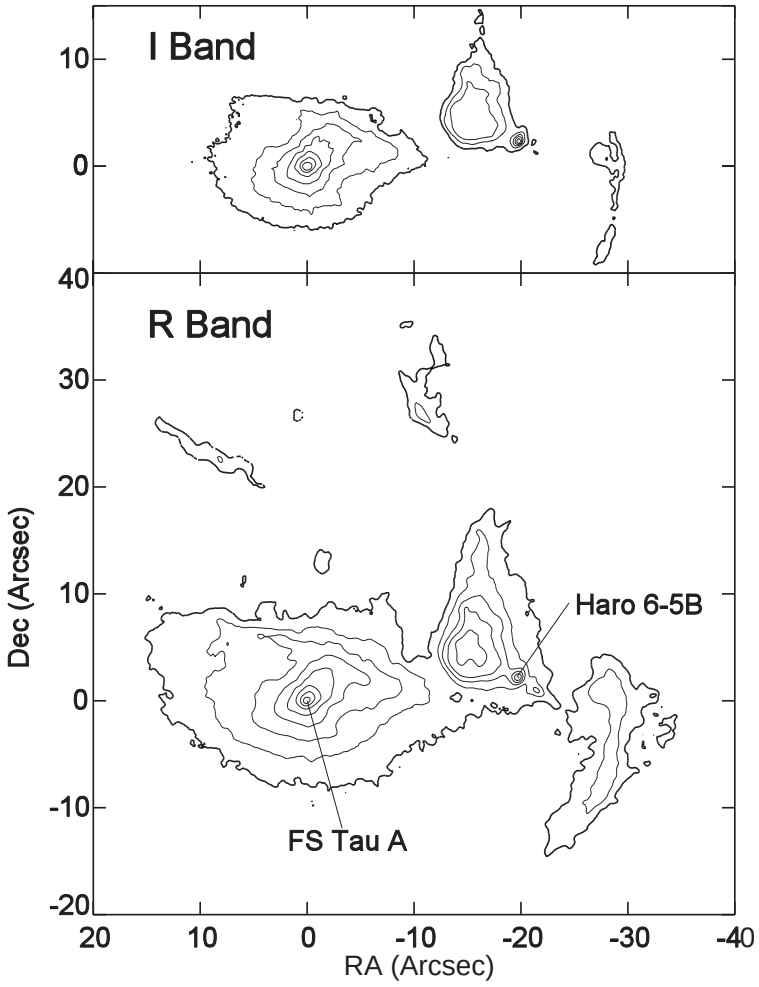

Figure 1.20: Surface brightness contour plots of FS Tau A and Haro 6-5B in F675W (R-band) and F814W (I-band) of the HST. The faintest contour in the R-band is 23 mag arcsec^{-2} and 21 mag arcsec^{-2} in the I-band. Contour spacings are in step of 1 mag arcsec^{-2}. (Krist et al. 1998)

Chapter 2

High Angular Resolution, Sensitive CS $J = 2 - 1$ and $J = 3 - 2$ Imaging of the Protostar L1551 NE: Evidence for Outflow-Triggered Star Formation ?

This chapter has been published in
The Astrophysical Journal 595, 266-278, 2003
as
"High Angular Resolution, Sensitive CS J=2-1 and J=3-2 Imaging of the Protostar L1551 NE: Evidence for Outflow-Triggered Star Formation ?"
by
Sozo Yokogawa[1,2], Yoshimi Kitamura[3], Munetake Momose[4] and Ryohei Kawabe[2]
(1) The Graduate University for Advanced Studies; (2) National Astronomical Observatory of Japan; (3) The Institute of Space and Astronautical Science; (4) Ibaraki University;

Abstract

High angular resolution and sensitive aperture synthesis observations of CS ($J = 2 - 1$) and CS ($J = 3 - 2$) emissions toward L1551 NE, the second brightest protostar in the Taurus Molecular Cloud, made with the Nobeyama Millimeter Array are presented. L1551 NE is categorized as a class 0 object deeply embedded in the red-shifted outflow lobe of L1551 IRS 5. Previous studies of the L1551 NE region in CS emission revealed the presence of shell-like components open toward L1551 IRS 5, which seem to trace low-velocity shocks in the swept-up shell driven by the outflow from L1551 IRS 5. In this study, significant CS emission around L1551 NE was detected at the eastern tip of the swept-up shell from $V_{\rm lsr} = 5.3$ km s^{-1} to 10.1 km s^{-1}, and the total mass of the dense gas is estimated to be 0.14 ± 0.02 $M_{\odot}$. Additionally, the following new structures were successfully revealed: a compact disklike component with a size of ≈ 1000 AU just at L1551 NE, an arc-shaped structure around L1551 NE, open toward L1551 NE, with a size of ~ 5000 AU, i.e., a bow shock, and a distinct velocity gradient of the dense gas, i.e., deceleration along the outflow axis of L1551 IRS 5. These features suggest that the CS emission traces the post-shocked region where the dense gas associated with L1551 NE and the swept-up shell of the outflow from L1551 IRS 5 interact. Since the age of L1551 NE is comparable to the timescale of the interaction, it is plausible that the formation of L1551 NE was induced by the outflow impact. The compact structure of L1551 NE with a tiny envelope was also revealed, suggesting that the outer envelope of L1551 NE has been blown off by the outflow from L1551 IRS 5.

2.1 Introduction

Star formation is often affected by various external disturbances due to active phenomena such as expansion of H II regions, UV radiation from massive stars, and shock waves from supernova remnants. In contrast, the Taurus Molecular Cloud (TMC), the most intensively studied low-mass star-forming region lying at a distance of 140 pc (Elias 1978), has been regarded as a site where star formation occurs spontaneously: the formation of each star progresses in an isolated environment. This is supported by the following two facts: 1) Although the TMC is located near the center of the Cas-Tau OB association, the association is old ($\sim$25 Myr) and has already been dispersed into a wide area of $90^{\circ} \times 40^{\circ}$ (Blaauw 1991). 2) Since the number density of the YSOs in the association is quite low, $10 - 20$ stars pc^{-3} (Gomez et al. 1993), the neighboring systems cannot gravitationally interact with each other during star

formation. In the L1551 dark cloud, however, the protostars such as L1551 IRS 5 (hereinafter IRS 5), L1551 NE (hereinafter NE), HL Tau, and HH 30 might be mutually affected through their outflows. IRS 5, the most luminous protostar ($L_{\rm bol} \approx 30 L_{\odot}$) in the TMC, has powerful outflows, and NE is located just in its red-shifted outflow lobe. It is therefore likely that the environment around NE is strongly affected by the outflows (Bachiller et al. 1994). Furthermore, both HL Tau and HH 30 have optical jets deeply penetrating the L1551 region, which would disturb the entire cloud: recent studies have revealed that dozens of parsec-scale HH flows driven by low-mass young stars are thought to disrupt surrounding molecular cloud cores and drive supersonic turbulence (Reipurth et al. 1997; Reipurth & Bally 2001). Consequently, even in the TMC, outflows can play important roles in neighboring star formation.

L1551 NE, which was discovered by Emerson et al. (1984), is the second brightest protostar ($L_{\rm bol} \approx 6 L_{\odot}$) in the TMC, and is categorized as a class 0 object (e.g., Barsony & Chandler 1993). Recent high angular resolution observations at $\lambda = 3.6$ cm have revealed that NE is a close binary of sources A and B with a separation of $0\farcs5$ at P.A. of 297° (Reipurth et al. 2002). The sources are likely to drive Harbig-Haro objects HH 28, HH 29, and HH 454 as well as the well collimated infrared [Fe II] jet (Devine et al. 1999; Reipurth et al. 2000). In addition, the interaction features between NE and the outflow lobe of IRS 5 have been revealed: high-velocity CS emission was detected around NE, and the distribution of the emission has a clumpy and shell-like structure open toward IRS 5, suggesting that the swept-up shell of the outflow from IRS 5 has impacted on NE (Plambeck & Snell 1995). The detailed spatial and velocity structures of the swept-up shell, however, are still unknown owing to the insufficient angular resolutions and sensitivities. To investigate the detailed structures of the dense gas around NE and to reveal the relationship between NE and the red-shifted outflow lobe of IRS 5, we made aperture synthesis observations of NE in CS ($J = 2 - 1$) and CS ($J = 3 - 2$) emissions, which trace high-density and shocked gas, with higher angular resolution and better sensitivity.

2.2 Observations

2.2.1 CS ($J = 2-1$) and CS ($J = 3-2$) emissions with the Nobeyama Millimeter Array

Aperture synthesis observations of NE were carried out in CS ($J = 2-1$) (97.980968 GHz) and CS ($J = 3 - 2$) (146.969049 GHz) with the Nobeyama Millimeter Array (NMA), which

consists of six 10 m antennas, during a period from 1999 November to 2002 February. The CS images were obtained using all the array configurations, D, C, and AB, whose ranges of the projected baseline lengths were $3-27$, $6-55$, and $15-110$ kλ at 98 GHz, and $5-40$, $10-80$, and $25-160$ kλ at 147 GHz, respectively. The system noise temperatures of SIS receivers in DSB mode were about 150 K at 98 GHz and 200 K at 147 GHz toward the zenith. We used a 1024 channel FX spectrocorrelator with a total bandwidth of 32 MHz, resulting in velocity resolutions of 0.095 km s^{-1} at 98 GHz and 0.063 km s^{-1} at 147 GHz. The center of the field was set on the NE position of (α_{2000}, δ_{2000}) = (4^h 31^m $44^s.42$, $+18^\circ$ $08'$ $32''.3$). The FWHM sizes of the primary beam were $70''$ for 98 GHz and $51''$ for 147 GHz. Since the minimum baseline lengths at 98 GHz and 147 GHz were 3 kλ and 5 kλ, respectively, our observations were insensitive to structures extending more than $69''$ (10^4 AU at 140 pc) at 98 GHz and $41''$ (6×10^3 AU) at 147 GHz. The response across the observed passband for each sideband was determined from $30-40$ minutes observations of 3C454.3 and 3C279. Gain calibrators 0446+112, 0507+179, 0528+134 were observed every $10-20$ minutes. The flux density of each calibrator was derived from observations of Uranus. The overall uncertainty in the flux calibration was about 10 %. After these calibrations, only the data taken under good weather conditions were used in imaging. Using the AIPS package developed at the NRAO, we CLEANed maps by natural weighting with no taper in the UV plane.

The continuum data were also obtained with the digital spectral correlator UWBC (Okumura et al. 2000), which has 128 frequency channels and a 1024 MHz bandwidth per baseline. Visibility data of 100 GHz ($\lambda = 3$ mm) continuum emission in both the lower (98 ± 0.512 GHz) and upper (110 ± 0.512 GHz) sidebands were obtained simultaneously with a phase-switching technique. The data of 150 GHz ($\lambda = 2$ mm) continuum emission were obtained in the lower (135 ± 0.512 GHz) and upper (147 ± 0.512 GHz) sidebands. More details of the observational parameters are summarized in Table 2.1.

2.2.2 CS ($J = 2-1$) emission with the Nobeyama 45 m telescope

Mapping observations of the CS ($J = 2-1$) emission were carried out in 2001 February with the Nobeyama 45 m telescope. The beam size (HPBW) was $16''$ at the frequency of CS ($J = 2-1$). The main-beam efficiency, $\eta_{\rm MB}$, was about 0.5. We used a cooled SIS receiver with a single sideband filter. The typical system noise temperature was 350 K (in SSB) at an elevation of 70°. At the backend, an acousto-optic-spectrometer (AOS) which has 2048 channels with a 40 MHz bandwidth was employed, and the frequency resolution was 37 kHz

corresponding to 0.11 km s^{-1} for CS ($J = 2 - 1$). A $2' \times 2'$ area whose center is the NE position was mapped with a grid spacing of $10''$. The typical noise level in the map was 0.2 K in T_A^*.

2.3 Results

2.3.1 3 mm and 2 mm continuum emission

We have obtained $\lambda = 3$ mm and 2 mm continuum maps of NE with $6'' - 1''$ resolutions. Continuum emission at these wavelengths is thought to mainly come from thermal radiation of dust particles. Maps with the lowest and highest angular resolutions are shown in Figure 2.1. To obtain higher signal-to-noise ratios (S/N) in the 3 mm and 2 mm images, the data of both the lower and upper sidebands were combined into final images. Therefore, the center frequency of the 3 mm continuum images is 104 GHz ($\lambda = 2.88$ mm), and that of the 2 mm continuum images is 141 GHz ($\lambda = 2.12$ mm). The total flux densities of the continuum emission are 92.5 ± 9.4 mJy at 104 GHz and 202 ± 22 mJy at 141 GHz with the D configuration, and are 68.3 ± 7.1 mJy at 104 GHz and 130 ± 13 mJy at 141 GHz with the AB configuration (see Table 2.2). Both the images in the AB configuration show disklike structures elongating along the direction at P.A. = $159° \pm 13°$ with the mean size of $1''.39 \times 1''.00$ (FWHM) (200 AU $\times$ 140 AU), which is almost perpendicular to both the [Fe II] jet (Reipurth et al. 2000, P.A. $\approx 243°$) and the HH jets HH 28, HH 29, and HH 454 (Devine et al. 1999, P.A. $\approx 242°$). The peak positions of the continuum emission are (α_{2000}, δ_{2000}) = ($04^h\ 31^m\ 44^s.487$, $+18°\ 08'\ 31''.57$) at 3 mm, and (α_{2000}, δ_{2000}) = ($04^h\ 31^m\ 44^s.482$, $+18°\ 08'\ 31''.58$) at 2 mm. Since the typical positional error, which includes the effect of atmospheric seeing, is $0''.3$, both the peak positions are the same within the errors. We regard these positions as the source position of NE.

Recent VLA observations at $\lambda = 3.6$ cm revealed that NE is a close binary system with a $0''.5$ separation, corresponding to 70 AU at 140 pc. The stellar positions are (α_{2000}, δ_{2000}) = ($04^h\ 31^m\ 44^s.497$, $+18°\ 08'\ 31''.67$) for NE-A, and (α_{2000}, δ_{2000}) = ($04^h\ 31^m\ 44^s.465$, $+18°\ 08'\ 31''.88$) for NE-B (Reipurth et al. 2002), which are shown as crosses in Figure 2.1. Since both the binary components are surrounded by the disklike structure we revealed, this corresponds to a circumbinary disk around the stars. The peak positions of the 3 mm and 2 mm continuum emission, however, are almost consistent with the position of NE-A which probably ejects the [Fe II] jet (Reipurth et al. 2000), suggesting that the dust is more concentrated at NE-A than

NE-B. In Figure 2.1, one cannot identify any inner hole, which could be generated by tidal force from the binary system. This is probably because NE is still in an active accretion stage and the accreting matter prevents the growth of the inner hole. To spatially resolve such a detailed structure of the circumbinary disk, extremely high angular resolution observations are required, and will be done with the Atacama Large Millimeter/ submillimeter Array (ALMA). The presence of another companion located to the 1.″4 south of NE-A and B is suggested by Moriarty-Schieven et al. (2000), but we did not detect such a companion in both the 3 mm and 2 mm images in spite of our sufficient angular resolutions.

Assuming that the dust continuum emission around NE is optically thin at the millimeter wavelengths, and the dust temperature, $T_{\rm dust}$, is uniform, we can estimate the mass of the disklike structure by

$$M_{\rm NE} = \frac{F_\nu d^2}{\kappa_\nu B_\nu(T_{\rm dust})}, \tag{2.1}$$

where κ_ν is the dust mass absorption coefficient which is usually given by $0.1(\nu/10^{12}\ {\rm Hz})^\beta\ {\rm cm^2\ g^{-1}}$ (Beckwith et al. 1990), $B_\nu(T)$ is the Planck function, F_ν is the total flux density of the continuum emission, and d is the distance to NE (140 pc). The power-law index of κ_ν, β, is derived as 0.70 from our results and the previous interferometric studies at 87 GHz and 230 GHz (Saito et al. 2001; Moriarty-Schieven et al. 2000). With $T_{\rm dust} = 42$ K (Moriarty-Schieven et al. 1994), a mass of $0.032 \pm 0.003\ M_\odot$ is obtained.

2.3.2 CS emission

CS ($J = 2 - 1$) and CS ($J = 3 - 2$) emissions with the Nobeyama Millimeter Array

The emission above the 3 σ level is detected within the velocity range of $V_{\rm lsr} = 5.32 - 10.11$ km s^{-1} for CS ($J = 2 - 1$) and $V_{\rm lsr} = 5.43 - 10.04$ km s^{-1} for CS ($J = 3 - 2$). The total intensity maps integrated over these ranges are shown in Figure 2.2. Both the images have revealed extended and clumpy components on the west side of NE. The brightest peak is seen to the $15'' - 20''$ northwest of NE. Another bright component is seen in the vicinity of NE. The elongated emission from the NE position to the southwest, which looks like a ridge with $20''$ in length, is seen in the CS ($J = 2 - 1$) map, and a corresponding southwest peak is seen in the CS ($J = 3 - 2$) map. No distinct emission, however, is seen on the east side of NE.

Figure 2.3 shows the CS ($J = 2 - 1$) and CS ($J = 3 - 2$) line profiles integrated over a $50''$ square around NE as well as the CS ($J = 2 - 1$) line profile in the same region obtained with the 45 m telescope, which will be described in detail in § 2.3.2. Both the NMA profiles

can be decomposed into three components: a blue-shifted component smaller than ~ 6.5 km s^{-1} (hereafter low-velocity blue: LVB), a red-shifted component in $7 - 8.5$ km s^{-1} (hereafter low-velocity red: LVR), and a highly red-shifted wing component greater than ~ 8.5 km s^{-1} (hereafter high-velocity red: HVR). The emission around the systemic velocity of 6.7 km s^{-1}, which was determined by the optically thin $H^{13}CO^+$ line emission (Saito et al. 2001), is not detected owing to self-absorption and resolving out of extended components caused by the lack of short spacing data in our observations. The three components can also be identified in channel maps (Figures 2.4 & 2.6) and a position-velocity (P-V) diagram along the outflow axis from IRS 5 (Figure 2.8a), which will be described later.

Figure 2.4 shows channel maps of CS ($J = 2 - 1$) with a velocity resolution of 0.19 km s^{-1}. From $V_{\rm lsr} = 5.42$ km s^{-1} to 6.19 km s^{-1}, the CS gas is mainly distributed to the northwest of NE. In just the vicinity of NE, however, there is no emission in the range of $V_{\rm lsr} = 5.42 - 5.81$ km s^{-1} and is only weak extended emission in $V_{\rm lsr} = 6.00$ and 6.19 km s^{-1}. No significant emission is detected in the range of $6.38 - 6.95$ km s^{-1}, including the systemic velocity, mainly owing to the resolving out. In the following channels from $V_{\rm lsr} = 7.14$ km s^{-1} to 7.53 km s^{-1}, a compact component is detected just at the NE position. The beam deconvolved size of the component is $11\farcs0 \times 6\farcs5$ (FWHM) (1540 $\times$ 910 AU) at P.A. of 60°. This component possibly comes from the disk/envelope system around NE (hereafter the NE component). In these channels, other strong peaks are seen to the northwest and southwest of NE, and an inclined "W" shaped structure, which contains all the peaks, can be recognized. From $V_{\rm lsr} = 7.72$ km s^{-1} to 8.29 km s^{-1}, the NE component and a peak located $\sim 20''$ northwest of NE are distinct. A new weak component $\sim 40''$ southwest of NE appears beyond $V_{\rm lsr} = 7.72$ km s^{-1}. In the channels from $V_{\rm lsr} = 8.48$ km s^{-1} to 10.01 km s^{-1}, the southwest and northwest components gradually merge into a west component which is apparent beyond $V_{\rm lsr} = 9.25$ km s^{-1}.

Figure 2.5 shows CS ($J = 2 - 1$) maps for the LVB ($V_{\rm lsr} = 5.32 - 6.47$ km s^{-1}), LVR ($V_{\rm lsr} = 7.04 - 8.57$ km s^{-1}), and HVR ($V_{\rm lsr} = 8.57 - 10.11$ km s^{-1}) components. The LVB component is mainly distributed to the northwest of NE and its total flux density integrated over the region above the 3 σ level is 6.8 Jy km s^{-1}. The LVR component shows an inclined "W" shaped structure with a southwest detached component. The overall emission is distributed along the north-south direction and is shifted to the west of NE. One bright peak is the NE component, and the other bright peaks show an arc-shaped structure open toward NE with a length of ~ 7000 AU, as shown by the dashed line in Figure 2.5b. Although all the peaks seem to compose an arc open toward the west or IRS 5 as previously suggested (e.g., Plambeck & Snell 1995), we consider that the NE peak corresponds to the circumbinary disk while the

other peaks, which originate from the gas swept up by the outflow from IRS 5, make the arc open toward NE. This arc-like structure is seen in the CS ($J = 2 - 1$) maps at $V_{\rm lsr} = 7.34$ km s^{-1} and 7.53 km s^{-1} in Figure 2.4, and becomes more prominent in the CS ($J = 3 - 2$) maps at $V_{\rm lsr} = 7.36$ km s^{-1} and 7.61 km s^{-1} in Figure 2.6. The arc can also be identified in the CS ($J = 2 - 1$) maps from $V_{\rm lsr} = 8.48$ km s^{-1} to 10.01 km s^{-1} in Figure 2.4: the peak seen in $V_{\rm lsr}$ ≥ 9.25 km s^{-1} gradually splits into the two peaks at the lower red-shifted velocities, which can be explained in terms of a bow shock around NE caused by the outflow from IRS 5. The middle part of the arc seems relatively weak, as easily recognized in the channel maps at $V_{\rm lsr}$ = 7.14 and 7.34 km s^{-1} of Figure 2.4. This might be due to the blowing off of the dense gas by the collimated outflows or the HH jets from NE at P.A. $\approx 243°$. The total flux density above the 3 σ level is 21.9 Jy km s^{-1}. The HVR component is distributed on the west side of the LVR component, and its total flux density is 8.1 Jy km s^{-1} (see Table 2.3).

Figure 2.6 shows channel maps of CS ($J = 3 - 2$) with a velocity resolution of 0.25 km s^{-1}. The features of the CS ($J = 3 - 2$) emission shows a good agreement with those of CS ($J = 2 - 1$) as follows: From $V_{\rm lsr} = 5.57$ km s^{-1} to 6.34 km s^{-1}, extended emission is seen to the north of NE. From $V_{\rm lsr} = 6.59$ km s^{-1} to 7.10 km s^{-1}, the emission is absent because of the resolving out. In the following channels from $V_{\rm lsr} = 7.36$ km s^{-1} to 8.12 km s^{-1}, particularly $V_{\rm lsr} = 7.36$ to 7.61 km s^{-1}, one can clearly see the bright NE component surrounded by clumpy arc-shaped components which open toward NE. The size of the NE component is $7\farcs4 \times 4\farcs6$ (FWHM) (1040 $\times$ 640 AU) at P.A. of 126°. In $V_{\rm lsr} = 8.38$ km s^{-1} to 9.91 km s^{-1}, clumpy emission is seen to the west of the source. Figure 2.7 shows CS ($J = 3 - 2$) maps for the LVB ($V_{\rm lsr} = 5.43 - 6.47$ km s^{-1}), LVR ($V_{\rm lsr} = 7.23 - 8.51$ km s^{-1}), and HVR ($V_{\rm lsr} = 8.51 - 10.04$ km s^{-1}) components. The overall features are almost consistent with those of CS ($J = 2 - 1$) in Figure 2.5, but the NE component in the LVR range is much more prominent compared to the CS ($J = 2 - 1$) case. This is probably because the NE component is denser and hotter than the surrounding extended component. The total flux densities of the LVB, LVR, and HVR components, are 22.9, 50.3, and 21.0 Jy km s^{-1}, respectively (see Table 2.3).

We estimate the total mass of the dense gas around NE. Although the CS emission is generally optically thick around a protostar, the lower limit of the mass can be obtained under the simple assumption of optically thin condition. The mass of the dense gas can be calculated by the following equation (Scoville et al. 1986):

$$M_{\rm H_2} = 1.43 \times 10^{-4}\ T_{\rm ex} \exp\left(\frac{7.06}{T_{\rm ex}}\right) \frac{\tau_{\rm CS}}{1 - \exp\left(-\tau_{\rm CS}\right)}$$

$$\left(\frac{d}{140\mathrm{pc}}\right)^2 \left[\frac{10^{-9}}{X(\mathrm{CS})}\right] \left(\frac{F_\nu}{[\mathrm{Jykms^{-1}}]}\right) M_\odot, \tag{2.2}$$

for CS ($J = 2 - 1$), and

$$M_{\mathrm{H_2}} = 3.57 \times 10^{-5}\ T_{\mathrm{ex}} \exp\left(\frac{14.1}{T_{\mathrm{ex}}}\right) \frac{\tau_{\mathrm{CS}}}{1 - \exp\left(-\tau_{\mathrm{CS}}\right)} \left(\frac{d}{140\mathrm{pc}}\right)^2 \left[\frac{10^{-9}}{X(\mathrm{CS})}\right] \left(\frac{F_\nu}{[\mathrm{Jykms^{-1}}]}\right) M_\odot, \tag{2.3}$$

for CS ($J = 3-2$), where T_{ex} is the excitation temperature, $X(\mathrm{CS})$ is the fractional abundance of CS relative to H_2, d is the distance to NE, and F_ν is the integrated flux density of CS ($J = 2 - 1$) or CS ($J = 3 - 2$). With $X(\mathrm{CS})$ of 10^{-9} (Linke & Goldsmith 1980) and T_{ex} of 20 K (Plambeck & Snell 1995), the total mass of the dense gas is estimated to be $0.14 \pm 0.02\ M_\odot$, and the mass of the NE component detected in the LVR range is estimated to be $(9.0 \pm 2.0) \times 10^{-3}\ M_\odot$. The mass estimate is not sensitive to the adopted temperature: in the case of $T_{\mathrm{ex}} = 50$ K, the upper limit temperature (Plambeck & Snell 1995), the total mass becomes $0.26 \pm 0.04\ M_\odot$, and the NE component mass becomes $(1.7 \pm 0.4) \times 10^{-2}\ M_\odot$. Our total mass is in good agreement with the previously reported mass of $0.016 - 0.02\ M_\odot$ from CS observations, considering $X(\mathrm{CS}) = 10^{-8}$ they adopted (Plambeck & Snell 1995). The mass of the NE component, however, is about a half of the mass derived from the continuum observations, suggesting that the CS emission is optically thick.

Figure 2.8 shows P-V diagrams of the CS ($J = 2 - 1$) and CS ($J = 3 - 2$) emission of NE. In the diagram along the direction between IRS 5 and NE (P.A. = 78°, Figures 2.8a & b), which is roughly parallel to the outflow and jets of IRS 5 (Devine et al. 1999, P.A. $\approx 242°$), there exist three distinct components, corresponding to the LVB, LVR, and HVR components. Note that the emission near the systemic velocity ($V_{\mathrm{lsr}} \approx 6.7$ km s^{-1}) is absent, owing to the resolving out of extended components. Figure 2.8a clearly shows a velocity gradient along the direction between IRS 5 and NE: as farther from IRS 5 or closer to NE, the amount of redshift gets smaller (see also Figure 2.9). This can be interpreted in terms of deceleration of the swept up shell associated with the red-shifted outflow lobe of IRS 5. In the diagram of CS ($J = 2 - 1$) cut along the direction perpendicular to the outflow axis of IRS 5 (Figure 2.8c), on the other hand, no systematic motion was detected. The P-V diagrams of CS ($J = 3 - 2$) show similar features to those of CS ($J = 2 - 1$) (Figures 2.8b & d).

CS ($J = 2 - 1$) emission with the Nobeyama 45 m telescope

A total intensity map of CS ($J = 2 - 1$) emission around NE integrated over $V_{\rm lsr} = 5.0$ km s^{-1} to 11.0 km s^{-1}, which is obtained with the 45 m telescope, is shown as a gray scale image with contour lines in Figure 2.10. Two bright peaks can be seen: One is to the 15″ west of NE which corresponds to the bright northwest peak seen in the NMA images of Figures 2.2a & 2.5b, and the other is to the 40″ southwest of NE which corresponds to the southwest detached component seen in Figure 2.5b. The overall emission shows an arc-shaped structure (large-scale CS arc-shaped structure) which is open to the west, and NE is located at the eastern tip of the arc. The line profile integrated over a 50″ square around NE is shown in Figure 2.3. The profile is mainly red-shifted compared to the systemic velocity of NE ($V_{\rm lsr} =$ 6.7 km s^{-1}) where the self-absorption can be recognized. These features have been found in previous studies (e.g., Plambeck & Snell 1995), and the large-scale CS arc-shaped structure has been thought to trace the swept-up shell of the outflow powered by IRS 5. Another arc-shaped structure (small-scale CS arc-shaped structure) indicated by the white dashed line in Figure 2.10 has been newly discovered by this study (see also Figure 2.11).

In order to estimate the missing flux of the NMA observations, we compare the CS ($J =$ 2−1) flux densities with the NMA and the 45 m telescope in the same area of 50″ square around NE. The total flux density with the 45 m telescope is 129 Jy km s^{-1} in the range $V_{\rm lsr} = 5.0$ km s^{-1} to 11.0 km s^{-1}, while that with the NMA is 36.8 Jy km s^{-1} in almost the same velocity range $V_{\rm lsr} = 5.3 - 10.1$km s^{-1}. With the total flux density of the 45 m observations, equation (2.2) gives a total gas mass of 0.55 ± 0.07 $M_\odot$ under the same assumptions as in the NMA case. The flux difference can mainly be attributed to the resolving out of extended components in the NMA observations. In the LVB ($V_{\rm lsr} \lesssim 6.5$ km s^{-1}) and LVR ($V_{\rm lsr} \approx 7.0 - 8.5$ km s^{-1}) ranges, the fraction of the missing flux density is about 60−70 %. In the HVR range ($V_{\rm lsr} \gtrsim 8.5$ km s^{-1}) and around the systemic velocity ($V_{\rm lsr} \sim 6.7$ km s^{-1}), more than 80 % of the 45 m flux density is missing. These indicate that the smoothly extended components are dominant in the HVR range as well as around the systemic velocity, suggesting that the red-shifted outflow gas from IRS 5 has a smooth structure.

2.4 Discussion

The NMA observations of the CS ($J = 2-1/J = 3-2$) emissions have revealed the small-scale arc-shaped structure around NE and the deceleration of the outflowing gas, suggesting

that a distinct interaction exists between NE and the outflowing gas. We discuss the interaction between them in § 2.4.1. Next, we propose a plausible scenario of the outflow-triggered formation of NE in § 2.4.2. Finally, we discuss the possibility that the outflow from IRS 5 has blown off the outer envelope around NE in § 2.4.3.

2.4.1 Interaction between NE and the red-shifted outflow lobe of IRS 5

The circumstellar environment around NE has been strongly affected by the outflow from IRS 5, judging from the spatial distribution and velocity structure of the CS emission around NE. Figure 2.11 is a schematic illustration of NE and IRS 5, which briefly summarizes our results. The large-scale CS arc-shaped structure open toward IRS 5 around NE, which was revealed by the 45 m observations, is thought to trace the swept-up shell of the outflow from IRS 5, because the shell exhibits the highly red-shifted emission compared to the systemic velocities of IRS 5 and NE. Since NE is located at the leading edge of the shell, it is most likely that the shell has impacted on the natal core of NE.

The impact of the shell on NE is strongly supported by the small-scale CS arc-shaped structure, which is newly discovered by our observations. The arc is open toward NE and exhibits the distinct deceleration feature along the outflow axis of IRS 5. These suggest that the swept-up gas accelerated by the outflow from IRS 5 has impacted on NE or the natal core of NE, forming the bow-shock-like arc as well as the deceleration revealed in Figure 2.8a. Here, we estimate the deceleration of the gas, $a_{\rm dcl}$, under a simple assumption of constant deceleration. The projected distance between NE and the peak position of the HVR component in Figure 2.8a is 20″, corresponding to 2800 AU. The HVR component has $V_{\rm lsr} \approx 9.2$ km s^{-1}, whereas the gas associated with NE has $V_{\rm lsr} \approx 6.7$ km s^{-1}. Considering the inclination angle of the outflow from IRS 5 to be $50 - 70^\circ$ with respect to the plane of the sky (Liseau & Sandell 1986; Fridlund & Liseau 1994; Momose et al. 1998), $a_{\rm dcl}$ is estimated to be $(0.44 - 1.9) \times 10^{-3}$ km s^{-1} yr^{-1}, and the timescale of the deceleration becomes $(3.9 - 8.9) \times 10^3$ yr.

The comparison of the CS and $H^{13}CO^+$ emissions suggests that NE has formed at the shock front caused by the impact of the CS shell. Figure 2.12 shows the total intensity map of the $H^{13}CO^+$ emission (Saito et al. 2001) superposed onto the CS ($J = 2 - 1$) map of NE by this study. Although both the CS and $H^{13}CO^+$ emissions trace dense gas, their distributions show clear anti-correlation. The $H^{13}CO^+$ emission is mainly distributed to the east of the source, which can be interpreted in terms of the depletion of $H^{13}CO^+$ by the outflow (Saito et al.

2001): Bachiller & Perez Gutierrez (1997) suggested that the $H^{13}CO^+$ molecules are rapidly destroyed in shocked regions owing to dissociative recombination caused by enhanced electron abundance. Thus, the $H^{13}CO^+$ emission seems to be distributed in the pre-shocked region. On the other hand, CS, a tracer of dense and shocked gas, is mainly distributed to the west of NE, suggesting that the CS emission is distributed in the post-shocked region disturbed by the outflow of IRS 5. Therefore, it is most likely that NE is located at the interface between the pre-shocked and post-shocked regions. This interpretation is also consistent with the fact that the $H^{13}CO^+$ emission was only detected within a range of $V_{\rm lsr} = 5.84 - 7.72$ km s^{-1} and no high-velocity components were detected, whereas the CS emission was detected in a wide range of $V_{\rm lsr} \approx 5.3 - 10.1$ km s^{-1}.

The timescale for the interaction between the natal core of NE and the outflow of IRS 5 is characterized by the crossing time in which the outflow passes through the core, although there is ambiguity in the core radius. The curvature radius of the small-scale CS arc-shaped structure, 4×10^3 AU, can be taken as the lower limit for the core radius, giving an interaction timescale of $(1 - 2) \times 10^4$ yr. This timescale is only twice the timescale of the ongoing deceleration of the CS gas of $(3.9 - 8.9) \times 10^3$ yr. The upper limit of the core radius, on the other hand, should be $\sim 10^4$ AU as suggested by the continuum map at 1.3 mm (Motte & André 2001), giving a timescale of $(2 - 5) \times 10^4$ yr. Note that the radius of 10^4 AU agrees with the mean radius of the cores in the TMC (Onishi et al. 2002). The possible range of the interaction timescale, therefore, is $(1 - 5) \times 10^4$ yr. Since the separation between NE and IRS 5 is 2×10^4 AU, only twice larger than the above upper limit of the core radius, the upper limit timescale of the interaction can also be regarded as a possible traveling time from IRS 5 to NE of the outflow ($(4 - 10) \times 10^4$ yr).

2.4.2 Outflow-triggered star formation

In addition to the strong interaction between NE and the outflow of IRS 5, we discuss the possibility that the formation of NE was triggered by the impact of the outflow by comparing several timescales. Motte & André (2001) estimated the age of NE to be $(0.6 - 5.0) \times 10^4$ yr: The shortest age was derived from the assumption that the mass accretion rate declines exponentially given by

$$\dot{M}_{\rm acc}(t) = \frac{M_{\rm env}(t)}{\tau} = \frac{M_0 \exp(-t/\tau)}{\tau}, \tag{2.4}$$

and the longest one was derived from the steady mass accretion rate of 2.0×10^{-6} $M_\odot$ yr^{-1}. The interaction timescale between the NE core and the outflow from IRS 5, on the other hand,

is $(1-5)\times10^4$ yr, and this agrees with the above-mentioned age of NE. Although both the estimates of timescale contain uncertainty, this agreement suggests that the mass accretion of NE was triggered by the outflow from IRS 5: it is unlikely that the NE formation and the interaction between NE and the outflow have occurred independently but simultaneously at the same place in such a short span compared with a period of the protostellar phase ($\sim 10^5$ yr). This would be the first evidence for the outflow triggered star formation in low-mass star forming regions.

In the blueshifted outflow lobe of IRS 5, there is another CS clump which resembles the shell near NE in spatial distribution, sizescale and the amount of velocity shifts with respect to the systemic velocity of IRS 5 (see Fig.3 of Plambeck & Snell 1995). A straight line connecting these two shells or clumps passes directly through IRS 5, suggesting these two shells were simultaneously ejected from IRS 5 with similar velocities. The separation from IRS 5 of the blueshifted shell, however, is about twice larger than that of the redshifted shell near NE. This difference might be caused by the obstruction by the NE core in the redshifted outflow lobe of IRS 5. If this is the case, the duration of the interaction between the NE core and the outflow from IRS 5 should be comparable to the traveling time from IRS 5 to NE of the outflow.

2.4.3 Blown off envelope around L1551 NE

Class 0 protostars are usually surrounded by dense envelopes with a few $\times$ 1000 AU sizes. As they evolve, the dense envelopes are dispersed, and T Tauri stars without the envelopes appear (Looney et al. 2000; Saito et al. 2001). NE, however, might be an exceptional class 0 protostar with a tiny envelope, which is probably caused by the impact of the swept-up shell of IRS 5. The compactness of the NE envelope is clearly demonstrated by the 1.3 mm continuum imaging survey of YSOs with the IRAM 30 m telescope (Motte & André 2001). Figure 2.13 shows the compactness of YSOs defined by the ratio of the peak intensity with an $11''$ beam to the flux density within a diameter of $60''$ at 1.3 mm. Although NE has a low bolometric temperature of 75 K, the degree of the compactness of 60 % is considerably high compared to the other class 0 objects. Moriarty-Schieven et al. (2000) also showed that the 1.3 mm flux density of 0.851 $\pm$ 0.084 Jy obtained by the OVRO interferometer ($1\farcs29 \times 1\farcs07$ in HPBW) agrees with that of 0.83 $\pm$ 0.03 Jy obtained by the JCMT ($20''$ in HPBW) within the errors, indicating that the dust emission is centrally condensed. Furthermore, the NE component seen in Figures 2.4 & 2.6 has a small size of $\sim$ 1000 AU, suggesting the gas envelope is also compact. One possible interpretation of such an unusually compact envelope is that the swept-up shell

accelerated by the outflow from IRS 5, which likely to trigger the NE formation, has blown off the outer parts of the envelope.

The outflow of IRS 5 seems to have enough power to blow off the circumstellar envelope around NE as follows: The momentum flux put into the dense gas around NE by the decelerating swept-up shell is given by

$$P_{\rm shell} = M_{\rm H_2} \times a_{\rm dcl}, \tag{2.5}$$

where $M_{\rm H_2}$ is the mass of the swept-up shell of 0.14 $M_\odot$, and is estimated to be $(0.62 - 2.6)\times$ 10^{-4} $M_\odot$ km s^{-1} yr^{-1}. Here we assume that all the momentum flux which the outflow lost is put into the dense gas for simplicity. On the other hand, for a typical protostar with a mass of 0.5 $M_\odot$ surrounded by an envelope with 2000 AU radius and $0.1M_\odot$ mass, the momentum required to dissipate the envelope would be 7.0×10^{-2} $M_\odot$ km s^{-1}. Since the age of NE is $(0.6-5)\times$ 10^4 yr, the momentum flux required to blow off the envelope have to be larger than $(0.14 - 1.2)\times$ 10^{-5} $M_\odot$ km s^{-1} yr^{-1}. This flux is one order of magnitude smaller than $P_{\rm shell}$, indicating that the outflow from IRS 5 might have blown off the outer parts of the envelope around NE.

2.5 Summary

We have presented the new results of the high angular resolution and high sensitivity CS ($J = 2-1/J = 3-2$) observations of the protostar L1551 NE. The main results are as follows:

1. Both the CS ($J = 2 - 1$) and ($J = 3 - 2$) emissions were detected from $V_{\rm lsr} \approx 5.3$ to 10.1 km s^{-1}, and their distributions are quite similar to each other. The arc-shaped structure open toward NE and the compact disklike structure at the NE position were clearly resolved. The total mass of the dense gas is estimated to be 0.14 ± 0.02 $M_\odot$, and the mass contained in the disklike structure is $(9.0 \pm 2.0) \times 10^{-3}$ $M_\odot$.

2. One-arcsec resolution imaging of 3 mm and 2 mm continuum emission has revealed the disklike structure, perpendicular to the [Fe II] jet and the HH jets HH 28, 29, and 454. The size of the structure is $1\farcs39 \times 1\farcs00$ (200 AU $\times$ 140 AU) at P.A. of $159 \pm 13^\circ$ and the estimated mass is 0.032 ± 0.003 $M_\odot$. Although NE is a binary system consisting of NE-A and NE-B, the main contributor of the dust continuum emission seems to be NE-A.

3. The CS gas around NE shows the distinct velocity gradient along the outflow axis of IRS 5. This can be explained by the deceleration of the swept-up shell accelerated by the outflow from IRS 5, suggesting that the swept-up shell has impacted on NE.

4. The distributions of the CS and $H^{13}CO^+$ emissions show clear anti-correlation, suggesting that CS is abundant in the post-shocked regions, whereas $H^{13}CO^+$ is abundant in the pre-shocked regions.

5. Since the timescale of the interaction is comparable to the age of NE, it is likely that the formation of NE was triggered by the impact of the swept-up shell of the outflow from IRS 5.

6. Our and previous results suggest that NE has a compact circumstellar envelope with a size of $\sim$ 1000 AU, although NE is categorized as a class 0 object. The outer parts of the envelope might be blown off by the outflow from IRS 5, because the momentum put in by the swept-up shell is sufficient to blow off the envelope.

CHAPTER 2. TABLE

Table 2.1: Observational Parameters

Molecular line	CS ($J = 2 - 1$)	CS ($J = 3 - 2$)
Frequency [GHz]	97.980968	146.969049
Velocity resolution [km s^{-1}]	0.19	0.25
Synthesized beam size	$6\farcs53 \times 6\farcs15$	$4\farcs35 \times 3\farcs86$
Position angle [°]	-56.0	-44.9
Noise level (1 σ) [Jy beam^{-1}]	0.12	0.18
Continuum [GHz]	98 ± 0.512, 110 ± 0.512	135 ± 0.512, 147 ± 0.512
Synthesized beam size (D/AB)*	$6\farcs28 \times 5\farcs87$ / $1\farcs52 \times 1\farcs35$	$4\farcs51 \times 4\farcs19$ / $1\farcs18 \times 1\farcs10$
Position angle [°] (D/AB)*	-49.9/ 5.2	-41.6/ 54.8
Noise level (D/AB)* [mJy beam^{-1}]	1.4 / 2.0	2.6 / 2.6
Phase & amplitude calibrator (flux density)	0507+179 (1.4Jy)	0446+112 (1.4Jy) 0507+179 (1.9Jy) 0528+134 (2.6Jy)
Bandpass calibrator	3C454.3, 3C279	
$T_{\rm sys}$ [K] (in DSB)	150 K	200 K

*: D and AB are the NMA array configurations D (lowest angular resolution) and AB (highest angular resolution), respectively.

Table 2.2: Total flux densities of the continuum emission of L1551 NE

Frequency [GHz]	Total flux density [mJy]	Peak flux density [mJy beam^{-1}]	Deconvolved size [″]	P.A. [°]	Beam size [″]	P.A. [°]	NMA config.
104	92.5 ± 9.4	74.6	3.99 × 2.64	147	6.28 × 5.87	-49.9	D
	68.3 ± 7.1	41.5	1.36 × 0.78	154	1.52 × 1.35	5.2	AB
141	202 ± 22	159	2.41 × 1.12	155	4.51 × 4.19	-41.6	D
	130 ± 13	60.4	1.43 × 1.29	180	1.18 × 1.10	54.8	AB

Table 2.3: CS ($J = 2 - 1$) and CS ($J = 3 - 2$) flux densities of L1551 NE

	CS (J=2-1)		CS (J=3-2)		
	$V_{\rm lsr}$ [km s^{-1}]	$\int S_\nu dv$ [Jy kms^{-1}]	$V_{\rm lsr}$ [km s^{-1}]	$\int S_\nu dv$ [Jy kms^{-1}]	Mean Mass [$10^{-2} \times M_\odot$]
Low-velocity blue (LVB)	5.32 - 6.47	6.8	5.43 - 6.47	22.9	3.1 ± 0.3
NE component	6.47 - 8.57	2.6	6.47 - 8.51	4.9	0.9 ± 0.2
Low-velocity red (LVR)	7.04 - 8.57	21.9	7.23 - 8.51	50.3	8.1± 0.8
High-velocity red (HVR)	8.57 - 10.11	8.1	8.51 - 10.04	21.0	3.2 ± 0.2
Total		36.8		94.2	14.4 ± 1.5

CHAPTER 2. FIGURES

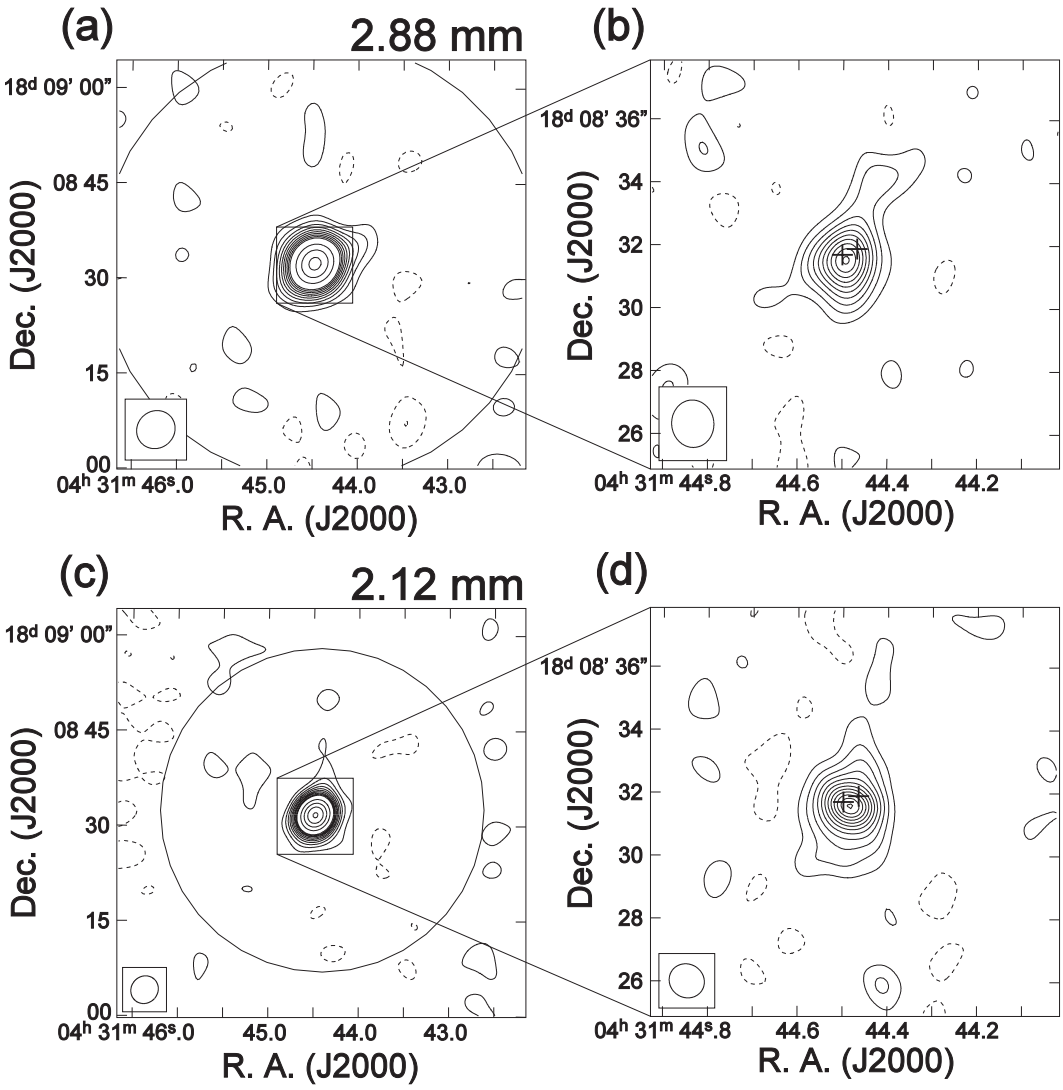

Figure 2.1: (a), (b) Lowest and highest angular resolution images with the D and AB configurations at $\lambda = 2.88$ mm, respectively. (c), (d) Lowest and highest angular resolution images with the D and AB configurations at $\lambda = 2.12$ mm, respectively. The contour lines of these maps start at ± 2.0 σ levels with intervals of 2.0 σ until 20 σ, and the intervals become 10 σ above 20 σ. The negative levels are indicated by broken lines. The two crosses in the (b) & (d) maps indicate the binary positions determined at $\lambda = 3.6$ cm with the VLA (Reipurth et al. 2002). The rms noise levels (1 σ) of the (a), (b), (c), and (d) maps are 1.4, 2.0, 2.6, and 2.6 mJy beam^{-1}, respectively. The open ellipse in the bottom left corner of each map is the synthesized beam size (HPBW).

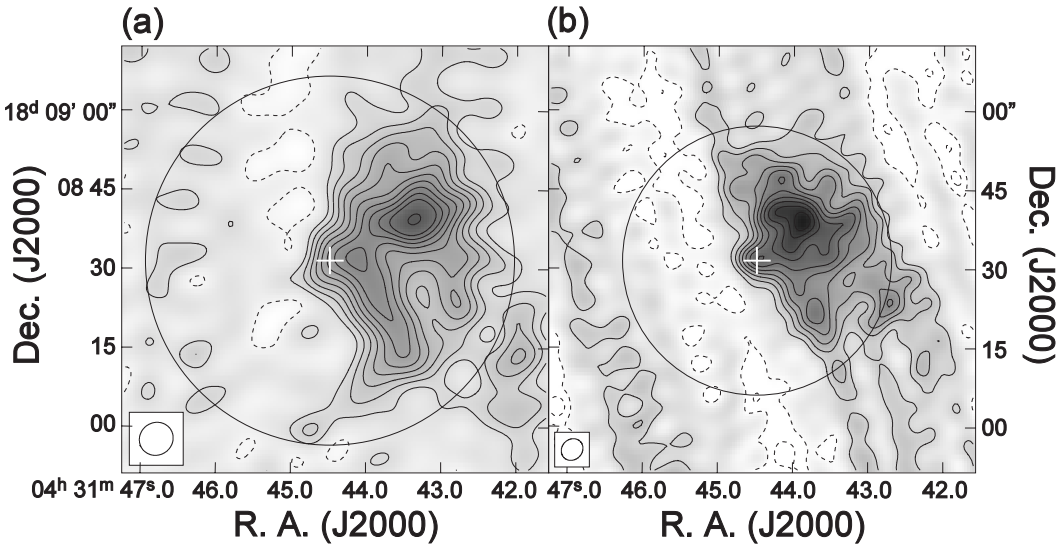

Figure 2.2: (a) Total intensity map of CS ($J = 2 - 1$) emission integrated from $V_{\rm lsr} = 5.32$ km s^{-1} to 10.11 km s^{-1}. The contour lines start at ± 2.0 σ levels with intervals of 2.0 σ until 20 σ, and the intervals become 4.0 σ above 20 σ. The negative levels are indicated by broken lines. The rms noise level (1 σ) is 0.025 Jy beam^{-1}, and the peak flux density is 0.61 Jy beam^{-1}. (b) Total intensity map of CS ($J = 3 - 2$) emission integrated from 5.43 km s^{-1} to 10.04 km s^{-1}. The contour lines are indicated in the same manner as in (a). The rms noise level (1 σ) is 0.040 Jy beam^{-1}, and the peak flux density is 0.86 Jy beam^{-1}. The circles on both the maps are the FWHM sizes of the primary beam. The open ellipse in the bottom-left corner in each map is the synthesized beam (HPBW). The central cross in each map is the position of NE.

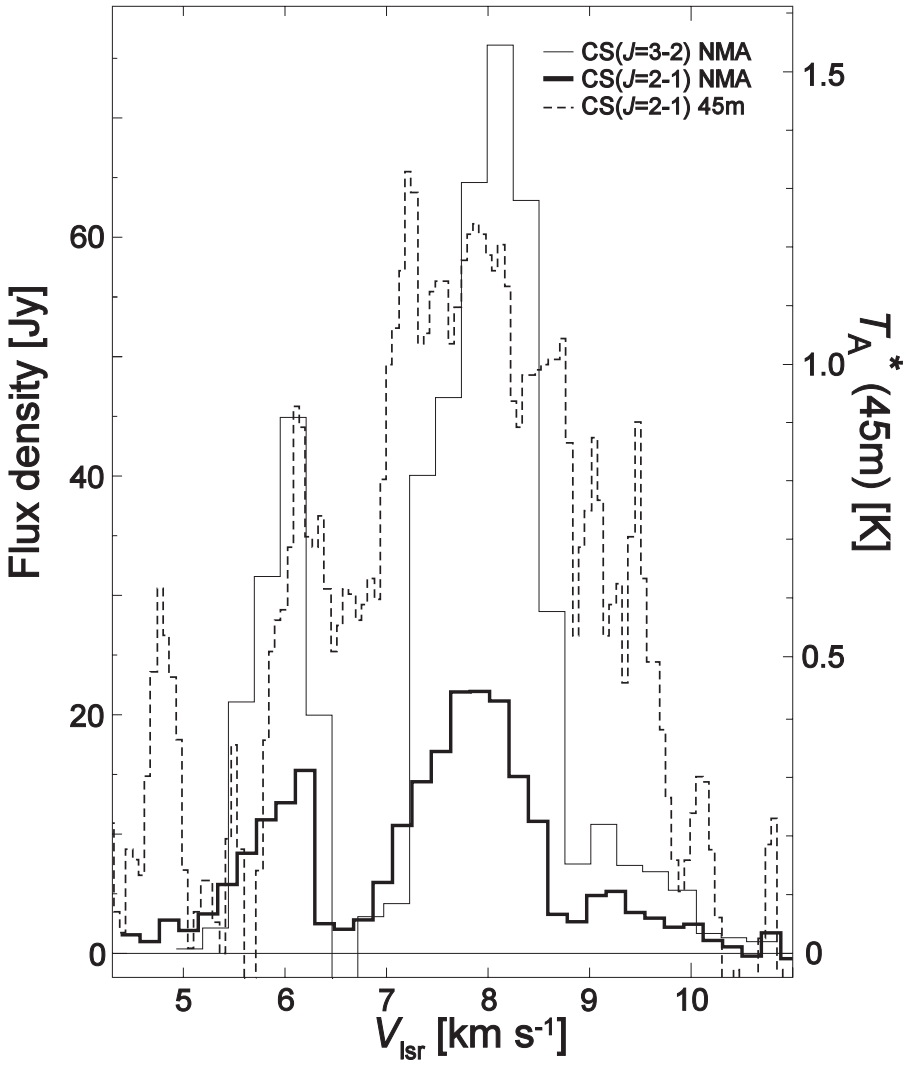

Figure 2.3: CS ($J = 2-1$) and ($J = 3-2$) line profiles taken with the NMA and the Nobeyama 45 m telescope. These profiles are integrated over a square region of $50'' \times 50''$ around NE. The solid lines represent the profiles taken by the NMA which is applied the correction for the primary beam attenuation: thick line is the profile of CS ($J = 2 - 1$) and thin one is that of CS ($J = 3 - 2$) in unit of Jy. The dashed line represents the CS ($J = 2 - 1$) profile taken by the 45 m telescope in unit of T_A^*. The T_A^* scale of the right axis is equivalent to the Jy scale of the left one.

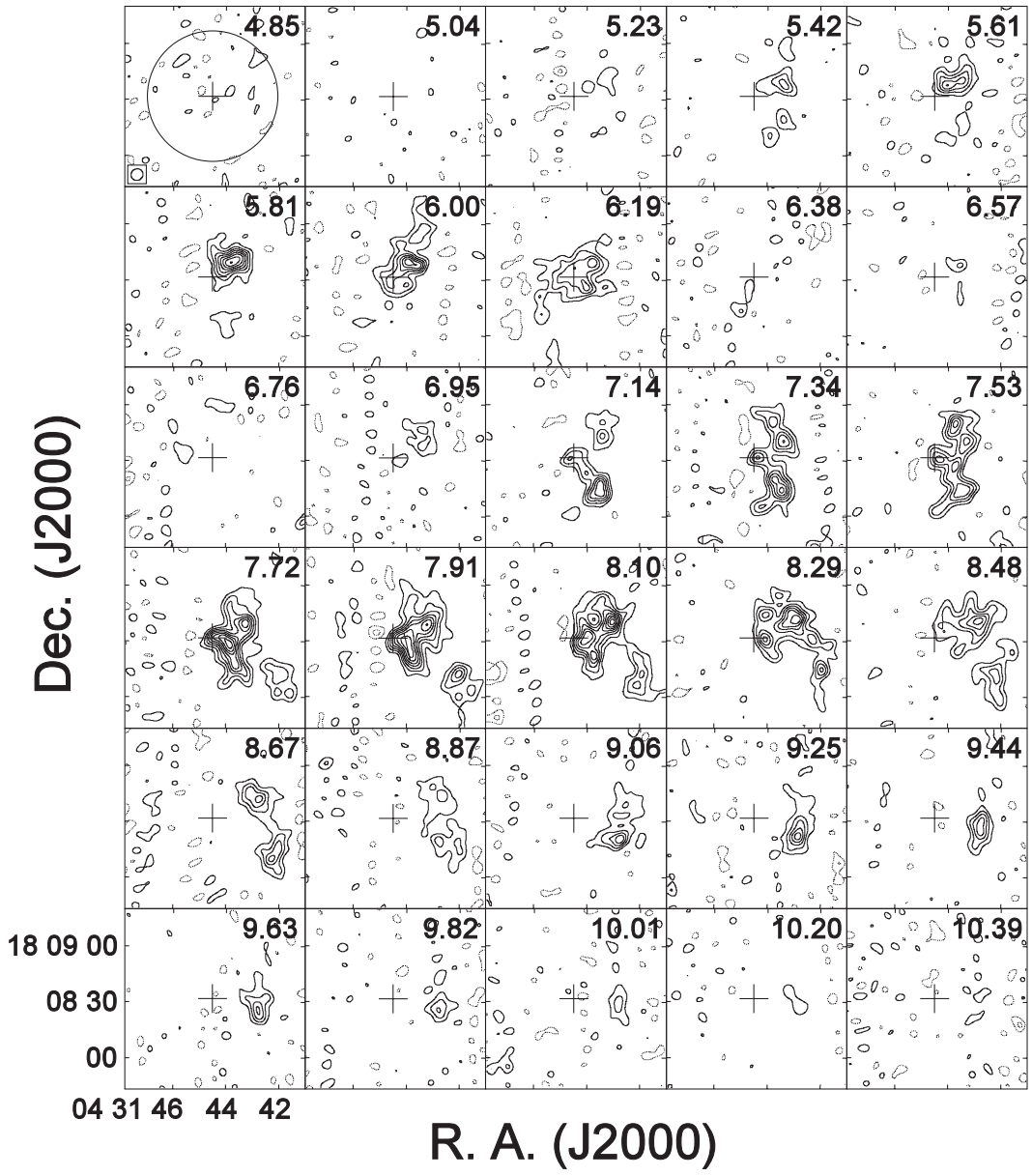

Figure 2.4: Velocity channel maps of CS ($J = 2 - 1$) emission. The central LSR velocity is denoted in unit of km s^{-1} at the upper right corner of each panel. The contour intervals are 2.0 σ, starting at $\pm$2.0 σ levels with 1 σ = 0.12 Jy beam^{-1}. The negative levels are indicated by broken lines. The central cross in each map exhibits the position of NE. The open ellipse in the bottom-left corner of the top-left panel is the synthesized beam (HPBW).

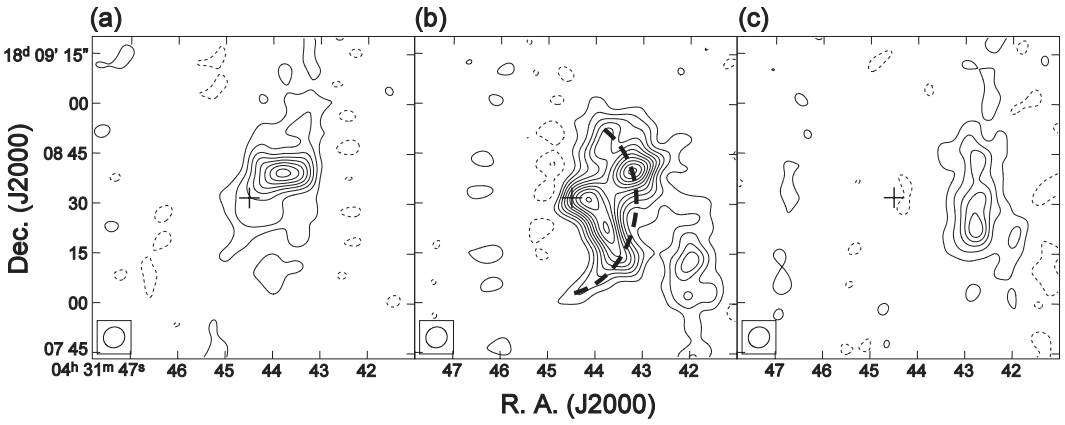

Figure 2.5: CS ($J = 2 - 1$) maps for (a) the low-velocity blue (LVB) component of $V_{\rm lsr} = 5.32 - 6.47$ km s^{-1}, (b) the low-velocity red (LVR) component of $V_{\rm lsr} = 7.04 - 8.57$ km s^{-1} , and (c) the high-velocity red (HVR) component of $V_{\rm lsr} = 8.57 - 10.11$ km s^{-1}. The contour lines of each map are written in the same manner as in Figure 2.4. The rms noise levels are 62 mJy beam^{-1}, 54 mJy beam^{-1}, and 57 mJy beam^{-1} for (a), (b), and (c), respectively. The central cross is the position of NE. The dashed line in (b) delineates the newly found small-scale arc open toward NE.

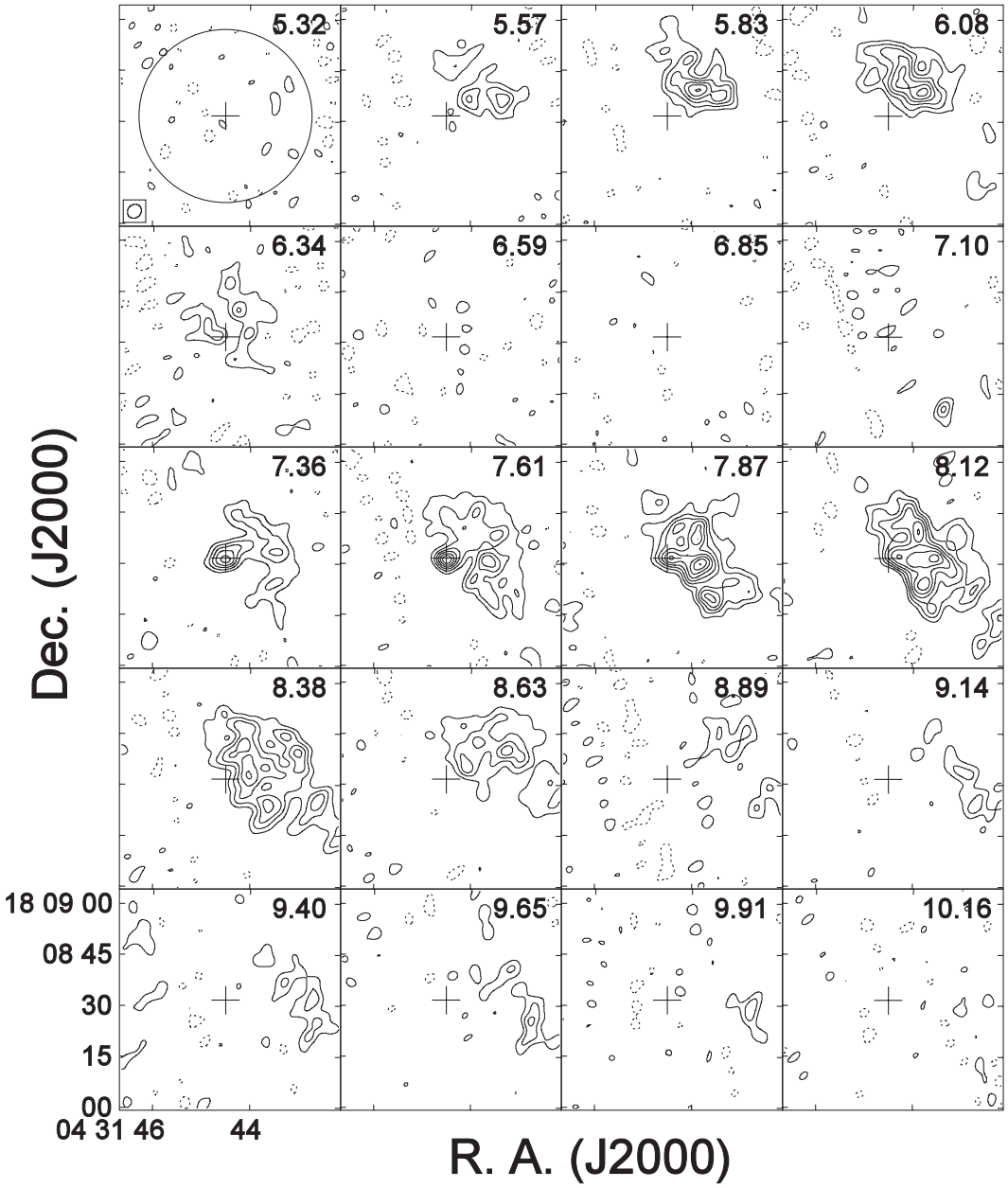

Figure 2.6: Velocity channel maps of CS ($J = 3 - 2$) emission. The central LSR velocity in unit of km s^{-1} is denoted in the upper right corner of each panel. The contour lines are written in the same manner as in Figure 2.4 with 1 σ = 0.18 Jy beam^{-1}. The central cross exhibits the position of NE. The open ellipse at the bottom-left corner of the top-left panel is the synthesized beam (HPBW).

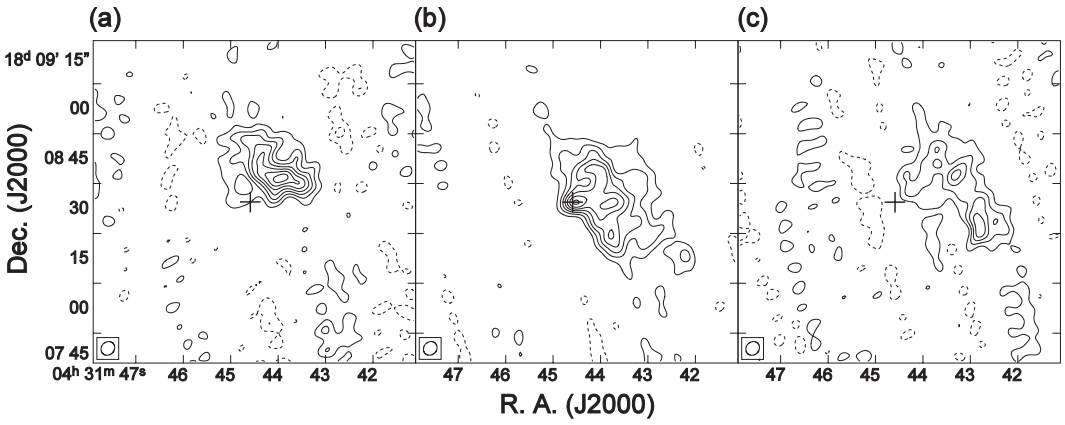

Figure 2.7: CS ($J = 3-2$) maps for (a) the LVB component of $V_{\rm lsr} = 5.43-6.47$ km s^{-1}, (b) the LVR component of $V_{\rm lsr} = 7.23-8.51$ km s^{-1}, and (c) the HVR component of $V_{\rm lsr} = 8.51-10.04$ km s^{-1}. The contour lines of each map are written in the same manner as in Figure 2.4. The rms noise levels are 94 mJy beam^{-1}, 125 mJy beam^{-1}, and 75 mJy beam^{-1} for (a), (b), and (c), respectively. The central cross is the position of NE.

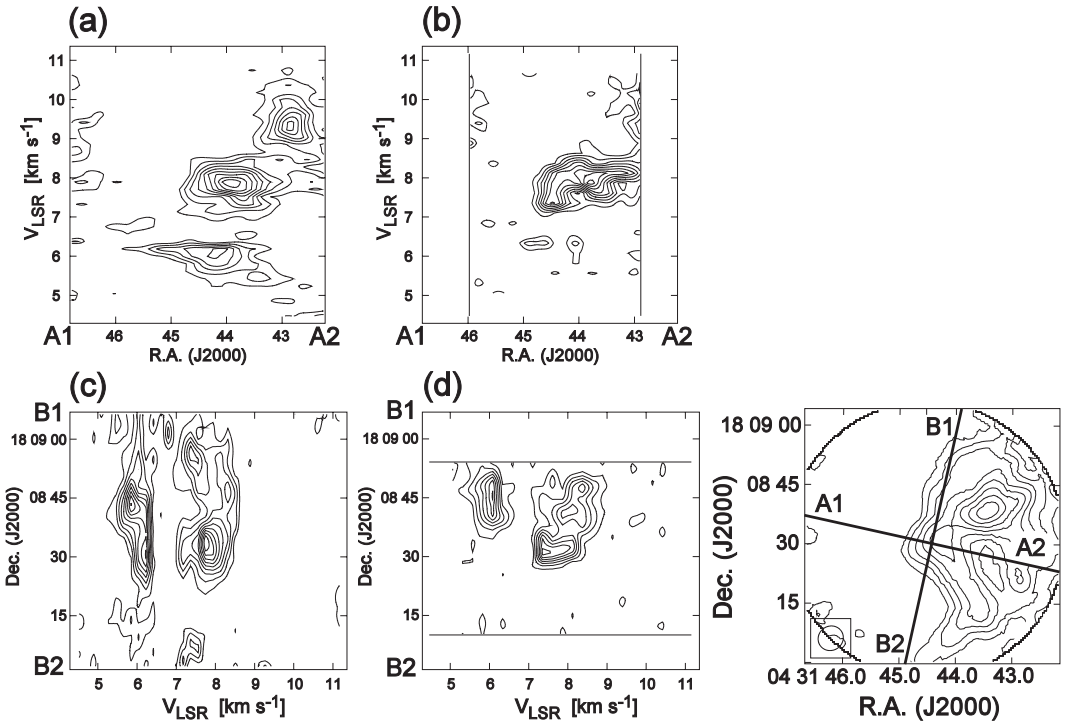

Figure 2.8: (a) Position-velocity diagram of CS ($J = 2 - 1$) emission cut along the line (A1 - A2) between L1551 NE and IRS 5, which is almost parallel to the outflow axis of IRS 5. (b) P-V diagram of CS ($J = 3 - 2$) emission along the line (A1 - A2). (c), (d) P-V diagrams of CS ($J = 2 - 1$) and CS ($J = 3 - 2$) emissions along the line (B1 - B2) perpendicular to the outflow axis. The contour levels of all the diagrams are in steps of 10% of the peak flux densities from 20% to 100%.

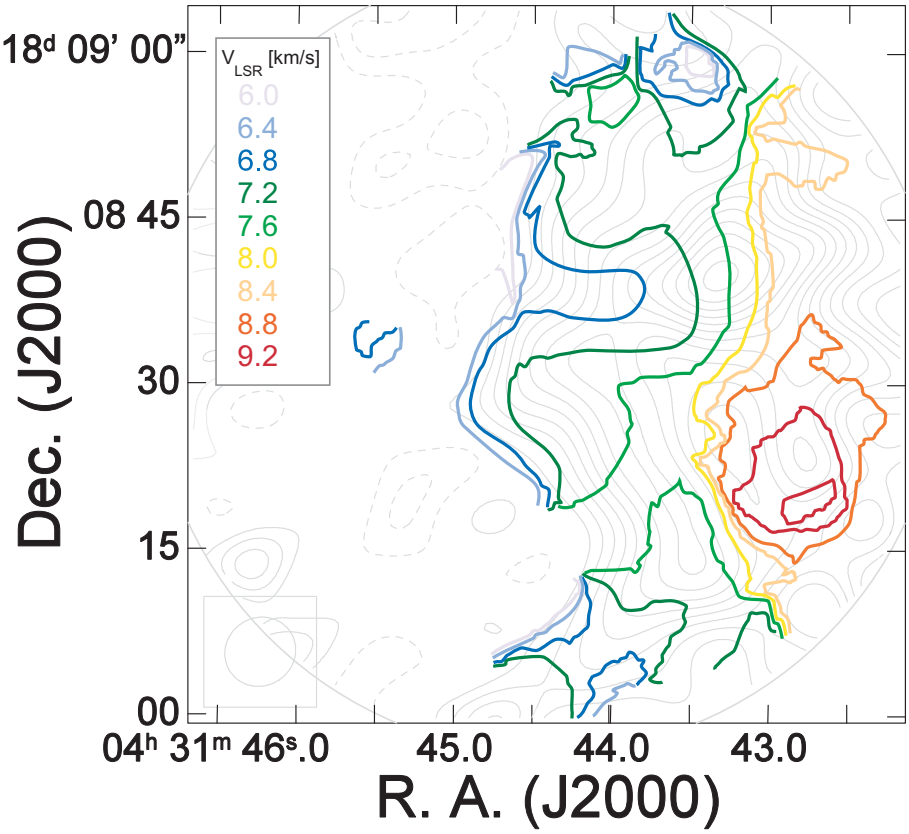

Figure 2.9: Intensity-weighted mean velocity map of L1551 NE obtained from the CS ($J = 2 - 1$) emission. The integrated intensity image is also shown by the gray contours, whose contour intervals are same as in Figure 2.2.

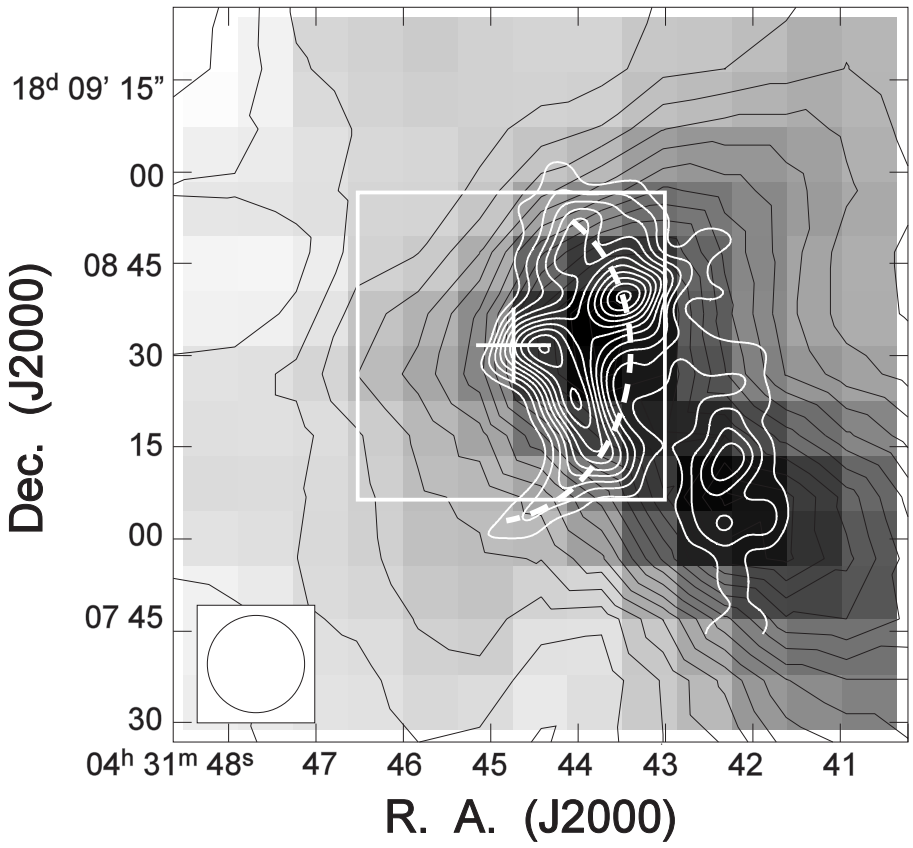

Figure 2.10: Map of the LVR component of CS ($J = 2 - 1$) emission ($V_{\rm lsr} = 7.04 - 8.57$ km s^{-1}) taken with the NMA superposed on a total integrated intensity map of CS ($J = 2 - 1$) over $V_{\rm lsr} = 5.0 - 11.0$ km s^{-1} taken with the Nobeyama 45 m telescope. Black contour lines with the gray scale image are from the 45 m telescope in steps of $T_A^* = 0.2$ K. Note the large scale CS arc-shaped structure open toward L1551 IRS 5 seen in the 45 m map and the small scale CS arc-shaped structure open toward L1551 NE seen in the NMA map which is denoted by a white dashed line. The white square shows an area of $50'' \times 50''$ around NE where the CS line profiles are calculated. The central cross indicates the position of NE. The open circle in the bottom-left corner is the angular resolution of the 45 m telescope ($16''$ in HPBW).

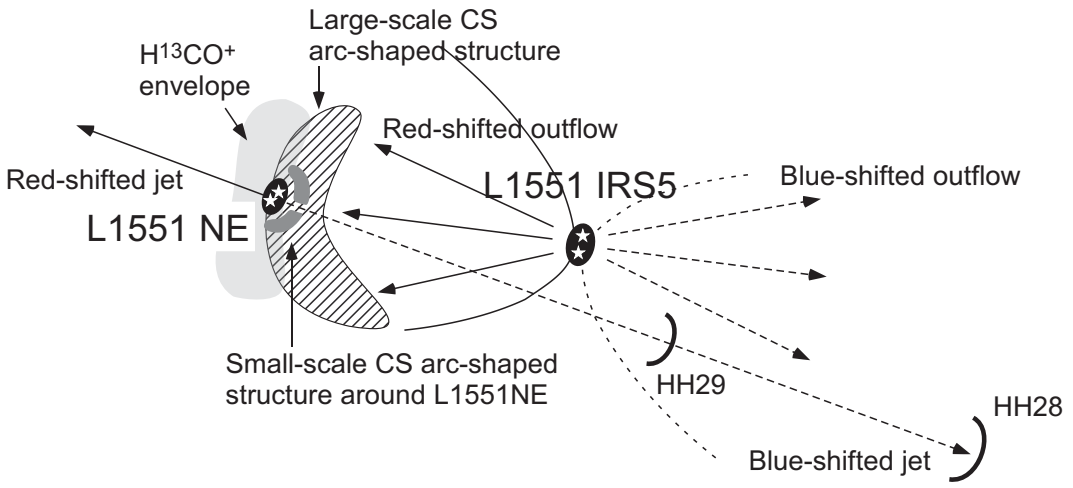

Figure 2.11: Schematic illustration of the relationship between L1551 NE and IRS 5. The large-scale CS arc-shaped structure open toward IRS 5 represents the swept-up dense shell by the outflow from IRS 5. The small-scale CS arc-shaped structure open toward NE seems to be a bow-shock around NE caused by the impact of the dense shell. The $H^{13}CO^+$ emission is distributed in the pre-shock region on the east side of NE, whereas the CS emission is mainly distributed in the post-shock region on the west side of NE.

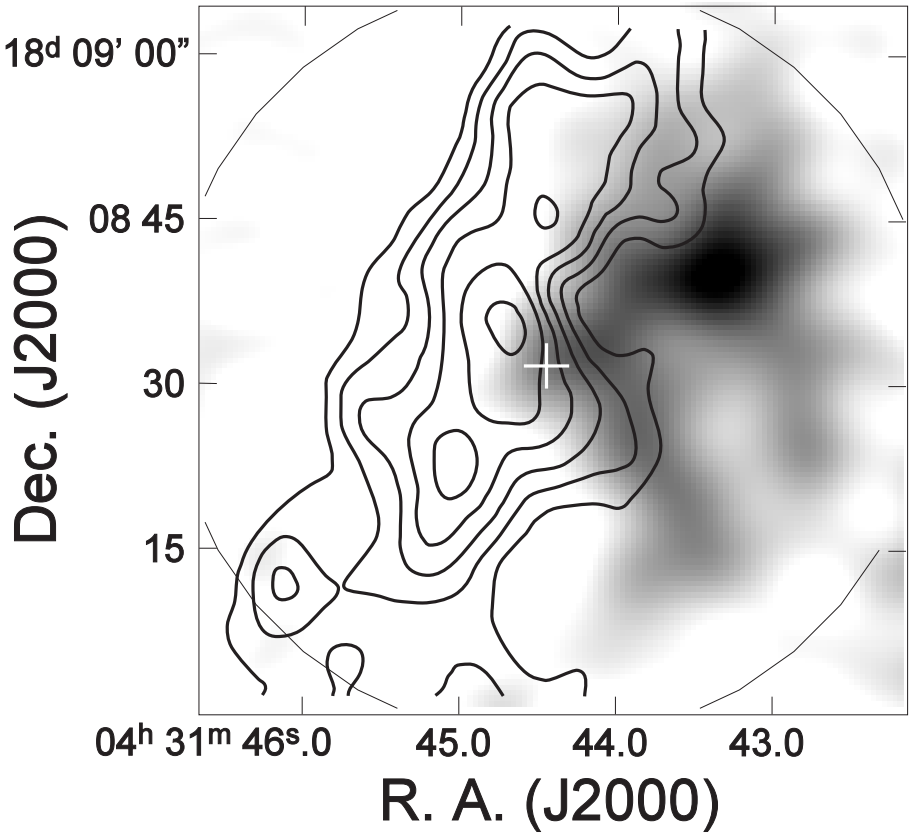

Figure 2.12: Total intensity map of $H^{13}CO^+$ (solid contour) superposed onto the total intensity map of CS ($J = 2 - 1$) in gray scale. The central cross indicates the position of NE.

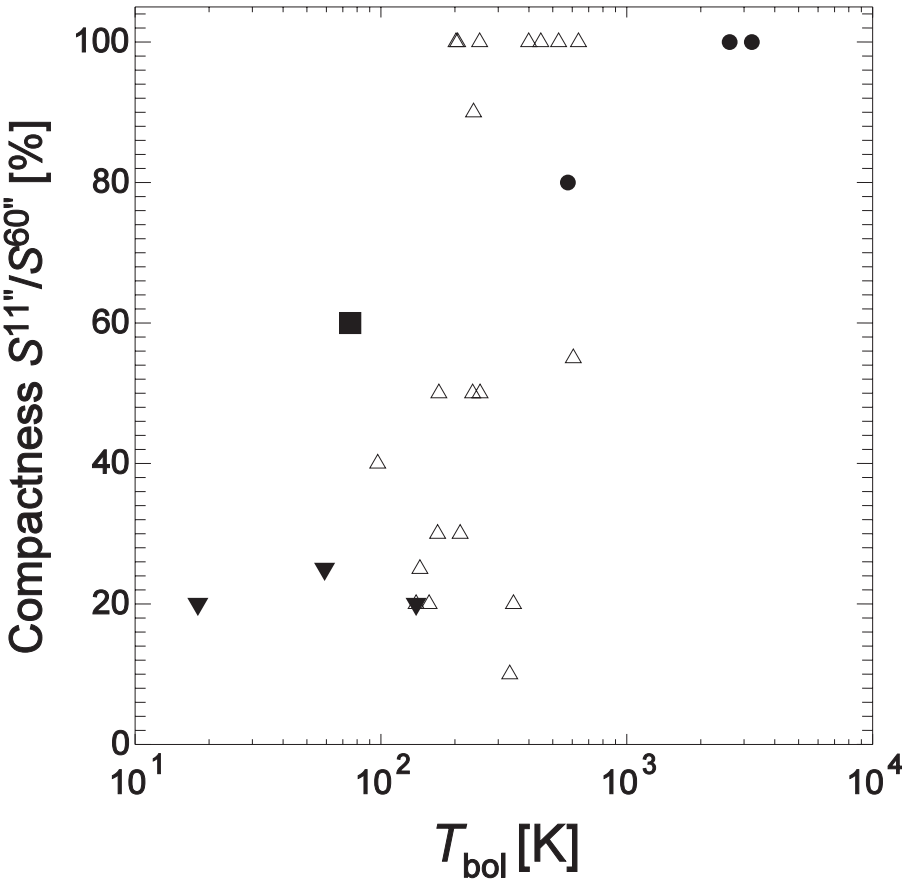

Figure 2.13: Compactness of 1.3 mm continuum emission of YSOs in the TMC. The vertical axis shows the ratio of the peak flux density in an 11″ beam to the total flux density in a 60″ diameter circle. All the data are compiled from the survey with the IRAM 30 m telescope (Motte & André 2001). The filled triangles show class 0 objects, the open triangles show class I objects, and the filled circles show class II objects. The filled square indicates L1551 NE.

Chapter 3

Aperture Synthesis ^{13}CO $J = 1 - 0$ and $J = 2 - 1$ Observations of Protostar L1551 IRS 5: Formation of a Protoplanetary Disk in a Protostelar Envelope

A part of this chapter is submitted to
The Astrophysical Journal
as
"Aperture Synthesis ^{13}CO ($J = 2 - 1$) Observations of L1551 IRS 5: Formation of a Keplerian Disk in a Protostellar Envelope"
by
Sozo Yokogawa[1,2], Yoshimi Kitamura[3], Munetake Momose[4], Masato Bando[5] and Ryohei Kawabe[2]
(1) The Graduate University for Advanced Studies; (2) National Astronomical Observatory of Japan; (3) The Institute of Space and Astronautical Science; (4) Ibaraki University; (5) The University of Tokyo;

Abstract

Aperture synthesis observations of ^{13}CO ($J = 1 - 0$) and ($J = 2 - 1$) line emissions toward a protobinary system L1551 IRS 5, made with the Nobeyama Millimeter Array, are presented. The ^{13}CO ($J = 1 - 0$) observations revealed a centrally condensed envelope component whose size of $\approx$ 2000 AU in diameter and extended X-shaped components around L1551 IRS 5. The envelope shows infall and rotation motion toward the central sources. The infall velocity of the envelope is consistent to the free-fall velocity around a central mass of $\approx 0.5\ M_{\odot}$, whereas the rotational velocity of 0.24 km s^{-1} at 700 AU in radius with radial dependence of r^{-1} would be valid, suggesting the specific angular momentum of the gases has conversed during the contraction of the protostellar envelope. The X-shaped components have symmetrical structures centered on L1551 IRS 5 and trace the swept-up gases along the outer shell of the blue- and red-shifted outflow. These components have a wide opening angle of 120° and the gases have accelerated with an uniform acceleration, like a Hubble-law.

The ^{13}CO ($J = 2 - 1$) emission shows a disklike structure with a FWHM size of 3.″16 × 2.″04 at P.A. of 138° in the central part of the envelope. A distinct velocity gradient is detected along the major axis of the disklike structure, which is parallel to the elongation of the envelope, whereas no prominent gradient is detected along the minor axis, suggesting the presence of a purely rotating disk. The ^{13}CO total map gives a disk radius of 350 ± 40 AU and the PV diagram along the major axis gives a binary mass of $0.6 - 1.4\ M_{\odot}$. This radius is significantly larger than the centrifugal radius of $23 - 53$ AU derived from the local specific angular momentum of the envelope, although a Keplerian disk with the centrifugal radius is theoretically thought to form. The turbulent viscosity with a large coefficient of $\alpha \sim 1$ is likely to make a small disk with the centrifugal radius efficiently expand, whereas the gravitational interaction between the disk and the binary sources would not be efficient. It is also possible that the natal core of IRS 5 was not rigidly rotating but more rapidly rotating with large specific angular momentum in the inner part of the core.

3.1 Introduction

Recent progresses of observational and theoretical studies have revealed the outline of the low mass star formation scenario. YSOs in the early phase, which are called protostars, are accompanied with powerful outflows and surrounded by massive envelope gases exhibiting infall motions. As they evolve, their outflows have dispersed the surrounding envelopes, and finally T

Tauri stars with rotating disks (i.e., protoplanetary disks) have appeared. Survey observations of YSOs in millimeter continuum emission showed that the dust emission around protostars is more extended than that of T Tauri stars (Ohashi, Hayashi, Kawabe, & Ishiguro 1996; Looney et al. 2000), suggesting that disks as well as central stars grow by accretion of matter. Furthermore, the radial expansion of the disks with decreasing their accretion luminosities has been revealed by Kitamura et al. (2002). Although an evolution of protoplanetary disks has been revealed, the formation mechanism of the disks, which must be formed in an envelope around a protostar, has not well understood.

We performed the aperture synthesis observations of L1551 IRS 5 (hereinafter IRS 5) to reveal the formation process of the protoplanetary disk in the envelope. IRS 5, categorized as a class I object, is the most luminous protostar ($L_{\rm bol} \approx 30\ L_{\odot}$) in the Taurus Molecular Cloud lying at a distance of 140 pc (Elias 1978). Recent VLA observations revealed that IRS 5 is a protobinary system with a 45 AU separation (Rodriguez et al. 1998). IRS 5 is surrounded by a massive envelope with several $\times$ 1000 AU radius, which exhibits rotation and infall (Momose et al. 1998), suggesting the rotation disk might have formed at the inner part of the envelope, the formation process of a Keplerian disk has not been well understood. One of the promising probes to extract the disk from the envelope is a higher J transition of molecules which is likely to trace denser and hotter parts of the envelope, i.e., the protoplanetary disk.

3.2 Observations

Aperture synthesis observations of IRS 5 were carried out in ^{13}CO ($J = 1 - 0$) (110.201353 GHz) and ^{13}CO ($J = 2 - 1$) (220.398686 GHz) line emissions with the Nobeyama Millimeter Array (NMA), which consists of six 10 m antennas, during a period from 2001 January to 2002 April. All the array configurations D, C and AB were adopted for ^{13}CO ($J = 1 - 0$) observations: whose projected baseline lengths ranged from $3 - 30$, $6 - 55$ and $15 - 110$ kλ. Two array configurations D and C, whose projected baseline lengths ranged from $6 - 60$ from $12 - 110$ kλ respectively, were adopted for ^{13}CO ($J = 2 - 1$) observations. The system noise temperatures of SIS receivers in DSB mode were typically 150 K at 110 GHz and 500 K at 220 GHz toward the zenith, respectively. We used a 1024 channel FX spectrocorrelator with a total bandwidth of 32 MHz, resulting in a velocity resolution of 0.084 km s^{-1} and 0.0425 km s^{-1} at 110 and 220 GHz, respectively. The center of the field was set on the IRS 5 position of (α_{2000}, δ_{2000}) = ($4^h\ 31^m\ 34^s.15$, $+18^\circ\ 08'\ 04''.99$). The FWHM size of the primary beams at 110 GHz and 220 GHz (i.e., field of view) were $62''$, $30''$. Since the minimum baseline length

at 110 GHz and 220 GHz were 3 kλ and 6 kλ, respectively, our observations were insensitive to structures extended more than 69″ and 34″ (10^4 AU, 5×10^3 AU at 140 pc). The responses across the observed passband were determined from 30-60 minute observations of 3C454.3 and 3C279. A gain calibrators 0446+112, 0420-014 were observed every 10-20 minutes, and these flux densities were determined to be $(1.7 - 2.6)$ Jy for 0446+112 and 6.4 Jy for 0420-014 from observations of Uranus. The overall uncertainties in the flux calibrations were about 10 % at 110 GHz and less than 20 % at 220 GHz. After the calibrations, we made final images only from the data taken under good weather conditions. Using the AIPS package developed at the NRAO, we CLEANed maps by natural weighting with no UV taper.

The continuum data were obtained with the digital spectral correlator UWBC (Okumura et al. 2000), which has 128 frequency channels and a 1024 MHz bandwidth per baseline. Visibility data in both the lower (98 ± 0.512, 220 ± 0.512 GHz) and upper (110 ± 0.512, 232 ± 0.512 GHz) sidebands were obtained simultaneously with a phase-switching technique. To obtain a higher S/N, the data of both the sidebands were combined into a final image: The center frequencies are 104 GHz ($\lambda = 2.88$ mm) and 226 GHz ($\lambda = 1.33$ mm). The observational parameters are summarized in table 3.1.

3.3 Results

3.3.1 ^{13}CO ($J = 1 - 0$) emission

A significant ^{13}CO ($J = 1 - 0$) emission above the 3 σ level is detected within the velocity range of $V_{\rm LSR} = 4.5 - 7.9$ km s^{-1}, with a typical sensitivity of ≈ 0.32 Jy beam^{-1} and the velocity resolution of 0.169 km s^{-1}. The total intensity map integrated over these ranges, superposed onto the near-infrared (J + K' bands) image taken with the SUBARU (Itoh et al. 2000), is shown in Figure 3.1. Since a reflection nebula at the red-shifted side of IRS 5 is hidden by the ambient medium, only the blue-shifted side of the nebula which seems to trace the inner-wall of the cavity excavated with the outflow activities of IRS 5 can be seen. The ^{13}CO emission can be decomposed into two components: a centrally condensed component at the vicinity of the stellar position of IRS 5 corresponding to the envelope, and an extended X-shaped structure which stretches from the central component to the north-east, south-east, north-west, and south-west directions at lower contour levels, which is likely to trace the cavity wall of the outflow indicated as dashed lines in Figure 3.1. The FWHM size of the centrally condensed component is about 9.″1 × 8.″3 (1300 ×1200 AU) at the P.A. of 5.8°. Since the

major axis of the IRS 5 envelope is known at P.A. $\approx 162^\circ$ (e.g., Momose et al. 1998), the P.A. of the condensed component is roughly parallel to the major axis of the envelope. The total intensity of the condensed component is 26.9 Jy km s^{-1}, whereas the entire intensity above the 3 σ level is 100.4 Jy km s^{-1}. Figure 3.2 shows the ^{13}CO ($J = 1 - 0$) and C^{18}O ($J = 1 - 0$) line profiles integrated around IRS 5 (over a 20″ square) and over an entire region of the field (over a 50″ square). Although C^{18}O emission has a symmetric profile around the systemic velocity indicating optically thin emission, the ^{13}CO emission has a strong self-absorption around the systemic velocity, which is also easily recognized in the channel maps of Figure 3.3, suggesting that the ^{13}CO emission is optically thick.

Figure 3.3 shows channel maps of ^{13}CO ($J = 1 - 0$) with velocity resolution of 0.169 km s^{-1}. From $V_{\rm LSR} = 4.5 - 4.8$ km s^{-1} which are blueshifted with respect to the systemic velocity of ≈ 6.2 km s^{-1} (Momose et al. 1998), the only centrally condensed envelope components are found. In the channels from $V_{\rm LSR} = 5.0 - 5.7$ km s^{-1}, not only the envelope components but also the extended blue-shifted outflow components are found at the west-side of IRS 5. From $V_{\rm LSR} = 5.8 - 6.4$ km s^{-1} including the systemic velocity of ≈ 6.2 km s^{-1}, the emission shows clumpy and complex structure with relatively weak intensity, mainly owing to the resolving out of the smooth components and the self-absorption effect. In the following channels from $V_{\rm LSR} = 6.5$ to 7.9 km s^{-1}, which are redshifted with respect to the systemic velocity of IRS 5, the envelope components and the red-shifted outflow components stretching southeastward and northeastward are clearly seen. Figure 3.4 is the intensity-weighted mean velocity map of L1551 IRS 5. The integrated intensity map is shown as the gray contours for comparison the distribution of the emission. The contour for $V_{\rm lsr} = 6.2$ km s^{-1} passes through the stellar position, and the northeast part of the component is red-shifted with respect to the systemic velocity whereas the southwest part of one is blueshifted. The velocity gradient align between the major and minor axis of the envelope structure, suggesting that the infall and rotation motion exist in the envelope.

The total mass of the central component can be estimated from the total intensity using the following equation (Scoville et al. 1986):

$$M_{\rm LTE} = 5.37 \times 10^{-5} T_{\rm ex} \exp\left(\frac{5.29}{T_{\rm ex}}\right) \frac{\tau_{^{13}{\rm CO}}}{1 - \exp\left(-\tau_{^{13}{\rm CO}}\right)} \left(\frac{d}{140{\rm pc}}\right)^2 \left[\frac{10^{-6}}{X(^{13}{\rm CO})}\right] \int S_\nu dv M_\odot, \tag{3.1}$$

where $T_{\rm ex}$ is the excitation temperature, $\tau_{^{13}{\rm CO}}$ is the optical depth of ^{13}CO, $X(^{13}{\rm CO})$ is the fractional abundance of ^{13}CO relative to H_2, and d is the distance to the source. Under

the assumption of that the optical depth of ^{13}CO is ≈ 3 estimated from $\tau_{\rm C^{18}O}$ of 0.6 (Fuller et al. 1995) and the fractional abundance of ^{13}CO to C^{18}O of 5.5, $T_{\rm ex} = 20 - 50$ K, and $X(^{13}{\rm CO}) = 10^{-6}$, the total flux density of 26.9 Jy km s^{-1} gives a mass of $0.12 - 0.24 M_{\odot}$, which is consistent with the mass of the envelope (e.g., Ohashi, Hayashi, Kawabe, & Ishiguro 1996; Saito, Kawabe, Kitamura, & Sunada 1996; Momose et al. 1998) (see table 3.3).

3.3.2 ^{13}CO $(J = 2 - 1)$ emission

A top-left panel of Figure 3.5 shows a total intensity map of the $^{13}{\rm CO}(J = 2 - 1)$ emission integrated from $V_{\rm lsr} = 3.77$ km s^{-1} to 8.87 km s^{-1}. An elongated disklike structure is found just at the source position. The total flux density integrated above the 2σ level is 13.4 Jy km s^{-1} with a peak flux density of 5.63 Jy km s^{-1} beam^{-1}. The beam-deconvolved size of the structure is $3\farcs16 \times 2\farcs04$ (FWHM) at P.A. = 138°, corresponding to 440 × 290 AU: the inclination angle, i, is estimated to be 50° (= arccos($2\farcs04/3\farcs16$)) for a geometrically thin disk. The major axis of the structure is almost parallel to that of the envelope (Momose et al. 1998, P.A. = 162°), and is perpendicular to the optical jet (Itoh et al. 2000, P.A. $\approx$ 245°).

The other panels of Figure 3.5 show channel maps with a velocity resolution of 0.51 km s^{-1}. In the panels of $V_{\rm lsr} = 6.06$ and 6.57 km s^{-1}, which are close to the systemic velocity, $V_{\rm sys}$, of 6.2 km s^{-1}(Momose et al. 1998), only weak emission was detected probably owing to the resolving out caused by the lack of short spacing data in our observations. The blueshifted emission of $V_{\rm LSR} = 4.02 - 5.55$ km s^{-1} with respect to $V_{\rm sys}$ is distributed to the south of IRS 5, while the redshifted emission of $7.08 - 8.10$ km s^{-1} is distributed to the north. Furthermore, the higher blue- and red-shifted components are distributed on the nearer sides of IRS 5 than the lower blue- and red-shifted ones. These results strongly suggest a Keplerian rotating disk. The presence of the rotating disk is more clearly demonstrated by an intensity-weighted mean velocity map which is shown in the bottom-right panel of Figure 3.5: a clear velocity shift along the major axis of the disk and no prominent shift along the minor axis. The disk radius, $R_{\rm out}$, is estimated to be 350 ± 40 AU from the 2 σ contour level of the total map, which is corrected for the convolution with the synthesized beam of $2\farcs30 \times 2\farcs00$. Although the estimation seems highly dependent on the noise level of our observations, it is not likely that the disk is much more extended than our image. This is because the north-east part of the mean velocity map, which deviates from the pure rotation, agrees with the velocity field of the infalling and rotating envelope, suggesting the inner boundary of the envelope.

A peak intensity ratio between the $^{13}{\rm CO}(J = 1-0)$ and $(J = 2-1)$ data which deconvolved

to the angular resolution of the ^{13}CO ($J = 1 - 0$) is ≈ 0.7, and the H_2 gas density and the excitation temperature $T_{\rm ex}$ are estimated to be $\sim 10^4$ cm^{-3} and 40 K, respectively, on the basis of the LVG analysis. We estimate the LTE mass by the following equation (Scoville et al. 1986):

$$M_{\rm LTE} = 1.34 \times 10^{-5} T_{\rm ex} \exp\left(\frac{15.9}{T_{\rm ex}}\right) \frac{\tau_{^{13}\rm CO}}{1 - \exp\left(-\tau_{^{13}\rm CO}\right)} \left(\frac{d}{140\rm pc}\right)^2 \left[\frac{10^{-6}}{X(^{13}\rm CO)}\right] \int S_\nu dv M_\odot, \quad (3.2)$$

where $T_{\rm ex} = 40$ K, the fractional abundance of ^{13}CO to H_2, $X(^{13}$CO), is 10^{-6}, and the optical depth of the ^{13}CO(J=2-1) emission, $\tau_{^{13}\rm CO}$, is 3 from $\tau_{\rm C^{18}O}$ of 0.6 (Fuller et al. 1995). The total flux density of 13.4 Jy km s^{-1} gives a mass of 0.03 $M_\odot$. The estimated mass is much smaller than the envelope mass which estimated in the previous section, suggesting that the ^{13}CO ($J = 2 - 1$) emission trace only innermost part of the envelope and/ or a circumbinary disk component.

3.3.3 Continuum images of L1551 IRS 5

Figure 3.6 shows 3 mm continuum images of IRS 5 with high and low angular resolutions. The total flux densities of the 3 mm continuum emission are 174 ± 17 mJy with the D configuration, and are 111 ± 11 mJy with the AB configuration. The peak position of the continuum emission is $(\alpha_{2000}, \delta_{2000}) = (04^h31^m34^s.141 \pm 0^s.007, +18°08'04''.78 \pm 0''.14)$, and is consistent with the midpoint of both the binary sources revealed by the VLA within the positional error of 0″.3 including the effect of atmospheric seeing (Rodriguez et al. 1998). In this paper, we regard the peak position of the continuum emission in Figure 3.6b as the central position of IRS 5. Figure 3.7 shows a 1.3 mm continuum image of IRS 5. An elongated disklike structure is clearly resolved with a beam-deconvolved size (FWHM) of 1″.87 × 1″.27 (262 AU × 178 AU) at P.A. = 152°. Since both the distributions of the 1.3 mm continuum and ^{13}CO($J = 2 - 1$) line emission are quite similar, the continuum emission is also thought to trace the rotating disk. The inclination angle of the disk can be estimated to be 47° (= $\cos^{-1}(1''.27/1''.87)$). The total flux density integrated above the 2 σ level is 0.56 Jy. The peak position of the continuum emission, however, agrees with neither of the stellar positions of the binary within the positional accuracy, which offsets about 0″.5 to the west of the binary positions. Since the X-rays are also detected not at the stellar positions but at the west side of

the binary system (Bally, Feigelson, & Reipurth 2003) as in the background gray scale image in Figure 3.7, hot gas and dust components might exist at the west side of IRS 5.

Assuming that the continuum emission around IRS 5 is optically thin at the millimeter wavelengths and the dust temperature within the disk, $T_{\rm dust}$, is uniform, we can estimate the entire disk mass by

$$M_{\rm disk} = \frac{F_\nu d^2}{\kappa_\nu B_\nu(T_{\rm dust})}, \tag{3.3}$$

where $B_\nu(T)$ is the Planck function at the temperature of $T_{\rm dust}$, κ_ν is the dust mass absorption coefficient of $\kappa_\nu = 0.1 \times (\nu/10^{12})^\beta$ cm^2 g^{-1} (Beckwith et al. 1990), and F_ν is the total flux density of the continuum emission. With $\beta = 1$; the the typical value of protostars, and $T_{\rm dust} = 50 - 120$ K (Osorio et al. 2003; Keene & Masson 1990), our total flux densities give a disk mass of $0.02 - 0.1 M_\odot$. In the case of $\beta = 0$ which is derived from the SED of the 1.3 mm and 3 mm continuum emissions, the mass becomes $(4 - 10) \times 10^{-3} M_\odot$.

3.4 Discussion

3.4.1 Visibility Fitting of the Circumstellar Disk around L1551 IRS 5

To examine radial flux density distributions of the continuum emission around L1551 IRS 5, we made the visibility plot as a function of UV distance as shown in Figure 3.8. Here, we assume that the inclination angle of 60°. Since IRS 5 is known as a binary system, we take into account three components to fit the visibility data of IRS 5: binary star components, a circumstellar disk around binary stars, and an extended envelope component. As shown in Figure 3.8, since the binary components have compact structure which can not be resolved in our observations, the visibility flux of binary components is almost constant of 40 mJy which is derived from the VLA observations (Rodriguez et al. 1998). Temperature and surface density distributions of the circumbinary disk are provided as power law distributions of $T = T_{\rm 100AU} \times (r/100{\rm AU})^{-q}$ [k], $\Sigma = \Sigma_{\rm 100AU} \times (r/100{\rm AU})^{-p}$ [g cm^{-3}]. For a simplicity, we ignore a vertical structure of an envelope, since the envelope around IRS 5 has flattend structure. The derived radius of the circumbinary disk is $\approx$ 450 AU and that of the envelope of $\approx$ 1400 AU, which is consistent to the gas envelope of IRS 5. The estimated mass of the circumstellar disk is $\approx$ 0.09 $M_\odot$, which is consistent to the simple estimation of the mass of IRS 5. The mass of the envelope is

estimated to be $\approx 0.26\ M_{\odot}$, and is consistent to the mass of the envelope which is estimated by the ^{13}CO $(J = 1 - 0)$ emission.

3.4.2 A Simple Analysis of the Position-Velocity Diagrams

The position-velocity diagrams provide the characteristics of the velocity field of the circumstellar gases around a protostar. Figure 3.9 shows the P-V diagrams of the IRS 5 envelope along four different cuts: Figure 3.9(b) is cut along the major axis of the envelope (P.A.=162°; the cut B1-B2 in Figure 3.9(e)). Although the emission around the $V_{\rm sys}$ is resolved out, the following features can be found: (1) the peak position of the blue-shifted emission is slightly shifted to the south (the relative position is less than $0''$), and that of the red-shifted emission is shifted to the north. (2) the amount of the velocity shift of blue- and red-shifted components increase as the positions approach the central sources. These features indicate the rotation motion of the envelope. Figure 3.9(d) is the cut along the minor axis of the cut D1-D2 in Figure 3.9(e), which is perpendicular to the cut B1-B2. This minor axis P-V diagram shows the following features: (1) the peak position of the blue-shifted emission is slightly shifted to the west, whereas that of the red-shifted emission is shifted to the east. (2) the detached components which sequentially aligned seen at lower contour levels of $10 - 20$ % of the peak emission, and the amount of the velocity shift of these components increase as the positions apart from the central sources. The former feature suggests the infall motion of the envelope, and the latter feature suggests the acceleration of the outflowing gases. Figure 3.9(a) and (c) are the cuts offset by $2''.00$ northeast and southwest to the cut B1-B2, respectively. Since the highly blue-shifted component in Figure 3.9(a) is shifted to the south, whereas the highly red-shifted component in Figure 3.9(c) is shifted to the north toward IRS 5, the direction of the rotation of the envelope is counterclockwise, which is consistent to the C^{18}O envelope (Momose et al. 1998).

The velocity structure in the P-V diagrams of ^{13}CO $(J = 1 - 0)$ emission shown in Figures 3.9 is well fitted by a combination of infall and rotation motion as mentioned above, which are represented as the dashed lines in Figures 3.9. The rotation law can be represented as

$$V_{\rm rotation} = 0.24 \left(\frac{r}{700{\rm AU}} \right)^{-1} \ {\rm km\ s^{-1}}, \tag{3.4}$$

which is the same rotation law proposed by Momose et al. (1998). This rotation curve is described as a dashed line as shown in Figure 3.9(b), which passes through both the peak emission of red-shifted and blue-shifted. In 3.9(a),(c), high velocity blue- and red- components

are slightly shifted southward and northward, respectively, and the rotation curve is well fitted the south and north shifts, suggesting that the amount of rotation is appropriate. The rotation motion around IRS 5, however, might be faster than this estimation. The P-V diagram in Figure 3.9(b) shows the high velocity rotation components exist, which is much well fitted with the rotation law of 0.48 km s^{-1} or 0.96 km s^{-1} at 700 AU represented as solid lines in Figure 3.9(b). Since the peak of emission in the P-V diagram is well fitted with the rotation curve of $V_{\rm rot} = 0.24$ [kms^{-1}] $\times$ 700AU and that of the optically thin C^{18}O emission is also reproduced with the rotation motion, this slow rotation of the envelope would be valid.

Three dashed curves in Figures 3.9(a), (c), and (d) are corresponding to the free-fall motions around the enclosed mass of $M = 0.1, 0.5$, and $1.0 M_{\odot}$, which is represented as

$$V_{\rm infall} = \left(\frac{2GM}{r}\right)^{-1/2} = 1.59 \left(\frac{M}{1M_{\odot}}\right)^{-1/2} \left(\frac{r}{700{\rm AU}}\right)^{-1/2} \ {\rm km\ s^{-1}}. \tag{3.5}$$

The P-V diagram along the minor axis of Figure 3.9(d) shows that the infall motion can be fitted with the curves of $0.1 - 0.5\ M_{\odot}$ although the emission around the systemic velocity is resolved out. The curve of 1.0 $M_{\odot}$ seems too large infall velocity than the emission detected. On the other hand, the offeseted P-V diagrams of Figures 3.9(a) and (c), the high velocity components are well fitted with the curves of $0.5-1.0 M_{\odot}$, but that of 0.1 $M_{\odot}$ can not reproduce the high velocity components. Judging from these characteristics of the P-V diagrams, the enclosed mass of IRS 5 seems to be $\sim 0.5\ M_{\odot}$. Here, we adopted the inclination angle of the envelope as a typical value of 60° (e.g., Momose et al. 1998).

Next, we focus the outflowing gas around IRS 5. Observations of molecular outflows accompanied with low-mass stars have revealed that outflows exhibit acceleration motion as apart from central sources, like a Hubble-law (Lada & Fich 1996). The acceleration motion can be interpreted due to the combination of momentum conservation of the protostellar winds and density decreases away from the driving sources of the outflow (e.g., Shu et al. 1991). Hydrodynamic jet entrainment models also result in Hubble-law-like Position-Velocity (P-V) diagrams (e.g., Smith et al. 1997; Downes & Ray 1999). Owing to the high sensitive observations, ^{13}CO ($J = 1 - 0$) emission which originates from the outflow of IRS 5 are detected as shown in Figure 3.10. The P-V diagrams along the cavity wall of the outflow of IRS 5 clearly shows the outflow component which exhibits acceleration motion as apart from the central source as shown in the dashed lines in Figure 3.10(a), (b). The total mass of the outflowing gases under the simple assumptions that the optically thin condition, $T_{\rm ex} = 20$ K, $X(^{13}{\rm CO}) = 10^{-6}$, and the entire extended emission traces the outflowing gas, can be estimated to be $0.1 M_{\odot}$.

Following Beuther, Schilke, & Stanke (2003), we estimated the dynamical timescale and the outflow rate as follows:

$$t = \frac{r}{(\delta V_{\rm blue} + \delta V_{\rm red})/2}, \tag{3.6}$$

$$\dot{M}_{\rm outflow} = M_{\rm outflow}/t, \tag{3.7}$$

The dynamical timescale and the outflow rate are estimated to be 1×10^4 yr and $1.0 \times 10^{-5} M_\odot$, respectively. These values are an order of magnitude smaller than the outflow at massive star-forming regions (Beuther, Schilke, & Stanke 2003). The estimated outflow rate contains large ambiguity such as uncertainties of the inclination and the mass of the outflowing gases, but the order of the outflow rate is comparable to the previously reported mass infall rate as summarized in table 3.4.

Figure 3.11 shows the P-V diagrams of the ^{13}CO ($J = 2 - 1$) line emission around IRS 5. Figure 3.11(a) is cut along the major axis of the disklike structure (P.A.=162°; the cut A1-A2 in Figure 3.11(c)). Although the emission around the $V_{\rm sys}$ is resolved out, the following features can be found: (1) the peak position of the blue-shifted emission is clearly shifted to the south (the relative position is less than 0″), whereas that of the red-shifted emission is shifted to the north. (2) As shown in the P-V diagram in ^{13}CO ($J = 1-0$), the amount of the velocity shift of blue- and red-shifted components increase as the positions approach the central sources. These features suggest the rotation motion of the envelope. In the Figure 3.11(b), the cut along the minor axis of the B1-B2, however, no obvious velocity shift can be detected, suggesting that there are little outflow or infall motion. These major and minor axes of the P-V diagrams strongly suggest that the disklike structure which detected in ^{13}CO ($J = 2-1$) emission traces the purely rotating disk which deeply embedded in the infalling envelope. This is the first case which succeeds to directly detect the rotating disk (i.e., protoplanetary disk) just forming in the active accreting envelope. In addition, the velocity structure along the major axis suggests Keplerian rotation: The fitted curves correspond to the Keplerian rotation around 0.2, 0.6, 1.0, and 1.4 $M_\odot$ central masses with a disk inclination angle, i, of 50°, which is corrected for the convolution of the synthesized beam, and the two peaks suggest the mass range of $0.6-1.4$ $M_\odot$.

3.4.3 Model Analysis of the Rotation Motion of ^{13}CO ($J = 2 - 1$) emission

We analyzed the ^{13}CO(J=2-1) velocity field on the basis of a model for a disk/envelope system, to estimate the physical parameters of the star/disk system of IRS 5. Since the ^{13}CO(J=2-1) emission is optically thick ($\tau_{^{13}\mathrm{CO}} \sim 3$), we considered only the velocity field of the emission. We adopted the following simple model: a Keplerian rotating disk with an outer radius of R_{out} around a central binary system with a total mass of $M_\star$, which is surrounded by an infalling and rotating envelope truncated at an inner radius of R_{out}. R_{out} and M_* are free parameters to fit the velocity field. We assume that the disk and envelope are geometrically thin. Since the masses of the disk and envelope are much smaller than that of the binary system, the velocity field of the disk is determined by the binary mass, $M_\star$. We adopted the velocity field of the envelope revealed by Momose et al. (1998): $V_{\mathrm{rot}} = 0.24\ (r/700\ \mathrm{AU})^{-1}$ and $V_{\mathrm{infall}} = 0.5\ (r/700\ \mathrm{AU})^{-1/2}$ km s^{-1}.

By applying the model to the mean velocity map of ^{13}CO ($J = 2 - 1$) which is shown in Figure 3.12, we obtained the best-fit solution shown in Figure 3.13: $M_\star = 0.6 \pm 0.2\ M_\odot$ and $R_{\mathrm{out}} = 490 \pm 50$ AU. Here we considered the convolution with the synthesized beam of $2\farcs3 \times 2\farcs0$ at P.A. = 153°. The total mass of the binary system agrees well with the previous values and is also consistent to the mass which derived from the P-V diagrams of ^{13}CO ($J = 2 - 1$) emission within the error. On the other hand, the radius is slightly larger than the disk radius of 350 ± 50 AU which is estimated from the intensity-weighted mean velocity map.

3.4.4 Formation of a Keplerian disk in an infalling envelope

The disk radius (R_{out}) seems significantly larger than the centrifugal radius, R_{cen}, the key parameter characterizing the disk formation process in a protostellar envelope. R_{cen} can be estimated from observations of the envelope. Momose et al. (1998) revealed that the flattened envelope around IRS 5 has rotating and infalling motion: $V_{\mathrm{rot}} = 0.24(r/700\mathrm{AU})^{-1}$ km s^{-1} and $V_{\mathrm{infall}} = 0.5(r/700\mathrm{AU})^{-1/2}$ km s^{-1} for an inclination angle of 64°, indicating the conservation of the specific angular momentum of the envelope gas during the infall. Ohashi et al. (1997) also showed that the specific angular momentum seems constant for several infalling envelopes. If the specific angular momentum is conserved, R_{cen} is simply given by

$$R_{\mathrm{cen}} = (R_{\mathrm{rot}} V_{\mathrm{rot}})^2 / G M_\star, \tag{3.8}$$

where $R_{\rm rot}$ is the radial distance of the place where $V_{\rm rot}$ is detected in the envelope, G is the gravitational constant, and $M_\star$ is a stellar mass. In the case of IRS 5, we have $R_{\rm cen} = 23 - 320$ AU considering the mass range of the central stars from 0.1 to 1.4 $M_\odot$ (e.g., Momose et al. 1998). Despite the uncertainty of the central stars, the ^{13}CO(J=2-1) disk radius (350 - 490 AU) is larger than $R_{\rm cen}$. Since pure rotation of gas near the central sources is more directly related to the stellar masses, we regard $0.6 - 1.4$ $M_\odot$ as the plausible mass range for $M_\star$; The upper limit is almost consistent with the mass of the binary stars derived from their proper motion (Rodríguez et al. 2003). In this case, $R_{\rm cen}$ becomes $23 - 53$ AU, comparable to the projected separation of the binary system (45 AU), and is much smaller than $R_{\rm out}$. Even if we adopt the inclication angle of the disk of 64°, $R_{\rm cen}$ becomes only 20% larger, and the significant difference between $R_{\rm out}$ and $R_{\rm cen}$ still remains.

To explain the difference between $R_{\rm cen}$ and $R_{\rm out}$, we consider the following two physical processes: 1) gravitational interaction between a circumbinary disk and a binary system, 2) turbulent viscosity generated in a disk at its accretion stage. The gravitational interaction causes the angular momentum transport from a binary to a disk, possibly resulting in radial expansion of a disk. Artymowicz, Clarke, Lubow, & Pringle (1991) investigated the interaction by SPH simulations. According to their empirical formulae, 20% of the total angular momentum of the IRS 5 binary system ($10^{53} - 10^{54}$ g cm^2 s^{-1}) can be transported into the disk during the protostar stage of $\sim 10^5$ yr. This interaction would shorten the binary separation by ~ 10% and spread the disk from ~ 50 AU to ~ 500 AU in radius. This mechanism, however, seems to have a serious drawback that the gravitational interaction effectively occurs only at resonance points near the binary stars. Although waves launched at the resonances can carry angular momentum outwards in the disk, the waves are theoretically thought to be damped locally (e.g., Lubow & Artymowicz 2000). Consequently, the gravitational interaction could transport the angular momentum from the binary system to only the innermost region of the disk, and therefore, the outer regions of the disk would not radially expand.

The second mechanism is the radial expansion of the disk due to outwards transport of angular momentum caused by the MHD turbulence in the disk (e.g., Hartmann, Calvet, Gullbring, & D'Alessio 1998; Kitamura et al. 2002). Nakamoto & Nakagawa (1995) theoretically studied the growth of a protoplanetary disk in a protostellar envelope, taking account of the turbulent viscosity. According to their Equation (20), the disk can expand from ~ 50 AU to ~ 500 AU in radius, only if the parameter α of the viscosity takes large values of ~ 1, one order of magnitude larger than those theoretically expected. Thus, it is also unlikely that the turbulent viscosity enlarges the disk. On the other hand, magnetic fields threaded through the

disk play an important role in transporting angular momentum (e.g., Konigl & Pudritz 2000), as well as their major role in the MHD turbulence. In this case, however, the magnetic fields remove the angular momentum from the disk, leading to radial contraction of the disk.

On the other hand, the gas which initially formed the large rotating disk might possess large angular momentum than that of the envelope which now observed, although this is one possibility. Recently, a comprehensive study of IRS 5 by Osorio et al. (2003) also revealed the presence of 300 AU scale binary disk, supporting the presence of large circumbinary disk. Investigations of the mechanism how to form such a large circumbinary disk in the envelope will be one of the most important issue of the studies concerning IRS 5.

3.4.5 Comparison to the circumbinary disk around GG Tauri

Our observations have revealed the veloctiy structure around the binary protostar L1551 IRS 5. In this section, we briefly discuss about the evolution of the circumbinary disk from the comparison IRS 5 with the closed-binary classical T Tauri star GG Tau. The separation of the binary stars of IRS 5 is estimated to be $\sim$ 45 AU and the reduced mass of both the binary stars is $0.6 - 1.4 M_{\odot}$ which derived from the kinematics of the disk and envelope and the proper motion of the binary stars. On the other hand, the separation of the binary stars of GG Tauri is 40 AU with the reduced mass of 1.3 $M_{\odot}$, indicating both the IRS 5 and GG Tau systems are quite similar although the evolution phases are different.

The parameters of the circumbinary disk around GG Tau are as follows: The outer radius of 260 AU, the inner radius of 180 AU, total mass of the disk is 0.12 $M_{\odot}$. On the other hand, those around IRS 5 are as follows: The outer radius has been revealed to be $\approx$ 500 AU, but the inner hole can not be found. The mass of the circumbinary disk which deduced from ^{13}CO ($J = 2 - 1$) emission is estimated to be 0.03 $M_{\odot}$ (the mass derived from the continuum emission is $0.02 - 0.1 M_{\odot}$), suggesting that the disk around GG Tau seems to be massive than that around IRS 5. Although $0.5 - 1''$ resolution imagings of millimeter continuum emission have been performed until now toward IRS 5, the inner hole around the binary system can not be found. In the case of the other closed-binary protostar L1551 NE whose separation of 70 AU which reported in the previous chapter of this thesis, no inner hole was detected with $1''$ resolution imaging. The reason of the absence of inner hole around the binary protostar can be interpreted as follows: Because young protostars such as IRS 5 and NE are still in an active accretion stages and the accreting matter prevents the growth of the inner hole, suggesting no inner hole or quite small scale of inner hole might exist around binary stars. To detect such

primitive inner holes around young protostars, high-J transition molecule emission which can trace inner hot region with much higher angular resolution imaging are strongly required.

3.5 Summary

We have presented the new results of the high angular resolution and high sensitivity ^{13}CO ($J = 1 - 0$) and ($J = 2 - 1$) observations of the protostar L1551 IRS 5. The main results of our observations are summarized in Figure 3.14 and itemized as follows:

1. ^{13}CO ($J = 1 - 0$) emission was detected from $V_{\rm lsr} = 4.5 - 7.9$ km s^{-1}. The emission confirmed the infall and rotation motion around IRS 5, whose enclosed mass is ≈ 0.5 $M_{\odot}$, and the rotatinal motion is consistent to the previous C^{18}O imagings. The total mass of the gas is estimated to be $0.12 - 0.24 M_{\odot}$.

2. ^{13}CO ($J = 1 - 0$) emission was detected along the cavity wall of the outflow. The emission shows clear acceleration. The estimated mass outflow rate is $\sim 10^{-5}$ $M_{\odot}$ yr^{-1}, suggesting that the rate is consistent to the mass infall rate around IRS 5.

3. ^{13}CO ($J = 2 - 1$) emission was revealed the presence of purely rotation disk embedded in the infalling envelope. The rotation radius is considerably larger than the centrifugal radius of IRS 5 estimated from the angular momentum of the envelope. The turbulent viscosity with a large coefficient of $\alpha \sim 1$ is likely to make a small disk with the centrifugal radius efficiently expand, whereas the gravitational interaction between the disk and the binary sources would not be efficient. It is also possible that the natal core of IRS 5 was not rigidly rotating but more rapidly rotating with large specific angular momentum in the inner part of the core.

4. No significant inner hole around the binary system can be detected with $1''$ resolution imaging, suggsting that an active accreting matter prevents the growth of the inner hole.

CHAPTER 3. TABLE

Table 3.1: Observational Parameters

Observation period	2001 January - 2002 April	
Molecular line	^{13}CO ($J = 2 - 1$)	^{13}CO ($J = 1 - 0$)
Frequency [GHz]	220.398686	110.201353
Velocity resolution [km s^{-1}]	0.51	0.17
Synthesized beam size	$2\farcs30 \times 2\farcs$	$5\farcs35 \times 4\farcs79$
Position angle [°]	$-37.2°$	$-56.7°$
Noise level (1 σ) [Jy beam^{-1}]	0.37	0.32
Continuum [GHz]	220 ± 0.512, 232 ± 0.512	98 ± 0.512, 110 ± 0.512
Synthesized beam size (D/C/AB)*	$2\farcs87 \times 2\farcs62$ / $1\farcs41 \times 1\farcs08$ / —	$6\farcs51 \times 5\farcs81$ / — / $1\farcs47 \times 1\farcs34$
Position angle [°] (D/C/AB)*	-61.0 / -30.9 / —	-70.0 / — / 7.9
Noise level (D/C/AB)* [mJy beam^{-1}]	22 / 16 / —	1.7 / — / 2.3
Phase & amplitude calibrator (flux density)	0420-014 (6.4 Jy)	0446+112 ($1.7 - 2.6$ Jy)
Bandpass calibrator	3C279	3C454.3
$T_{\rm sys}$ [K] (in DSB)	500 K	150 K

* D, C and AB are the NMA array configurations D (lowest angular resolution), C (medium angular resolution) and AB (highest angular resolution), respectively.

Table 3.2: Continuum peak position of L1551 IRS 5

	α_{2000}	δ_{2000}
VLA IRS5-A	$04^h\ 31^m\ 34^s.143$	$+18^\circ\ 08'\ 05''.09$
VLA IRS5-B	$04^h\ 31^m\ 34^s.141$	$+18^\circ\ 08'\ 04''.74$
NMA 3 mm	$04^h\ 31^m\ 34^s.141 \pm 0^s.007$	$+18^\circ\ 08'\ 04''.78 \pm 0''.14$

Table 3.3: Other emission lines of L1551 IRS 5

line	abundance [X]	Total flux density [Jy km s^{-1}]	Beam size [$''$]	Mass [$M_\odot$]	Size [AU]	reference
$H^{13}CO^+$ (1-0)	10.2×10^{-11}	7.3	7.9×5.8	0.15	5600×2800	Saito et al. 2001
^{13}CO (1-0)	10^{-6}	9.12	5.1×3.9	$0.039 - 0.081$	1200×670	Ohashi et al. 1996
$C^{18}O$ (1-0)	2.5×10^{-7}	18.6	2.8×2.5	0.106	2380×1050	Momose et al. 1998
CS (2-1)	10^{-9}	15	5.1×4.5	0.11	2300×1600	Ohashi et al. 1997
CS (3-2)	10^{-9}	17.3	4.2×3.8	0.06	2200×2000	Yokogawa et al. in prep.

The ^{13}CO ($J = 1 - 0$) flux of L1551 IRS5 is derived within the radius of 600 AU.

Table 3.4: Mass infall rate of L1551 IRS 5

line	mass infall rate [$M_\odot$ yr^{-1}]	reference
^{13}CO ($J = 1 - 0$)	$1.3 - 2.6 \times 10^{-5}$	Ohashi et al. 1996
$H^{13}CO^+$ ($J = 1 - 0$)	1.1×10^{-5}	Saito et al. 1997
$C^{18}O$ ($J = 1 - 0$)	6.4×10^{-6}	Momose et al. 1998

CHAPTER 3. FIGURES

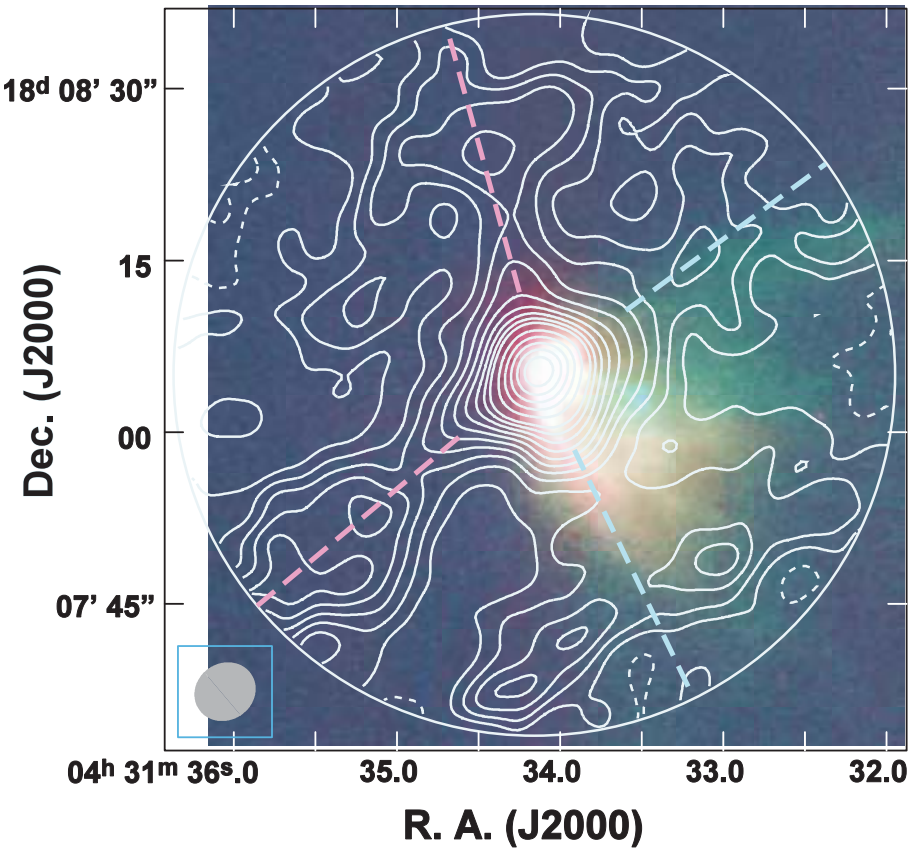

Figure 3.1: Total intensity map of ^{13}CO(J=1-0) emission of L1551 IRS 5 superposed on the near-infrared (J + K' bands) image taken with the SUBARU. The map is integrated from $V_{\rm lsr}$ = 4.5 km s^{-1} to 7.9 km s^{-1}. The contour lines start at $\pm$2.0 σ levels with intervals of 2.0 σ until 20 σ, and intervals of 4.0 σ over 20 σ. The negative levels are indicated by broken lines. The rms noise level (1 σ) is 73.0 mJy beam^{-1}. The total intensity over the entire region is 100.4 Jy km s^{-1}, and the central component is 26.9 Jy km s^{-1}. The primary beam collection is applied. The ellipse in the bottom-left corner is the synthesized beam (FWHM).

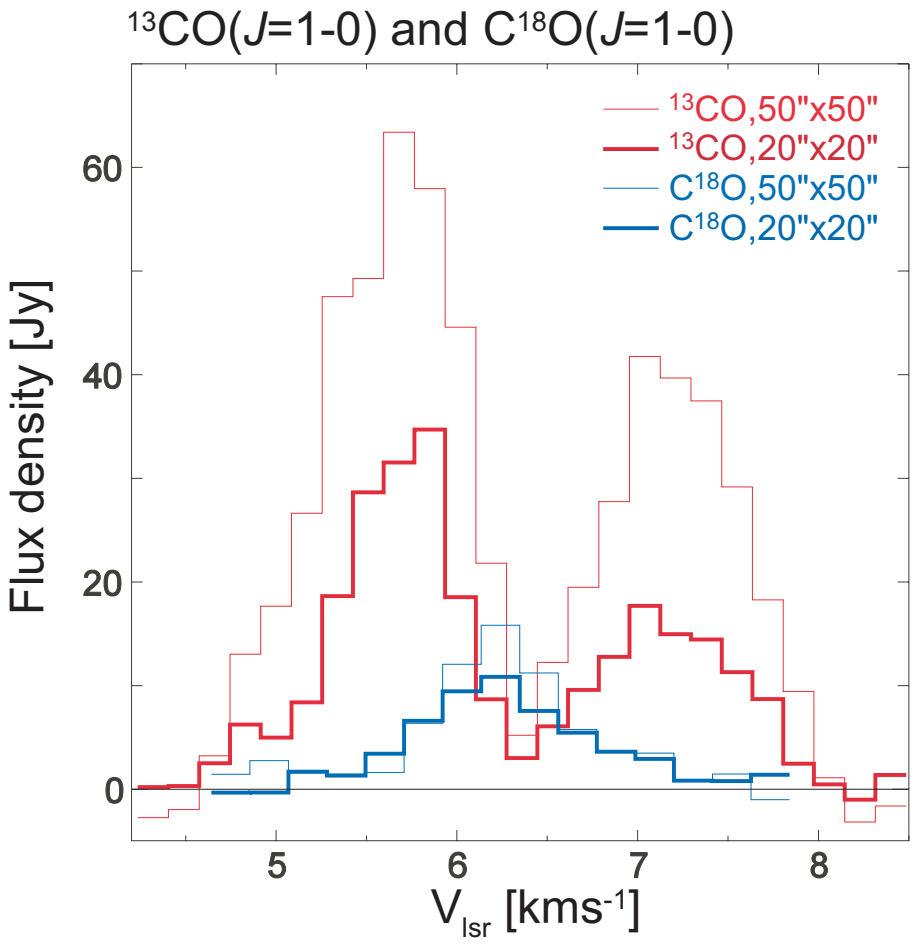

Figure 3.2: ^{13}CO(J=1-0) and C^{18}O(J=1-0) line profiles in units of flux density (Jy). The red lines are the profiles of ^{13}CO and the blue lines are those of C^{18}O. The thin lines are the emissions from the entire region ($50'' \times 50''$), and the thick lines are the emissions from the centrally condensed components ($20'' \times 20''$).

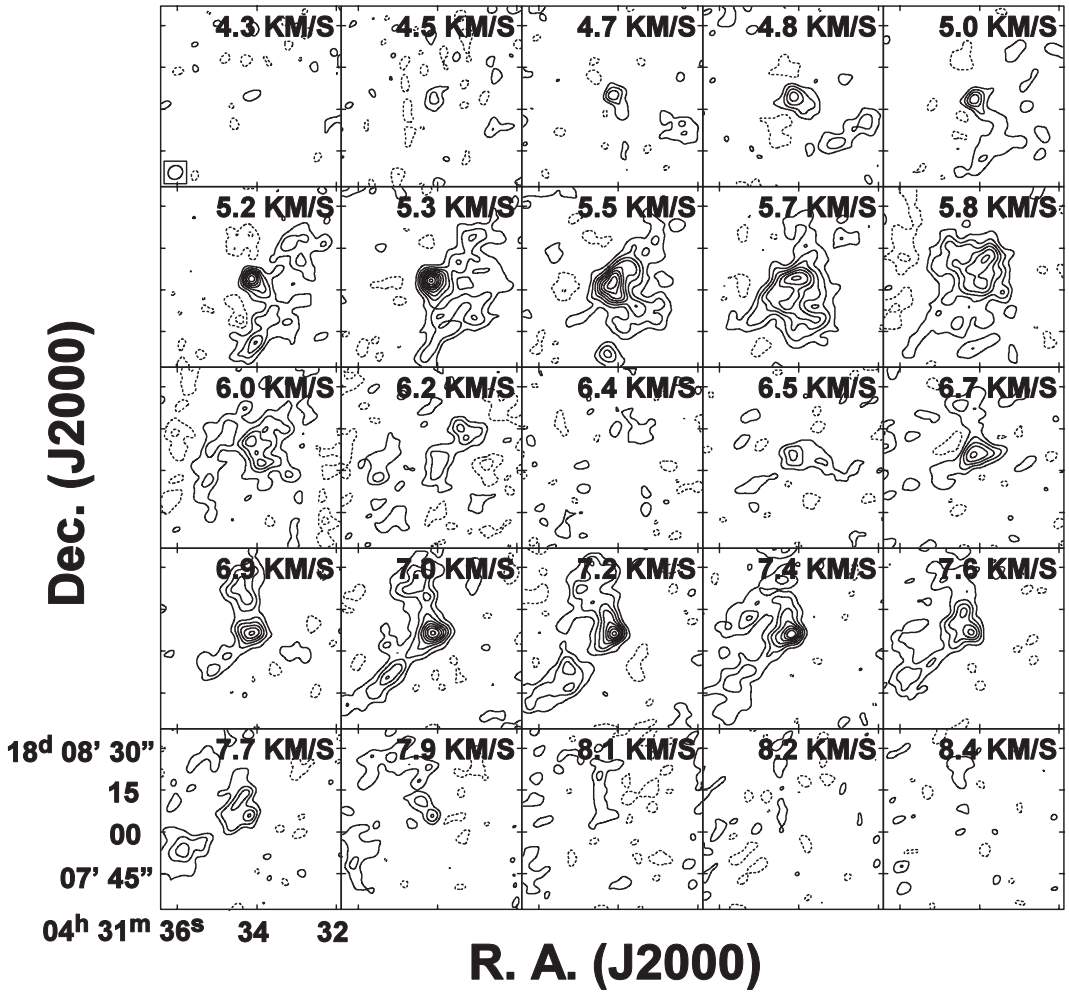

Figure 3.3: Velocity channel maps of ^{13}CO ($J = 1 - 0$) emission of L1551 IRS 5. The central LSR velocity with a velocity width of 0.169 km s^{-1} is denoted at the upper-right corner of each panel. The rms noise level is 0.318 Jy beam^{-1}. The contour lines starts at ± 2.0 σ levels with intervals of 2.0 σ. The negative levels are indicated by broken lines.

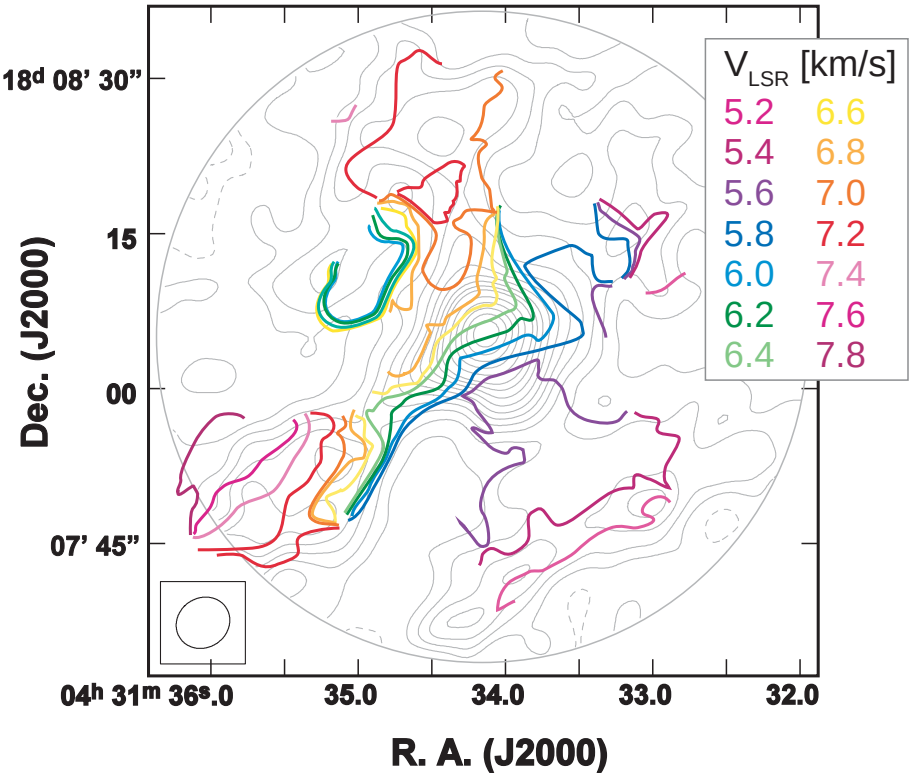

Figure 3.4: Intensity-weighted mean velocity map of L1551 IRS 5 obtained from ^{13}CO(J=1-0) emission. The integrated intensity distribution is also shown by gray lines, whose contours are the same as in Figure 3.1.

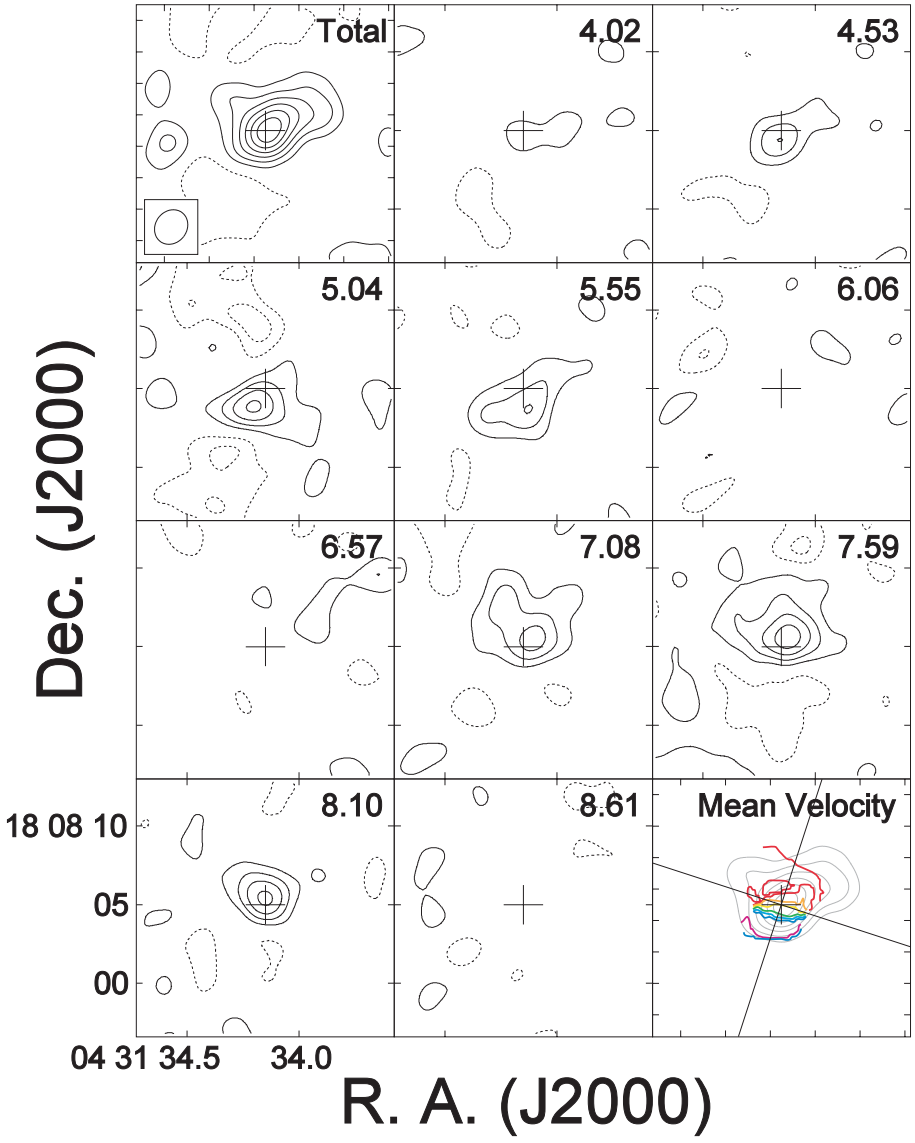

Figure 3.5: Top-left panel shows the velocity-integrated line intensity map of ^{13}CO ($J = 2-1$) over the range of $V_{\rm LSR} = 3.77 - 8.87$ km s^{-1}. The contour lines start at $\pm 2.0\sigma$ with intervals of 2.0σ, where $1\sigma = 0.110$ Jy beam^{-1} (0.56 Jy km s^{-1} beam^{-1}). The ellipse at the bottom left corner in the top left panel indicates the beamsize in FWHM, and the central cross indicates the stellar position. Other panels show Velocity channel maps of the emission. The central LSR velocity in km s^{-1} is shown at the upper right corner of each panel. The contour lines are written in the same manner as in the top-left panel, where $1\sigma = 0.37$ Jy beam^{-1}.

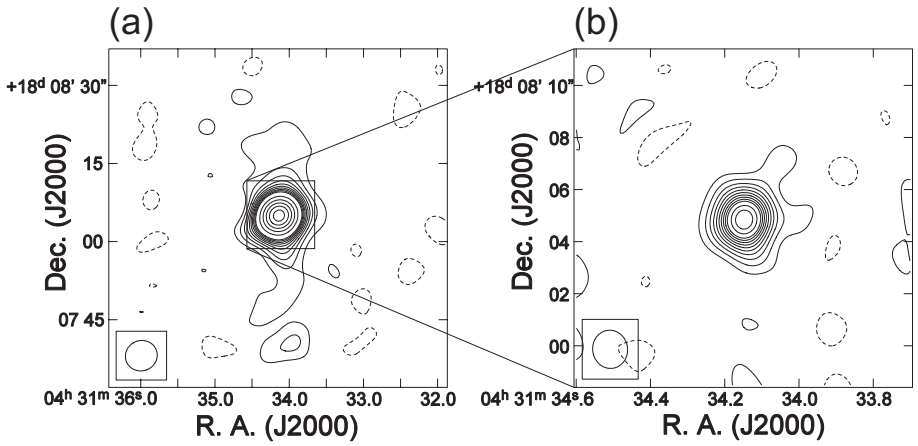

Figure 3.6: (a) Lowest angular resolution image of L1551 IRS 5 with the D configuration at $\lambda = 2.88$ mm. The contour lines start at $\pm 2.0\sigma$ levels with intervals of 2.0σ until 20σ. The intervals become 10σ over 20σ. The rms noise level (1σ) is 1.7 mJy beam^{-1}. The open ellipse in the bottom left corner is the synthesized beam size (HPBW) of $6\farcs51 \times 5\farcs81$ at P.A. = -70.0°. (b) Highest angular resolution image of L1551 IRS 5 with the AB configuration at $\lambda = 2.88$ mm. The contour lines start at $\pm 2.0\sigma$ levels with intervals of 2.0σ until 20σ. The intervals become 4 σ over 20σ. The rms noise level is 2.3 mJy beam^{-1}, and the synthesized beam size is $1\farcs47 \times 1\farcs34$ at P.A. = 7.9°.

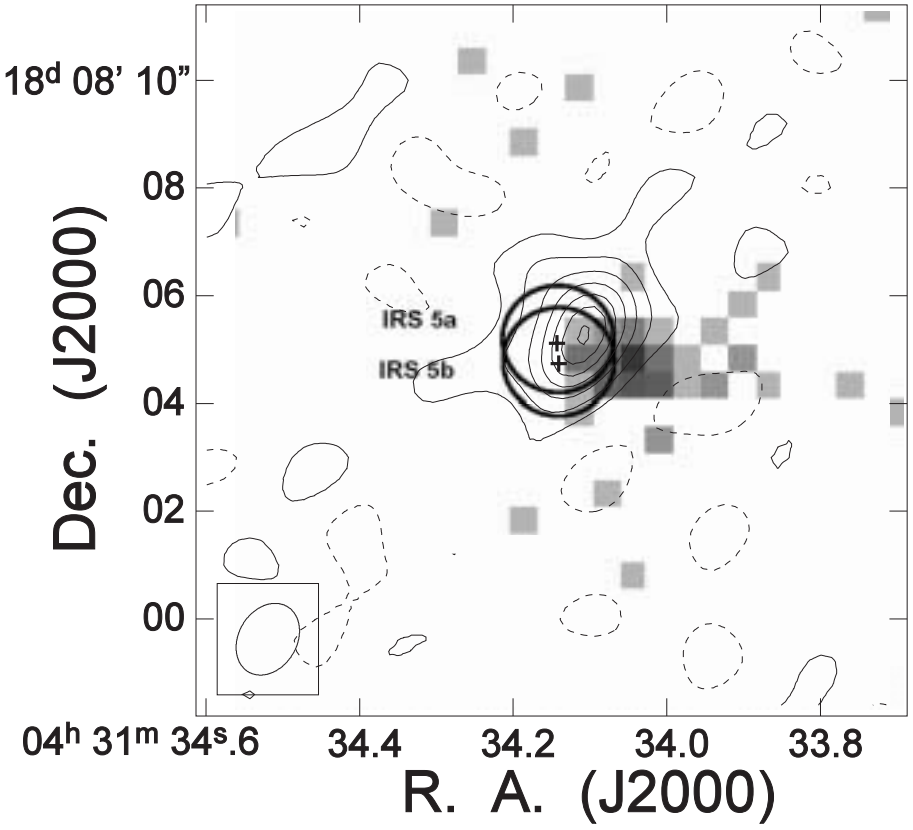

Figure 3.7: Map of 1.3 mm continuum emission superposed onto the X-ray image (Bally et al. 2003). The size of the synthesized beam (FWHM) is $1''.41 \times 1''.08$ at P.A. = 159°, shown as the ellipse at the bottom left corner. The contour lines start at $\pm 2.0\sigma$ with intervals of 2.0σ, where $1\sigma = 16.0$ mJy beam^{-1}. The total flux density over the area above the 2σ level is 0.56 Jy with a peak flux density of 0.23 Jy beam^{-1}.

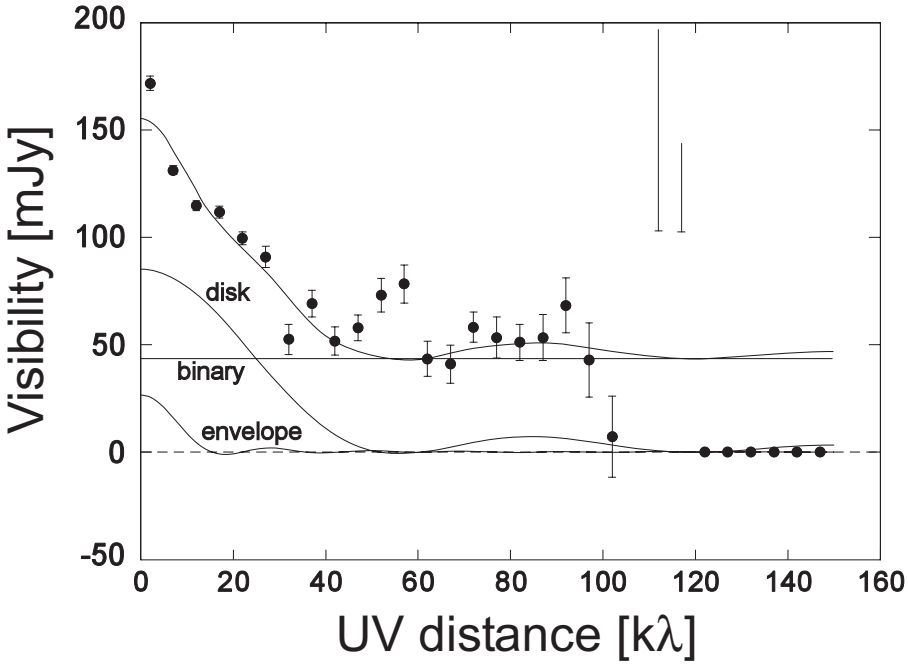

Figure 3.8: The u, v flux density data of 3 mm continuum emission of L1551 IRS 5. The fitted curve consists of a binary component, a circumbinary disk component, and an envelope component.

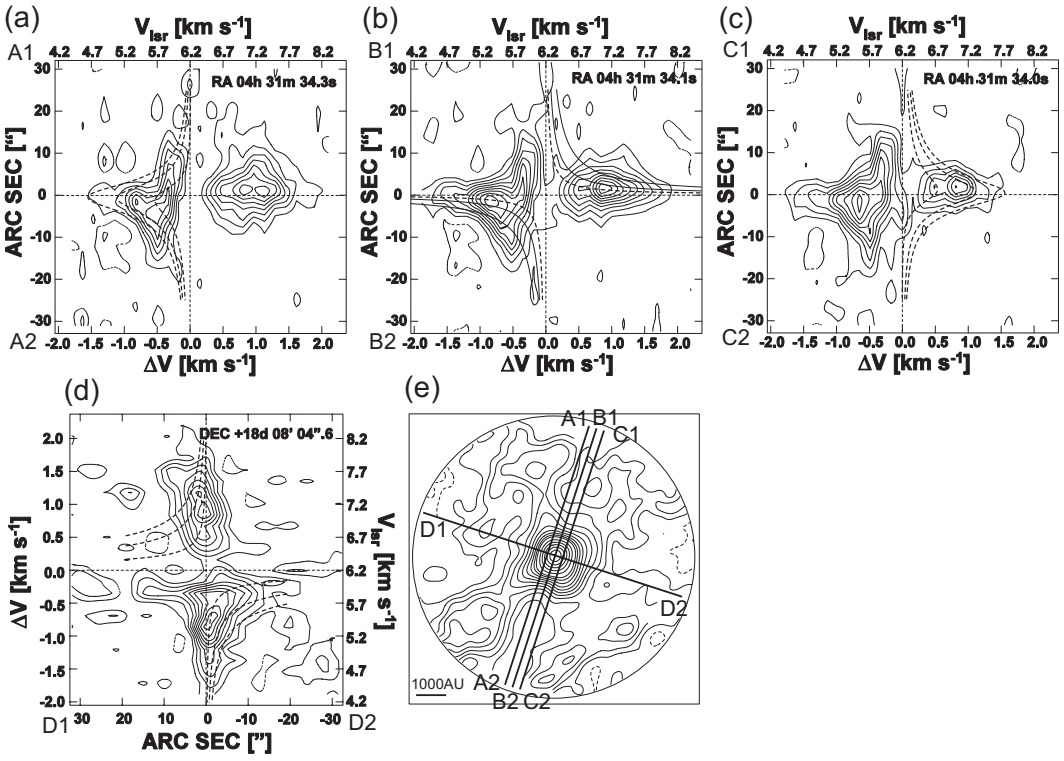

Figure 3.9: Position-velocity diagrams (a),(b),(c),(d) of the ^{13}CO(J=1-0) emission along four different cuts shown in the ^{13}CO integrated intensity map (e). Contours in (a)-(d) are indicated in step of 10 % of the peak flux densities, and those in (e) are in the same manner as in Figure 3.1. (a) The P-V diagram along the cut A1-A2 offset by 2″.0 northeast from the major axis. (b) The P-V diagram along the major axis, B1-B2. (c) The P-V diagram along the cut C1-C2 offset by 2″.0 southwest from the major axis. (d) The P-V diagram along the minor axis, D1-D2.

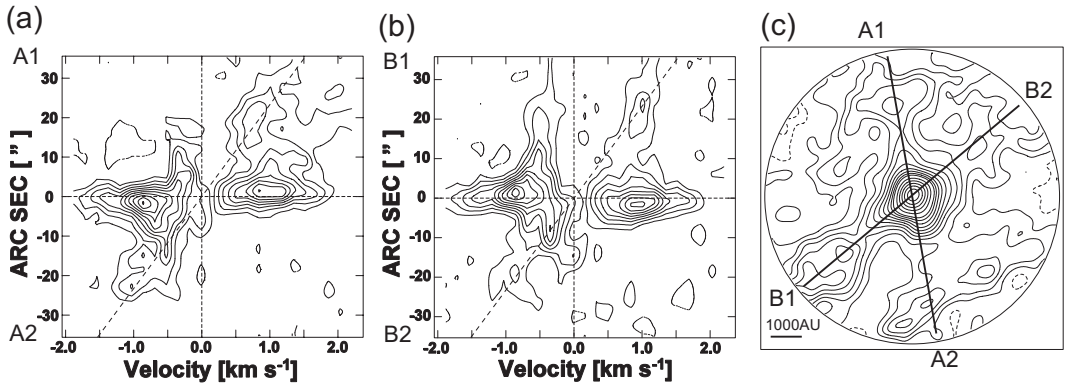

Figure 3.10: Position-velocity diagrams (a),(b) of the ^{13}CO(J=1-0) emission along two different cuts shown in the ^{13}CO integrated intensity map (c). Contours in (a) and (b) are indicated in step of 10 % of the peak flux densities, and those in (c) are in the same manner as in Figure 3.1. (a) The P-V diagram along the cut A1-A2, the shell of the conical outflow. (b) The P-V diagram along the cut B1-B2. The dashed lines indicate the uniform accelerated motion of the outflow.

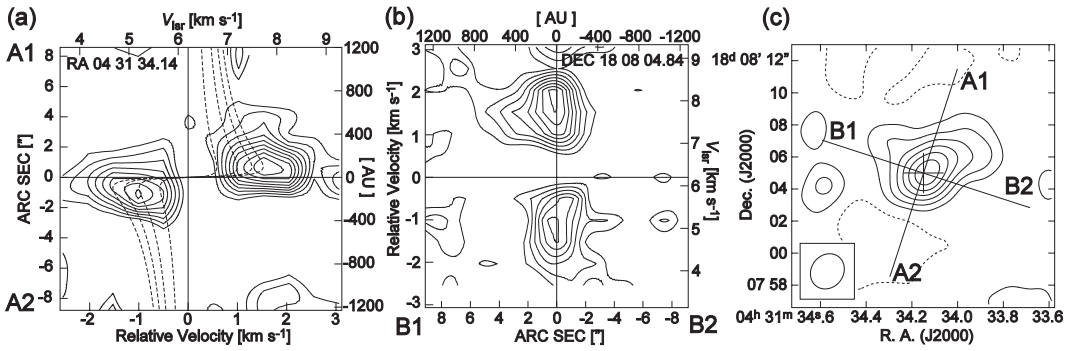

Figure 3.11: (a) Position-velocity diagram of the ^{13}CO($J = 2 - 1$) emission along the major axis at P.A. = 162° of the infalling envelope. The contour lines are in steps of 10% of the peak flux density from 10% to 100%. The dashed curves indicate Keplerian rotation around central masses of 0.2, 0.6, 1.0, and 1.4 $M_\odot$ respectively, with an inclination angle of 50°. (b) Position-velocity diagram of the ^{13}CO($J = 2 - 1$) emission along the minor axis at P.A. = 72°.

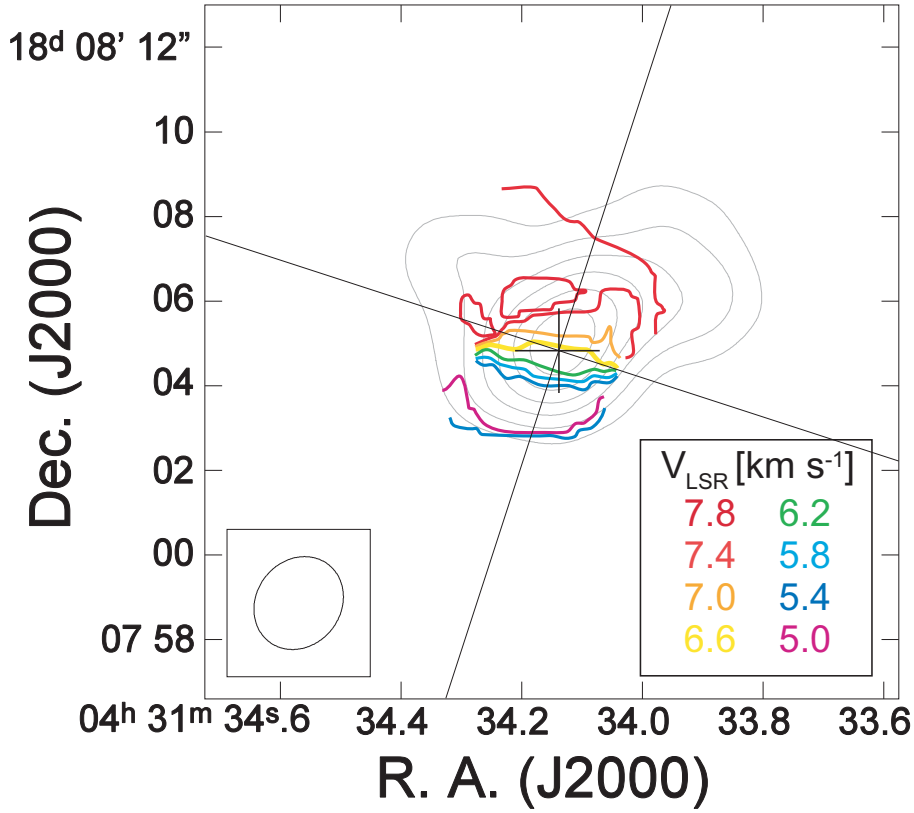

Figure 3.12: Mean velocity map of the ^{13}CO($J = 2 - 1$) emission. The blue and red colors show the blue- and redshifted The southern part shows blueshifted emission, while the northern part shows redshifted emission. The ellipse at the bottom left corner indicates the FWHM beamsize.

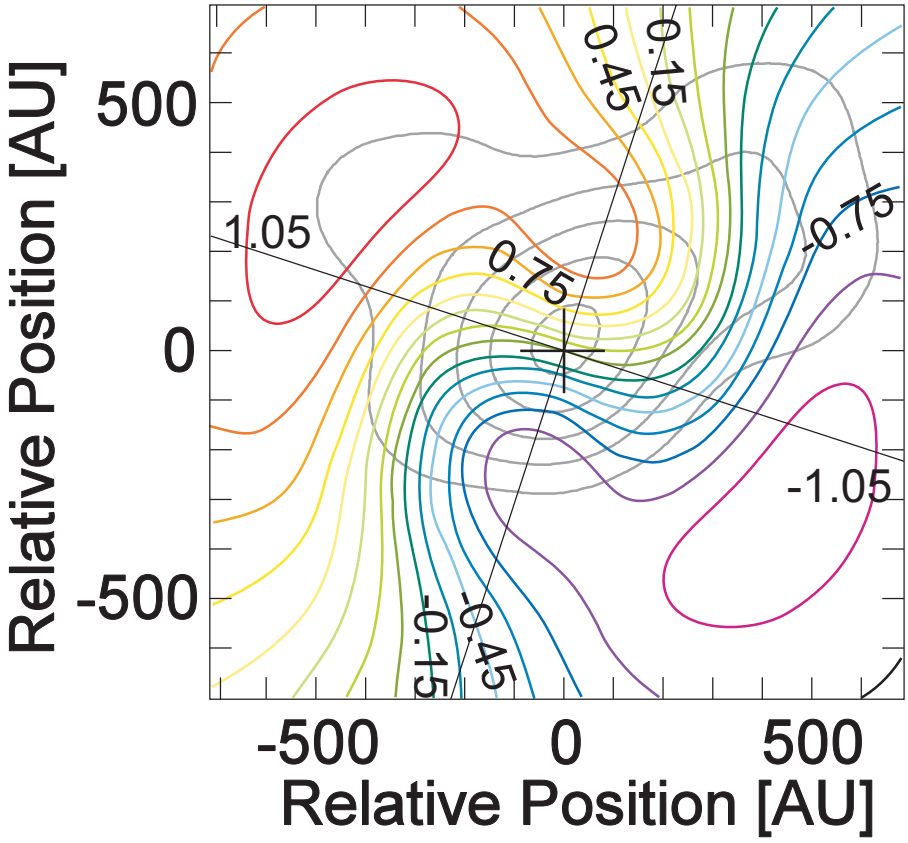

Figure 3.13: Best fit solution of the velocity field of the ^{13}CO($J = 2 - 1$) emission around L1551 IRS 5 calculated on the basis of the disk/ envelope model described in the manuscript.

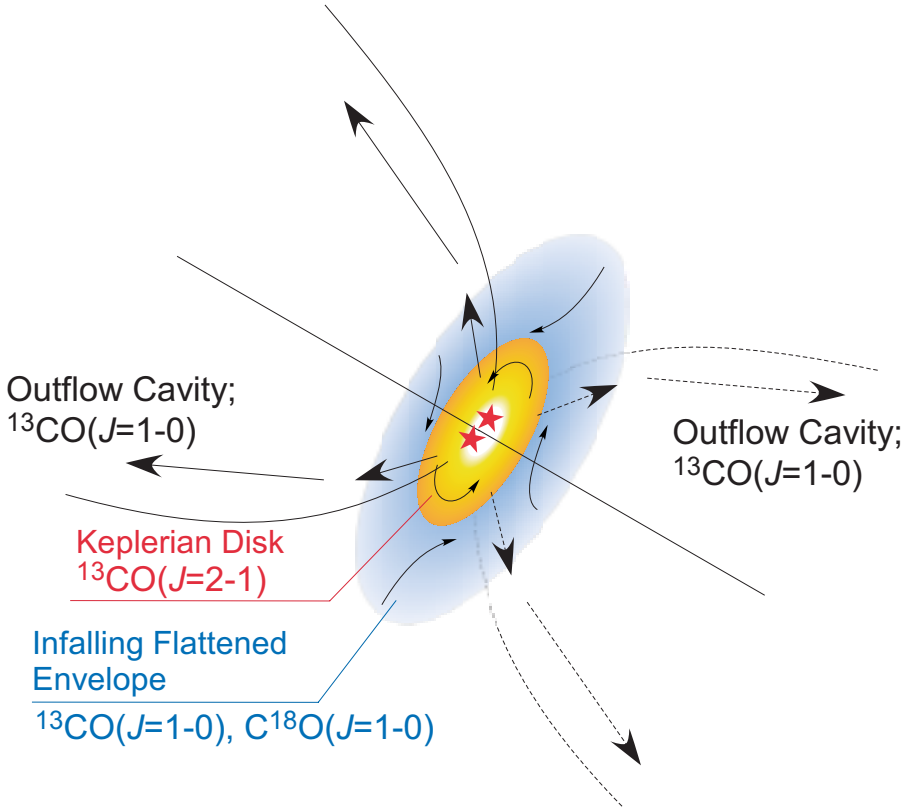

Figure 3.14: Schematic illustration of L1551 IRS 5. ^{13}CO ($J = 1 - 0$) emission traces the infalling envelope and the outflow cavity which excavated by the outflow, whereas ^{13}CO ($J = 2 - 1$) emission traces the Keplerian rotating disk around the central binary system.

Chapter 4

Detailed Structure of the Circumstellar Envelope around the Protostar Candidate HL Tau

Abstract

Aperture synthesis observations of ^{13}CO (J=1-0), C^{18}O (J=1-0) and ^{13}CO (J=2-1) line emissions toward the protostar candidate HL Tau, made with the Nobeyama Millimeter Array (NMA), are presented. ^{13}CO (J=1-0) observations revealed the detailed structure of the circumstellar envelope exhibiting an infall motion to a central source, whereas optically thick ^{12}CO ($J = 3 - 2$) gas taken with the Atacama Submillimeter Telescope Experiment (ASTE) clearly shows the acceleration of outflowing gas. Although previous works indicate the presence of rotational motion of the envelope, our ^{13}CO ($J = 1 - 0$) observations exhibit only slight rotation of the envelope. To reveal the presence of a Keplerian rotating disk at the innermost part of the envelope, we performed ^{13}CO ($J = 2 - 1$) observations. Although extended components elongated perpendicular to the outflow axis were detected, the rotation motion was not revealed, suggesting a Keplerian disk around HL Tau is much smaller than that around L1551 IRS 5 of $\sim$ 500 AU. Since only slight rotation is detected around HL Tau envelope, a small rotating disk might be due to the small angular momentum of the envelope itself. These results might indicate that a YSO with large angular momentum of an envelope will form a large Keplerian disks whereas a YSO with small angular momentum of an envelope will form a small Keplerian disk.

On the other hand, C^{18}O (J=1-0) observations have revealed the clumpy shell-like structure of the dense gas around HL Tau and XZ Tau, indicating that the most of the dense gas has already dissipated owing to the outflow activities.

4.1 Introduction

Previous researches of low-mass star formation have revealed that most of low mass young stellar objects (YSOs) are accompanied by disks and envelopes which contain gases and dust grains. Early phase YSOs such as class 0 and/or I objects (i.e., protostars) are usually surrounded by massive envelope gases which exhibit infall motions with powerful outflows. As they evolve, their outflows have dispersed surrounding envelopes, and finally T Tau stars with rotating disks (i.e., protoplanetary disks) have formed in the central part of envelopes. In the view points of kinematics, it has revealed that the specific angular momenta of infalling envelopes and Keplerian disks are relatively constant of $\sim 10^{-3}$ km s^{-1} pc and are an order of magnitude smaller than those of molecular cloud cores, suggesting that the dynamical collapses of cloud cores take place inside radii of $\sim$ 0.03 pc (6000 AU) while the regions outside

the radius remain dynamically stable (Ohashi et al. 1997). Theoretically, protoplanetary disks, which will form planetary system in the future, are thought to be formed at the radii where the centrifugal forces and the gravity forces to circumstellar matter are balanced (i.e., centrifugal radii). In the previous chapter, we have revealed the presence of the protoplanetary disk embedded in the central part of the infalling envelope around the binary protostar L1551 IRS 5. However, the formation processes of protoplanetary disks around single stars and the difference of the initial conditions between single system and binary system are still unknown.

To reveal a protoplanetary disk formation around a single young star, we performed the aperture synthesis observations with ^{13}CO ($J = 2 - 1$), ($J = 1 - 0$) and C^{18}O ($J = 1 - 0$) line emissions toward the single YSO, HL Tau. HL Tau was used to be classified as a CTTS in the Herbig Bell Catalog (HBC), but now is thought to be a protostar candidate, whose luminosity of $L_{\rm bol} \approx 7.6\ L_{\odot}$. HL Tau is a member of the L1551 dark cloud in the Taurus Molecular Cloud (TMC) whose distance of 140 pc (Elias 1978). Although more than half of YSOs in the TMC are thought to compose binary or multiple systems, HL Tau is thought to be a single star since the high resolution VLA observations could not find any companions (Rodriguez et al. 1994). Previous ^{13}CO observations of HL Tau have revealed the dense envelope with several $\times$ 1000 AU radius, and it exhibits an infall and rotation motion (Hayashi, Ohashi, & Miyama 1993). The rotation motion of the envelope, however, has denied by the following studies (Cabrit et al. 1996), and they suggested that the envelope is almost purely infalling or outflowing with a slight rotation.

4.2 Observations

Aperture synthesis observations of HL Tau were carried out in ^{13}CO (J=1-0) (110.201353 GHz), C^{18}O (J=1-0) (109.782160 GHz) and ^{13}CO ($J = 2 - 1$) (220.398686 GHz) line emissions using the Nobeyama Millimeter Array (NMA), which consists of six 10 m antennas, during 2000 November and 2002 December. The images were obtained using all the array configurations, D, C and AB for ^{13}CO (J=1-0) and C^{18}O (J=1-0) line emissions: the ranges of the projected baseline lengths are 3-27, 6-55, and 15-110 kλ, and only the D configuration for ^{13}CO (J=2-1) line emission: the ranges of the projected baseline lengths are 6-60 kλ. The system noise temperatures with SIS receivers in DSB mode were about 150 K at 110 GHz and 400 K at 220 GHz toward the zenith. The line emission data were obtained by using a 1024 channel FX spectrocorrelator with a total bandwidth of 32 MHz, corresponding to a velocity resolution of 0.084 km s^{-1} at 110 GHz and 0.0425 km s^{-1} at 220 GHz. The center of the field was set on

the position of (α_{1950}, δ_{1950}) = (4^h 28^m $44^s.42$, +18° 07′ 36″.2). The sizes of the primary beam (i.e., the field of view) were 62″ (HPBW) at 110 GHz and 31″ (HPBW) at 220 GHz. Since the minimum baseline lengths were 3 kλ at 110 GHz and 6 kλ at 220 GHz, our observations were insensitive to structures extended larger than 62″ for 110 GHz and 31″ for 220 GHz (9×10^3 AU, and 4×10^3 AU at 140 pc, respectively). The response across the observed passband for each sideband was determined from 30-40 minutes observations of 3C454.3 for 110 GHz and from 140 minutes observations of 0420-014 for 220 GHz. Gain calibrators 0446+112, 0528+134 and 0420-014 were observed every 10-20 minutes. The flux density of each calibrator was derived from observations of Uranus . The overall uncertainties in the flux calibration were about 10 % at 110 GHz and 20 % at 220 GHz. After the calibration, we made final images only from the data taken under good weather conditions. Using the AIPS package developed at the NRAO, we CLEANed the maps by natural weighting with no taper in the UV plane.

The continuum data were also obtained with the digital spectral correlator UWBC (Okumura et al. 2000), which has 128 frequency channels and a 1024 MHz bandwidth per baseline. Visibility data of 100 GHz ($\lambda = 3$ mm) continuum emission in both the lower (98 ± 0.512 GHz) and upper (110 ± 0.512 GHz) sidebands were obtained simultaneously with a phase-switching technique. The data of 230 GHz ($\lambda = 1.3$ mm) continuum emission were obtained in the lower (220 ± 0.512 GHz) and upper (232 ± 0.512 GHz) sidebands. More details of the observational parameters are summarized in Table 4.1.

4.3 Results

4.3.1 ^{13}CO ($J = 1 - 0$)

^{13}CO ($J = 1-0$) emission above 3 σ level is detected in the velocity range of $V_{\rm lsr} = 4.5-8.8$ km s^{-1} with a typical sensitivity of ≈ 0.11 Jy beam^{-1}. No emission more than 3 σ level is detected outside this range. The total intensity map integrated over the range is shown in Figure 4.1. A strong emission which extends along north-south direction is revealed. A peak of the emission is slightly shifted southward to the source position of HL Tau. A ridge structure which extends toward XZ Tau, a classical T Tauri star located at 20″ east of HL Tau, is found. The integrated flux density above 3σ levels is 56.7 Jy km s^{-1} with the peak flux density of 3.65 Jy km s^{-1} beam^{-1}. The contour intervals at the east side of HL Tau is much denser than that at the west side of HL Tau as easily recognized in Figure 4.2.

Figure 4.3 shows the ^{13}CO ($J = 1 - 0$) line profiles integrated over a 20″ square (2800 AU

$\times$ 2800 AU) and a 50″ square (7000 AU $\times$ 7000 AU) around HL Tau. Since the absorption feature is seen around the systemic velocity of 6.7 km s^{-1}, which is derived from the optically thin H^{13}CO+ emission (Saito et al. 2001), the ^{13}CO line emission around the $V_{\rm sys}$ might be optically thick. Compared both the line profiles between that of the central region and the entire region, we found that the wind emission ($V_{\rm lsr} \geq$ 7.5 km s^{-1} or $\leq$ 5.5 km s^{-1}) is almost consistent with each other, suggesting that high velocity components concentrated in the central part around HL Tau.

Figure 4.4 shows channel maps of ^{13}CO ($J = 1-0$) line emission with a velocity resolution of 0.169 km s^{-1}. From $V_{\rm lsr} = 4.5-5.5$ km s^{-1}, the ^{13}CO gas is mainly distributed in the vicinity of the source position of HL Tau. In $V_{\rm lsr} \geq 5.7$ km s^{-1}, two clumps, one is at southeast and the other is at northwest of HL Tau, are found. As approaching to the systemic velocity of 6.7 km s^{-1}, the southeast component becomes much brighter. The ridge-like structure connecting between HL Tau and XZ Tau is found in the channel maps of $V_{\rm lsr} = 6.2$ and 6.4 km s^{-1}. From $V_{\rm lsr} = 6.5$ and 6.9 km s^{-1}, around the systemic velocity, the emission seems to be relatively weak, probably owing to the resolving out of an extended emission and the self-absorption effect. In these channels, the emissions extend along the northwest-southeast direction. The weak emission which seems to accompany to the XZ Tau is also found in $V_{\rm lsr} = 6.5$ and 6.7 km s^{-1}. In the following channel maps from $V_{\rm lsr} = 7.6 - 8.8$ km s^{-1}, the centrally condensed emission is found around HL Tau.

Figure **??** shows the distributions of the intensity-weighted mean velocity map around HL Tau. The integrated intensity map is shown as the gray contours for comparison the distribution of the emission. The contour for $V_{\rm lsr} = 6.7$ km s^{-1} passes through the stellar position, and the northeast part of the component is blueshifted with respect to the systemic velocity whereas the southwest part of one is redshifted. The velocity gradient clearly align the minor axis of the flattened envelope or parallel to the outflow axis, suggesting that the infall motion is dominant within the envelope.

4.3.2 C^{18}O ($J = 1 - 0$)

C^{18}O ($J = 1-0$) emission above 3 σ level was detected in the velocity range of $V_{\rm lsr} = 5.3-7.7$ km s^{-1} with a typical sensitivity of $\approx$ 0.10 Jy beam^{-1}. The total intensity map integrated over the range is shown in Figure 4.7. The image revealed clumpy emission which is elongated along north-south direction, roughly perpendicular to the outflow axis of HL Tau, but no emission is detected which accompanied with both HL Tau and XZ Tau. The total intensity

integrated over the 3 σ levels is 3.93 Jy km s^{-1} with the peak flux density of 0.22 Jy km s^{-1} beam^{-1}. The peak is not coincident to the source position of HL Tau but is corresponding to the south detached condensations shown in the ^{13}CO ($J = 1 - 0$) image. Figure **??** shows the C^{18}O ($J = 1 - 0$) line profiles integrated over a central part around HL Tau (20″ square) and an entire region of the field of view (50″ square). Since the C^{18}O gas seems to have been dispersed, emission is widely spreaded around the central source. The absorption feature around the systemic velocity is not found, suggesting that the emission is optically thin.

The velocity channel maps of C^{18}O ($J = 1 - 0$) emission is shown in Figure 4.9 whose velocity resolution of 0.169 km s^{-1} and sensitivity of 0.10 Jy beam^{-1}. In the channel maps of the blue-shifted range from $V_{\rm lsr} = 5.3 - 6.3$ km s^{-1}, only weak clumpy emission is detected around HL Tau. In the range around the systemic velocity of $V_{\rm lsr} = 6.5 - 6.8$, the emission is detected at west of HL Tau and the concentrated emission can be found at the 20″ south of HL Tau. In the red-shifted range from $V_{\rm lsr} = 7.0 - 7.7$ km s^{-1}, only the south concentrated emission is found. Although the clumpy emission is detected from $V_{\rm lsr} = 5.3 - 7.7$ km s^{-1}, the emission which accompanied with the source positions of HL Tau and XZ Tau can not be found, suggesting that almost all the dense gases have been already dissipated owing to the outflow activities of HL Tau and XZ Tau.

4.3.3 ^{13}CO ($J = 2 - 1$)

^{13}CO ($J = 2 - 1$) emission above the 3 σ level was detected within the velocity range of $V_{\rm lsr} = 4.46 - 8.88$ km s^{-1} with a typical sensitivity of ≈ 0.39 Jy beam^{-1}. The total intensity map integrated over the range is shown in Figure 4.10. The image revealed extended components around HL Tau and the brightest peak is shifted about 2″ southwest toward the source position. The integrated flux density above 3σ levels is 40.3 Jy km s^{-1} with the peak flux density of 5.31 Jy km s^{-1} beam^{-1}. The emission is slightly elongated along the direction from the north-west to the south-east, almost parallel to the outflow axis of HL Tau.

Figure 4.11 shows channel maps with a velocity resolution of 0.34 km s^{-1}. In the highly blue-shifted range from $V_{\rm lsr} = 4.63$ km s^{-1} to 5.31 km s^{-1}, the ^{13}CO gas is mainly distributed to the north of HL Tau. In the following channels from $V_{\rm lsr} = 5.65$ km s^{-1} to 6.67 km s^{-1}, the emission is distributed to the southeast of HL Tau. The emission around the systemic velocity of 6.7 km s^{-1} (6.33, 6.67, 7.01 km s^{-1} channels) seem to be relatively weak compared to the other channel maps, probably because of the resolving out of extended components caused by the lack of short spacing data in our observations. In the red-shifted range from $V_{\rm lsr} = 7.01$

km s^{-1} to 7.69 km s^{-1}, two bright peaks of ^{13}CO gas are revealed: One is at the vicinity of the source position of HL Tau, the other is the south of the source position. In the highly red-shifted velocity ranges from $V_{\rm lsr} = 8.03$ km s^{-1} to 8.71 km s^{-1}, the ^{13}CO gas is distributed to the south of HL Tau. Figure 4.12 shows the two color maps which integrated over the blue-shifted ranges ($V_{\rm lsr} = 4.46 - 6.50$ km s^{-1}) and the red-shifted ranges ($V_{\rm lsr} = 6.50 - 8.88$ km s^{-1}). The distinct velocity gradient is seen along the optical jet axis and is perpendicular to the major axis of the flattened envelope, suggesting the ^{13}CO ($J = 2 - 1$) gas traces the infall motion or outflow motion around HL Tau and the rotation motion seems to be small.

4.3.4 Estimation of gas mass

We estimate the entire mass of the dense gas around HL Tau from the total intensity of ^{13}CO ($J = 1 - 0$) emission. Although the ^{13}CO emission is generally optically thick around a protostar, the lower limit of the mass can be obtained under the simple assumption of optically thin condition. Since previous studies of HL Tau show the line-center optical depth of ^{13}CO ($J = 1 - 0$) emission is less than $\tau_{\rm ^{13}CO} \sim 0.8$ (Cabrit et al. 1996), our assumption seems to be valid. The mass of the gas can be calculated by the following equation (Scoville et al. 1986):

$$M_{\rm H_2} = 5.37 \times 10^{-5} T_{\rm ex} \exp\left(\frac{5.29}{T_{\rm ex}}\right) \frac{\tau_{\rm ^{13}CO}}{1 - \exp\left(-\tau_{\rm ^{13}CO}\right)} \left(\frac{d}{140{\rm pc}}\right)^2 \left[\frac{10^{-6}}{X(^{13}{\rm CO})}\right] \int S_\nu dv M_\odot, \quad (4.1)$$

where $T_{\rm ex}$ is the excitation temperature, $X(^{13}{\rm CO})$ is the fractional abundance of ^{13}CO relative to H_2, d is the distance to HL Tau, and F_ν is the integrated flux density of ^{13}CO ($J = 1 - 0$). With $X(^{13}{\rm CO})$ of 10^{-6} and $T_{\rm ex}$ of 20 K (Cabrit et al. 1996), the total mass of the dense gas is estimated to be 0.08 ± 0.01 $M_\odot$. The estimated mass is about a half of the mass estimated by the IRAM 30 m telescope observations, suggesting that the extended emission which can not be detected with the NMA exists around HL Tau (Cabrit et al. 1996). Since our observations are sensitive and the detected flux is as large as twice of the previous NMA observations by Hayashi, Ohashi, & Miyama (1993), the esitimated mass is also as large as twice. The mass of the clumpy shell which detected in the C^{18}O ($J = 1 - 0$) is also estimated to be 0.05 ± 0.005 $M_\odot$ with same temperature and $X({\rm C^{18}O})$ of 10^{-7}.

4.3.5 Continuum emission

We have obtained $\lambda = 3$ mm and 1.3 mm continuum maps of HL Tau with $6''-1''$ resolutions. Continuum emission at these wavelengths is thought to mainly come from thermal radiation of dust particles. Maps with the lowest and highest angular resolutions at 3 mm continuum are shown in Figure 4.14. To obtain higher signal-to-noise ratios (S/N) in the images, the data of both the lower and upper sidebands were combined into final images. Therefore, the center frequency of the 3 mm continuum images is 104 GHz (λ = 2.88 mm), and that of the 1.3 mm continuum images is 226 GHz (λ = 1.33 mm). The total flux densities of the 3 mm continuum emission are 100.3 ± 11.0 mJy with the D configuration and 81.9 ± 9.0 mJy with the AB configuration. That of the 1.3 mm continuum emission is 656 ± 70 mJy with the D configuration. Although the circumstellar disk around HL Tau has been revealed in previous millimeter wavelengths studies (Mundy et al. 1996; Kitamura et al. 2002), our insufficient angular resolutions of the D configuration prevent to spatially resolve the circumstellar disk structure, and only the 3 mm continuum image of the AB configuration shows the marginally resolved disklike structure perpendicular to the outflow axis. The peak positions of the continuum emission are (α_{1950}, δ_{1950}) = (04^h 28^m $44^s.39$, $+18^\circ$ $07'$ $34''.9$). The typical positional error, which includes the effect of atmospheric seeing, is $0''.3$, and the position is consistent to the previous works.

Since the continuum emission is expected to be optically thin, we can estimate the disk mass. Assuming that the dust temperature within the disk, $T_{\rm dust}$, is uniform, the disk mass is given by

$$M_{\rm disk} = \frac{F_\nu d^2}{\kappa_\nu B_\nu(T_{\rm dust})}, \tag{4.2}$$

where κ_ν is the mass absorption coefficient by dust grains, $B_\nu(T)$ is the Planck function, F_ν is the total flux density of the continuum emission, and d is the distance to HL Tau (140 pc). With $T_{\rm dust}$ = 20 K, $\kappa_{\rm 220GHz} = 0.1 \times (220{\rm GHz}/10^{12})^\beta$, and $\beta = 1$, the total flux densities of our images give a disk mass of 0.12 ± 0.02 $M_\odot$. With $T_{\rm dust}$ = 50 K, the disk mass becomes 0.06 ± 0.01 $M_\odot$. Since the flux densities of the 3 mm continuum emission of the AB configuration is more than 80 % of the flux of the D configuration, suggesting that the dust emission is concentrated at the circumstellar disk around HL Tau.

4.4 Discussion

4.4.1 Detailed Structure of the Infalling Envelope

A Keplerian rotation around HL Tau was firstly proposed by Sargent & Beckwith (1987, 1991), and the following studies by Hayashi, Ohashi, & Miyama (1993) has revealed the gas exhibits not only rotational motion but infall motion, suggesting the presence of a infalling envelope. Cabrit et al. (1996), however, pointed out the contamination of the outflow gases around HL Tau is serious and the infall motion must be strongly influenced by the outflow. They also pointed out that the rotational motion around HL Tau is negligible. We discuss whether the velocity structure around HL Tau exhibit an infall motion or outflow motion.

Recent observations of molecular outflows have revealed that outflows exhibit acceleration motion as apart from central sources, like a Hubble-law (Beuther, Schilke, & Stanke 2003). The acceleration motion can be interpreted due to the combination of momentum conservation of the protostellar winds and density decreases away from the driving sources of the outflow (e.g., Shu et al. 1991). Hydrodynamic jet entrainment models also result in Hubble-law-like Position-Velocity (P-V) diagrams (e.g., Smith et al. 1997; Downes & Ray 1999). These studies indicate that gases accompany with outflows will show acceleration motions away from the central sources whereas gases accompany with infalling envelopes show reverse radial dependence, acceleration motions as approaching sources.

Figure 4.15 shows the total intensity map of ^{12}CO ($J = 3-2$) emission and the P-V diagram along the outflow axis of HL Tau taken with the ASTE (Atacama Submillimeter Telescope Experiment) at Pampa la Bola (elevation 4800 m) in Atacama, Chile. Since this is a part of pilot observations of the ASTE and flux calibrations are not well-studied, only the morphology of the gas is used for discussion. ^{12}CO ($J = 3 - 2$) emission is generally optically thick and is known as a good tracer of molecular outflows. Although the total intensity map integrated over $V_{\rm lsr} = 0 - 12$ km s^{-1} shows widely spreaded emission over the field of view, the P-V diagram along the outflow axis at P.A. of 50° shows ambient cloud components concentrate around $V_{\rm lsr} \approx 5-9$ km s^{-1}: corresponding to the "ambient cloud component" in the right panel of Figure 4.15. Another feature of the P-V diagram is the south-west component exhibiting red-shifted to the systemic velocity and the north-east component exhibiting blue-shifted to the systemic velocity. These components clearly exhibit an acceleration motion as apart from central sources, suggesting the outflowing gases: corresponding to the "outflow component" in the right panel of Figure 4.15. On the other hand, the P-V diagrams of ^{13}CO ($J = 1 - 0$)

emission, taken with the NMA superposed onto that of the ^{12}CO ($J = 3 - 2$), exhibits quite different velocity structure to the outflowing gases. The total intensity map of the ^{13}CO ($J = 1 - 0$) extended perpendicular to the outflow axis as shown in the left panel of Figure 4.15, and the P-V diagram exhibits the acceleration motion as approaching the central sources with a $r^{-0.5}$ radial dependence, indicating the infall motion of the envelope: corresponding to the "infalling envelope component" in the right panel of Figure 4.15. Since the radial dependences of the velocities of the infalling gas and outflowing gas show opposite sense, both of the components are easily distinguished. Next, we compare ^{13}CO ($J = 1 - 0$) images with the ^{13}CO ($J = 2 - 1$) images in Figure 4.17. Figure 4.17(c) shows the superposed image of the ^{13}CO ($J = 2 - 1$) image onto the total intensity map of ^{13}CO ($J = 1 - 0$). Since the ^{13}CO ($J = 2 - 1$) components trace the central part of the envelope and the P-V diagram along major and minor axes of the envelope trace the central high velocity components, the ^{13}CO ($J = 2 - 1$) emission seems to trace the inner most part of the infalling envelope. As a result, we conclude that the velocity gradient shown in ^{13}CO ($J = 1 - 0$) and ^{13}CO ($J = 2 - 1$) emission along the minor axis (e.g., outflow axis) of HL Tau indicates the infall motion although some contamination of outflow might be included.

We confirm the infall motion by inspecting the P-V diagrams of ^{13}CO ($J = 1 - 0$) line emission as shown in Figure 4.16. Figure 4.16 shows the P-V diagrams along four different cuts of the envelope: Figure 4.16(b) is a cut along the major axis through the central source position (B1-B2 cut in Figure 4.16(e)); (a) and (c) are the cuts parallel to the (b) (A1-A2, C1-C2 cuts in (e)) offset by $2''.0$ northeast and southwest, respectively; (d) is a cut along the minor axis or outflow axis through the central source position (D1-D2 cut in (e)). The infall motion around HL Tau can be found in Figure 4.16(a), (c), and (d) panels. The fitted curves indicate the velocity pattern given by $V_{\rm infall} = (2GM/r)^{-1/2}$ with rotation. Three curves correspond to the velocities with the central masses of 0.1, 0.5, 1.0 $M_\odot$ respectively. Here, we adopted the inclination angle of the envelope as a typical value of 60° (e.g., Hayashi, Ohashi, & Miyama 1993; Close et al. 1997; Kitamura et al. 2002). To reproduce the P-V diagrams, especially the high velocity components shown in (a), (c), the central mass of $0.5 - 1.0$ $M_\odot$ is required. Although the detached component seen in north-east of the source (D1 direction) in Figure **??**(d) are well fitted in the case of the central mass of 0.1 $M_\odot$, the component is too far from the central source ($\sim 5000 - 10000$ AU) and is unlikely to trace the infall motion. To fit the inner part of the P-V diagram in (d) panels, the central mass of $0.5 - 1.0$ $M_\odot$ seems to be valid.

4.4.2 Rotational Motion of the Infalling Envelope

Next, we discuss a rotational motion in the envelope. In previous works, Hayashi, Ohashi, & Miyama (1993) claimed the presence of rotation motion of 0.2 km s^{-1} at 700 AU, whereas Cabrit et al. (1996) pointed out the lack of rotation motion in the envelope. Since the angular resolutions of our observations are comparable to these works but the sensitivities are dramatically improved, our observations will be able to conclude whether the envelope has rotational motion or not. Hayashi, Ohashi, & Miyama (1993) estimated the rotation motion from the spatial and velocity distributions of two bright components in the P-V diagram along the major axis. These two components are also detected in our P-V diagrams, are corresponding to the components A and B as shown in Figure 4.16(b). Since the systemic velocity of HL Tau which estimated from the optically thin $H^{13}CO^+$ emission is 6.7 km s^{-1} and both the components are blue-shifted toward the $V_{\rm sys}$, these components does not trace rotational motion around HL Tau.

Since specific angular momenta of infalling envelopes are thought to be conserved during contractions (e.g., Ohashi et al. 1997; Momose et al. 1998), the radial dependence of rotational motion is in inverse proportion to the radius; $V_{\rm rot} \propto r^{-1}$. In Figure 4.16(a), the cut along the major axis of the envelope with 2″ offsetted to northeast, the emission is distributed mainly with blue-shifted to the $V_{\rm sys}$ and the high velocity blue-shifted components ($V_{\rm lsr} \approx 5$ km s^{-1}) are slightly shifted to the northwest. On the other hand, in Figure 4.16(c), the cut along the envelope with 2″ offseted to southwest, the red-shifted emission becomes much brighter and the high velocity red-shifted components ($V_{\rm lsr} \approx 8$ km s^{-1}) are slightly shifted to the southeast. These feature can be explained with the rotational motion around HL Tau. To fit these features: high blue- and red-shifted components in Figure 4.16 (a),(c), the required rotational motion is estimated to be $V_{\rm rot} = 0.8$ km s^{-1} at 1400 AU. The dashed lines presented in Figure 4.16 indicate the velocity patterns of the previously mentioned infall motion with a rotation whose velocity of $V_{\rm rot} = 0.8$ km s^{-1} $\times$ $(r/1400{\rm AU})^{-1}$. Although the rotational motion of $V_{\rm rot} = 0.8$ km s^{-1} $\times$ $(r/1400{\rm AU})^{-1}$ is well fitted the features of high blue- and red-shifted components in Figure 4.16(a), (c), the structures around the $V_{\rm sys}$ are incomprehensible, owing to the resolving out and clumpy complex structures around HL Tau. As shown in Figure 4.16(b), since the red-shifted components at north-west of HL Tau and the blue-shifted components at south-east of HL Tau are likely to trace the rotation motion, the possibility of a clockwise rotation can not be excluded. Furthermore, if the rotation of $V_{\rm rot} = 0.8$ km s^{-1} $\times$ $(r/1400{\rm AU})^{-1}$ was real, the expected centrifugal radius becomes too large ($\sim 10^3$ AU with

an 1 $M_\odot$ central mass). Since we didn't detect such a large rotating disk around HL Tau, the rotational motion around HL Tau have to be much moderate.

The iso-velocity map in Figures **??**, 4.13 shows the clear velocity gradient along the minor axis of the envelope without the gradient along the major axis, suggesting that the rotational motion is negligible. Since the resolving out of ^{13}CO ($J = 1 - 0$) emission seems to be serious around the $V_{\rm sys} = 6.7$ km s^{-1}, we made 2 color maps of ^{13}CO ($J = 1 - 0$) emission integrated only the high red-shifted components ($V_{\rm lsr} \geq 7.7$ km s^{-1}) and the high blue-shifted components ($V_{\rm lsr} \leq 5.7$ km s^{-1}) as shown in Figure 4.6. In the P-V diagrams (see Figure 4.16), these velocity components distributed to the north side in Figure 4.16(a) and the south side in Figure 4.16(c), suggesting the rotation motion around HL Tau. In the 2 color maps, however, these components clearly align the minor axis of the envelope, suggesting that the infall motion is dominant with a small rotation.

To reveal a rotationally supported disk around HL Tau, much high angular resolution observations with higher J transition are strongly required. Although the disklike structure of $\sim 100 - 300$ AU in radius around HL Tau has been revealed in millimeter/ submillimeter continuum observations, these component seems to contain the extended envelope component.

4.4.3 Dispersed Dense Gas around HL Tau

C^{18}O ($J = 1 - 0$) emission has revealed clumpy and dissipated structure. Figure 4.18 shows the superposed image of the total intensity map of C^{18}O emission onto the wide field image ($3' \times 3'$) of ^{13}CO ($J = 1 - 0$) emission taken with the BIMA (Welch, Hartmann, Helfer, & Briceño 2000). Momose (1998, PhD thesis) revealed that the ring-like structures of C^{18}O emssion around flat-spectrum T Tauri stars, suggesting that the remnant cloud cores with central voids structure. The typical sizescale of the void is a few $\times$ 1000 AU, and are comparable to the sizescale of the dynamical collapse in the protostar phase. Such a ring-like structure is detected in our C^{18}O emission as shown in the red-dashed line in Figure 4.18, whose radius of $\sim 3 - 4 \times 10^3$ AU. The other void structure which was revealed with the BIMA is shown as the black-dashed line in Figure 4.18 around the binary T Tauri star XZ Tau, whose radius of $\sim 7 \times 10^3$ AU. Since the C^{18}O emission seems to be distributed along the edge of a concentric circle around XZ Tau, not only the accretion processes of HL Tau but also the stellar activities of XZ Tau might have influenced to the clumpy structure of C^{18}O emission.

4.5 Summary

We performed high sensitive CO and its isotope observations of the protostar candidate HL Tau. The main results are as follows:

1. ^{13}CO ($J = 1 - 0$) emission was detected in the velocity range of $V_{\rm lsr} = 4.5 - 8.8$ km s^{-1}. The emission revealed the elongated structure perpendicular to the outflow axis of HL Tau. The gas exhibits infall motion toward the central source, but the rotational motion is hardly detected.

2. ^{12}CO ($J = 3 - 2$) emission taken with the ASTE pilot obsevations have clearly revealed the outflowing gases. Comparison between the ^{12}CO and ^{13}CO emissions indicates that the velocity gradient detected in ^{13}CO ($J = 1 - 0$) emission traces the infall motion in the envelope. The required central mass is estimated to be $0.5 - 1.0$ $M_{\odot}$.

3. C^{18}O (J=1-0) emission was detected in the velocity range of $V_{\rm lsr} = 5.3 - 7.7$ km s^{-1}. The emission revealed the clumpy and ring-like structure around HL Tau, suggesting that the dense envelope around HL Tau has already dissipated, probably owing to the outflow activity and protostellar collapse of HL Tau.

4. ^{13}CO (J=2-1) emission was detected in the velocity range of $V_{\rm lsr} = 4.46 - 8.88$ km s^{-1}. Although the compact disklike emission was detected around HL Tau, no rotational motion was detected, suggesting the Keplerian rotating disk around HL Tau is much smaller than that around L1551 IRS 5.

CHAPTER 4. TABLE

Table 4.1: Observational Parameters

Observation period	2000 November - 2002 December		
Molecular line	^{13}CO ($J = 2 - 1$)	^{13}CO ($J = 1 - 0$)	C^{18}O ($J = 1 - 0$)
Frequency [GHz]	220.398686	110.201353	109.782160
Velocity resolution [km s^{-1}]	0.340	0.169	0.169
Synthesized beam size	3.06 × 2.88	5.66 × 4.77	5.31 × 4.88
Position angle [°]	-77.7	-41.4	-41.9
Noise level (1 σ) [mJy beam^{-1}]	390	22.9	25.0
Continuum [GHz]	220 ± 0.512, 232 ± 0.512	98 ± 0.512, 110 ± 0.512	
Synthesized beam size (D/AB)*	2.97 × 2.85/ –	6.27 × 5.48/ 1.37 × 1.28	
Position angle [°] (D/AB)*	79.2/ –	-45.2/ 6.7	
Noise level (D/AB)* [mJy beam^{-1}]	13/ –	1.2/ 2.0	
Phase & amplitude calibrator (flux density)	0420-014 (8.1 Jy)	0446+112 ($1.7 - 2.5$ Jy) 0528+134 (2.3 Jy)	
Bandpass calibrator	0420-014	3C454.3	
$T_{\rm sys}$ [K] (in DSB)	400 K	150 K	

* D and AB are the NMA array configurations D (lowest angular resolution) and AB (highest angular resolution), respectively.

CHAPTER 4. FIGURES

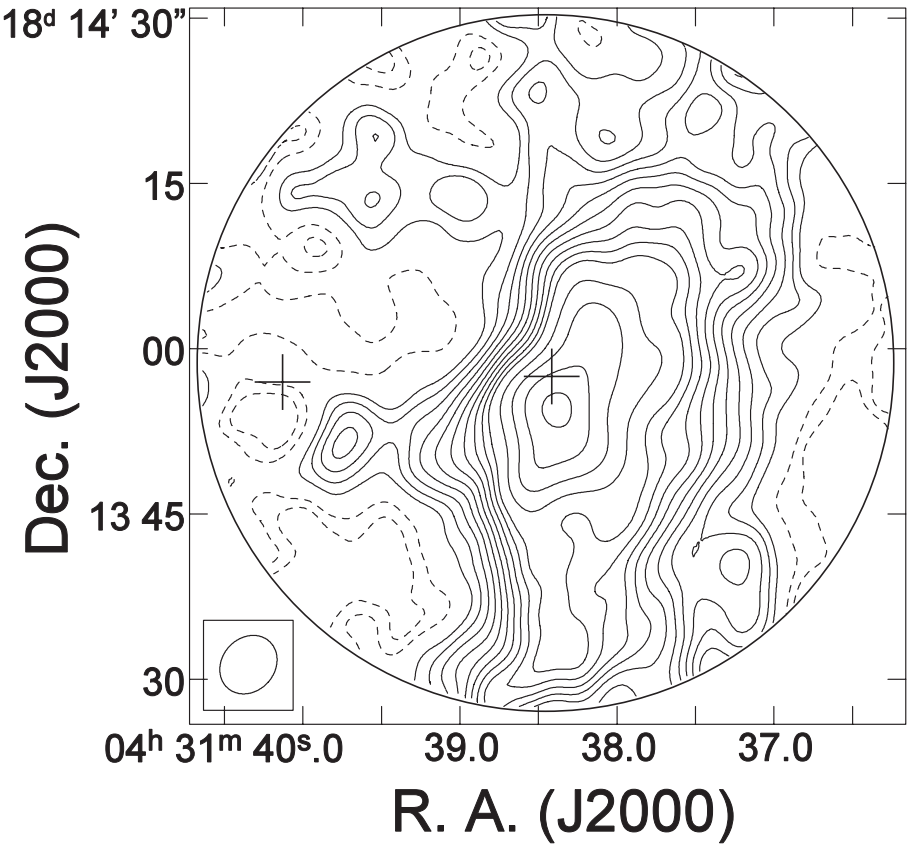

Figure 4.1: Total intensity map of ^{13}CO(J=1-0) emission of HL Tau integrated from $V_{\rm lsr}$ = 4.5 km s^{-1} to 8.8 km s^{-1}. The contour lines start at $\pm$2.0 σ levels with intervals of 2.0 σ until 20 σ, and intervals of 4.0 σ over 20 σ. The negative levels are indicated by broken lines. The rms noise level (1 σ) is 22.9 mJy beam^{-1}. The total intensity over the 6 σ region is 56.7 Jy km s^{-1} with a peak flux density of 0.85 Jy beam^{-1}. The primary beam collection is applied. The open circle in the bottom-left corner is the synthesized beam (FWHM).

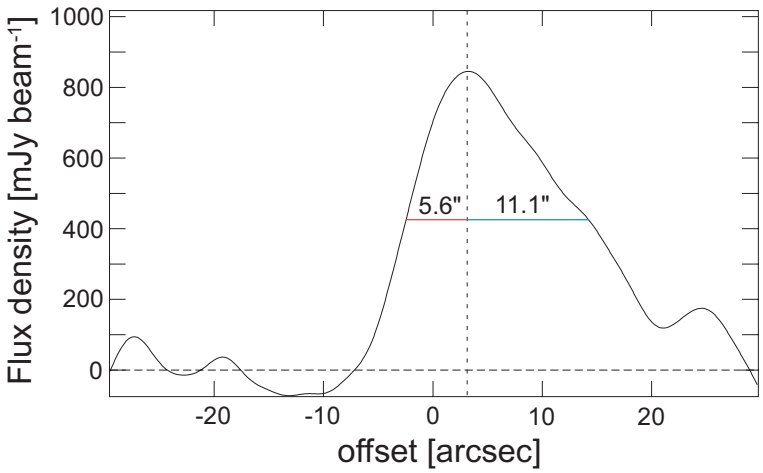

Figure 4.2: ^{13}CO(J=1-0) line profiles in units of flux density (mJy) cut parallel to the outflow axis of HL Tau through the source position of HL Tau. The peak is shifted south-westward.

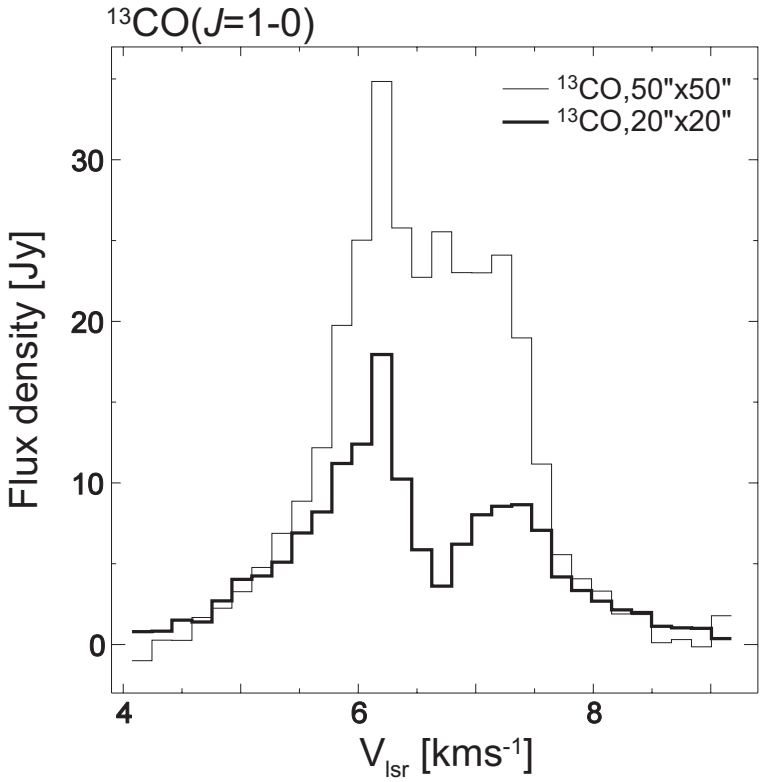

Figure 4.3: ^{13}CO(J=1-0) line profiles in units of flux density (Jy). The thin line indicates the emission from the entire region ($50'' \times 50''$), and the thick line indicates the emission from the centrally condensed components ($20'' \times 20''$).

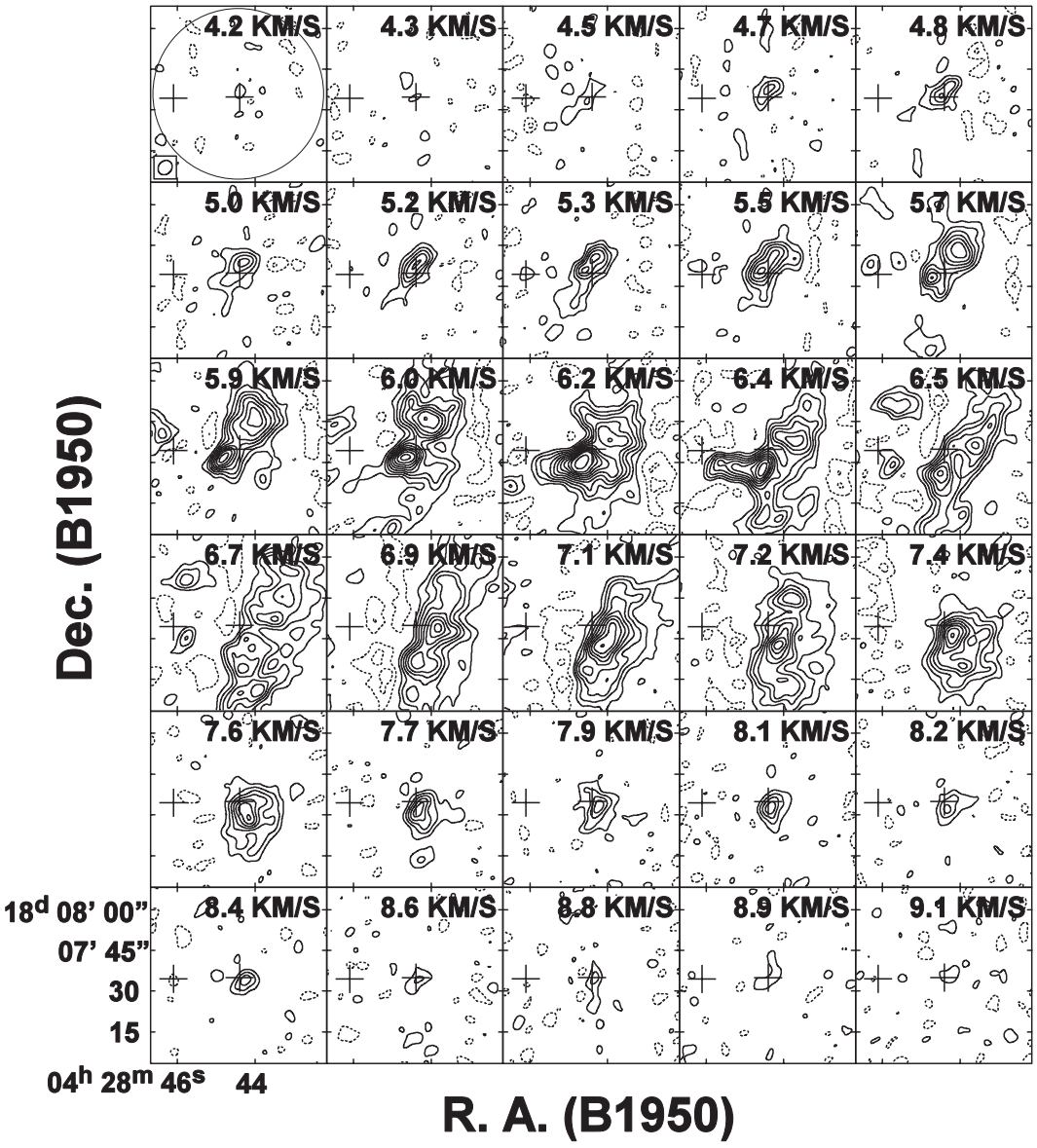

Figure 4.4: Velocity channel maps of ^{13}CO emission of HL Tau. The central LSR velocity with a velocity width of 0.169 km s^{-1} is denoted in unit of km s^{-1} at the upper right corner of each panel. The contour intervals are 2 σ, starting at $\pm$2.0 σ with 1 σ = 0.110 Jy beam^{-1}. The negative levels are indicated by broken lines.

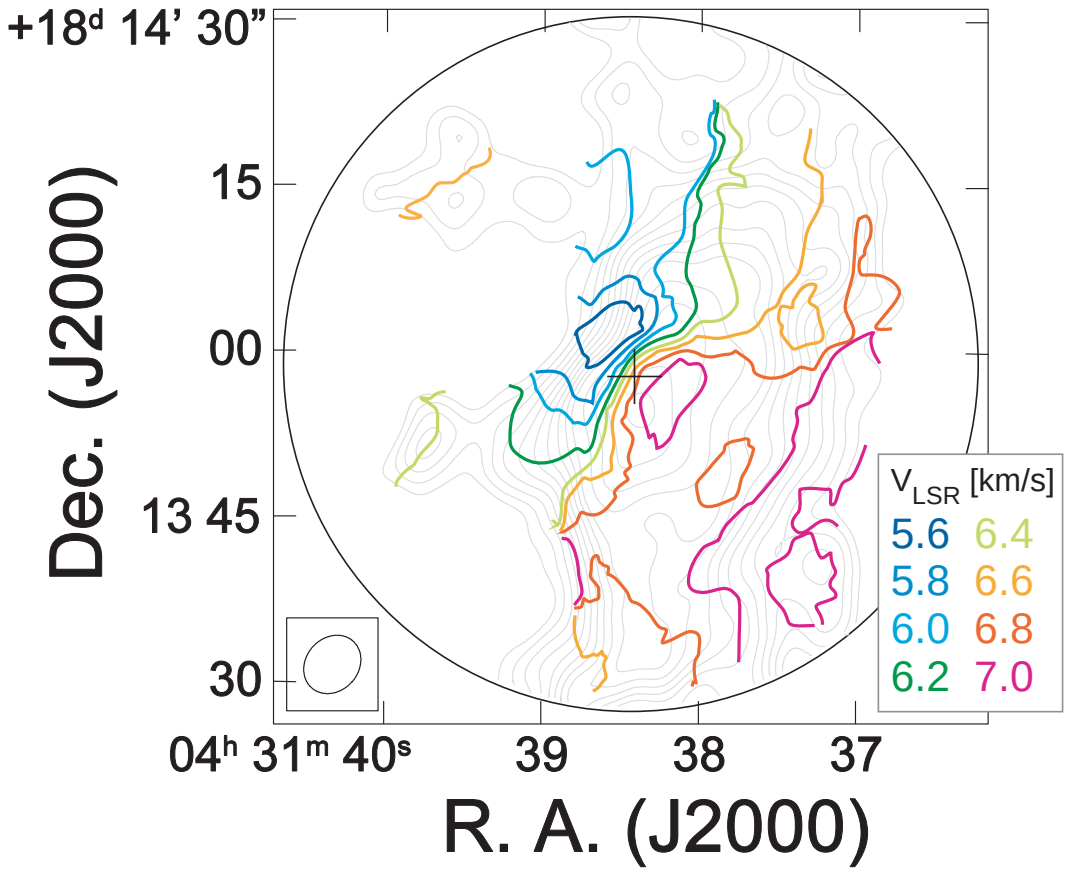

Figure 4.5: Intensity-weighted mean velocity map of HL Tauri obtained from ^{13}CO(J=1-0) emission. The integrated intensity distribution is also shown by gray lines, whose contours are the same as in Figure 4.1.

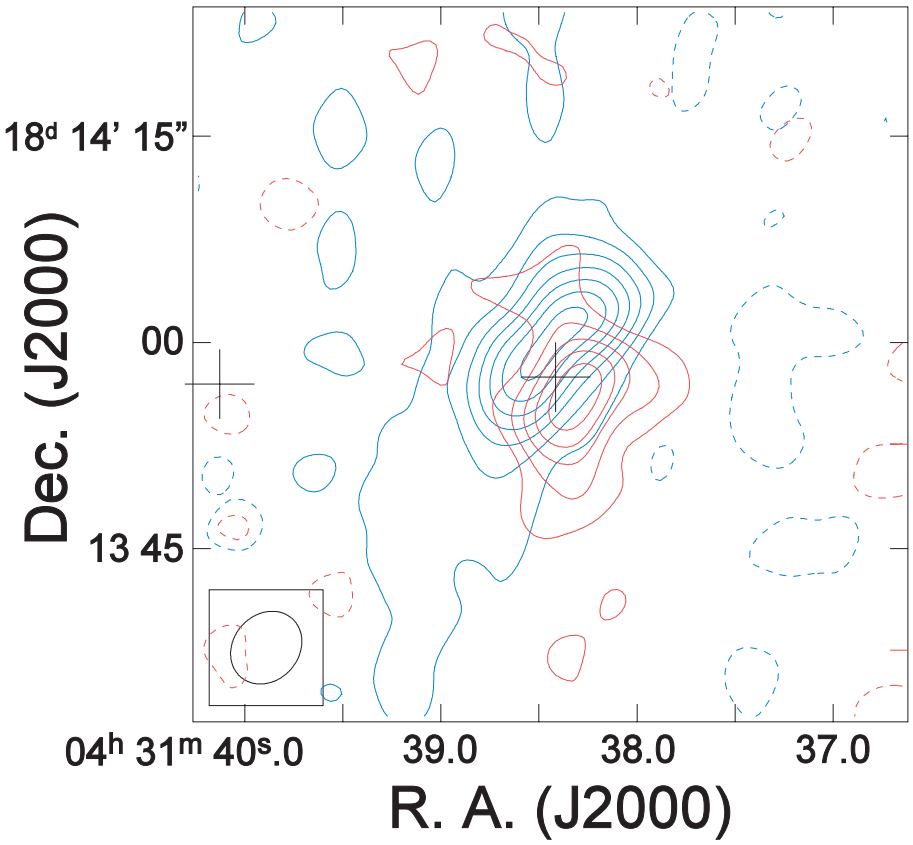

Figure 4.6: ^{13}CO ($J = 1 - 0$) maps integrated over $V_{\rm lsr} = 7.7 - 8.8$ km s^{-1} (Red-shifted components) and $V_{\rm lsr} = 4.5 - 5.7$ km s^{-1} (Blue-shifted components). Blue contours and red contours indicate the blue-shifted components and the red-shifted components, respectively.

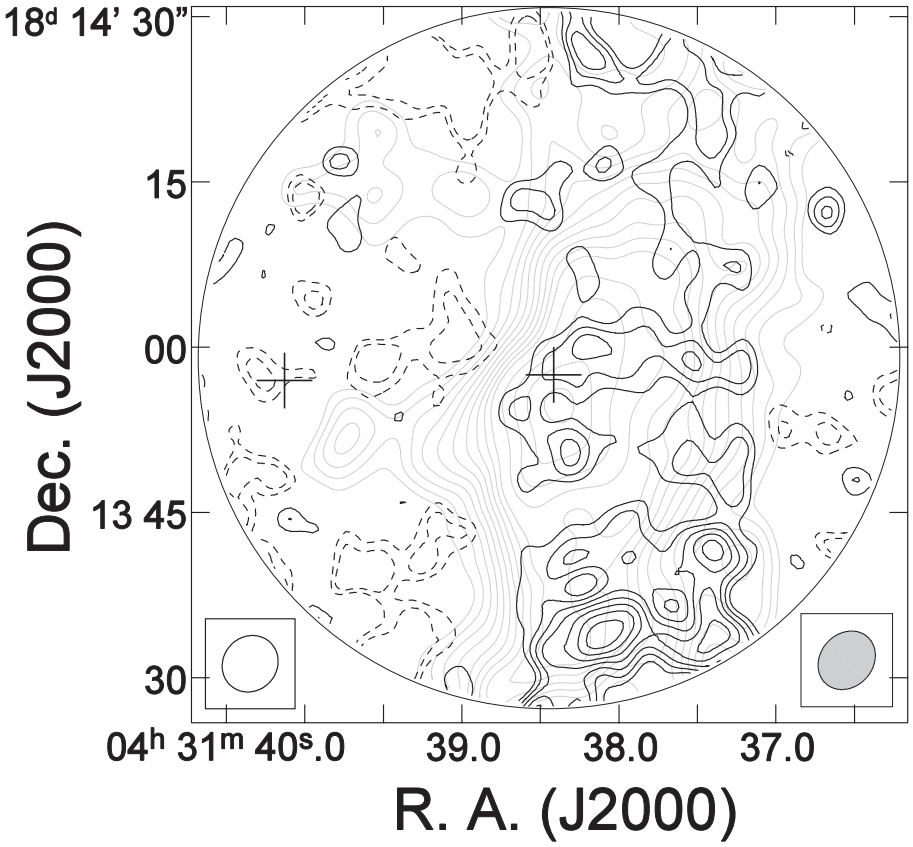

Figure 4.7: Total intensity map of $C^{18}O(J$=1-0) emission of HL Tau integrated from $V_{\rm lsr} = 5.4$ km s^{-1} to 7.7 km s^{-1} with that of $^{13}CO(J = 1 - 0)$ in gray scale. The contour lines start at $\pm 2.0\ \sigma$ levels with intervals of $1.0\ \sigma$. The negative levels are indicated by broken lines. The rms noise level ($1\ \sigma$) is 25.0 mJy beam^{-1}. The peak flux density is 0.22 Jy beam^{-1}. The primary beam collection is applied. The open circle in the bottom-left corner is the synthesized beam (FWHM).

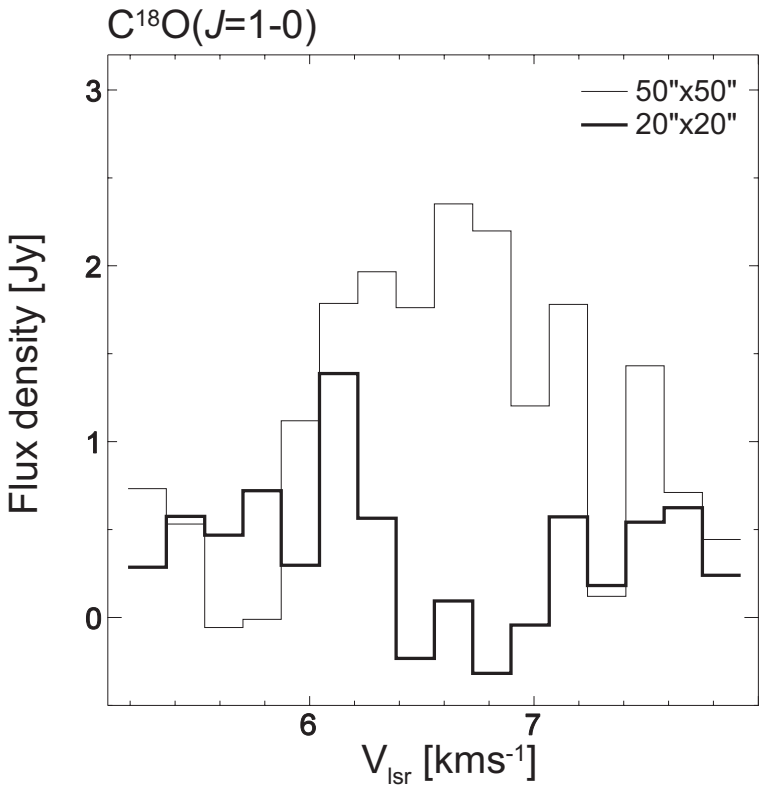

Figure 4.8: $C^{18}O(J$=1-0) line profiles in units of flux density (Jy). The thin line indicates the emission from the entire region ($50'' \times 50''$), and the thick line indicates the emission from the centrally condensed components ($20'' \times 20''$).

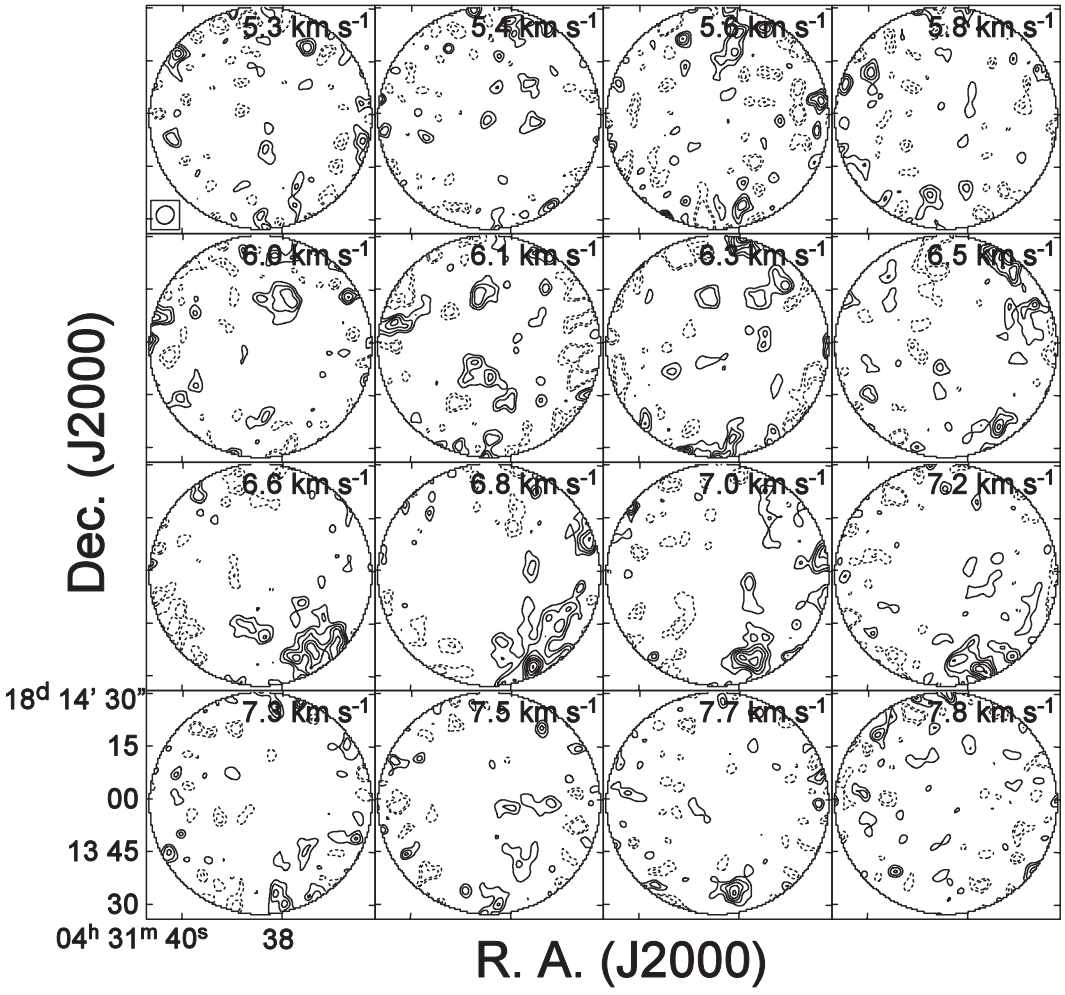

Figure 4.9: Velocity channel maps of $C^{18}O$ emission of HL Tau. The central LSR velocity with a velocity width of 0.169 km s^{-1} is denoted in unit of km s^{-1} at the upper right corner of each panel. The contour intervals are 1 σ, starting at ± 2.0 σ with 1 σ = 0.100 Jy $beam^{-1}$. The negative levels are indicated by broken lines.

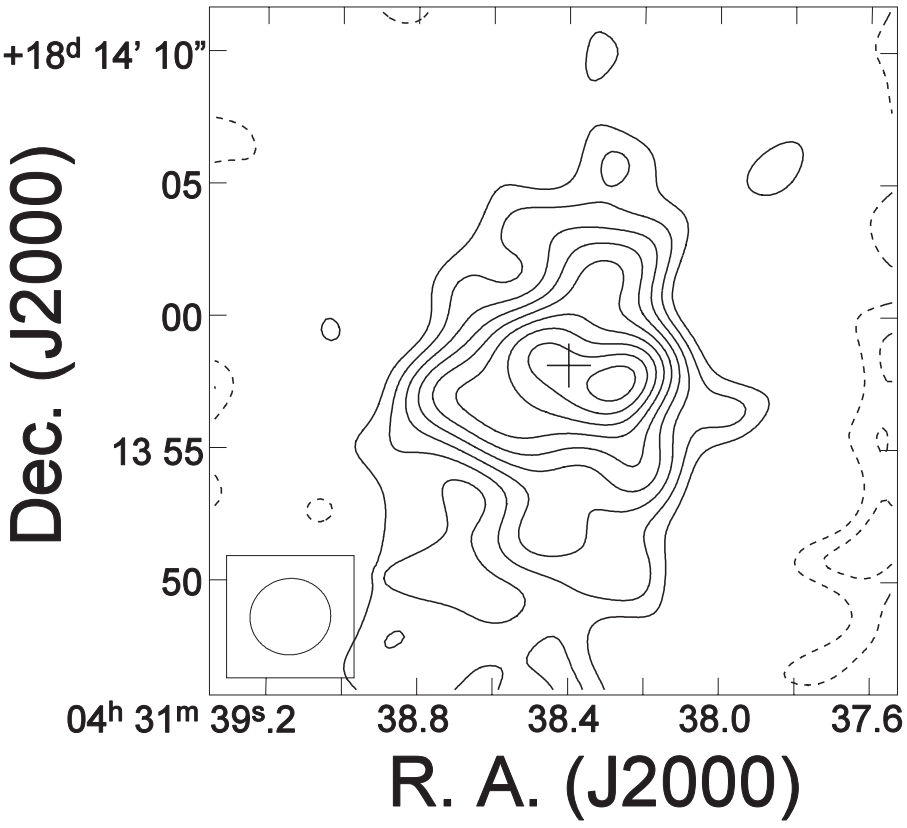

Figure 4.10: Total intensity map of ^{13}CO(J=2-1) emission of HL Tau integrated from $V_{\rm lsr}$ = 4.46 km s^{-1} to 8.88 km s^{-1}. The contour lines start at $\pm$2.0 σ levels with intervals of 1.0 σ. The negative levels are indicated by broken lines. The rms noise level (1 σ) is 0.52 Jy km s^{-1} beam^{-1}. The total intensity over the 2 σ region is 40.3 Jy km s^{-1} with a peak flux density of 5.31 Jy km s^{-1} beam^{-1}. The open circle in the bottom-left corner is the synthesized beam (FWHM).

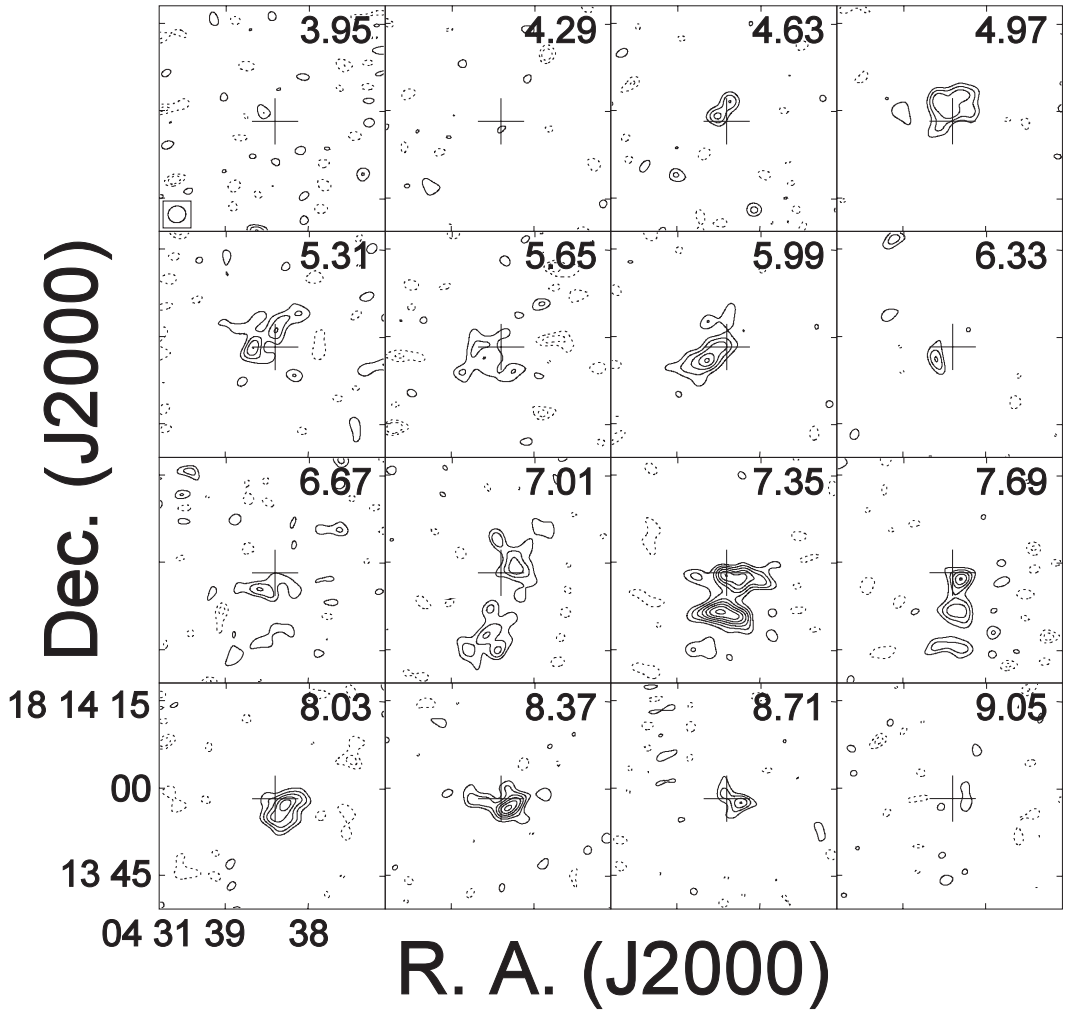

Figure 4.11: Velocity channel maps of ^{13}CO (J=2-1) emission of HL Tau. The central LSR velocity with a velocity width of 0.34 km s^{-1}. The rms noise level is 0.39 Jy beam^{-1}. The contour lines starts at $\pm$2.0 σ levels with intervals of 1.0 σ. The negative levels are indicated by broken lines.

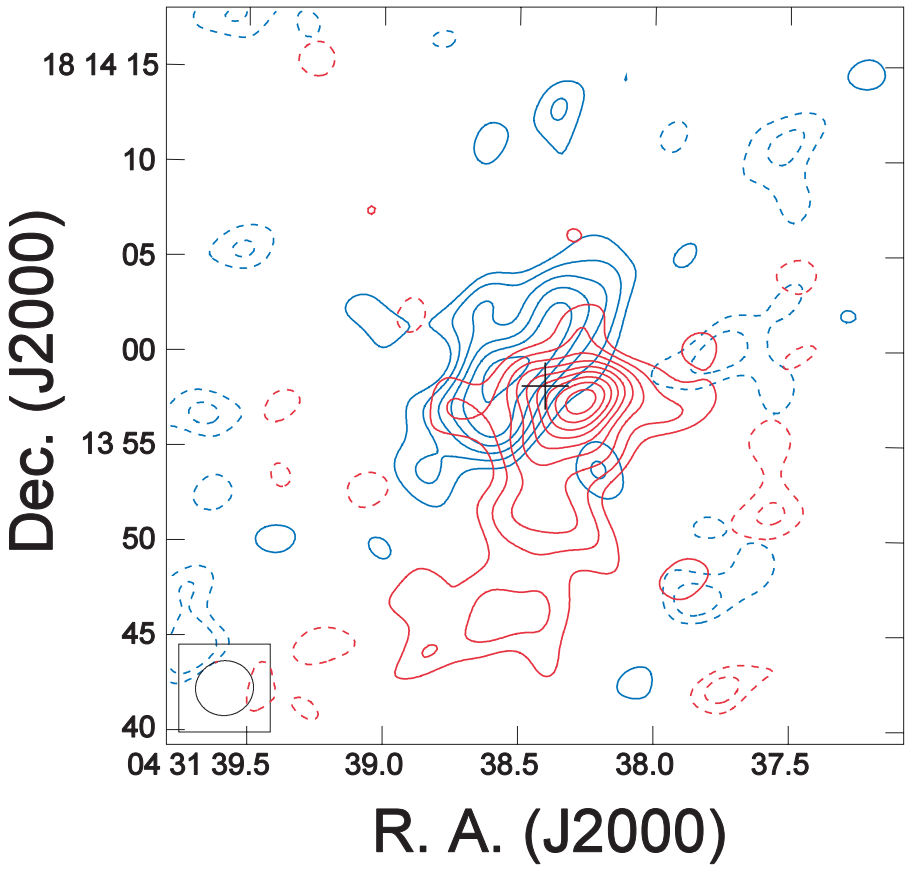

Figure 4.12: 2 color maps of ^{13}CO (J=2-1) emission. Blue contours indicates the blue-shifted component which is integrated over $4.46 - 6.50$ km s^{-1}, whose integrated intensity over the 2σ region is 14.2 Jy km s^{-1} with the peak flux density of 2.60 Jy km s^{-1} beam^{-1}. The rms noise level of the blue-shifted component is 0.17 Jy beam^{-1}. Red contours indicates the red-shifted component which is integrated over $6.50 - 8.88$ km s^{-1}, whose integrated intensity over the 2σ region is 25.4 Jy km s^{-1} with the peak flux density of 4.73 Jy km s^{-1} beam^{-1}. The rms noise level of the red-shifted component is 0.18 Jy beam^{-1}. The contour intervals are written in the same manner as in Figure 4.1.

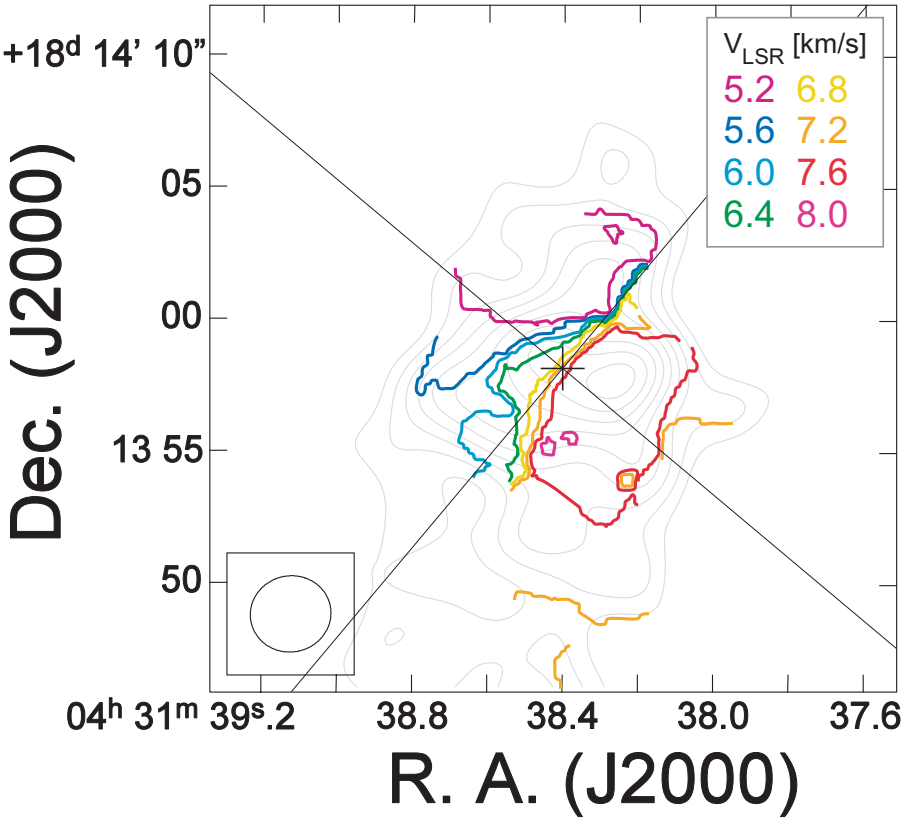

Figure 4.13: Intensity-weighted mean velocity map of HL Tau obtained from ^{13}CO($J = 2 - 1$) emission. The integrated intensity distribution is also shown by gray lines, whose contours are the same as in Figure 4.10. The axes parallel and perpendicular to the optical jet in [S II] are written in solid line (the P.A. of the jet axis is 50°.).

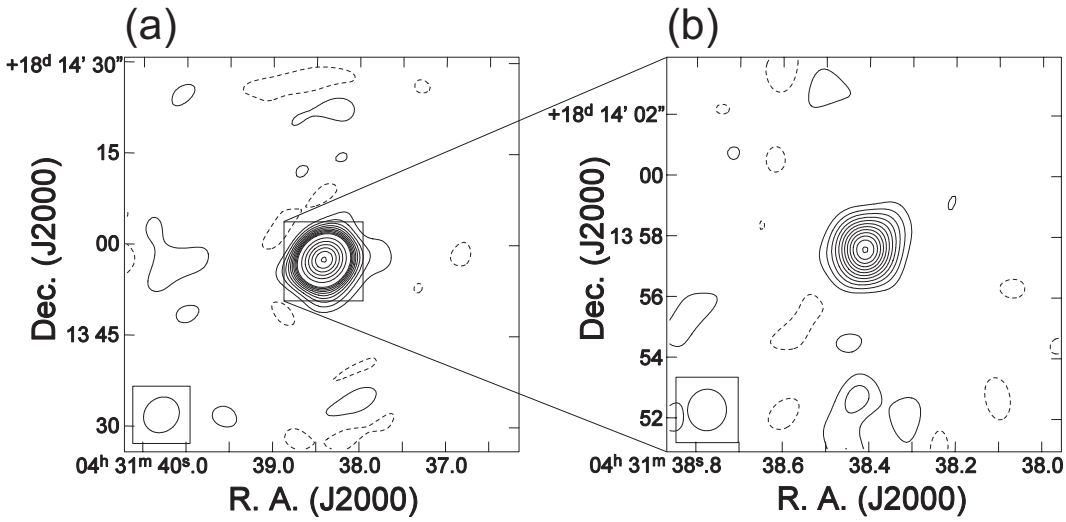

Figure 4.14: (a) Lowest angular resolution image of HL Tau with the D configuration at $\lambda =$ 2.88 mm. The contour lines start at $\pm 2.0\sigma$ levels with intervals of 2.0σ until 20σ. The intervals become 10σ over 20σ. The rms noise level (1σ) is 1.2 mJy beam^{-1}. The open ellipse in the bottom left corner is the synthesized beam size (HPBW) of $6\farcs27 \times 5\farcs48$ at P.A. = -45.2°. (b) Highest angular resolution image of HL Tau with the AB configuration at $\lambda = 2.88$ mm. The contour lines start at $\pm 2.0\sigma$ levels with intervals of 2.0σ until 20σ. The rms noise level is 2.0 mJy beam^{-1}, and the synthesized beam size is $1\farcs37 \times 1\farcs28$ at P.A. = 6.7°.

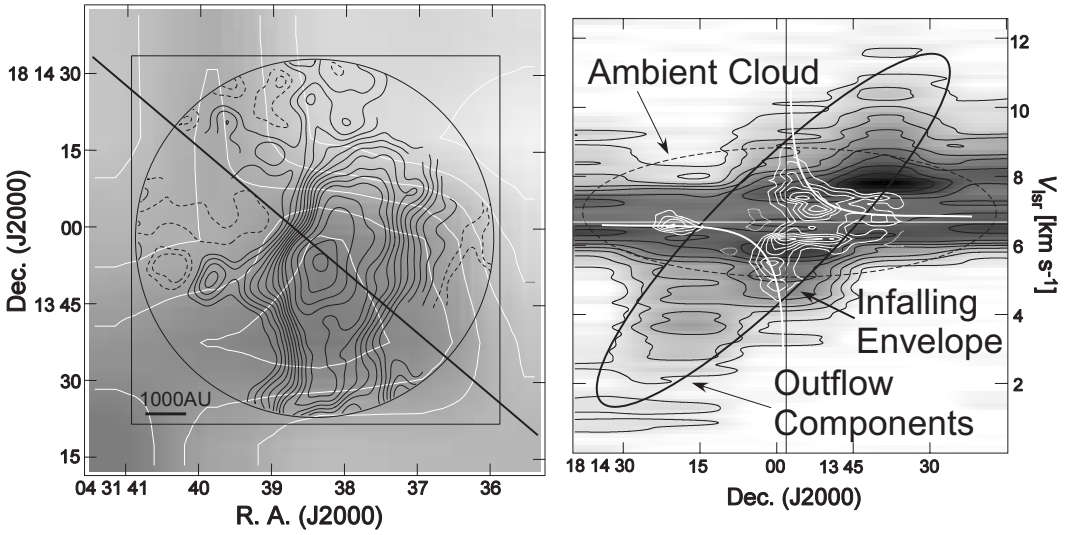

Figure 4.15: Left: Superposed image of the total intensity map of ^{13}CO ($J = 1 - 0$) emission onto that of ^{12}CO ($J = 3 - 2$) emission taken with the ASTE pilot observations. Right: The Position-Velocity diagram along the outflow axis at P.A. = 50° of HL Tau. A gray scaled image with the contours indicates the ^{12}CO ($J = 3 - 2$) data, and a white contours indicate the ^{13}CO ($J = 1 - 0$) data.

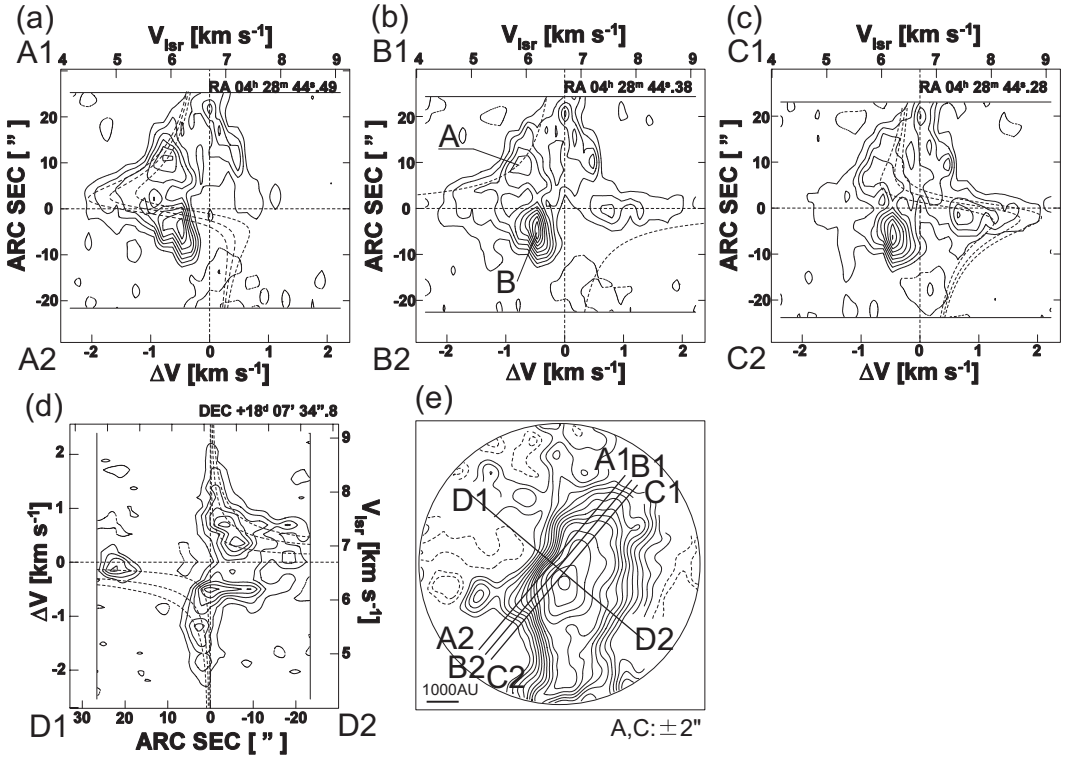

Figure 4.16: Position-velocity diagrams (a),(b),(c),(d) of the ^{13}CO(J=1-0) emission along four different cuts shown in the ^{13}CO integrated intensity map (e). Contours in (a)-(d) are indicated in step of 10 % of the peak flux densities, and those in (e) are in the same manner as in Figure 4.1. (a) The P-V diagram along the cut A1-A2 offset by 2″.0 northeast from the major axis. The curves indicate the velocity distribution of rotation motion proportional to r^{-1} (conservation of a specific angular momentum), and infall motion proportional to $r^{-0.5}$. The inner curve is for M = 0.1 $M_\odot$, and the outer curve is for M = 1.0 $M_\odot$. The middle curve is for 0.5 $M_\odot$. (b) The P-V diagram along the major axis, B1-B2. The curves are the same as in (a). (c) The P-V diagram along the cut C1-C2 offset by 2″.0 southwest from the major axis. The curves are same as in (a). (d) The P-V diagram along the minor axis, D1-D2. The curves are the same as in (a).

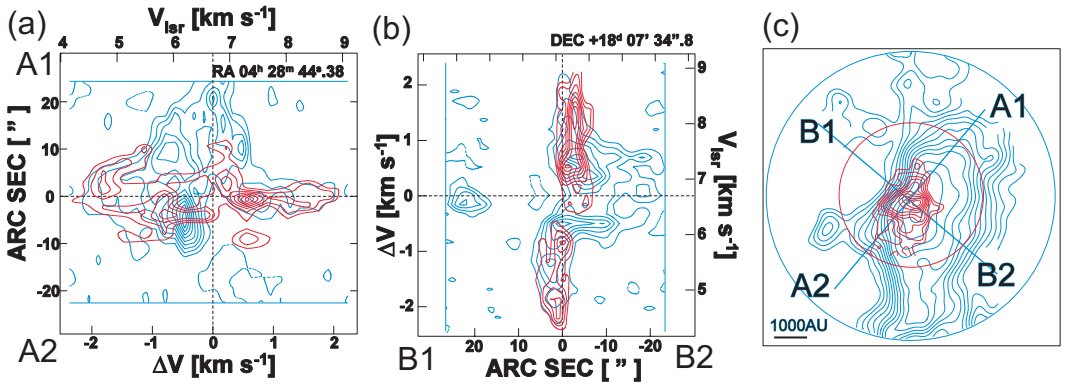

Figure 4.17: (a),(b): Superposed images of the Position-Velocity diagrams along the major and minor axes of HL Tau. Blue contours indicate the ^{13}CO ($J = 1 - 0$) emission. Red contours indicate the ^{13}CO ($J = 2 - 1$) emission. (c) Total integrated intensity maps of ^{13}CO ($J = 1 - 0$) and ($J = 2 - 1$) emissions.

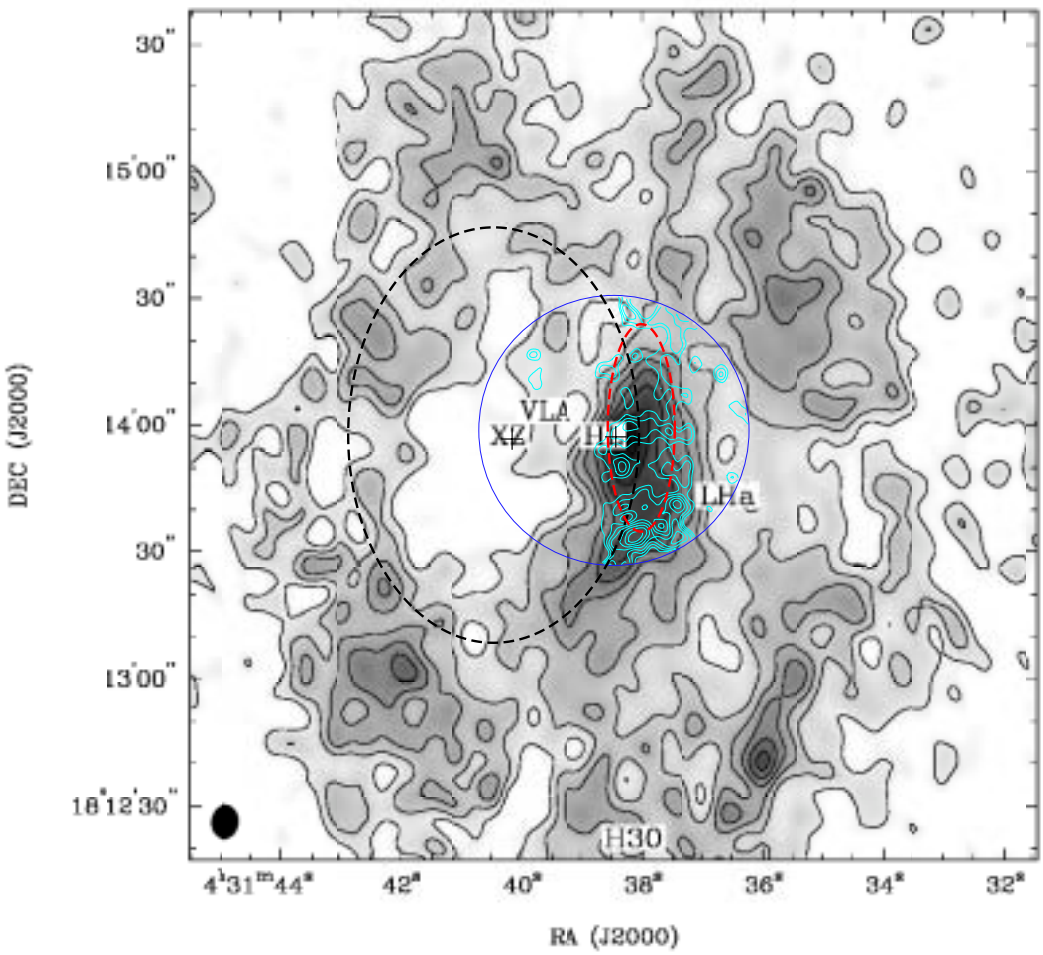

Figure 4.18: Superposed image of total intensity map of $C^{18}O$ emission onto $3' \times 3'$ ^{13}CO ($J = 1 - 0$) map around HL Tau taken with the BIMA (Welch et al. 2000).

Chapter 5

Aperture Synthesis Observations of Protostar Haro 6-5B: Discovery of the Rotating Disk and Dispersed Protostellar Envelope

A part of this chapter has been published in
The Astrophysical Journal 552, L59-L62, 2001
as
"Millimeter Continuum Image of the Circumstellar Disk around the Young Star Haro 6-5B"
by
Sozo Yokogawa[1,2], Yoshimi Kitamura[3], Munetake Momose[4], Yoshiharu Asaki[3], Motohide Tamura[2], Shigeru Ida[5] and Ryohei Kawabe[2]
(1) The Graduate University for Advanced Studies; (2) National Astronomical Observatory of Japan; (3) The Institute of Space and Astronautical Science; (4) Ibaraki University; (5) Tokyo Institute of Technology;

Abstract

Aperture synthesis observations of ^{13}CO ($J = 1 - 0$) line emission and dust continuum emission toward the class I protostar Haro 6-5B (FS Tau B) and the nearby binary T Tauri stars FS Tau A, made with the Nobeyama Millimeter Array (NMA), are presented. Millimeter continuum emission was only detected from Haro 6-5B, and it shows a disklike structure which coincides with the dark lane in the visible and near-infrared images of Haro 6-5B owing to a small synthesized beam of $1\farcs33 \times 1\farcs21$. The radius and inclination angle of the disk derived from the image are 309 ± 18 AU and $67 \pm 5°$, respectively. By model fitting of the spectral energy distribution (SED) of Haro 6-5B with these values, the power-law index of the dust opacity, β, is derived to be 1.05 ± 0.04 and the disk mass is calculated to be $0.021 \pm 0.002\,M_\odot$. No extended emission with 1000 AU scale is detected, suggesting that the envelope around Haro 6-5B has been almost dissipated. The ^{13}CO emission were detected from both the objects and shows disklike structures. The estimated masses of the structures under the assumption of optically thin conditions are 2.0×10^{-3} $M_\odot$ for Haro 6-5B and 1.8×10^{-3} $M_\odot$ for FS Tau A, respectively. The ^{13}CO emission from Haro 6-5B reveals an elongation parallel to the dust disk, and the rotational motion of 0.7 km s^{-1} at 4.0×10^2 AU in radius, which is corrected for inclination angle of 70°, is detected, whereas no infall motion along the minor axis is detected. The rotational motion requires a dynamical mass of 0.25 $M_\odot$ and the local specific angular momentum is estimated to be 1.34×10^{-3} km s^{-1} pc. Since the disk around Haro 6-5B seems to be rotationally supported and most of the infalling gases have already been dispersed, Haro 6-5B is likely a transient source from the protostar stage to the T Tauri stage.

5.1 Introduction

The formation of low-mass stars and their circumstellar disks is one of the most interesting themes in modern astronomy, because it is closely related to the origin of our solar system. Especially, it is important to study young stellar objects (YSOs) in the course of evolution from the protostar stage to the early T Tauri stage, because central stars and circumstellar disks grow by accretion of matter and their final masses are determined in these stages. The spectral energy distribution (SED) is one of good indicators of the evolution of YSOs. The SED classification divides the protostar stage into two stages of class 0 and class I. The youngest class 0 object shows a cold black-body like spectrum with its peak near $\lambda \sim$ 150-200 μm. The object is deeply embedded in the surrounding core and envelope, and is considered to be in an

active accretion phase. The next class I object shows a warmer spectrum which rises beyond 2 μm, and is probably in a late accretion phase. After these stages, the core and the infalling envelope disperse, and an optically visible classical T Tauri star (class II object) appears.

Recently, a millimeter continuum survey of protostars and classical T Tauri stars with a high angular resolution was performed by Looney et al. (2000). They revealed that protostars (class 0 and class I objects) show the dust emission dominated by circumstellar envelopes, whose radii are thousands AU, with the weak residual emission at small scales. On the contrary, emission associated with classical T Tauri stars (class II objects) mainly comes from compact disks whose radii are a few $\times$ 100 AU with the weak extended emission. These results are very important to investigate both the dissipation of the envelopes and the formation of the disks in the envelopes. However, such observations toward protostars or T Tauri stars have been made only for luminous objects, and are still insufficient.

This paper reports the results of high angular resolution, sensitive imaging of the class I object Haro 6-5B and its companion FS Tau A using the Nobeyama Millimeter Array (NMA). Haro 6-5B and FS Tau A are members of the FS Tau system in the Taurus Molecular Cloud, whose distance is estimated to be 140 pc (Elias 1978). Haro 6-5B was discovered by Mundt et al. (1984) as a Harbig-Haro object (HH157) located at the apex of the cone-like reflection nebulosity extending to the north-east, and the bipolar optical jet extends at Position Angle (P.A.) = 54° (Mundt, Brugel, & B*ü*hrke 1987). In addition, Haro 6-5B has a strong optical polarization ($\sim$ 9%) oriented at P.A. = 147 $\pm$ 7°, which is perpendicular to the jet (Gledhill, Warren-Smith, & Scarrot 1986). Recently, high angular resolution images at visible and near-infrared (NIR) wavelengths taken by the Hubble Space Telescope (HST) revealed a dark lane, which probably corresponds to a dust disk around Haro 6-5B (Krist et al. 1998; Padgett et al. 1999). The disk radius and inclination angle derived from the HST images are 250-300 AU and 70-80° (0° for face-on), respectively. Millimeter observations made by Osterloh and Beckwith (1995) and Reipurth et al. (1993) with single dish telescopes detected strong continuum emission toward Haro 6-5B, also suggesting that the circumstellar matter exists around this young star. The ^{13}CO imaging were also made by Dutrey et al.(1996), and the compact emission is detected around both Haro 6-5B and FS Tau A. However, insufficient sensitivity and velocity resolution pretend to reveal the detail spatial and velocity structure around the system.

5.2 Observations

Aperture synthesis observations of the field of Haro 6-5B and FS Tau A were carried out in the ^{13}CO($J = 1 - 0$) (110.201353 GHz) line emission and 2 mm continuum emission using the NMA, which consists of six 10 m antennas, from 1999 December to 2001 November. To detect a spatially extended gas emission, the NMA's D configuration whose projected baseline length ranges from 3 to 27 kλ was adopted for the ^{13}CO observations. On the other hand, two array configurations, D and AB, were used for the 2 mm continuum observations to achieve a high angular resolution: whose ranges of the projected baseline length are $(5-40)$ kλ and $(25-160)$ kλ, respectively. SIS receivers were employed and the system noise temperatures in DSB mode were about 150 K at 100 GHz and 250 K at 150 GHz toward the zenith. The line emission data were obtained by using a 1024 channel FX spectrocorrelator with a total bandwidth of 32 MHz, corresponding to velocity resolution of 0.084 km s^{-1} at ^{13}CO ($J = 1 - 0$) frequency. The digital spectral correlator UWBC (Okumura et al. 2000) were employed for the continuum observations. Visibility data of the continuum emission in both the lower and upper sidebands were obtained simultaneously with phase-switching technique. To obtain higher signal-to-noise ratios (S/N) of the continuum images, the data of both sidebands were combined into a final image.

The center of the field was set on the position of $(\alpha_{2000}, \delta_{2000}) = (4^h22^m00^s.69, +26^\circ57'32''.6)$. The sizes of primary beam (i.e., the field of view) were about $62''$ (FWHM) at 3 mm (^{13}CO $J = 1 - 0$) and $46''$ at 2 mm. The response across the observed passband for each sideband was determined from 30-40 minutes observations of 3C454.3. Gain calibrators 0507+179 and 0446+112 were observed as frequently as possible (every $8-10$ minutes) to minimize the phase error in the resultant image. The flux densities of calibrators were derived to be 1.8 Jy for 0507+179 at 2 mm and 2.6 Jy for 0446+112 at 3 mm, respectively, from observations of Uranus. The overall uncertainty in the flux calibration was less than 10 %. After these calibrations, we made the final image only from the data taken under excellent weather conditions. Using the AIPS package developed at the NRAO, we CLEANed the continuum map by natural weighting with no taper in the UV plane. The size of the resultant synthesized beam (HPBW) of the 2 mm continuum image in the AB + D configurations is $1''.33 \times 1''.21$ at P.A. = 134°. That of the ^{13}CO ($J = 1 - 0$) (HPBW) is $5''22 \times 4''54$. The rms noise level of the 2 mm continuum image is 2.6 mJy beam^{-1} in the clean map. Since the source size is much smaller than the field of view in the 2 mm map, the primary beam attenuation is negligible. The rms noise level of the ^{13}CO($J = 1 - 0$) map with the velocity resolution of 0.34km s^{-1} is 65 mJy beam^{-1},

corresponding to 0.27 K in T_B.

5.3 Results

5.3.1 Millimeter image of the circumstellar disk around Haro 6-5B

Figure 5.1a shows a map of 2 mm continuum emission from the circumstellar disk around Haro 6-5B superposed onto the NIR image of the same field taken by the HST/NICMOS (Padgett et al. 1999). The disk is clearly resolved by the small synthesized beam. The beam-deconvolved size of the disk (FWHM) is $2\farcs33 \times 0\farcs97$ at P.A. = 138°. After the correction for the atmospheric fluctuations (see § 3.2), the size of the disk becomes $2\farcs30 \times 0\farcs89$ (322 AU × 125 AU). Assuming a geometrically thin disk, the disk radius and inclination angle are calculated to be 161 ± 20 AU and 67 ± 5°, respectively. The total flux density of the disk is 36.7 ± 2.6 mJy. The peak position of 2 mm continuum emission is $(\alpha_{2000}, \delta_{2000}) = (04^h22^m00^s.69, +26°57'33\farcs0)$.

Our millimeter image traces well the entire disk because of the optically thin emission. Whereas, in the optically thick visible and NIR emission, the near side of the disk is seen as the dark lane and the far side as the reflection nebula (Krist et al. 1998; Padgett et al. 1999), as schematically shown in Figure 1b. The major axis of the disk (P.A. = 138 ± 7°) is almost parallel to both the dark lane (P.A. = 144°, Krist et al. 1998) and the polarization vector (P.A. = 147°, Gledhill et al. 1986), and is perpendicular to the optical jet (P.A. = 54°, Mundt et al. 1987). The relative positional error between the two images is considered to be less than $0\farcs5$. This is mainly caused by the baseline error, the finite S/N , and the atmospheric fluctuations in our millimeter observations.

3 mm continuum emission is also detected from Haro 6-5B, whose total flux densities are 12.3 ± 1.4 mJy beam^{-1} at 3.06 mm and 18.2 ± 2.0 mJy beam^{-1} at 2.73 mm, respectively. The angular resolution of each sideband image is $5''.91 \times 5''.13$ with P.A. = −70.5° at 3.06 mm and $5''.22 \times 4''.54$ with P.A. = −70.4° at 2.73 mm, respectively. Because of the lack of the angular resolutions of the 3 mm observations, the circumstellar disk recognized in the 2 mm imaging is not spatially resolved. The 3 mm peak position of Haro 6-5B is $(\alpha_{2000}, \delta_{2000})$ = $(04^h22^m00^s.70 \pm 0^s.01, +26°57'32\farcs7 \pm 0\farcs1)$, which agree with the 2 mm continuum peak position within the error. No significant emission, however, was detected at the position of the FS Tau A. 3σ upper limits of the continuum emission of FS Tau A are 1.95 mJy beam^{-1} at 3.06 mm and 2.40 mJy beam^{-1} at 2.73 mm.

5.3.2 Estimation of the atmospheric seeing size

To estimate the seeing size during our observations, we made a CLEANed map of the 141 GHz continuum emission from the gain calibrator 0507+179. The beam-deconvolved size of the calibrator in the clean map is $0\farcs41 \times 0\farcs37$ at P.A. = 74°. Since the angular size of the calibrator is considered to be much smaller than the NMA beam size ($1\farcs33 \times 1\farcs21$), the spatial extent of the calibrator in the clean map is attributed to the phase fluctuation due to the atmospheric turbulence (i.e., the seeing size toward 0507+179). We consider the size of the radio seeing disk toward Haro 6-5B is also $0\farcs39$ [$= (0\farcs41 \times 0\farcs37)^{1/2}$], though its angular distance from 0507+179 is about 15° and the integration time of the calibrator (2 minutes) is shorter than that of Haro 6-5B (4 minutes).

To check the dependence of the seeing size on the direction and the integration time, a similar analysis of the bandpass calibrator 3C454.3 has been made. The seeing size toward this object with 2 minutes integration ($0\farcs5$) is comparable to that toward 0507+179 in spite of large angular separation (85° apart from Haro 6-5B). Furthermore, the seeing size does not change even when we integrate the data in 4 minutes. These results suggest that the seeing size does not sensitively depend on the direction or the integration time. Therefore, the assumption that the seeing size toward Haro 6-5B is $0\farcs39$ would be valid.

5.3.3 ^{13}CO ($J = 1 - 0$) line emission

The ^{13}CO emission was detected between $V_{\rm LSR} = 5.1-9.5$ km s^{-1}, with a typical sensitivity of ≈ 65 mJy beam^{-1} or 0.27 K in brightness with the velocity resolution of 0.34 km s^{-1} as shown in Figure 5.2. From $V_{\rm LSR} = 4.7$ to 5.8 km s^{-1}, emission is not detected at both the stellar positions of Haro 6-5B and FS Tau A. The extended emission which distributed at the north side of Haro 6-5B is detected at 5.1 km s^{-1}, and the ridge structure which elongate along north-south direction is detected at the west side of the Haro 6-5B at 5.4 km s^{-1}. As shown in the ^{13}CO line profiles of Figure 5.3, the emission around the systemic velocity $V_{\rm sys}$ of $5.8-6.8$ km s^{-1} is weak, mainly owing to the resolving out to the extended components. From $V_{\rm LSR} = 6.1 - 6.8$ km s^{-1}, weak emission is detected from Haro 6-5B, and the peak is shifted to a few″ south-east of the continuum peak denoted by the cross marks in Figure 5.2. From $V_{\rm LSR} = 7.1 - 8.5$ km s^{-1}, the strong extended emission is detected at both the stellar positions of Haro 6-5B and FS Tau A, and is distributed at the perimeter of the reflection nebular which shown as the background image in Figure 5.4. Furthermore, the jet like structure which extends north-east direction originating from Haro 6-5B is also found at the 7.5, 7.8 and 8.1 km

s^{-1}. At the velocity range between 8.8 km s^{-1} and 9.5 km s^{-1}, the emission are detected at the position of Haro 6-5B. In contrast to the emission at the blue-shifted components (especially from 6.1 km s^{-1} to 6.8 km s^{-1} in the channel maps), the peak position of the emission is shifted about a few $''$ north-west direction toward the continuum peak position of Haro 6-5B. These 6.1-6.8 km s^{-1} and 8.5-9.5 km s^{-1} systematic features indicate the rotational motion around Haro 6-5B.

Figure 5.4 shows the total intensity map of ^{13}CO emission integrated over the velocity range of $5.1 - 9.5$ km s^{-1}. The sizes of the gas disks are derived to be 1300 × 600 AU (FWHM) for Haro 6-5B and 1300 × 860 AU (FWHM) for FS Tau A. The P.A. of the Haro 6-5B gas disk is estimated to be 150° ± 10°, which agrees with that of the 2 mm dust disk (P.A. = 138°) and is almost perpendicular to the optical jet of P.A. = 54°. The P.A. of FS Tau A of 95° ± 20° is also consistent to the polarization vector of FS Tau A of 84° within the error. Because the ^{13}CO peak position of FS Tau A is shifted about a few arcsec southward compared to the stellar position, the emission might be remained envelope components around FS Tau A.

Total mass of the gas disk can be estimated from the total integrated intensity using the following formula (Scoville et al. 1986):

$$M_{\rm gas} = 5.37 \times 10^{-5} T_{\rm ex} \exp\left(\frac{5.29}{T_{\rm ex}}\right) \frac{\tau_{^{13}\rm CO}}{1 - \exp\left(-\tau_{^{13}\rm CO}\right)} \left(\frac{d}{140\rm pc}\right)^2 \left[\frac{10^{-6}}{X(^{13}\rm CO)}\right] \int S_\nu dv M_\odot, \quad (5.1)$$

where $T_{\rm ex}$ is the excitation temperature, $\tau_{\rm 13CO}$ is the optical depth of ^{13}CO, X(^{13}CO) is the fractional abundance of ^{13}CO to H_2 and d is the distance to the source. On the simple assumption of optically thin ^{13}CO emission, i.e., $\tau_{\rm 13CO} \ll 1$, the integrated intensity of Haro 6-5B of 2.33 Jy km s^{-1} gives us the disk mass of 2.0×10^{-3} $M_\odot$ with an excitation temperature of 15K and a fractional abundance of 10^{-6}. On the contrary, the integrated intensity of FS Tau A is 2.08 Jy km s^{-1}, and the same parameters give us the estimated mass of 1.8×10^{-3} $M_\odot$. These masses must be lower limits, because the ^{13}CO emission in the disk might be optically thick.

5.4 Discussion

5.4.1 Does an extended dust envelope exist around Haro 6-5B ?

It is accepted that the dissipation of the envelope progresses from the protostar stage to the early T Tauri stage. In the case of Haro 6-5B, almost all the dust emission is found to come from the compact disk, as discussed below, and the major part of the envelope around Haro 6-5B seems to have already disappeared. This suggests that Haro 6-5B is a transient object evolving from the protostar stage to the T Tauri stage.

In order to check the presence of the dust envelope around Haro 6-5B, we first made two maps of 2 mm continuum image; one made only from the D configuration data, and the other only from the AB configuration data. Then we measured the flux density of Haro 6-5B in each map. In the D configuration, the total flux density is 34.6 $\pm$ 2.6 mJy beam^{-1} with the synthesized beam of $4\farcs47 \times 3\farcs97$ at P.A. = 127 °, and the emission from Haro 6-5B is point-like, suggesting no envelope. In the AB configuration, the disk is successfully resolved and the total flux density is 35.6 $\pm$ 3.0 mJy with the synthesized beam of $1\farcs14 \times 1\farcs04$ at P.A. = 134 °. If the envelope with $\sim$ 1000 AU size exists around Haro 6-5B and is resolved out in the AB configuration map, the flux density of the D configuration would be higher than that of the AB configuration. These two flux densities agree with each other within the errors, indicating that the major part of the extended envelope has already been dissipated around Haro 6-5B.

This idea is supported by other observations. Dutrey et al. (1996) detected the 2.7 mm dust continuum emission toward Haro 6-5B with the IRAM interferometer. The emission is point-like and its spatial extent of $\sim 0\farcs3 \pm 2\farcs0$ is compatible with our disk size. They also detected the envelope component in ^{13}CO($J = 1 - 0$) emission, but its mass was estimated to be $0.45 \times 10^{-3} M_{\odot}$. This mass is much smaller than the disk mass (see § 4.2) and consistent with our interpretation.

The flux densities at 230 GHz were measured with the IRAM 30 m and SEST 15 m telescopes (134 $\pm$ 6 mJy by Osterloh & Beckwith 1995; 141 $\pm$ 13 mJy by Reipurth et al. 1993), which never suffer from the resolving out (i.e., the missing flux problem). These emissions are also considered to come from the disk component, because the deviation of the 230 GHz data points from the best fit curve by the model fitting of the SED excluding the 230 GHz data is less than 5 %. Although the small remaining fraction might come from the residual envelope component, we do not take into account the minor component in the following discussion.

5.4.2 Physical properties of the dust disk around Haro 6-5B

The disk around Haro 6-5B is spatially resolved by the present 2 mm observations, but the insufficient spatial resolution and finite S/N does not allow us to make the complete modeling of the disk (e.g., Mundy et al.1996). We therefore estimate the radius and inclination angle of the disk based on the image prior to the model calculations in the following way: (1) The inclination angle of the disk, θ, is derived from the beam-deconvolved size of the disk; $\theta = \arccos((\text{minor axis})/(\text{major axis}))$. (2) The disk radius, $R_{\rm out}$, is determined from the equation of $R_{\rm out} = (S/\pi\cos\theta)^{1/2}$, where S is the area of the disk image which reproduces the observed flux density of 36.7 ± 2.6 mJy. (3) We subtract the seeing fluctuation of $0''.39$ from the disk assuming that both Haro 6-5B disk and seeing disk have Gaussian profiles. The resultant radius ($R_{\rm out}$) and inclination angle (θ) of the disk are 309 ± 18 AU and $67 \pm 5^\circ$, respectively, which agree with those in the HST observations. These disk radius and inclination angle are fixed in the following analysis with the power-law disk model.

The remaining parameters of the disk are determined from model fitting to the SED obtained so far. In the disk model, the surface density and temperature distributions have the power-law forms of $\Sigma(r) = \Sigma_{100}(r/100\,{\rm AU})^{-p}$ and $T(r) = T_0(r/1\,{\rm AU})^{-q}$, respectively, over the radial range of $R_{\rm in} \le r \le R_{\rm out}$ (e.g., Adams, Lada, & Shu 1988). The flux density F_ν emitted from a disk at a frequency ν can be expressed as

$$4\pi d^2 F_\nu = 4\pi\cos\theta \int_{R_{\rm in}}^{R_{\rm out}} B_\nu(T(r))(1-\exp(-\tau_\nu/\cos\theta))2\pi r dr, \tag{5.2}$$

where d is the distance to the disk (140 pc), $B_\nu(T(r))$ is the Planck function with a temperature $T(r)$, and τ_ν ($=\kappa_\nu \times \Sigma$) is the optical depth due to the dust opacity. The dust opacity coefficient κ_ν is assumed to have the relation of $\kappa_\nu = 0.1(\nu/10^{12}{\rm Hz})^\beta$ cm^{2}g^{-1} (Beckwith et al. 1990). We assume the following parameters of the central star. The effective temperature and the stellar radius are 4000 K and 0.01 AU, respectively, which are typical in protostars. The visual extinction toward Haro 6-5B, A_V, is known to be larger than 23 mag (Krist et al. 1998), and we adopt $A_V = 35$ mag to reproduce the NIR flux densities of the SED which come mainly from the central star. The best fit parameters of the disk are not seriously influenced by these stellar parameters.

Figure 5.5 shows the SED of Haro 6-5B from visible to millimeter wavelengths. The mid-infrared (MIR) and far-infrared (FIR) data (12, 25, 60, 100 μm) are those of IRAS 04189+2650 (Haro 6-5B + FS Tau A) in the IRAS Point Source Catalogue. Since the IRAS could not separate Haro 6-5B from FS Tau A with its large beam, the IRAS fluxes of Haro 6-5B are not

accurately known. It had been thought that most of the fluxes came from FS Tau A and the contribution of Haro 6-5B was negligible. We, however, consider that the contribution of Haro 6-5B may be dominant by the following reasons. (1) The millimeter observations (Osterloh & Beckwith 1995; Reipurth et al. 1993) showed that Haro 6-5B is a strong continuum source. Subsequently, the aperture synthesis observations of 2.7 mm continuum emission by Dutrey et al. (1996) detected strong emission toward Haro 6-5B and no emission toward FS Tau A. (2) The recent high-resolution observations in visible and NIR (Krist et al.1998, Padgett et al. 1999) actually revealed the disk as the dark lane in Haro 6-5B.

The model fitting to the SED is fairly good except the UV and visible wavelengths, as shown in Figure 5.6. The best fit parameters are listed in Table 1. In the most probable case of 100 % contribution of Haro 6-5B to the IRAS flux densities, the best fit parameters are as follows; $M_{\rm disk} = 0.021 M_\odot$, $\Sigma(r) = 1.1(r/100\,{\rm AU})^{-1.4}$ g cm^{-2}, $T(r) = 328(r/1\,{\rm AU})^{-0.61}$ K, $\beta = 1.05$, and $R_{\rm in} = 1.01$ AU, with the outer radius 309 AU and the inclination angle 67°. The disk mass of 0.021 $M_\odot$ is larger than the mass of ~ 0.01 $M_\odot$ derived from the HST observations by Krist et al. (1998). Because of the optically thick disk in a visible or NIR wavelength, their disk mass seems to be a lower limit. On the other hand, the optically thin millimeter emission can trace well the mass distribution in the disk. Although Dutrey et al. (1996) tried to estimate the disk parameters from their millimeter observations, the disk radius and inclination angle could not be determined owing to an insufficient angular resolution. On the contrary, our higher resolution imaging makes it possible to derive the more reliable parameters of the disk. The disk mass agrees with that in the minimum mass nebula model (Hayashi, Nakazawa, & Nakagawa 1985). The surface density at 100 AU, Σ_{100} (= 0.4-7.0 g cm^{-2}), is also consistent with the extrapolated value at 100 AU in the Hayashi model. However, we can not accurately determine the power law index p from the SED model fitting. In fact, the range of the index ($1.1 < p < 1.9$) allows both flat and steep distributions. The temperature at 1 AU, T_0 (= 328 K), is relatively hot compared with those of T Tauri stars by Beckwith et al. (1990). This means that Haro 6-5B is still in a mass accretion phase. The index β is significantly smaller than the value of the interstellar medium ($\beta \sim 2$), and is almost equal to the typical value of T Tauri stars ($\beta \sim 1$). One of the probable interpretations of $\beta \sim 1$ is the coagulation of dust particles in the circumstellar disk (Beckwith & Sargent 1991). Since Haro 6-5B is a relatively evolved class I object and most of the envelope component have already been dissipated, the dust particles in the disk around Haro 6-5B might have already coagulated into millimeter sizes. The inner radius of 1 AU ($R_{\rm in}$) seems to be considerably large. This would be mainly because our simple model does not take account of the self-shielding effect; emission at shorter

wavelengths from the inner hot part of the disk is absorbed by the outer flaring cool part, as the stellar radiation is, for a large inclination angle (Masunaga & Inutsuka 2000). The inner radius would be as small as the usual value of ~ 0.01 AU in an elaborate model including the self-shielding effect.

We discuss how the disk parameters are influenced by the ambiguity of the IRAS flux densities. Decreasing the fraction of the MIR and FIR flux densities of Haro 6-5B from 100 % to 25 %, the disk temperature at 1 AU, T_0, becomes cooler from 328 to 220 K, and as a result, the disk mass increases gradually from 0.021 to 0.037 $M_\odot$. The inner radius $R_{\rm in}$ decreases from 1 to 0.6 AU, because the gap between the MIR and NIR fluxes decreases and the strong self-shielding effect is no more needed. The other parameters of Σ_{100}, p, q, and β are almost constant for all the cases. We also consider the case that the fraction of Haro 6-5B in the IR fluxes is not constant. If the IR fraction changes from 25 % at 12 μm to 100 % at 100 μm, for example, the index q and the inner radius $R_{\rm in}$ become 0.46 and 0.3 AU, respectively. In this case, the outer part of the disk becomes relatively hot, and the disk mass decreases to 0.018 $M_\odot$. On the contrary, if the fraction changes from 100 % at 12 μm to 25 % at 100 μm, q becomes larger (0.74), and the outer part of the disk becomes cooler. As a result, the disk mass increases to 0.046 $M_\odot$. To exclude these ambiguities, high resolution MIR and FIR observations are strongly required.

5.4.3 Rotational motion of the circumstellar disk around Haro 6-5B

Figure 5.6 shows the observed ^{13}CO Position Velocity (P-V) diagram thorough the central stellar position of Haro 6-5B. Figure 5.6b, the observed P-V diagram at P.A. of 140° (B1-B2 in Figure 5.6d), shows a clear velocity gradient perpendicular to the optical jet axis. On the other hand, Figure 5.6a presents the P-V diagram along the jet axis (A1-A2 in Figure 5.6d), and the apparent velocity gradient which indicate the infall motion or outflow motion can not be found. The rotational velocity which along the major axis of Haro 6-5B is 0.7 km s^{-1} at 4.0×10^2 AU in radius, which is corrected for inclination angle of 70°. Because the north-west part is red-shifted with respect to the systemic velocity and opposite part is blue-shifted, the rotational motion is counterclockwise as look down on from the direction of the north-east side jet. The rotation around young star can be divided into two categories, one is rotationally supported disk like Keplerian disk around T Tauri stars, the other is infalling flattened envelope with non-Keplerian rotation around embedded source. The centrifugally supported disk shows the velocity which given by $V_{rot} = (GM_*/R_*)^{1/2}$, where G is the gravitational constant and

M_* is the mass contained within the radial distance R_*. On the other hand, infalling envelope with non-Keplerian rotation will show smaller velocity compared to that of Keplerian disk. If the rotational motion around Haro 6-5B is a Keplerian motion around the central mass, the required dynamical mass is 0.25 $M_\odot$ with the correction of the inclination angle of 70 °. The solid curved line in Figure 5.6(b) is best fitted, which trace the Keplerian rotation with 0.25 $M_\odot$, with the inclination angle of 70 °. The local specific angular momentum of Haro 6-5B is 1.34×10^{-3} km s^{-1} pc.

5.4.4 Age estimation of Haro 6-5B

Next, we estimate the age of Haro 6-5B. The total luminosity of Haro 6-5B is derived to be 1.02 $L_\odot$ from the spectral energy distribution with the infrared fluxes of IRAS 04189+2650. Because of the low angular resolution of the IRAS, the IRAS fluxes contains both the fluxes of Haro 6-5B and FS Tau A. Although the contribution of IRAS fluxes of Haro 6-5B contains ambiguity, we regarded the most of the IRAS fluxes come not from FS Tau A but from Haro 6-5B by following reasons: 1) the intensity at millimeter wavelength of Haro 6-5B is much stronger than that of FS Tau A. 2) The HST image reveals the existence of the dusty circumstellar disk around Haro 6-5B. So, the total luminosity of 1.0 $L_\odot$ of Haro 6-5B is reliable.

Because the circumstellar disk mass within the radius of 300 AU which derived from the continuum observation is $\sim$ 0.02 $M_\odot$, the central stellar mass is estimated to be 0.23 $M_\odot$. Haro 6-5B is in the accretion phase, and the bolometric luminosity can be interpreted as the accretion luminosity. The relation ship of the luminosity and the mass accretion rate is following;

$$L_\odot = \frac{GM_* dM/dt}{2R_*}, \tag{5.3}$$

With the typical central stellar radius of 0.01 AU ($\sim 2.3 R_\odot$) and the luminosity above, the mass accretion rate of Haro 6-5B is estimated to be 6.2×10^{-7} M$_\odot$. If the mass accretion is assumed to be steady in protostellar phase, the age of Haro 6-5B is estimated to be 3.6×10^5 years. Calvet et al. (2000) showed that mean accretion luminosities of class I sources in Taurus and ρ Oph are 10 - 20 % of the mean bolometric luminosities. So the reduced accretion luminosity of Haro 6-5B is about 0.15 $L_\odot$. In the case of the accretion luminosity we adopt, the mass accretion rate of Haro 6-5B is estimated to be 9.3×10^{-8} M$_\odot$, suggesting that the age of Haro 6-5B estimated to be 2.4×10^6 years.

Although Haro 6-5B is thought to be in a protostar phase, the extended envelope components have been dissipated and only the trace of the envelope is found as the reflection nebula in NIR and visible wavelengths. The estimated age is relatively large compared to the typical protostar age of 10^5 years, and is consistent to our claim that Haro 6-5B is a transient source from a protostellar phase to T Tauri star phase. Since an early protostar phase seem to be in a much active mass accretion phase, the real age of Haro 6-5B might be much younger.

5.4.5 Comparison between the ^{13}CO emission and the reflection nebula

The distributions of the ^{13}CO emission and the reflection nebula of the region show good anti-correlations. In visible and near-infrared wavelengths, the hourglass structure centered on Haro 6-5B can be seen, suggesting that the outflow activities of Haro 6-5B has excavated a cavity and scattered lights of inner wall of the cavity is seen as the reflection nebula. The conical nebula, which called R1 (following a nomeclator of Krist et al. 1998), is extended to the north-east direction and is interrupted as the limb-brightened cavity wall of the outflow. The opening angle of the conical nebula, R1, is estimated to be about 75 ° (Krist et al. 1998). Since the circumstellar disk of Haro 6-5B is nearly edge-on whose inclination angle of the disk is estimated to be 13 ° (Krist et al. 1998) and 23 ° (Yokogawa et al. 2001), the near side of the conical flow is located at the near side toward the plane of the sky and the far side flow is located at far side toward the plane of sky. The ^{13}CO blue-shifted emission at 5.1 km s^{-1} is located at north-east of Haro 6-5B, where the R1 nebula becomes opaque in the NIR image, suggesting that the ^{13}CO emission is distributed in front of R1 nebula hides the nebula as is shown in Figure 5.7(a). The 5.4 km s^{-1} components of ^{13}CO emission distributes at the west side of Haro 6-5B along north-south direction and is distributed outside of the hourglass structure in the NIR image, suggesting that the emission can be interpreted as the remained cavity wall components. Around systemic velocity of 7.0 km s^{-1}, the ^{13}CO emission shows the conical flow with the wider opening angle of $\sim$ 100 °. These components seem to trace the outside of R1 nebula, whose opening angle of 75°. At around 7.8 km s^{-1}, the red-shifted emission, the jet like emission can be found. This structure might be far side component of the ^{13}CO cavity wall or ^{13}CO outflow. The schematic illustration of possible distributions of ^{13}CO gases us summarized in Figure 5.7.

5.4.6 Are FS Tau A and Haro 6-5B gravitationally bounded ?

The FS Tau system is a binary system containing FS Tau A and Haro 6-5B whose separation of ∼3000 AU. To examine the system is gravitationally bound or not, the P-V map along Haro 6-5B and FS Tau A at the P.A. of 107 ° are shown in Figure 5.6c. The systemic velocity of each object is 7.0 km s^{-1} for Haro 6-5B and 7.7 km s^{-1} for FS Tau A, respectively, and the separation angle of both peak emission is roughly 23″ (3200 AU).

The dynamical mass of Haro 6-5B is estimated to be 0.25 $M_{\odot}$ from the Keplerian motion around Haro 6-5B as mentioned above. The mass of FS Tau A is estimated to be as follows: FS Tau A is a closed binary system consisting of FS Tau E and FS Tau W. The most reliable mass estimation of the system is derived from the proper motion measurements of the binary stars. Simon et al. (1992) observed the system and derived a separation angle of 0″.265 ± 0″.005 at P.A. = 60° ± 5° using data from 1989 March and September. After six years from Simon's observations, Krist et al.(1998) observed the system with the HST and derived a separation angle of 0″.239 ± 0″.005 at P.A. = 84° ± 2°. These observations suggest that the binary mass of FS Tau A of 1.5 $M_{\odot}$. As the results, the total mass of FS Tau system is estimated to be 1.8 $M_{\odot}$. The Keplerian rotational velocity of 1.8 $M_{\odot}$ with 3200 AU separation is 0.71 km s^{-1} ($i = 90°$) and 0.61 km s^{-1} ($i = 60°$). If the rotational plane of FS Tau A and Haro 6-5B is nearly edge-on, both the YSOs might be gravitationally bounded.

5.5 Summary

We have carried out the ^{13}CO ($J = 1 - 0$) line emission and 2 mm continuum emission observations of the field of Haro 6-5B. Our main results are summarized as follows:

1. The 2 mm continuum observations clearly resolved the circumstellar disk around Haro 6-5B, whose radius and inclination angle are estimated to be 309 ± 18 AU and 67 ± 5°. Since no 1000 AU scale emission is detected, most of the envelope around Haro 6-5B might have been dispersed.

2. The SED model fitting of Haro 6-5B using the disk geometry data shows that the disk mass of 0.021 ± 0.002 $M_{\odot}$ and the dust opacity index, β, of 1.05 ± 0.04.

3. The ^{13}CO emission are detected both from Haro 6-5B and FS Tau A whose size of 1300 × 600 AU and 1300 × 900 AU, and the mass of 2.0 × 10^{-3} $M_{\odot}$ and 1.8 × 10^{-3} $M_{\odot}$, respectively.

4. The rotational motion around Haro 6-5B is detected. The rotational velocity of 0.7 km s^{-1} at 400 AU in radius can be interpreted as the Keplerian rotation around the dynamical mass of 0.25 $M_{\odot}$ with the correction of the inclination angle of 70°.

5. Judging from the rotational motion of the ^{13}CO gas and the compact circumstellar dust disk, Haro 6-5B seems to be a transient source from the protostar phase to the classical T Tauri phase.

CHAPTER 5. TABLE

Table 5.1: Best fit parameters of the disk around Haro 6-5B. The 1st column shows the fraction of Haro 6-5B in the IRAS fluxes.

fraction	$M_{\rm disk}$ $[M_\odot]$	Σ_{100}[g cm^{-2}]	p	T_0 [K]	q	β	$R_{\rm in}$ [AU]
100%	0.021±0.002	1.1 [0.4-7.0]	$1.4^{+0.5}_{-0.2}$	328±3	0.61±0.01	1.05±0.04	1.01±0.04
75%	0.023±0.002	0.9 [0.4-6.6]	$1.4^{+0.5}_{-0.2}$	302±3	0.61±0.01	1.03±0.04	0.90±0.05
50%	0.026±0.002	1.1 [0.4-7.6]	$1.4^{+0.5}_{-0.2}$	270±4	0.61±0.01	1.01±0.04	0.78±0.06
25%	0.037±0.003	1.2 [0.4-7.6]	$1.3^{+0.5}_{-0.2}$	220±6	0.61±0.01	1.01±0.04	0.59±0.09

CHAPTER 5. FIGURES

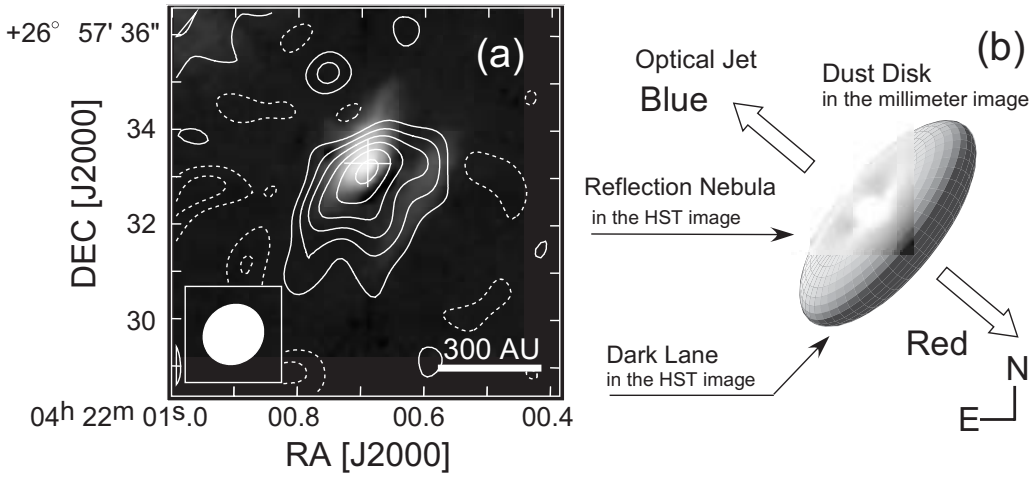

Figure 5.1: (a) Contour map of 2 mm continuum emission around Haro 6-5B with the AB+D configurations of the NMA superposed on the NIR image in gray scale taken by the HST/NICMOS (Padgett et al. 1999). The peak of the 2 mm continuum emission is located at (α[2000],δ[2000]) =(4^h22^m $00^s.69$, +26° 57′ 33.″0). The cross mark indicates the peak position of the NIR emission, (α[2000],δ[2000]) = (4^h 22^m $00^s.69$, +26° 57′ 33.″3) (Padgett et al. 1999). The white circle at the bottom left-hand corner is the synthesized beam. The contour intervals are 1σ, starting at $\pm1\sigma$ (1σ = 2.6 mJy beam^{-1}). Negative contours are shown in dashed lines. (b) Schematic illustration of the circumstellar disk around Haro 6-5B.

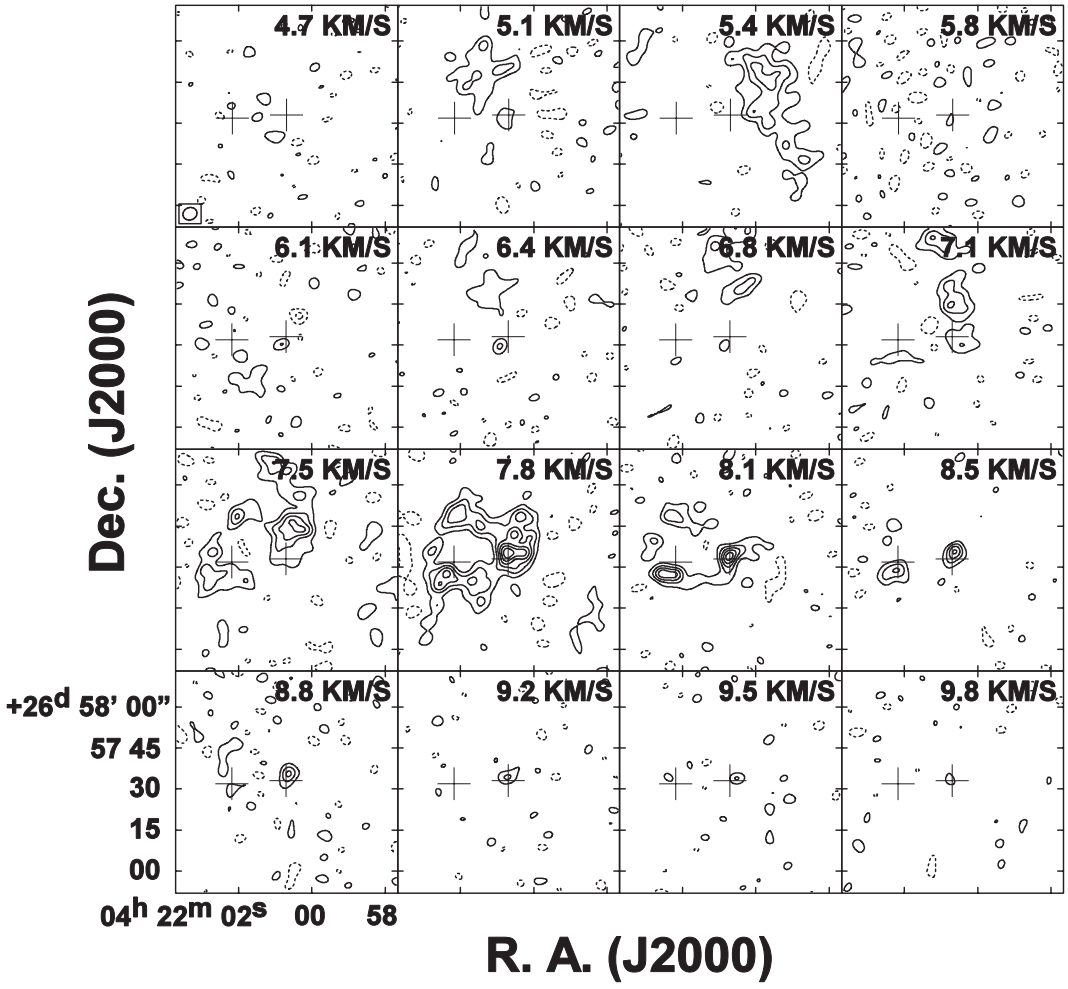

Figure 5.2: Channel velocity maps of ^{13}CO(1-0). Corresponding LSR velocities are denoted in the top-right corner in each panel. Contours intervals are 1 σ, starting at $\pm$ 2 σ. The 1 σ level corresponds to 65 mJy beam^{-1} with the velocity resolution of 0.34 km s^{-1}. The open circle at the top left panel indicates the beam size in FWHM.

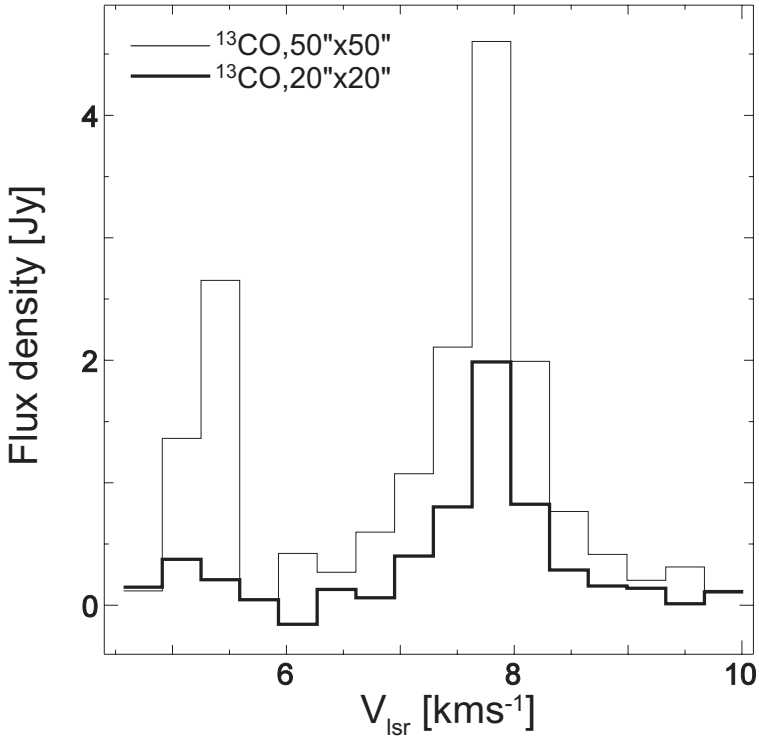

Figure 5.3: ^{13}CO(J=1-0) line profiles taken with the NMA. These profiles are integrated over a square region of $50'' \times 50''$ (thin line) and $20'' \times 20''$ (thick line) around Haro 6-5B.

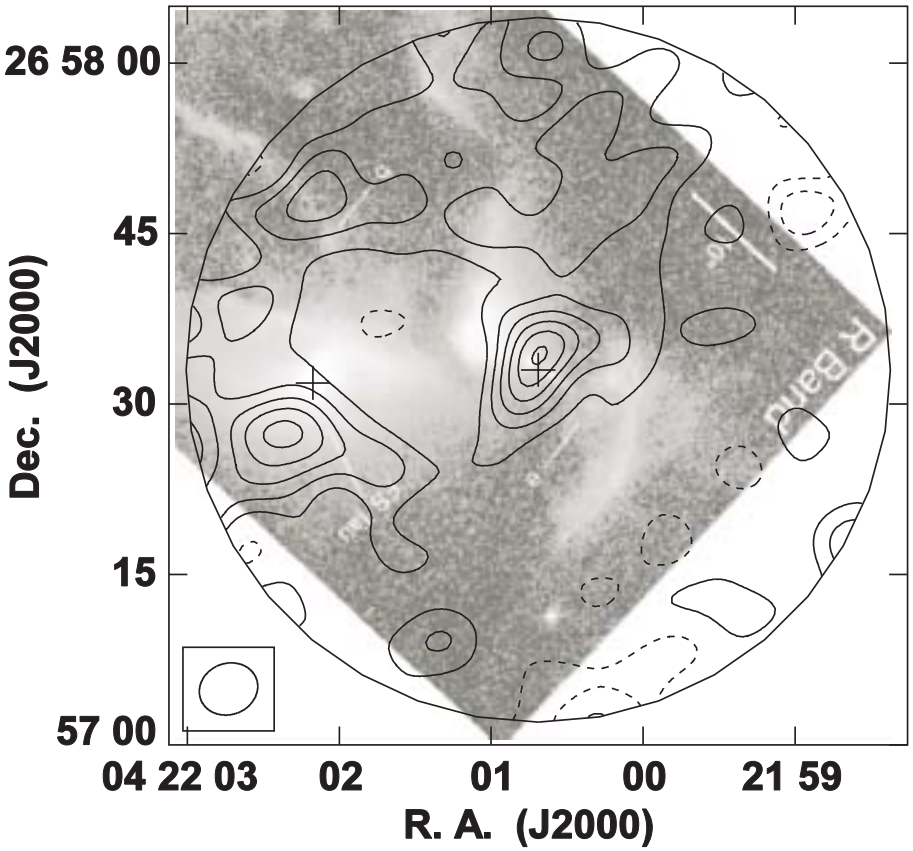

Figure 5.4: The superposed ^{13}CO(J=1-0) integrated image of Haro 6-5B and FS Tau A onto the R-band image taken by the HST (WFPC2 F675W). The ^{13}CO emission is integrated in the velocity range of 5.1-9.5 kms^{-1}. The 1 σ level corresponds to 18.3 mJy beam^{-1}. Contours are drawn every 2 σ level from 2 σ level for the positive contours (solid lines), and from the -2 σ level for the negative contours (dashed lines). The primary beam collection is applied. Total integrated intensity of Haro 6-5B is 2.33 Jy km s^{-1} and that of FS Tau A is 2.08 Jy km s^{-1} and the extended emission has the intensity of 6.99 Jy km s^{-1}.

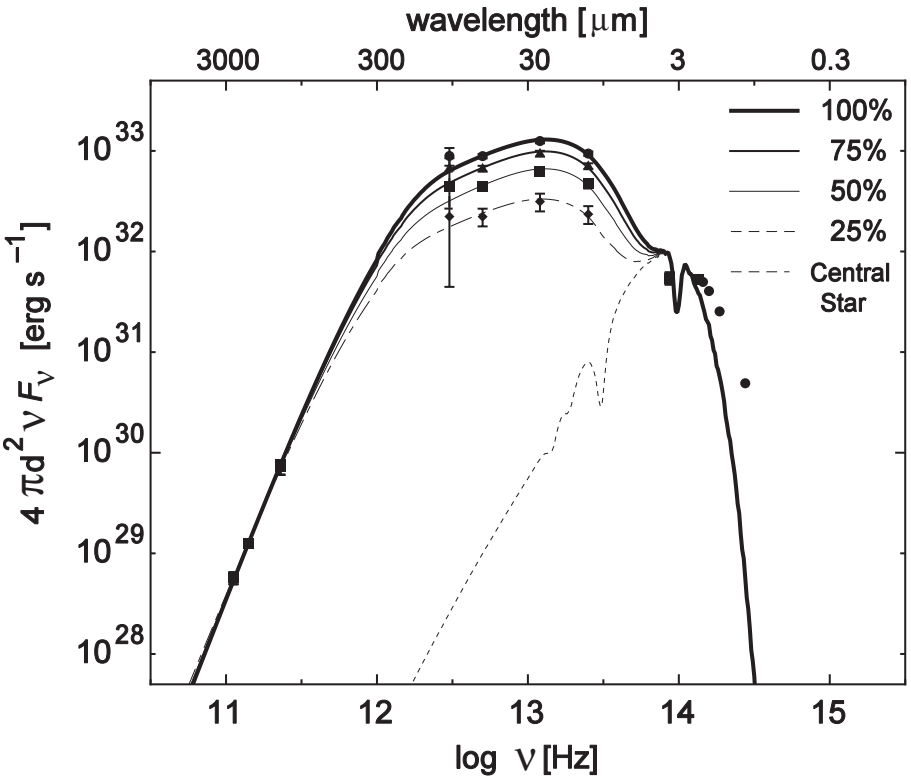

Figure 5.5: Spectral energy distribution (SED) of Haro 6-5B. The data points with error bars are compiled from Padgett et al. (1999), Vrba & Rydgren (1985), Kenyon & Hartmann (1995), Storm et al.(1989), Osterloh & Beckwith (1995), Reipurth et al. (1993), Dutrey et al. (1996), and our study. The thick solid line indicates the best fit curve in the case of 100 % contribution of Haro 6-5B to the IRAS fluxes of IRAS 04189+2650. The other best fit lines indicate the cases of 75 %, 50 % and 25 % contributions from Haro 6-5B, where the remaining fractions are from FS Tau A. The emission only from the central star is also shown by a broken line, and there are absorption features of water ice and silicate at 3 and 10 μm, respectively.

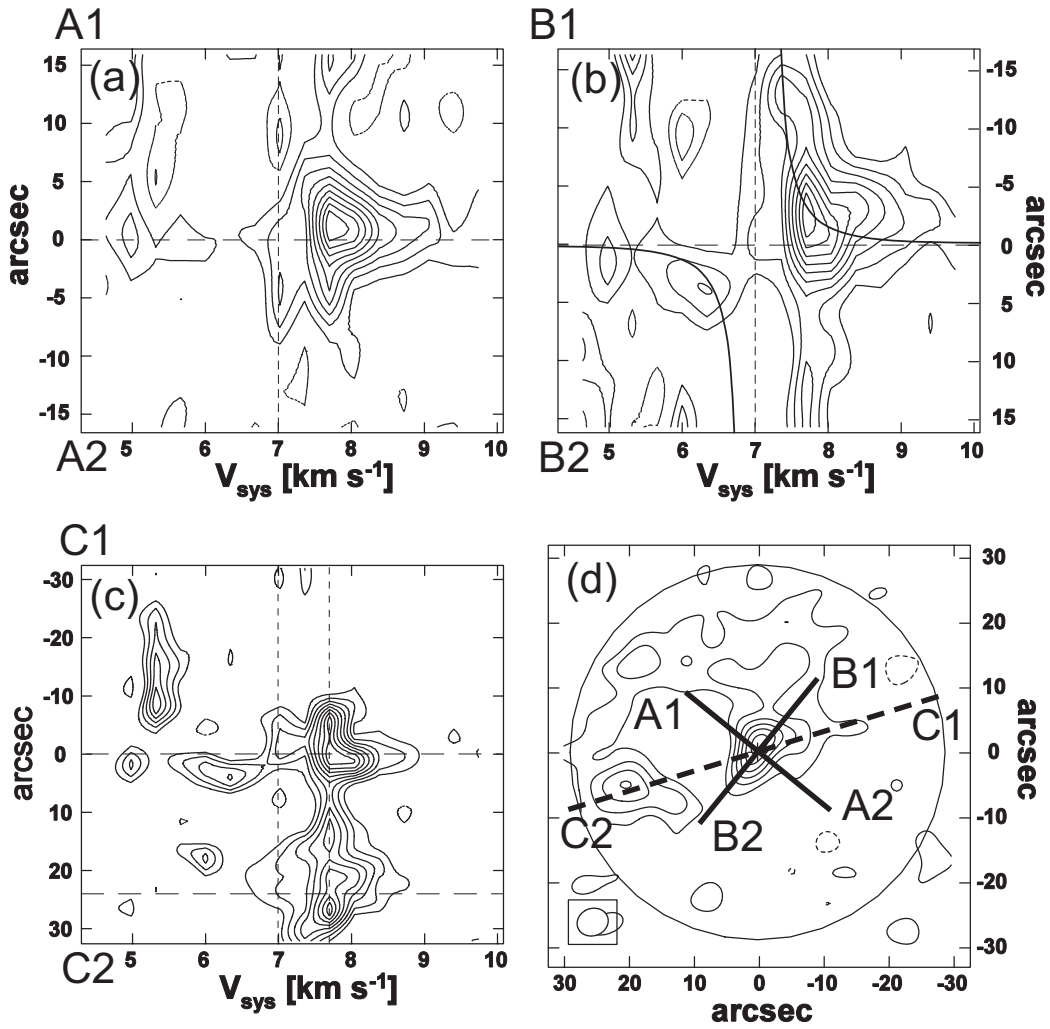

Figure 5.6: Position velocity diagrams (a),(b),(c) of the ^{13}CO ($J = 1 - 0$) emission along 3 different cuts shown in the ^{13}CO integrated map (d). The contour intervals are drawn in step of 10% of the peak intensity from 0% to 100%. The velocity resolution is 0.34 km s^{-1} and the spatial resolution is about 5 $''$. (a) The P-V diagram along the minor axis of Haro 6-5B disk. Vertical and horizontal dashed lines indicate the position of Haro 6-5B and the systemic velocity of 7.0 km s^{-1} of Haro 6-5B. (b) The P-V diagram along the major axis of Haro 6-5B disk. Vertical and horizontal dashed lines are the same meaning as (a). The thick curves demonstrate the radial velocity distribution of a Keplerian motion with the dynamical mass of 0.25 $M_\odot$ with the assumption of the inclination angle of the disk of 70 °. (c) The P-V diagram along Haro 6-5B and FS Tau A. Vertical and horizontal dashed lines are the same meaning as (a): the systemic velocity of FS Tau A is assumed to be 7.7 km s^{-1}. The projected distance between sources is $\sim$ 3200 AU.

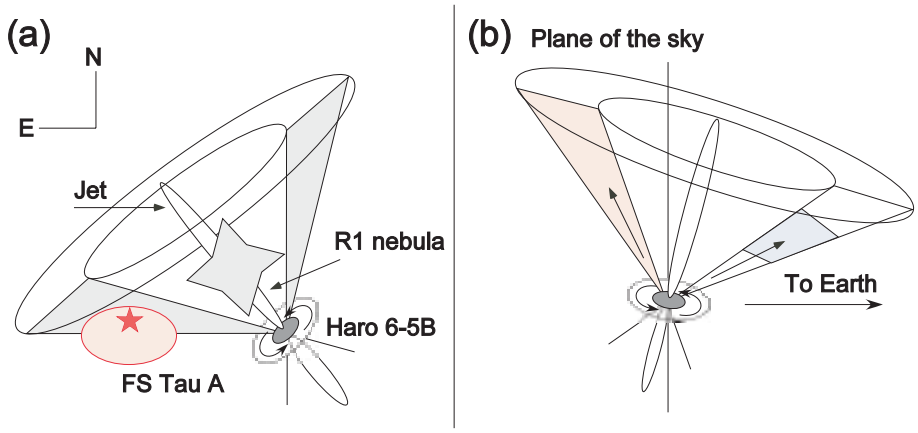

Figure 5.7: Schematic illustrations of the FS Tau system. (a) Front view of the system. The hatched area represents the ^{13}CO gas distributions. (b) Side view of the system. The near-side of the conical flow to the Earth corresponds to blue-shifted components and the far-side to the Earth corresponds to red-shifted components.

Chapter 6

Discussion and Conclusion: Formation Process of Protoplanetary Disks in Protostellar Envelopes

The observational results of individual sources are summarized in the previous chapters. In this chapter, we discuss what becomes clear according to our researches in addition to the previous scenario of low-mass star formations.

- In the chapter II, we suggested the possibility of outflow-induced star formation in a low-mass star forming region. It seems to be one factor which induces the diversity of a low-mass star and planetary system formation.

- In the chapter III, we performed the high angular imagings of the closed-binary protostar L1551 IRS 5 and revealed that the presence of a just forming rotating disk which embedded in the envelope. This is the first case which succeeds to directly detect a rotationally supported disk (circumbinary disk, strictly) in an infalling envelope. The deduced rotation radius of the circumbinary disk around IRS 5 have been revealed considerably larger than the radius expected from the local specific angular momentum of the envelope.

- In the chapter IV, we performed the imaging observations of the single protostar HL Tau, which is more evolved than IRS 5 (Flat T Tauri spectrum star), to detect a rotation disk in the envelope. However, only a little rotation motion has been detected even in the envelope and no rotationally supported disk has been found, suggesting that the infalling envelope around HL Tau has a small local specific angular momentum and the expected circumstellar disk is likely small. If a protostar with small angular momentum of an envelope produce a single star with a small protoplanetary disk, the comparative studies of the kinematics of envelopes (i.e., initial conditions of protoplanetary disk formation) are important to understand a formation process of a protoplanetary disk and a single or binary systems.

- In the chapter V, we performed the imaging observations of protostar Haro 6-5B, and have revealed the presence of a Keplerian rotating disk with a tiny envelope, suggesting that Haro 6-5B is a transient source from protostar phase to T Tauri phase. Since the rotation radius of Haro 6-5B is comparable with that of IRS 5, suggesting that Haro 6-5B is a binary system although it might be diversity of angular momentum of an envelope.

6.1 General Discussion

6.1.1 Triggered Star Formation in a Low Mass Star-Forming Region: Diversity of Initial Conditions of Protoplanetary Disk Formation

The formation of massive stars in OB associations is thought to occur in a sequential manner of star formation moves along the galactic plane from what was presumably one edge of a primordial cloud to its center or the other edge of the cloud (e.g., Elmegreen & Lada 1977). The evidence for such a progression is available from observations of the OB associations (Blaauw 1991). In giant molecular clouds, the interaction of newly formed massive stars is likely to trigger neighboring star formation. The intense UV radiation and stellar winds from the massive stars heat and compress the neighboring material, causing photo-dissociation regions (PDRs) through out the cloud. Not only massive stars, but also some low mass stars are recently thought to be occur sequentially. Recent studies have revealed that dozens of parsec-scale HH flows driven by low-mass young stars. They are thought to disrupt surrounding molecular cloud cores and drive supersonic turbulence (Reipurth et al. 1997; Reipurth & Bally 2001). Consequently, outflows can play important roles in neighboring star formation even in the case of low-mass star formation.

Our observational studies of the protostar L1551 NE have directly revealed an evident interaction between NE itself and the outflow from L1551 IRS 5 which is located $\sim 2''$ west of NE. Clear deceleration feature of CS gas around NE suggests the impact of the outflow to the natal core of NE, and the dynamical timescale of the interactions is consistent to the age of NE. This is the first case of a triggered star formation in low-mass star forming regions. However, a probablity of successive star formations which will be triggered by the NE outflow, as those in the OB associations, are not high, since the triggered formation of NE has arisen from the luck that both the protostar's positions and the direction of the outflow of IRS 5 was exquisite. The other important feature of the outflow-triggered star formation is a cause of diversity such as the disk mass, size and angular momentum, since the outer envelope components around NE seems to have been blown off by the outflow of IRS 5. As a result, although NE is a class 0 protostar, the circumstellar materials exhibit very high compactness compared to other class 0 objects even class I objects as shown in Figure 6.3.

6.1.2 Formation Process of a Protoplanetary Disk in an Infalling Envelope

Local Specific Angular Momentum

We compare the local specific angular momenta of the low-mass protostars compiled from the previous observations and our results as shown in Figure 6.4. Figure 6.4 shows that local specific angular momenta of the dense cores systematically decreases with decrease of the radii of the cores and it becomes almost constant of 10^{-3} km s^{-1} pc for the infalling envelopes around protostars and rotationally supported disks around T Tauri stars as suggested by Ohashi et al. (1997). Although the specific angular momenta of infalling envelopes and rotational disks remain almost constant at 10^{-3} km s^{-1} pc within the scale of 0.03 pc ($\approx$ 6000 AU), there is no systematic difference of the local specific angular momenta between single stars and binary systems.

The expected sizes of the rotational supported disk (i.e., protoplanetary disk) can be estimated from the following equation:

$$R_{\rm cen} = (R_{\rm env} V_{\rm rot})^2 / G M_{\star}, \tag{6.1}$$

where $R_{\rm env}$ is the radius of the envelope and G is the gravitational constant. With the typical mass of the YSOs of 0.5 $M_{\odot}$ in the Taurus Molecular Cloud, the local specific angular momentum of 10^{-3} km s^{-1} pc gives the radius of $R_{\rm cen} \approx 100$ AU of a Keplerian disk. The local specific angular momentum of 3×10^{-4} km s^{-1} pc gives 10 AU and that of 3×10^{-3} km s^{-1} pc gives 1000 AU disks, as indicated by the dashed lines in Figure 6.4. Almost all the data of YSOs with infalling envelopes and rotation disks are placed between these ranges. Although the cause of the diversity is still unsolved problem, magnetic fields, thermal conditions and initial masses and densities of the protostellar cores might be affected to the diversity of the YSOs circumstellar conditions. Another possibility is the effect of the dissipation of the envelope by the neighbor outflow activities as reported in chapter I. Since there is no apparent differences between single YSOs and binary YSOs, the formations of binary systems are not determined by the amount of the angular momenta of the parent envelopes, but small disturbances which can not be observed might determine binary systems or single stellar systems. Theoretical studies of protostellar cores under almost virial equiriburium condition suggest that it depends on the rotation law and angular velocity of a cloud core whether fragmentation of a core take places or does not happen (e.g. Matsumoto & Hanawa 2003), and it seems difficult to determine whether binary systems are formed or single systems are formed from the current

observations.

Next, we discuss about the rotational motion of L1551 IRS 5. Figure 6.5 shows the radial dependence of the rotation motion and radius of the circumstellar disk or envelope. The dashed line indicates the rotation law of $V_{\rm rot} = 0.24$ km s^{-1} $\times (R/700{\rm AU})^{-1}$, the data of the rotation motion of the envelope show good agreements. Since the expected central mass of IRS 5 ranges from $0.5 - 1.4 M_{\odot}$ from our observations and that derived from the proper motion measured with the VLA indicates the mass of 1.2 $M_{\odot}$, the centrifugal radius of IRS 5 is expected to be $\sim$ 50 AU, suggesting that the detected radius of the rotation disk in ^{13}CO ($J = 2 - 1$) emission is considerable large. The turbulent viscosity with a large coefficient of $\alpha \sim 1$ is likely to make a small disk with the centrifugal radius efficiently expand, whereas the gravitational interaction between the disk and the binary sources would not be efficient. Another possibility is the inhomogeneous rotation law of the initial cloud core of IRS 5: the inner part of the core which had formed the circumbinary disk, rotate rapidly, whereas the outer part of the core, which is now observed as infalling envelope, rotate moderately.

Comparison of Outflow Momenta between Single and Binary Systems

Our observations of L1551 IRS 5 and HL Tau have revealed that the rotating disk around IRS 5 shows considerably larger than the centrifugal radius, whereas that around HL Tau can not be detected, might suggesting that the disk is as small as the centrifugal radius. Since L1551 IRS 5 and HL Tau consist of a binary and a single stellar system, respectively, the difference of the size of their disks, large rotating disk around IRS 5 and small rotating disk around HL Tau, might be caused by the difference of the angular momentum of the envelope. The comparison of the local specific angular momenta, however, shows no apparent differences exist between single stars and binary stars.

To reveal the difference of the formation process of the circumstellar disks around IRS 5 and HL Tau, we compared the momentum of the outflows. Since the angular momentum of infalling envelope or rotating disk between binary and single system can not be found, there might exist some difference of outflowing momentum: e.g., single stellar systems have much powerful outflowing gases than those of binary systems. In Figure 6.6, we show the relations between outflow's activities and bolometric temperature of YSOs compiled from Furuya et al. 2003. Closed-binary stars which we observed, L1551 IRS 5, L1551 NE, and the close-binary protostar L1527 are denoted as the filled squares. The triangles indicate upper-limits. Although we expect that outflow activities of single stars are more active than those of binary

systems, no correlation is found between the outflow activities which normalized bolometric luminosities, $L_{\odot}$, and bolometric temperatures. Preferablly, the outflow activity of L1551 IRS 5 is stronger than that of typical YSOs. The trend that outflow activities clam down as their evolution, which previously reported, can be reconfirmed.

Finally, we discuss about a large Keplerian rotating disk radius around Haro 6-5B. The circumstellar disk radius of Haro 6-5B is 400 AU in ^{13}CO ($J = 1 - 0$) emission and 300 AU in 2 mm continuum emission, suggesting that the radius is comparable to IRS 5 rather than HL Tau. Although there is no high angular resolution cm continuum observation made with such as the VLA, Haro 6-5B is believed to be a single star. The reasons why Haro 6-5B has a large rotating disk are: 1) Since Haro 6-5B is more evolved than IRS 5 and HL Tau judging from the compact gas disklike structure without an envelope, there is enough time to expand from a small disk to a few $\times$ 100 AU disk with a large viscosities. 2) As shown in Figure 6.4, the local specific angular momenta of the YSOs have a diversity about one order of magnitude. Haro 6-5B might be formed from a stellar system which possess large angular momentum in an envelope. 3) Since the geometry of Haro 6-5B is nearly edge-on, it is difficult to judge whether disklike structure around Haro 6-5B has infall motion or not. Haro 6-5B might exhibit infall motion. 4) The most simple way of explanation, Haro 6-5B is a binary system. To answer the questions, high angular resolution imagings are required.

6.2 Conclusion

We carried out the aperture synthesis observations toward four protostars in the TMC region to reveal the formation processes of protoplanetary disks in protostellar envelopes. We here 5summarize our main results of this thesis.

- Low-mass star forming regions, such as the Taurus Molecular Cloud (TMC), has been regarded as a site where star formation occurs spontaneously: the formation of each star progresses in an isolated environment. Our high sensitive CS ($J = 2 - 1$) and ($J = 3 - 2$) imagings of protostar L1551 NE have revealed that the formation of L1551 NE is strongly affected by the outflow of the nearby protostar L1551 IRS 5, suggesting that the formation of L1551 NE is plausible to be triggered by the outflow of L1551 IRS 5. This is the first case of the outflow-induced star formation in the Taurus star forming region. We believe that this new formation scenario of low mass stars provide diversities of the physical properties of low-mass star formation such as disk sizes, masses, angular

momenta of star and protoplanetary disk systems.

- ^{13}CO ($J = 1-0$) and ($J = 2-1$) observations of L1551 IRS 5 have revealed the presence of rotation disk embedded in the infalling envelope. The obtained image indicates that the disk radius is considerably larger than the centrifugal radius which estimated from the angular momentum of the envelope of L1551 IRS 5. These results might suggest that some mechanism which extend the disk radius from the centrifugal radius to the observed radius exist in protostellar phase. Another possibility is the gases which form rotating disk have larger angular momentum than that forms envelope which now observed as an infalling envelope. These results might suggest the inhomogeneous rotation motion in the protostellar core.

- ^{13}CO observations of HL Tau can not be detect any rotating disklike structure, suggesting that circumstellar disk around HL Tau is smaller than that around L1551 IRS 5. Since the centrifugal radius which estimated from the rotation motion of the envelope is smaller than the upper-limit of the rotating disk size around HL Tau, much high angular resolution imaging of ^{13}CO ($J = 2 - 1$) or much higher J transition observations are strongly required. In addition, C^{18}O gases around HL Tau shows clumpy and dissipated distribution, suggesting that the dense envelope components around HL Tau has already dissipated.

- ^{13}CO ($J = 1 - 0$) observations of Haro 6-5B can not detect widely spread ($\sim$ a few $\times$ 1000 AU scale) envelope structure but compact disklike structure whose radius of 400 AU. The disklike structure exhibits rotational motion without infall or outflow motions, suggesting that the infalling envelope has already dissipated. Since the estimated disk radius is larger than that around single stars such as HL Tau, might indicate Haro 6-5B is a binary system.

In this thesis, I performed detailed obaservational studies of individual protostars in the Taurus Molecular Cloud. Our results suggest the disagreement of the rotating supported disk radius and the centrifugal radius estimated from the rotation motion of the envelope toward the binary protostar L1551 IRS 5, whereas the rotating disk around the single protostar HL Tau seems to be as small as the centrifugal radius, although we can not detect any rotating supported disklike structure around HL Tau mainly owing to insufficient angular resolutions of our observations. To probe into a problem of formation processes of protoplanetary disk around low-mass young stars, a large number of samples of ^{13}CO ($J = 2 - 1$) or much higher

transition observations are strongly required. Such observations toward low-mass YSOs are very important theme in modern astronomy, especially star formation studies.

CHAPTER 6. FIGURES

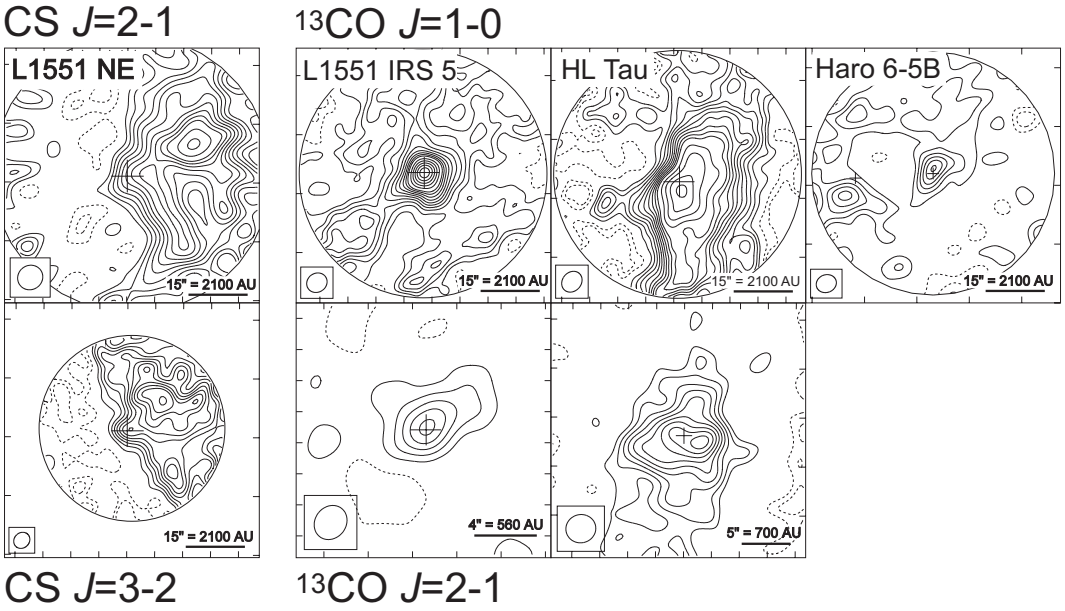

Figure 6.1: Summary of total intensity maps of four protostars, L1551 NE, L1551 IRS 5, HL Tau and Haro 6-5B. The contour intervals of CS $J = 3 - 2$ and $J = 2 - 1$ emissions of L1551 NE and ^{13}CO $J = 1 - 0$ emissions of L1551 IRS 5 and HL Tau are 2 σ levels until 20 σ, and the intervals become 4 σ above 20 σ. The contour lines of other maps start at $\pm$ 2σ levels with intervals of 1 σ levels.

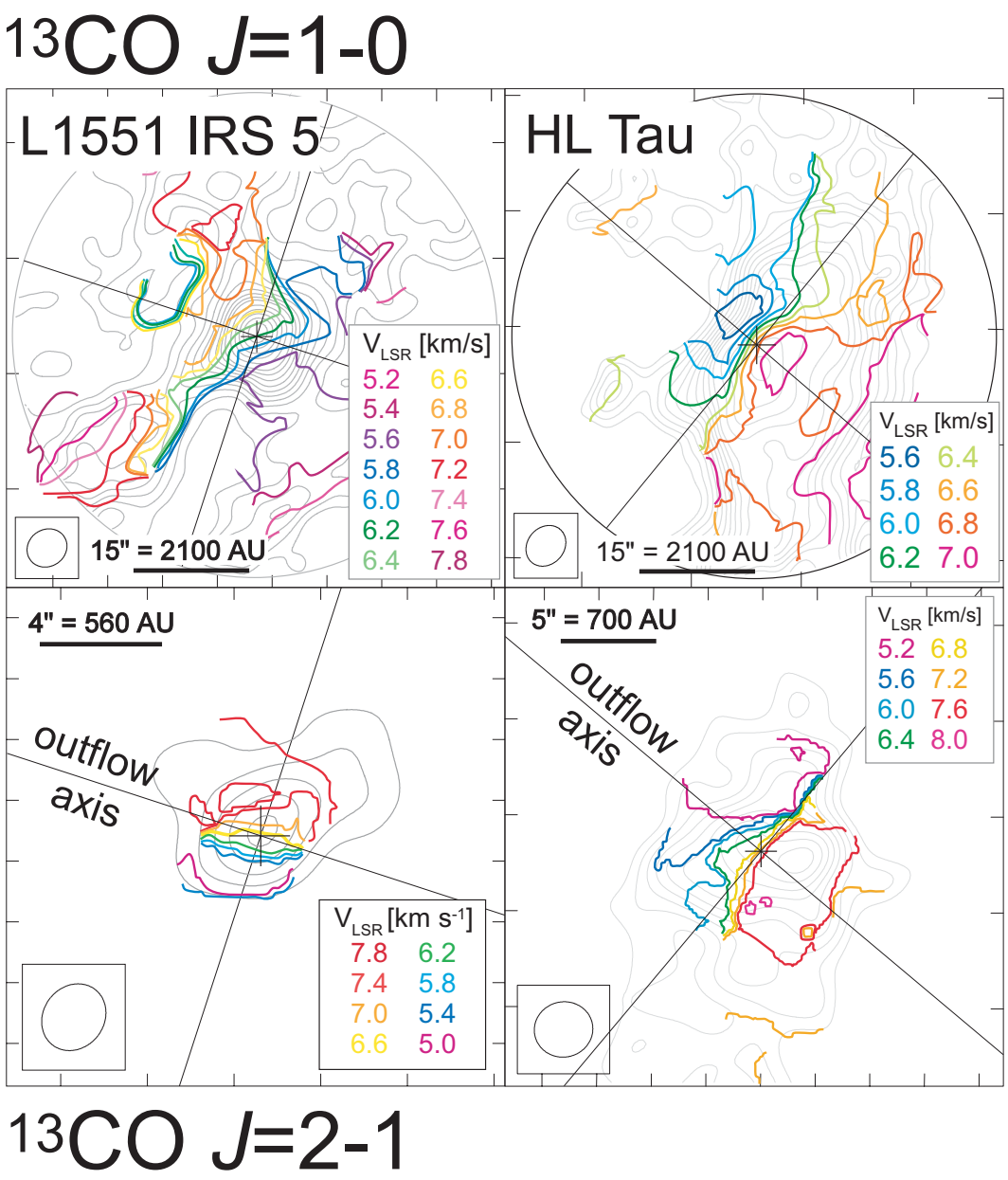

Figure 6.2: Intensity-weighted mean velocity maps of the binary protostar L1551 IRS 5 (left panels) and the single protostar HL Tau (right panels) both in ^{13}CO $J = 1 - 0$ (upper panels) and $J = 2 - 1$ (lower panels) emission. The integrated intensity maps of each map are shown by gray lines. The cross lines which across the field of views indicate the major and minor axes (P.A. = 160° for IRS 5, P.A. = 140° for HL Tau).

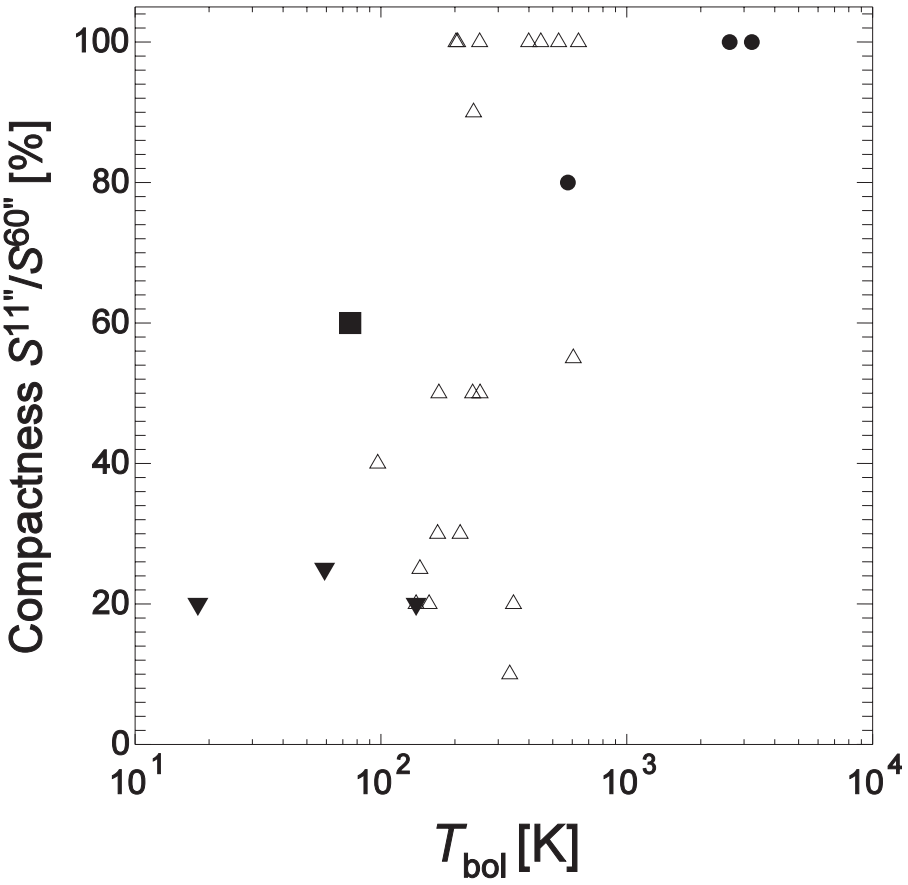

Figure 6.3: Compactness of 1.3 mm continuum emission of YSOs in the TMC. The vertical axis shows the ratio of the peak flux density in an 11″ beam to the total flux density in a 60″ diameter circle. All the data are compiled from the survey with the IRAM 30 m telescope (Motte & André 2001). The filled triangles show class 0 objects, the open triangles show class I objects, and the filled circles show class II objects. The filled square indicates L1551 NE.

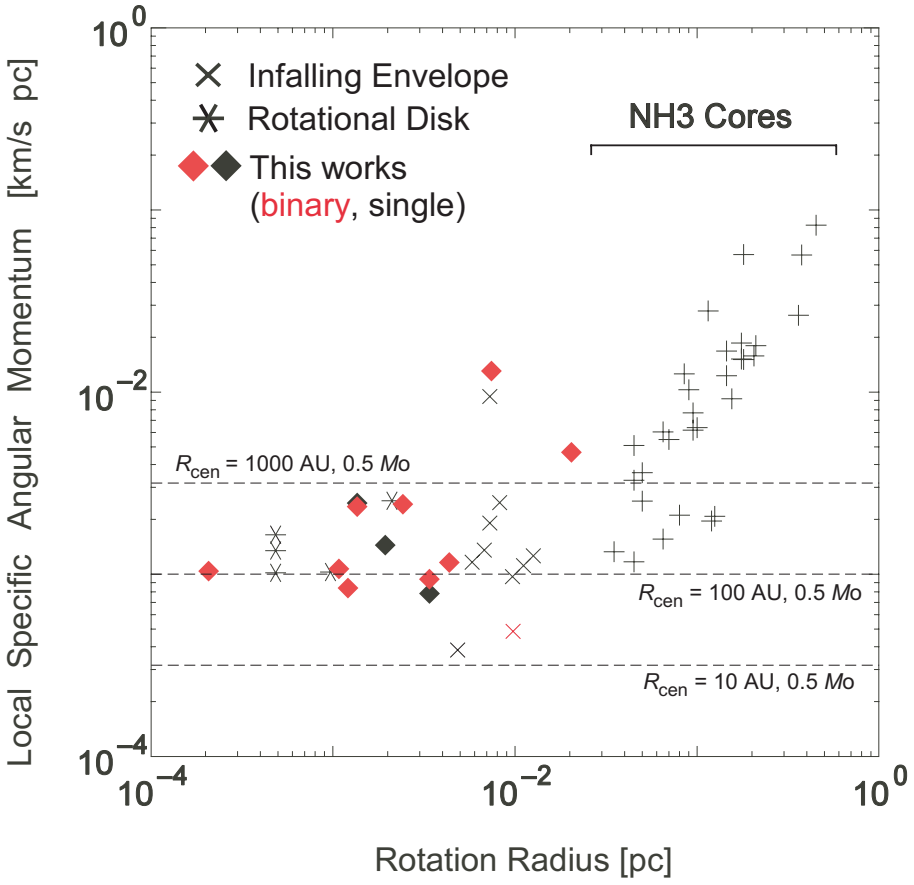

Figure 6.4: Local specific angular momentum plotted as a function of the rotation radius. Crosses represent data for NH3 cores (Goodman et al. 1993). Asterisks represent data of Keplerian rotating disk. Red color symbols indicates the binary sources. Diamonds indicate the protostars which we observed: L1551 IRS5, L1551 NE, HL Tau and Haro 6-5B.

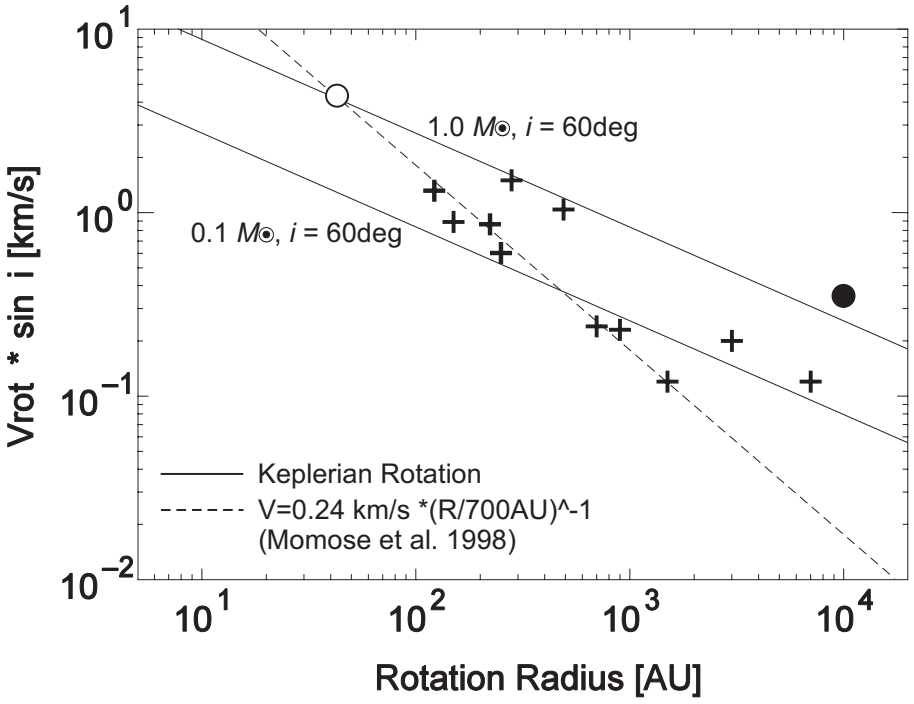

Figure 6.5: Rotation velocities of the envelope around L1551 IRS 5 as a function of the rotation radii. An open circle indicates the data of the binary stars taken by the VLA (Rodríguez et al. 2003). A filled circle indicate the large scale envelope taken by Kaifu et al. (1984). The other data are compiled from (Sargent, Keene, Masson, & Beckwith 1988; Ohashi et al. 1996; Saito, Kawabe, Kitamura, & Sunada 1996; Momose et al. 1998, This work).

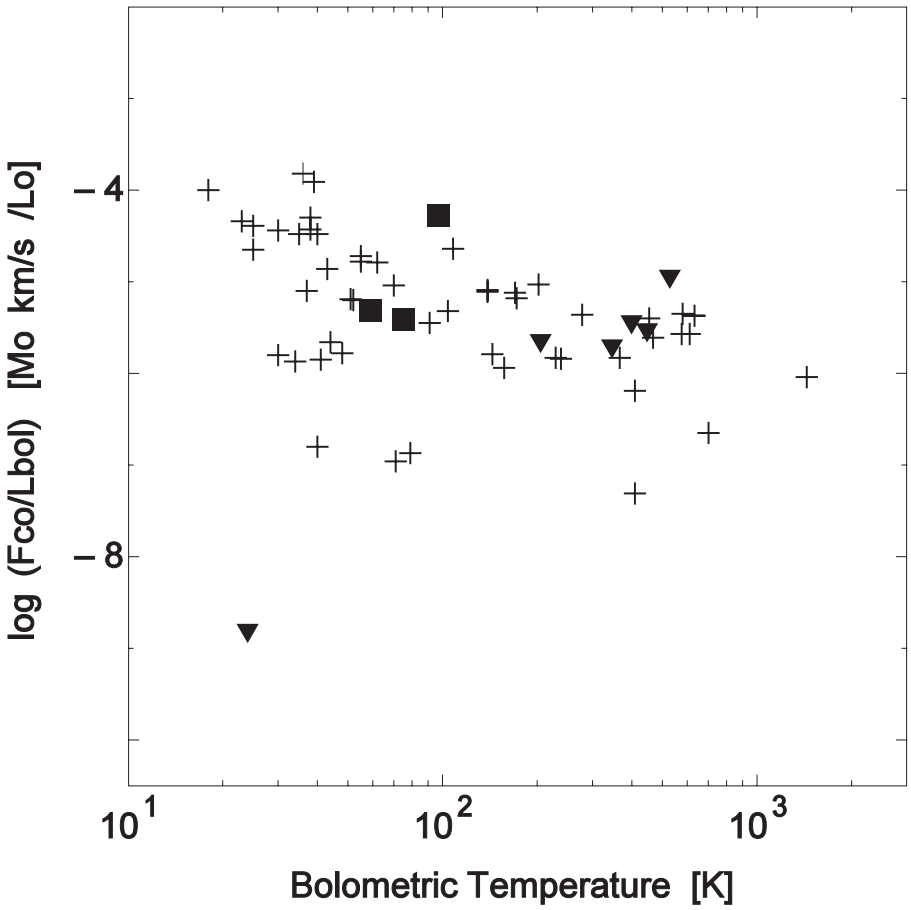

Figure 6.6: A ratio of momentum flux of CO outflow and bolometric luminosity as a function of bolometric temperature. Triangles indicate upper limit. Squares indicate the binary protostar in the TMC: L1551 NE, L1551 IRS 5 and L1527 (Furuya et al. 2003).

Bibliography

Adams, F. C., Lada, C. J., & Shu, F. H. 1987, ApJ, 312, 788

Adams, F., Lada, C., & Shu, F. 1988, ApJ, 326, 865

Andre, P., Ward-Thompson, D., & Barsony, M. 1993, ApJ, 406, 122

Artymowicz, P., Clarke, C. J., Lubow, S. H., & Pringle, J. E. 1991, ApJ, 370, L35

Bachiller, R., Tafalla, M., & Cernicharo, J. 1994, ApJ, 425, L93

Bachiller, R. & Perez Gutierrez, M. 1997, ApJ, 487, L93

Bally, J., Feigelson, E., & Reipurth, B. 2003, ApJ, 584, 843

Barsony, M. & Chandler, C. J. 1993, ApJ, 406, L71

Beckwith, S. V. W., Sargent, A. I., Chini, R. S., & Guesten, R. 1990, AJ, 99, 924

Beckwith, S., & Sargent, A. 1991, ApJ, 381, 250

Beuther, H., Schilke, P., & Stanke, T. 2003, ArXiv Astrophysics e-prints, 6101

Blaauw, A. 1991, NATO ASIC Proc. 342: The Physics of Star Formation and Early Stellar Evolution, 125

Cabrit, S., Guilloteau, S., Andre, P., Bertout, C., Montmerle, T., & Schuster, K. 1996, A&A, 305, 527

Close, L. M., Roddier, F., Northcott, M. J., Roddier, C., & Graves, J. E. 1997, ApJ, 478, 766

Close, L. M. et al. 1997, ApJ, 489, 210

Devine, D., Reipurth, B., & Bally, J. 1999, AJ, 118, 972

Downes, T. P. & Ray, T. P. 1999, A&A, 345, 977

Dutrey, A., Guilloteau, S., Durvert, G., Prato, L., Schuster, K., & Menard, F. 1996, A&A, 309, 493

Dutrey, A., Guilloteau, S., Prato, L., Simon, M., Duvert, G., Schuster, K., & Menard, F. 1998, A&A, 338, L63

Eislöfeel, J., & Mundt, R. 1998. AJ, 115, 1554

Elias, J. H. 1978. ApJ, 224, 857

Elmegreen, B. G. & Lada, C. J. 1977, ApJ, 214, 725

Emerson, J. P., Harris, S., Jennings, R. E., Beichman, C. A., Baud, B., Beintema, D. A., Wesselius, P. R., & Marsden, P. L. 1984, ApJ, 278, L49

Fridlund, C. V. M. & Liseau, R. 1994, A&A, 292, 631

Fuller, G. A., Ladd, E. F., Padman, R., Myers, P. C., & Adams, F. C. 1995, ApJ, 454, 862

Gledhill, T. M., Warren-Smith, R., F., & Scarrot, S. M. 1986, MNRAS, 223, 867

Gomez, M., Hartmann, L., Kenyon, S. J., & Hewett, R. 1993, AJ, 105, 1927

Hartmann, L., Calvet, N., Gullbring, E., & D'Alessio, P. 1998, ApJ, 495, 385

Hayashi, C., Nakazawa, K., & Nakagawa, Y. 1985, in Protostars and Planets II, ed. D. C. Black & M. S. Matthews (Tucson: Univ. Arizona Press), 1100

Hayashi, M., Ohashi, N., & Miyama, S. M. 1993, ApJ, 418, L71

Itoh, Y. et al. 2000, PASJ, 52, 81

Kaifu, N. et al. 1984, A&A, 134, 7

Keene, J. & Masson, C. R. 1990, ApJ, 355, 635

Kenyon, S., & Hartmann, L. 1995, ApJS, 101, 117

Kitamura, Y., Momose, M., Yokogawa, S., Kawabe, R., Tamura, M., & Ida, S. 2002, ApJ, 581, 357

Konigl, A. & Pudritz, R. E. 2000, Protostars and Planets IV, 759

Krist, J. E. et al. 1998, ApJ, 501, 841

Lada, C. J. 1987, IAU Symp. 115: Star Forming Regions, 115, 1

Lada, C. J. & Fich, M. 1996, ApJ, 459, 638

Lay, O. P., Carlstrom, J. E., & Hills, R. E. 1997, ApJ, 489, 917

Linke, R. A. & Goldsmith, P. F. 1980, ApJ, 235, 437

Liseau, R. & Sandell, G. 1986, ApJ, 304, 459

Looney, L. W., Mundy, L. G., & Welch, W. J. 1997, ApJ, 484, L157

Looney, L. W., Mundy, L. G., & Welch, W. J. 2000, ApJ, 529, 477

Lubow, S. H. & Artymowicz, P. 2000, Protostars and Planets IV, 731

Masunaga, H., & Inutsuka, S. 2000, ApJ, 531, 350

Menten, K. M., Harju, J., Olano, C. A., & Walmsley, C. M. 1989, A&A, 223, 258

Momose, M., Ohashi, N., Kawabe, R., Nakano, T., & Hayashi, M. 1998, ApJ, 504, 314

Moriarty-Schieven, G. H., Wannier, P. G., Keene, J., & Tamura, M. 1994, ApJ, 436, 800

Moriarty-Schieven, G. H., Powers, J. A., Butner, H. M., Wannier, P. G., & Keene, J. 2000, ApJ, 533, L143

Motte, F. & André, P. 2001, A&A, 365, 440

Mundt, R., B*ü*hrke, T., Fried, J.W., Neckel, T., Sarcander, & M., Stocke, J. 1984, A&A, 140, 17

Mundt, R., Brugel, E.W., &

Mundt, R., Buehrke, T., Solf, J., Ray, T. P., & Raga, A. C. 1990, A&A, 232, 37

Mundy, L. G. et al. 1996, ApJ, 464, L169

Nakamoto, T. & Nakagawa, Y. 1995, ApJ, 445, 330

Ohashi, N., Hayashi, M., Kawabe, R., & Ishiguro, M. 1996, ApJ, 466, 317

Ohashi, N., Hayashi, M., Ho, P. T. P., Momose, M., & Hirano, N. 1996, ApJ, 466, 957

Ohashi, N., Hayashi, M., Ho, P. T. P., Momose, M., Tamura, M., Hirano, N., & Sargent, A. I. 1997, ApJ, 488, 317

Okumura, S. K. et al. 2000, PASJ, 52, 393

Onishi, T., Mizuno, A., Kawamura, A., Tachihara, K., & Fukui, Y. 2002, ApJ, 575, 950

Osorio, M., D'Alessio, P., Muzerolle, J., Calvet, N., & Hartmann, L. 2003, ApJ, 586, 1148

Osterloh, M., & Beckwith, S. 1995, ApJ, 439, 288

Padgett, D. L., Brandner, W., Stapelfeldt, K. R., Strom, S. E., Terebey, S., & Koerner, D. 1999, AJ, 117, 1490

Plambeck, R. L. & Snell, R. L. 1995, ApJ, 446, 234

Pyo, T., Hayashi, M., Kobayashi, N., Terada, H., Goto, M., Yamashita, T., Tokunaga, A. T., & Itoh, Y. 2002, ApJ, 570, 724

Reipurth, B., Krügel, E., Kreysa, E., & Sievers, A. 1993, A&A, 273, 221

Reipurth, B., Bally, J., & Devine, D. 1997, AJ, 114, 2708

Reipurth, B., Yu, K., Heathcote, S., Bally, J., & Rodríguez, L. F. 2000, AJ, 120, 1449

Reipurth, B. & Bally, J. 2001, ARA&A, 39, 403

Reipurth, B., Rodríguez, L. F., Anglada, G., & Bally, J. 2002, AJ, 124, 1045

Rodriguez, L. F., Canto, J., Torrelles, J. M., & Ho, P. T. P. 1986,ApJ, 301, L25

Rodriguez, L. F., Canto, J., Torrelles, J. M., Gomez, J. F., Anglada, G., & Ho, P. T. P. 1994, ApJ, 427, L103

Rodriguez, L. F. et al. 1998, Nature, 395, 355

Rodríguez, L. F., Curiel, S., Cantó, J., Loinard, L., Raga, A. C., & Torrelles, J. M. 2003, ApJ, 583, 330

Saito, M., Kawabe, R., Kitamura, Y., & Sunada, K. 1996, ApJ, 473, 464

Saito, M., Kawabe, R., Kitamura, Y., & Sunada, K. 2001, ApJ, 547, 840

Sargent, A. I. & Beckwith, S. 1987, ApJ, 323, 294

Sargent, A. I., Keene, J., Masson, C., & Beckwith, S. 1988, ApJ, 333, 936

Sargent, A. I. & Beckwith, S. V. W. 1991, ApJ, 382, L31

Scoville, N. Z., Sargent, A. I., Sanders, D. B., Claussen, M. J., Masson, C. R., Lo, K. Y., & Phillips, T. G. 1986, ApJ, 303, 416

Shu, F. H., Ruden, S. P., Lada, C. J., & Lizano, S. 1991, ApJ, 370, L31

Smith, M. D., Suttner, G., & Yorke, H. W. 1997, A&A, 323, 223

Stapelfeldt, K. R. et al. 1995, ApJ, 449, 888

Strom, K., Strom, S., Edwards, S., Cabrit, S., & Skkrutskie, M. 1989, AJ, 97, 1451

Vrba, F. J., & Rydgren, A. E., Zac, D. S. 1985, AJ, 90, 2074

Welch, W. J., Hartmann, L., Helfer, T., & Briceño, C. 2000, ApJ, 540, 362

Wilking, B. A., Lada, C. J., & Young, E. T. 1989, ApJ, 340, 823

Wilner, D. J., Ho, P. T. P., & Rodriguez, L. F. 1996, ApJ, 470, L117

Yokogawa, S., Kitamura, Y., Momose, M., Asaki, Y., Tamura, M., Ida, S., & Kawabe, R. 2001, ApJ, 552, L59

Yokogawa, S., Kitamura, Y., Momose, M., & Kawabe, R. 2003, ApJ, 595, 266

Yokogawa, S., Kitamura, Y., Momose, M., Bando, M., & Kawabe, R. submitted to ApJ